The Fates of Mesenchymal Stem Cells and Perivascular Cells in Eye Disease

---

A Dissertation

Presented to

the faculty of the School of Engineering and Applied Science

University of Virginia

---

in partial fulfillment
of the requirements for the degree

Doctor of Philosophy

by

Howard Clifton Ray III

May 2019

APPROVAL SHEET

This Dissertation
is submitted in partial fulfillment of the requirements
for the degree of
Doctor of Philosophy

Author Signature: 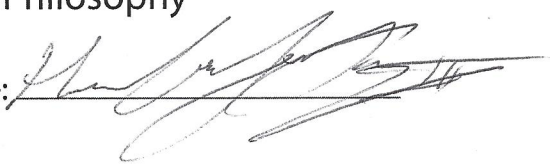

This Dissertation has been read and approved by the examining committee:

Advisor: Paul Yates, M.D., Ph.D.

Committee Member: Shayn Peirce-Cottler, Ph.D.

Committee Member: Tom Barker, Ph.D.

Committee Member: Jenny Munson, Ph.D.

Committee Member: Gary Owens, Ph.D.

Committee Member: Eli Zunder, Ph.D.

Accepted for the School of Engineering and Applied Science:

Craig H. Benson, School of Engineering and Applied Science

May 2019

DEDICATION

I am extremely grateful for being able to go through this graduate school journey, and there are many individuals that deserve substantial amount of credit for leading, teaching, and encouraging me throughout these last several years. I have to first thank my mentor, Dr. Yates, for bringing me into the lab and challenging me in my research and scientific skills. There were many times where I felt that I could not solve the many issues and problems of graduate school and research, but you would often have me push through and overcome the challenges with your ingenuity and support. I will also remember how you imparted in me the importance of scientific diligence and virtue, and I will look to hold to these standards in the future. I would also like to say thank you to my co-advisor Dr. Peirce-Cottler and her support with my research project. You essentially adopted me as another graduate student and was always open to mentoring me into a better scientist. Your generosity and collaborative spirit really inspires me to do the same with others.

I would like to say a big thank you to my thesis committee for challenging me in my graduate school career and providing direction for my project. Dr. Owens, thank you for your support and teaching on vascular smooth muscle cells and pericytes, as well as your mentoring during my short time on the cardiovascular research training grant. Dr. Munson, thank you for your support in my teaching assistant tenure in IDEAS lab, your advice on *in vitro* culture systems, and your willingness to give career advice. Dr. Zunder, thank you for teaching and assisting me with mass cytometry experiments within MSCs, and thank you for also sharing your general knowledge of stem cells. Dr. Barker, thank you for your sharing your expertise on fibrosis and your perspective on perivascular cells contributing to the fibrotic lineage.

My lab research journey first started out at Central Virginia Governor's School for Science and Technology, and I would like to thank Dr. Lindeman and Ms. Beasley for assisting me in my first true scientific research project, which examined how zinc and vitamin C controlled for planarian worm regeneration. These two individuals are to thank for steering me in the right direction from the beginning because during this time I became interested in biomedical engineering, which I pursued as a degree in my undergraduate career. In undergrad, I was able to work with Dr. Reichert and Dr. Satterwhite, who mentored me on a research project that explored constructing vasculature networks and tissue-engineered vascular grafts. This research experience helped shape my scientific interest and preliminary research skills, which I used almost every day in my graduate school career.

To the members in the Yates and Peirce-Cottler lab, I would like to thank you for your encouragement and help, too. It was pleasure working alongside everyone. I will miss our lab social outings, happy hours, lunches, dinners, and even the occasional amusement park trips. Bijan, thank you for mentoring me early in my graduate school career during your time as a post-doc in the Yates' lab. Your assistance early on pushed my Ph.D. project forward and helped shape it to what it is today. Max, although you came into the lab late in my Ph.D. training, I would like to thank you for your help in my project and stepping up to help me with experiments when needed.

Anthony, thank you for managing the lab work and mouse breeding work that you provided; this work would have largely been impossible if not for your assistance and hard work. Scott, Joe, Kyle, Bruce and Molly thank you for working alongside me and assisting me with my research. To the "younger" lab members—Sadegh, Bill, Michaela, Lee, Riley, and Helen—thank you as well. It was a joy to be in lab with all of you, and I wish you all success in your own careers. Thank you to my undergraduate research assistants, Janice, Jennifer, and Sam. Your energy and enthusiasm rejuvenated me throughout my time here, and it was great seeing how I could help with your career goals after undergrad.

To everyone else in the department, I would like to say thank you as well. Many of you have inspired and motivated me during my time at UVa. It was awesome being able to escape from lab and bond over our similar hobbies and interests. Scott and Sameer, I would like to thank you two especially for giving me constant every day sports talk entertainment. Also, thank you to my soccer team and workout buddies for allowing me to capture the joy of sports and the days of being an athlete.

Thank you to my friends and family for your encouragement, and pushing me to strive for excellence throughout my education journey. I know all of you were there for me and were always eager to check on me and my sanity. Thank you Mom and Dad for having me see the importance of education and instilling the importance of perseverance and hard-work in my life. Your parenting was so important to creating me into the person I am today. Thank you GeKeela, Tyler, and Megan for being supportive siblings and making everyday fun and blissful. I could not have asked for a better support group than you guys.

Lastly, I would like to thank my wife and best friend, Amber. You have displayed incredible patience, love, and encouragement while I pursued my Ph.D. At times I felt like quitting, but you were there to pick me back up on my feet and place a smile on my face. Just being able to step out of the lab and be in your presence made my day. This Ph.D. could not have been done without your support and I am forever grateful to you.

CONTENTS

LIST OF FIGURES AND TABLES

ABSTRACT

Degenerative eye diseases, such as diabetic retinopathy, threaten the vision of millions of people across the world. Current treatment strategies, such as small molecule therapy and laser photocoagulation, attempt to slow the breakdown of diseased tissue, but fail to regenerate damaged ocular tissue. Furthermore, these clinical interventions are often destructive, leaving patients with few safe and viable treatment options. The use of adult mesenchymal stem cells (MSCs) in the treatment of ocular diseases could be a novel approach to addressing these issues. Mesenchymal stem cells are regarded as multipotent, pro-angiogenic, and immunomodulatory cells that, when locally delivered, could potentially regenerate healthy ocular tissue through multiple modes of action. However, questions remain about the origin and cellular function of MSCs due to discrepancies across studies, which make it difficult to predict therapeutic efficacy. Also, recent delivery of MSCs into the eyes of human patients has led to detrimental side-effects, including vision loss, further demonstrating a poor understanding of the innate behavior of MSCs. To fully appreciate a MSC-based therapy for ocular diseases, we need a refined understanding of both MSC *in vitro* and *in vivo* cell behavior. Thus, the overall goal of this work was to (i) investigate the cell fates of MSCs once delivered into eye diseases, and (ii) determine if these fates also correspond with those found in the endogenous, perivascular MSC population that is activated in the wound healing of ocular disease. Throughout this thesis, we develop and apply novel statistical models, transgenic mice, and preclinical eye injury models to ascertain MSC bioactivity and cellular differentiation into specific cell types. The work presented in this thesis highlights: (i) determining the proclivity of adipose-derived mesenchymal stem cells to adopt a perivascular support position in ischemic retinal neovascularization, (ii) evaluating adipose vascular smooth muscle cells and pericytes as a newly defined source of mesenchymal stem cells that improve retinal vascular growth, while (iii) also identifying retinal vascular smooth muscle cells and pericytes as a contributor to retinal fibrosis, and (iv) demonstrating mesenchymal stem cells as a potential cell source to replace damaged corneal endothelial cells in cornea injury. Taken together, this work provides insight on the complexity of MSCs and promotes the strategic engineering of these cells to provide both a safe and effective therapy for eye diseases.

CHAPTER 1

INTRODUCTION

Diabetic Retinopathy

The United States is currently facing a health, societal, and financial crisis around diabetes mellitus. As of now, there are over 35 million people in the United States with diabetes, and this population is expected to increase by 54% to approximately 55 million people in the year 2030[1]. The increasing prevalence of diabetes, and not increased patient costs[2], is projected to cost the United States $622 billion in 2030. Worldwide, the projected trends of diabetes prevalence are similar to the United States, with 382 million people of the world's population with diabetes is expected to increase to approximately 600 million people in 2035[3]. Unfortunately, the diabetes epidemic is estimated to cost the world $2.2 trillion in medical and societal costs[4].

The consequence of the hyperglycemia in both type 1 and type 2 diabetes results in chronic neurological, macrovasculature, and microvasculature complications throughout the body[5,6]. Diabetic retinopathy (DR), a diabetic complication that leads to the breakdown of the retinal microvasculature in the eye, is responsible for one of the leading causes of vision impairment and blindness in working adults[7,8]. The estimated global prevalence of DR among diabetic patients is 35.4%, with prevalence of DR higher in type 1 diabetes (77.3%) than type 2 diabetes (25.2%)[9–11].

The exact pathological mechanisms in which hyperglycemia damages the retinal microvasculature still remain elusive, however, the breakdown of blood vessels is largely due to the biochemical and metabolic changes associated with the increase in blood glucose. In the presence of high glucose, there is an increase in the activation of the hexosamine and protein kinase C (PKC) pathway, as well as an increase in polyols, reactive oxygen species, and advanced glycation end (AGE) products[12–16]. The accumulation of these changes produces cytokines, chemokines, and growth factors that consequently contributes to retinal hypoxia, inflammation, and the eventual destruction of the retinal microvasculature. At the early stage of this disease

progression, which is clinically diagnosed as non-proliferative DR (NPDR), the retina often features soft exudates, venous beading, and microanneuryms, which can result in some vision loss due to edema[17]. As the disease worsens to the proliferative phase (PDR), retinal microvasculature dysfunction increases, leading to the upregulation of vascular endothelial growth factor (VEGF). In turn, retinal angiogenesis ensues, leading to the induction of preretinal or vitreous hemorrhaging, macular edema, and fibrosis. If PDR is left untreated, diabetic patients can experience retinal detachment resulting in blindness.

Current Clinical Treatments for DR

The pathophysiology of DR begins with chronic hyperglycemia, thus reducing blood glucose levels in diabetic patients has traditionally been explored as a treatment option for DR. Although results vary from different reports, multiple clinical trials demonstrate that controlling diabetic patients blood glucose levels can potentially prevent the onset and progression of DR[18–23]. However, meta-analysis of observational studies has recently suggested through that that insulin therapy is associated with the increased risk of macular edema[24]. Also, there is evidence reported by the Diabetes Control and Complications Trial that intensive blood glucose control results in early worsening of DR[25]. Similarly, other groups find that intensive insulin therapy may be detrimental in increasing the severity of DR[26–28]. To somewhat explain these enigmatic findings around intensive blood glucose control, one research group has suggested that exogenous insulin acts synergistically with VEGF to promote neovascularization and the progression of DR[29].

When DR does progress and diabetic patients become symptomatic, the gold-standard clinical treatment of DR is laser photocoagulation. This paradoxical treatment focuses on burning, killing, and scaring the peripheral retinal tissue in order to close leaky peripheral blood vessels, increase oxygenation to the inner retina, and upregulate antiangiogenic factors released from the

retinal pigment epithelium[30,31]. Although laser photocoagulation decreases the chance of edema and vision loss[32,33], this treatment results in the reduction of contrast sensitivity, peripheral vision, and night vision[34,35].

As mentioned above, the breakdown of the retinal vasculature from chronic hyperglycemia prompts the upregulation of VEGF within the retina. Within clinical trials, the intravitreal injection of monoclonal anti-VEGF antibodies, including afibercept (EYLEA®)[36], bevacizumab (Avastin®)[37], pegaptanib (Macugen®)[38], and ranibizumab (Lucentis®)[39,40], has demonstrated some improvement in reducing symptoms and visual outcomes over laser and sham treatment in DR patients. However, there are some adverse risks associated with these injections, such as the increase in intraocular pressure, hemorrhaging, and inflammation. Furthermore, while eliminating VEGF limits neovascularization and leaky retinal blood vessels, there is concern that the constant and chronic removal of VEGF may have a negative impact on neuronal[41] and photoreceptor cell physiology[41]. Lastly, ocular anti-VEGF therapies are exceedingly expensive and inconvenient, as DR patients need monthly or bimonthly intravitreal injections due to the relative short half-life of anti-VEGF antibodies.

Laser photocoagulation technology is improving and new therapeutic agents to target other molecules are currently being explored. Still, the current clinical treatments fail to target the multiple molecular and pathophysiology pathways of DR, which neglects the repair of the retinal microvasculature and regeneration of damaged tissue. The limitation of the current clinical treatments warrants an investigation for a more systematic approach for treatment, where multiple pathways negatively impacted by chronic hyperglycemia are targeted, particularly in regards to restoring healthy retinal microvasculature.

Mesenchymal Stem Cells (MSCs) as a Treatment Option for DR

In the 1960s and 1970s, Friedenstein and colleagues discovered a subset of cells that existed within the stroma of bone marrow that attached to plastic and formed distinct fibroblastic colonies (CFU-Fs)[42–44]. The "stem cell" aspect of these bone marrow stromal cells would later be displayed after the progeny of the bone marrow stromal cells generated bone, fibrous tissue, cartilage, and adipose after *in vivo* transplantation[45]. In 1991, the term "mesenchymal stem cell" (MSCS) by Arnold Caplan was given to the particular bone stromal cells first investigated by Friedenstein and his coworkers[46]. In 2006, the International Society for Cellular Therapy (ISCT) met and defined the criteria to define MSCs once harvested from a donor: 1) cells adhere to plastic, 2) cells are capable of differentiating into chondrocytes, adipocytes, and osteocytes, 3) cells are CD105+, CD73+, CD90+, and 4) cells are CD45-, CD34-, CD11b-, CD14-, CD79a-, HLA-, HLA-DR-[47]. Additional reports now suggest that other surface markers such as STRO-1, CD29, CD44, CD106, and CD146 also mark MSCs *in vitro* and *in vivo*, with some these surface markers differing across tissue[48–50]. Furthermore, human MSCs are now implied to differentiate into mesoderm, endoderm, and ectoderm lineages *in vitro*[50]. However, the three-germ layer differentiation capability of MSCs has not been adequately conferred *in vivo*, largely in part of the lack of fate-tracing technology and in-depth protein and genetic analysis of *in vivo* delivered MSCs.

Expanding on the original work on MSCs, research groups have now demonstrated MSCs can be isolated in adult tissues outside of bone mostly through the use of enzymatic digestion and filtration of the stromal vascular fraction (SVF), specifically the SVF of adipose tissue, heart, liver, dental tissue, Wharton's jelly, skin, salivary glands, and the skin[51]. The exact origin(s) of MSCs still remains elusive, however, reports points to perivascular cells, such as PCs, fibroblasts, macrophages, and adventitial cells, harboring the assumed identity of MSCs[52–56]. It is even

suggested that *in vivo,* the perivascular source of MSCs are able to differentiate into a MSC-like state and provide paracrine support or direct cell differentiation to repair wounded tissue[57,58], however, this hypothesis is still debated in the scientific community[55].

In recent years, the promise of MSC regenerative therapy has generated much interest and even controversy around its safety and therapeutic efficacy. From a practical standpoint, MSCs are an attractive cellular therapeutic due to their ability to expand abundantly in culture in a relatively short amount of time throughout multiple passages. With MSCs being multipotent, low immunogenic, and immunomodulatory cells, MSCs are often investigated as a biological therapy for chronic diseases[59–63]. Shown through various work, MSCs are argued to repair tissue through different mechanisms, including the secretion of paracrine activity that promotes wound healing, direct cell replacement through cell differentiation, the release of extracellular vesicles (EVs), and the transfer of molecules organelles such as mitochondria through tunneling nanotubes[64]. Given the amount of research conducted on MSCs, we summarize the potential MSC bioactivity that could be therapeutically beneficial once MSCs are locally injected into DR patients (Figure 1.1). It is still unclear on which MSC mechanisms are favored in the context of locally delivery into the eye, however, we will discuss in more detail in the next section below the main MSC bioactivities that would be successful in treating DR, as well as other eye diseases.

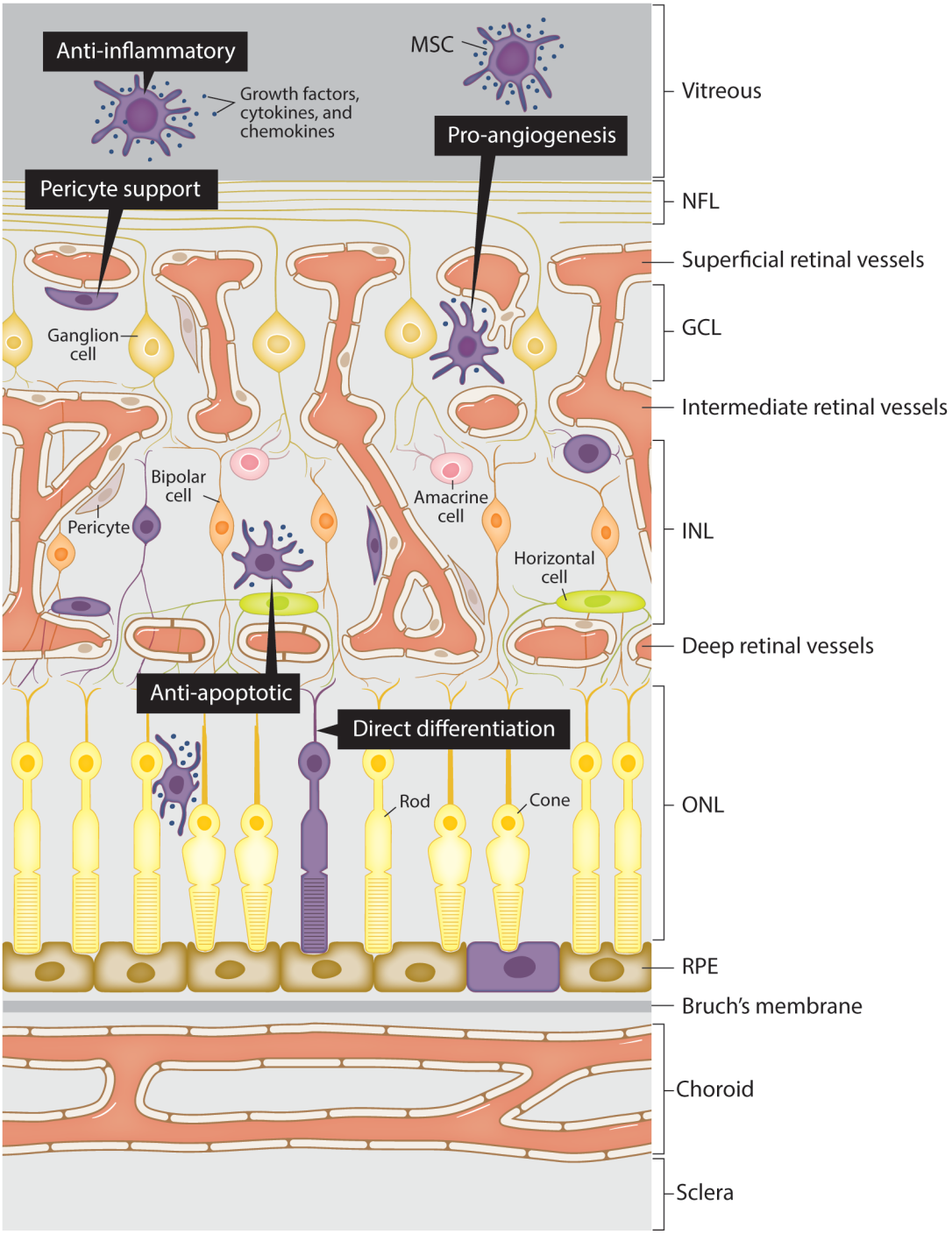

Figure 1.1 Dynamics of mesenchymal stem cells (MSCs) in the wound healing process of diabetic retinopathy (DR).
Within DR, delivered MSCs (purple) are able to integrate into different parts of the retina and provide direct structural support through differentiation into specialized or specialized-like cells. MSCs are also able to remodel and heal tissue through trophic secretion of pro-angiogenic factors, anti-inflammatory factors, and anti-apoptotic factors. Abbreviations: NFL: nerve fiber layer, GCL: ganglion cell layer, INL: inner nuclear layer, ONL: outer nuclear layer.

Different Target Mechanisms of MSC Therapy

Restoring and Protecting the Retinal Vasculature

The degeneration of the retinal vasculature is a hallmark of DR, where the progression of the disease is strongly correlated with the health of the retinal vasculature. In view of this, most of the work presented in this thesis, particularly within Chapter 2 and Chapter 3, will focus on the MSC therapy around restoring and remodeling the vasculature in preclinical DR models. As described above, the molecular dysfunction caused by chronic hyperglycemia has a devastating impact on the retinal microvasculature, and this is particularly true for retinal perivascular cells. In the 1960s, Cogan discovered that during the progression of diabetes, the retinal pericytes—cells that ensheath the microsvasculature by direct cell contact with endothelial cells—are decreased in number.[65] Approximately forty years later, it was discovered that both the retinal pericytes and vascular smooth muscle cells were also loss during diabetes[66,67]. When vascular smooth muscle cell and pericyte coverage decreases, the retinal vessels regress, resulting in ischemia within the retinal tissue.

Chronic hyperglycemia also produces physiological changes within retinal endothelial cells. The exposure to high glucose leads to mitochondrial fragmentation and the disruption of connexin 43 and ZO-1 junctional binding, both of which trigger apoptosis in the retinal endothelial cells[68]. Unsurprisingly, the breakdown of the retinal vasculature has a downstream effect on the surrounding neural retinal cell populations. In response to the ischemia, the retinal ganglion cells[69] and Müeller glial cells[70] secrete VEGF in an attempt to restore loss retinal vasculature coverage, and thus, perfusion of oxygen and nutrients across the retinal tissue. However, this attempt to re-perfuse the tissue results in leaky vessels, and in turn, edema and occasionally scarring can occur in the retina. If these symptoms are left unchecked, patients most likely will lose their vision.

There is considerable evidence that advocates exogenously delivered MSCs can rescue the ischemic retinal tissue, particularly found in NPDR patients, by stimulating a healthy proangiogenic response. Injection of MSCs into the ischemic environments of hindlimb acute ischemia[71–74] and myocardial infarction[75–78] preclinical models indicate that MSCs promote neovascularization, and consequently, the preservation or rescue of tissue function. Most of therapeutic benefit, particularly the blood vessel growth, is contributed to the paracrine response of injected MSCs since there is low engraftment and cell viability of the transplanted MSCs[79]. March and colleagues have reported that injected human adipose-derived MSCs in hindlimb ischemia murine models contribute to the formation of functional revascularization rather than pathologic angiogenesis[80]. The authors suggest this finding was largely due to the paracrine response of the injected MSCs because of the significant detected *in vitro* levels of VEGF, hepatocyte growth factor (HGF), and transforming growth factor-beta (TGF-β). Kwon et al. further expanded on this finding and demonstrated that the conditioned media of human MSCs contains relatively high concentrations of VEGF, HGF, monocyte chemotactic protein-1 (MCP-1), interleukin-6 (IL-6), and TGFβ1[81]. The conditioned media alone was able to increase endothelial angiogenesis *in vitro,* as well as angiogenesis in acute hindlimb ischemia. Essentially, the secretion of pro-angiogenic factors by MSCs is equated to their exposure to pathologic hypoxic environments, as several groups demonstrate the upregulation of pro-angiognenic factors when cultured in hypoxia. Some of these augmented pro-angiogenic factors include VEGF, angiopoietin-1, hypoxia-inducible factor 1 (HIF-1), and matrix metalloproteinase-9 (MMP-9)[82–85]. Given these observations, it is expected that MSCs delivered in DR patients would have a similar trophic response given the ischemia retinal environment, thus prompting MSCs to release a paracrine profile to promote healthy retinal blood vessel growth. All together, these pro-angiogenic

secreted factors are recognized to work in tandem to promote endothelial cell and perivascular cell growth, migration, survival, and differentiation.

Similar to the release of cytokines and chemokines, MSCs are able to secrete pro-angiogenic miRNA in extracellular vesicles (EVs)—specifically, miR-30b, miR-30c, miR-424 and let-7f—that are transferred to endothelial cells to promote *in vitro* and *in vivo* angiogenesis[86]. In fact, it is also suggested that hypoxic exposure is responsible for increasing the release of EVs in MSCs and EV protein content that is associated with VEGF signaling[87]. The exact cellular and molecular mechanisms in which secreted EVs increase blood vessel growth is still misunderstood. However, it was demonstrated that MSC secreted EVs were able to increase endothelial network growth *in vitro* from the activation of gene expression of the wound healing Akt, ERK, and STAT signaling pathways[88]. Furthermore, it was observed that MSC secreted EVs activated endothelial cell trophic signaling pathways of hepatocyte growth factor (HGF), insulin-like growth factor-1 (IGF1), nerve growth factor (NGF), and stromal-derived growth factor-1 (SDF1). This suggests that the EVs contain protein and nucleotide content that serve as a positive feedback loop to generate the production of pro-angiogenic growth factors, cytokines, and chemokines.

In addition to MSCs releasing a complex paracrine profile to promote vasculature growth and integrity, MSCs also possess the ability to stabilize the aberrant retinal angiogenesis in DR though differentiation to perivascular support cells. In the process of angiogenesis, endothelial cells respond to angiogenic factors by migrating and proliferating to form tube networks, and afterwards, pericytes are attracted to the network to form a stable mature blood vessel[89]. It has been demonstrated that MSCs adopt a perivascular and smooth muscle phenotype when in contact with endothelial cells[90–92], and the differentiation of MSCs into more of a smooth muscle phenotype is enhanced with the pretreatment of TGFβ[93,94]. Similarly, pretreatment of MSCs with

angiotensin-II seems to enhance the migration, recruitment, and adhesion pathways of MSCs in relation to ECs, and thus increase EC tube network[95,96]. Because pericytes are often argued as the *in vivo* cell source of MSCs, it is not too surprising that reintroducing MSCs into tissue after transplantation or local delivery causes MSCs to readopt a perivascular position and stabilize blood vessel networks. Considering vascular smooth muscle cells and pericytes are loss in DR, it is expected that delivered MSCs could serve as a new reservoir of retinal perivascular cells, particularly in cases of PDR where retinal neovessels are present without pericyte coverage. This type of treatment strategy would ideally limit the microvascular dysfunction in DR patients by controlling for abnormal angiogenesis and protecting the existing retinal vasculature from further damage experienced by diabetes.

Neuronal Cell Protection

Chronic hyperglycemia also leads to the cell death of the neuronal cells, or the cells that are responsible for receiving and transmitting visual signals in the eye and to the brain. Neuronal cell apoptosis is caused by several pathways impacted by high blood glucose, including the upregulation of crystallins, inflammatory apoptosis induced by AGE products, and oxidative stress caused by the dependency on the polyol pathway[97]. At the early onset of diabetes, changes in neuronal cells are evident, as glial cell reactivity and metabolism are modified in the neuronal retina[98]. Later in the disease progression, PDR patients have a higher concentration of peripheral blood mononuclear cell reaction oxygen species (ROS), and vitreous nitrite and nitrotyrosine when compared between diabetic patients without DR and healthy patients[99]. Most notably, vitreous glutamate concentrations are also found at increased levels in PDR patients[99], and plasma glutamate concentrations are at a higher level in diabetic patients and animals when compared to

healthy controls[100]. The excessive amounts of glutamate elicits glutamate excitotoxicity, or the overstimulation of NMDA and AMPA receptors, which eventually evokes apoptosis to occur within the neuronal cell[97,101].

There is evidence to support MSC therapy in DR potentially reducing the neuronal damage caused by glutamate excitotoxicity. An *in vitro* model of murine neuronal cell death caused by glutamate excitotoxicity was protected after 24 h pre-treatment with murine bone marrow-derived MSCs[102]. The conditioned media derived from the MSCs was also found to be sufficient for *in vitro* neuronal protection, which was associated with decreased mRNA expression of NMDA receptor subunits. Lastly, this same report also demonstrated that exogenous MSCs protected against glutamate excitotoxicity *in vivo* within a kainic acid epilepsy murine model. Another study showed similar findings, where human adipose-derived MSCs and the conditioned media inhibited cell death and promoted nerve growth of rat cortical neurons within an *in vitro* model of glutamate excitotoxicity[103]. Interestingly, the authors of this study showed enhanced levels of ATP, NAD+, NADH, and NAD+/NADH while mitochondrial membrane potential was relatively unchanged. This result suggested that MSC conditioned media reduced cell apoptosis by regulating bioenergy pathways of the neurons.

The neural retina will upregulate neuroprotective soluble factors in the attempt to counteract the neural damage due to degenerative diseases. Ciliary neurotrophic factor (CNTF) is cytokine of particular interest due to its neuroprotection of photoreceptor cells, and neuroprotection and axogenesis of ganglion cells[104–106]. Similarly, glial cell-line-derived neurotrophic factor (GDNF) signaling has been attributed to the neuroprotection of photoreceptor cells and glial cells in retinal degeneration[103]. Within streptozotocin-induced diabetic rats, the intraocular delivery of GDNF is able to rescue apoptosis in retinal neurons through the

upregulation of GLAST, which is responsible for removing excess glutamate from the extracellular space of the retina[107]. When compared to the vitreous of nondiabetic patients, the vitreous of DR patients contain higher levels of brain-derived neurotrophic factor (BDNF), neurotrophin-3 (NT-3), and neurotrophin-4 (NT-4)[108]. BDNF and NTs are both suggested to promote neuronal cell survival through the TrkB signaling pathway[109].

MSCs have also promoted the cell survival and growth of neuronal cells in different models through the secretion of these neuroprotective factors. Human umbilical cord-derived MSCs secrete BDNF, GDNF, as well as NT-3[110]. Using the conditioned-media from these MSCs increased the viability and proliferation of Schwann cells, as well as the neurite growth in dorsal root ganglion explants. One group has demonstrated that MSCs derived from Wharton's Jelly and bone marrow exhibit paracrine profiles that also support neuroprotection and neurogenesis[111]. In this same report, primary rat neuron and glial cells neurite growth and cell survival was increased when co-cultured with either MSC population in a transmembrane system with either MSC populations.

When intravitreally injected in the rat glaucoma eyes[112,113] or optic nerve injury models[114,115], there are similar neuroprotective and neurodegenerative effects observed when MSCs are co-cultured with neuronal cells *in vitro*. In these models of retinal neuronal degeneration, bone marrow derived MSCs increase the survival of retinal ganglion cells and regenerate axon growth away from the cite of lesions. Interestingly, it was demonstrated that dental pulp-derived MSCs when compared to bone marrow-derived MSCs were able to further increase retinal ganglion cell survival and axon regeneration after intravitreal transplantation[115], suggesting that neural crest-derived MSCs may be more applicable in CNS diseases[116]. From these reports, the authors concluded that the neuroprotective effects were most likely caused from the paracrine

profile of the injected MSCs since there was no evidence of MSC differentiation into neuronal cell types. Therefore, when delivered in DR, MSCs would most likely provide neuroprotection through the release of soluble factors that promote neuronal cell growth and survival.

Immunomodulation

Inflammation is commonly involved in the wound healing process of most tissues, and there is substantial evidence to suggest that chronic inflammation is a major contributor to the pathology of DR[117]. Inflammation is largely induced by the oxidative stress, NF-κB activation, dysregulation of nitric oxide synthase (NOS), and the formation of advanced glycation endpducts (AGEs) in the retina[118], which leads to a buildup of inflammatory molecules in the retinal tissue. From reports examining the vitreous, serum and the retina of diabetic animal models and patients, there is an increase in pro-inflammatory markers, namely TNF-α[119–121], IL-1β[120,122,123], MCP-1[124], MIP[125], IL-6[126,127], ICAM-1[128], and VCAM-1[128,129]. With the accumulation of these cytokines and chemokines in the eye, blood vessels become leaky due to leukostasis, or the large recruitment and accumulation of leukocytes within the retinal blood vessels[130]. From the buildup of leukocytes inside the vessel walls, there is subsequently increase in endothelial cell apoptosis[131] and breakdown of the blood retinal barrier[132].

MSCs by their nature express little to no MHC I and MHC II molecules and co-stimulatory molecules, which protects them from natural killer cells[133]. In fact, when MSCs are exposed to a pro-inflammatory environment, MSCs typically respond by releasing or upregulating a series of immunosuppressive factors, such as indoleamine 2,3-dioxygenase (IDO), HGF, IL-10, TGFβ, iNOS, CXCL9, CXCL10, and CXCL11[134–137]. The secreted trophic response of MSC has an effect on different inflammatory mediators, including T cells. From the secretion of IL-1β by CD14+

monocytes[138] or treatment with TNFα and IFNγ[139], MSCs secrete multiple soluble factors to limit the proliferation of T cells. Similarly, in the presence of different populations of immune cells MSCs secrete trophic factors to shift the T cell helper state to an anti-inflammatory Th2 position[140]. From the measurement of cytokines in the serum of healthy and DR patients, Th1 cytokine secretion was found to be higher than Th2 cytokine secretion, suggesting a more pro-inflammatory state in the retina because of DR[141]. Given the strong cross-talk between inflammatory cells and MSCs, and the ability of MSCs shift the helper axis of T cells, the delivery of MSCs could potentially bring the state of the retina to an anti-inflammatory state, and thus, a more tissue regenerative environment.

The tissue-resident macrophages of the retina are microglial cells, and the activation of these cells are associated with DR symptoms. In a healthy state, these cells are located in the plexiform layer and are continually searching for and phagocytosing cell debris. Once the retina contains leaky blood vessels and infiltrating inflammatory cells, the microglial cells become activated and exhibit a "ramified" and "amoeboid" phenotype to increase phagocytosis[142]. In the stage of NPDR, HLA-DR+, CD45+, or CD68+ microglial cells congregate around the microaneurysms, exudates, hemorrhagic lesions, and the optic nerve of the histological sections of patients. In PDR patients, microglial presence is increased in the optic nerve region, as well as around the neovascularized membrane in the vitreous of the eye, indicating microglial activation plays a role in the progression of DR[68]. As with the T cell helper axis, MSC therapy could impact the microglial cell polarization to an anti-inflammatory state to provide a more regenerative condition in the retina. In the CNS, after injury, MSCs are shown to promote M2 polarization of microglia and induce an anti-inflammatory state in the tissue[143,144]. A proposed mechanism of

action for this process is the secretion of TSG-6 by MSCs, which inhibits pro-inflammatory gene expression in microglial cells, including NF-κB and MAPK activation[145].

There is evidence to suggest that MSC therapy in DR could target and impede leukostasis, and thus, deter the pro-inflammatory conditions in the retina. Luu and colleagues have demonstrated within an *in vitro* flow chamber system, the co-culture of MSCs and ECs reduced the adhesion and transendothelial migration of flowing neutrophils and lymphocytes[146]. In this study, the co-culture of MSCs and ECs also suppressed the upregulation of ICAM-1 and VCAM-1 after treatment with TNF-α and IFN-γ. Based on antibody and siRNA experiments, the authors proposed the crosstalk between ECs and MCs prompted MSCs to release IL-6, which consequently, prompted ECs to inhibit the observed leukocyte recruitment.

In different *in vivo* models for eye inflammation, delivered MSCs show different mode of actions when targeting inflammation. When compared to dexamethasone (DEX) efficacy in a recurrent experimental autoimmune uveitis (rEAU) model of rats, MSC treatments were more beneficial than tapering dexamethasone (DEX) therapy over the course of 50 days of the disease[147]. MSCs were able to reduce retinal damage, photoreceptor loss, and the presence of Th1 and Th17 cells in the eye. Similarly, Oh et al., showed that intraperitoneal infusion of human MSCs in mice experimental autoimmune uveitis (EAU) models decreased Th1 and Th17 cells in draining lymph nodes after EAU immunization[148]. The intraperitoneal injections of human MSCs resulted in a decrease of IFN-γ levels in the eye and protection of the photoreceptor layer. The work of Ko et al. suggests intravenously administered MSCs suppress the immune responses in EAU through a TNF-α-simulated gene/protein-6 (TSG) mechanism, where TSG-6 knockdown in MSCs failed to decrease intraocular inflammation and retinal damage[149].

MSC Differentiation and Cell Replacement

Because MSCs have been shown to differentiate into multiple lineages *in vitro*, it is hypothesized that the delivery of pre-differentiated or undifferentiated MSCs may replace the retinal differentiated cell types loss from the progression of DR. Table 1.1 provides a reference on several research reports suggesting the capability of MSCs to differentiate into specialized or specialized-like cells that are found in the retina. However, there is some caveats with these same reports. Within these studies there is limited in-depth analysis of the function of the injected MSCs, and most analyses are based on limited marker expression. Some of the protein markers expressed by the MSCs in the different models, are also found on multiple cell types other than MSCs, which makes it difficult to conclude whether MSC differentiation actually occurred. A clinical study involving three human patients demonstrated MSCs were able to suppress inflammatory activity in advanced Behcet's disease retinal vasculitis, however, there was no indication after one year of intra-ocular transplantation that the delivered MSCs were able to create new blood vessels or differentiate into cone cells[150]. Therefore, it is important that work rigorously investigates the differentiation of MSCs engrafted into the retina, as well as their long-term viability in the chronic disease state of diabetes.

Table 1.1 MSC Replacement and Differentiation Capability to Specialized Cells in the Retina

Differentiated Cell Type	Source of MSCs	Model of Replacement/Differentiation	Reference
Retinal Pigment Epithelium (RPE)	Mouse bone marrow	Retinal degeneration model using sodium iodate ($NaIO_3$)	[151,152]
	Rat bone marrow	Retinal degeneration model using $NaIO_3$	[153]
	Human bone marrow	Co-culture with pig RPE in a transwell system	[154]
	Human adipose	Cultured with RPE-conditioned medium	[155]
	Rat bone marrow	Co-cultured with RPE cells in RPE cell-conditioned medium and photoreceptor outer segments	[156]
	Mouse bone marrow	Co-cultured with adult RPE cells and retinal degeneration model using $NaIO_3$	[157]
	Mouse bone marrow	Retinal degeneration model using sodium iodate ($NaIO_3$) and retinal neovascularization model by breaching Bruch's membrane	[158]
	Mouse bone marrow	Rhodopsin knockout (Rho-/-) model	[159]
	Rat bone marrow	Laser-injured rat retinas	[160]
Photoreceptor Cells: Rods and Cones	Human bone marrow	Co-cultured with human RPE cell layer	[161]
	Rat bone marrow	Retinal degeneration model using $NaIO_3$	[153]
	Human trabecular meshwork	Cultured on amniotic membrane	[162]
	Rat bone marrow	Cultured and induced by activin A, taurine, and epidermal growth factor *in vitro;* Royal College of Surgeon rats	[163]
	Human conjunctiva	Poly-L-lactic acid (PLLA) nanofibrous scaffolds	[164]
Bipolar Cells	Human trabecular meshwork	Cultured on amniotic membrane	[162]
Endothelial/Endothelial-Like Cells	Human bone marrow	Cultivation in fetal calf serum and vascular endothelial growth factor	[165]
	Human bone marrow	Matrigel and polymeric constructs *in vitro* and within NMRI-nude mice	[166]
	Canine bone marrow	Canine Chronic Ischemia Model	[167]
	Human bone marrow	Matrigel and collagen plugs in non-obese diabetic-severe combined immunodeficient (NOD-SCID) mice	[168]
	Canine bone marrow	Cultivation under shear stress	[169]

	Human umbilical cord	Cultivation on fibronectin and endothelial differentiation medium and ischemic hindlimb mouse model	[73]
	Rat bone marrow	Vein grafting in a rat model	[170]
Amacrine Cells	Rat bone marrow	Laser-injured rat retinas	[160]
Bipolar Cells	Rat bone marrow	Laser-injured rat retinas	[160]
Astrocytes	Human bone marrow	Astrocyte differentiation medium and in the rat model of Parkinson's Disease, 6-hydroxydopamine-lesioned rats	[171]
	Human umbilical cord	Lateral ventricles of neonatal mouse brain	[172]
	Mouse bone marrow	Lateral ventricle of neonatal mouse brains	[173]
	Mouse bone marrow	Cultured with epidermal growth factor (EGF) or brain-derived neurotrophic factor (BDNF)	[174]
	Rat bone marrow	Acute permanent brain ischemia model in rats	[175]
Oligodendrocytes	Human placenta	Cultivation on collagen with retinoic acid and human brain-derived neurotrophic factor	[176]

MSC-Therapy in Pre-Clinical Models of DR

Researchers have developed several animal models to explore the basic science and treatment options for DR. With animal models, the goal is to produce a comparable disease phenotype to that of human DR patients, whether that is early stage or late stage in the disease. There are various type 1 and type 2 DR animal models based on animals such as the zebrafish, mice, rats, rabbits, dogs, and monkeys[177]. Different degrees of pathological severity can differ between these models, and it is essential to choose the correct model and time point in which to study MSC therapy. For instance, the two common murine DR models, Akita ($Ins2^{Akita}$)[178–180] and STZ-induced diabetes[181–184], exhibit pericyte loss, increased vascular permeability, neuronal cell apoptosis in the ganglion cell layer (GCL), and amacrine cell loss in the inner nuclear layer (INL). The recently developed Akimba mouse ($Ins2^{Akita}VEGF^{+/-}$) recapitulates human severe NPDR/PDR with profound retinal

ischemia, aberrant neovascularization, vascular leakage, retinal edema, neural retina loss, and reactive gliosis[185,186]. This model is a cross between the Kimba ($VEGF^{+/-}$)[187,188] mouse, which initiates chronic progressive retinal ischemia by transiently over-expressing human VEGF in photoreceptors, and the diabetic Ins2Akita mouse, with hyperglycemia causing synergistic damage to the retinal vasculature and neural retina. Because animal models differ in severity of DR, future work on MSC therapy in DR needs to take account the disease state in which MSCs are delivered.

Still, studies show that there is promise of MSC therapy in both late- and early-stage DR. Rajashekhar et al. demonstrated that intravitreal injection of adipose-derived MSCs in a STZ-induced DR model adopted a perivascular location in the retinal vasculature, improving visual function and decreasing inflammatory expression in the retina[189]. Yang et al. showed that intravenously injected human adipose-derived MSCs decreased blood glucose levels and recovered BRB integrity[190]. The donated human adipose-derived MSCs were able to integrate in the outer nuclear layer (ONL), INL, and GCL while expressing both rhodopsin and GFAP, markers for photoreceptor cells and astrocytes, respectively. We have shown that in an oxygen-induced retinopathy (OIR) model and the Akimba model that intravitreal injected human adipose-derived MSCs and mouse adipose-derived MSCs are able to incorporate into the retinal vasculature and adopt a pericyte morphology, ultimately protecting capillary dropout in both models[93]. Supplementing the MSCs with TGF-β *in vitro* further enhanced their contractile capability and improved their protection against capillary dropout. We later showed intravitreal injected ASCs from a diabetic source have impaired vasoprotection of DR in the Akimba mouse model through impaired integration into the retinal vasculature and a pro-angiogenic secretome[191]. A study revealed that intravitreal administration of MSCs prevented retinal ganglion cell loss at least 12 weeks after administration in STZ-induced diabetes in C57Bl/6 mice[192]. There was poor retinal

integration of the delivered MSCs, yet intraocular levels of NGF, GDNF, and bFGF increased, which are responsible for preventing RGC and photoreceptor loss[193,194]. Johnson et al. suggests that MSC low engraftment is caused by activated glial cells[195], implying that reducing the deactivation of neuronal cells may improve the efficacy of MSC tissue incorporation and therapy.

Potential for MSCs in Other Ocular Diseases

Besides DR, research supports that MSCs are a potential therapeutic for various ocular pathologies. Similar to the approaches of MSC therapy in DR, MSCs can be used for cell replacement and immune modulation in different eye disease models. A characteristic of age-related macular degeneration (AMD) is the disruption and death of the retinal pigment epithelium (RPE). It is suggested that MSCs are able to differentiate into functional RPE cells[156], while subretinal injected-MSCs are exhibit some form of differentiation into RPE cells within a sodium iodate-damaged rat retina[153]. Glaucoma, a disease characterized by the loss of retinal ganglion cells (RGCs) and alterations in the optic nerve, is also a prime target for MSC therapy. Through secretion of neurotrophic factors[196], intravitreal injected-MSCs are able to protect RGCs and ocular hypertension[112,113,197]. In uveitis, or inflammation in the uvea, MSC therapy seems to be mostly responsible for immunomodulatory affects in the disease, specifically through regulation of T cell proliferation and cytokine production[198,199].

In Chapter 4, I will describe a study in which we investigate whether MSCs can serve as a potential cell source for cornea endothelial cells, which when damaged by aging and injury, leads to vision loss. Within corneal diseases, previous reports have examined the potential of MSCs to treat the corneal epithelium layer and cornea stroma layer through similar mechanisms as described above[200]. Human umbilical cord-derived MSCs delivered in the dysregulated corneas of *Lum*-/- mice exhibited differentiation into a keratocyte morphology and function needed to maintain

healthy cornea stromal homeostatis and collagen fibril structure[201,202]. Similarly, bone-marrow derived MSCs were claimed to differentiate into surface corneal epithelial cells after transplant into injured corneal tissue[203,204]. Also, when engrafted into the cornea after chemical injury to the surface of the tissue, MSCs are contributed to decreasing the endogenous pro-inflammatory cytokines, while increasing anti-inflammatory cytokine production[205,206]. Taken together, these reports demonstrate that locally delivered MSCs also represent another treatment option for ocular diseases other than DR.

Controversy Around Clinical MSC Therapy for DR

Typically, transplanted or locally injected MSCs have been shown to be reasonably safe for human patients as there is no reported indication of harmful side effects in approved clinical trials for several different diseases[207]. However, this same investigation has not been extended to eye research.

Much of the current ocular stem cell basic science and clinical trial efforts focuses on cellular replacement of a particular ocular cell, such as a retinal pigment epithelial cell for example, reviewed well by Huang and colleagues[208]. In a preclinical model for retinitis pigmentosa, the subretinal injection of human Wharton's Jelly-derived MSCs into RCS rats resulted in no detectable safety issues based on the lack of MSC systemic migration and no differences being found in ERG analyses between groups[209]. As of now, there are over 100 clinical trials registered with the NIH that are exploring the use of stem cells for treatment of ocular diseases (ClinicalTrials.gov; Search Terms: eye, stem cells), including various retinopathies, glaucoma, and auto-immune neuropathies. There are currently two clinical trials that are focused on treating DR. One of the trials is investigating bone-marrow MSC treatment in ischemic retinopathy and DR (RetinaCell, ClinicalTrials.gov, NCT01518842), while the second trial is examining the treatment

of autologous bone-marrow CD34+ endothelial progenitor cells in DR (ClinicalTrials.gov, NCT01736059). These two trials highlight the "infancy" of MSC ocular therapy, particularly around the establishment of safety data for future efficacy trials required for FDA approval.

Unfortunately, due to malpractice and unethical decision-making of several individuals, the efficacy and safety of MSCs has been severely questioned. Notably, within a "stem-cell clinic", three patients received intravitreally injections of autologous adipose-derived SVF for treatment of age-related macular degeneration[210]. In the span of days, the patients experienced proliferative vitreoretinopathy, lens subluxation, retinal detachment, and loss of vision. Furthermore, the "stem-cell clinic" that performed this procedure required the patients to pay under the false claim that the procedure was FDA-approved and currently under clinical trial. Due to the lack of scientific understanding on MSC ocular injections, it is unknown how the injected cells caused the devastating complications. Interestingly, it was stated through personal communication (Nolta J, Pugh E, Zawadzki R) that MSCs injected into the vitreous transformed into bony or fibrous cells in the eyes of animals, which later lead to retinal detachment[211].

Unfortunately, these types of clinics are all too common. The "stem cell" nature of MSCs and the published therapeutic potential of these cells has steered walk-in clinics to advertise and offer "MSC stem cell therapy" for a wide range of conditions, including chronic diseases, cosmetic concerns, and sexual enhancements[212]. A significant portion of these clinics lack advertisement around the efficacy or inefficacy and regulatory status of their "stem cell therapies", and, disappointedly, are often supported by trained, medical professionals. These "unproven stem cell therapies" are rampant and this multi-billion dollar global industry[213] often capitalizes on the desperation of patients to find a cure for their diseases. The Commissioner of the FDA has recently announced new oversight and productive efforts to attempt to eliminate the dishonest hype and

unethical actions of "unproven stem cell clinics"[214]. The most productive change will come from understanding the science behind MSCs and their innate function, which is done by performing meticulous and innovative testing in preclinical models. Thus, these gaps and controversies that were presented in this chapter are a central component of this current thesis and has largely acted as a motivation for the experiments described in the following chapters.

Overview of Thesis

For MSC therapy to become a feasible treatment for DR and other ocular diseases, we require more refined understanding of the MSC "stem cell" behavior and function. Although there are promising therapeutic results, there still is no consensus on the dynamic behavior and function of MSCs, which is underlined by the different results found within different disease models and research groups. Markedly, there is inconsistency in culturing MSCs across research groups, particularly with media conditions, and combining this variation with the heterogeneity of MSC populations[215], it is difficult to study the cellular dynamics of what defines a MSC. Conditions such as cell plating density, cell media, passage number, and cell culture substrates can change the innate characteristics of MSCs and their wound healing capability[216].

Once MSCs are delivered or transplanted, it is obvious that MSCs possess some ability to regenerate or remodel diseased tissue, but some aspects of this process need to be elucidated before a clinical therapy is fully appreciated. In regards to the integration with the vasculature, there are some aspects that are currently unexplored. For one, the process of how MSCs migrate and incorporate to a pericyte-like position in microvasculature is still unknown, however, it is likely that this process involves some of the cellular mechanisms and pathways observed in developmental and neonatal angiogenesis. Additionally, it is uncertain whether integrated perivascular MSCs are prone to adopt a pericyte-like postion greater than random chance, meaning

that there is a lack of statistical evidence to suggest that chemotaxis or chemokenesis causes engrafted MSCs to position themselves on vascular endothelial cells. In-depth examination of MSC retinal vasculature incorporation would grant insight on the proclivity of MSCs to a pericyte-like state, which is a cell state needed to replace loss microvasculature smooth muscle cells and pericytes in DR.

Further, there needs to be a definitive conclusion on the origin of MSCs. It is suggested that MSCs come from a perivascular origin, but until a marker is found to differentiate these cells from other cell-types it is unclear where these cells originate. Lineage-tracing technology is beneficial in addressing this issue[217,218], where labelling and isolating a particular population of cells *in vivo*, and studying their MSC characteristics will lead to greater understanding of what defines an MSC throughout its cell lifespan . There may be multiple sources of MSCs found in the tissue, and during the appropriate circumstance, all or a subset of these cells activate stem cell factors to aid in wound healing. Most of the literature points to the fact that vascular smooth muscle cells, pericytes, a subset of pericytes, adventitial cells, or perhaps another perivascular cell type are the source of MSCs.

It is even suggested that once these perivascular cells are exposed to a disease environment *in vivo*, these cells become activated MSCs and regulate the wound healing process, orchestrated through a paracrine immunosuppressive, angiogenic, and antifibrotic response[219,220]. The retinal pericytes themselves may indeed be tissue-resident MSCs, and controlling for retinal pericyte MSC function may be a strategy to control DR disease progression. Pericytes seem to move away from retinal microvessels in animal models of diabetes, however, it is still unknown if the pericytes are loss due to cell death or differentiate into other cell types, such as fibroblast or glial cells, in order to remodel the disease retinal tissue.

The importance of the *in vivo* observation of the putative MSC perivascular population cannot be understated. As these cells work in concert with other retinal and immune cells, removal of them from their *in vivo* environment for assay on tissue culture plastic can be problematic without elegant and direct *in vivo* validation. Especially considering that tissue culture itself is reported to alter the marker expression and possibly differentiation capabilities of MSCs, *in vivo* correlation is necessary to advance the field both scientifically and translationally. From these approaches, we can adopt more of a safe and effective implementation of MSC therapy for DR and other ocular diseases.

Our lab and collaborators have traditionally focused on angiogenesis in preclinical diabetic retinopathy models, and using adipose-derived MSCs to facilitate angiogenesis and serve as a source of perivascular support cells, namely pericytes. Our lab uses adipose-derived MSCs due to several practical advantages. First, liposuction aspiration and fat grafting procedures are relatively common clinical cosmetic and reconstructive procedures, thus obtaining the stromal vasculature fraction (SVF) and MSCs from unwanted adipose tissue is relatively easier than other tissue, such as dental pulp and bone marrow. In fact, harvesting MSCs from adipose has proven far more efficient than harvesting them from bone marrow (5,000 MSCs per gram of adipose versus 100-1000 MSCs per gram of bone marrow)[221]. Also, adipose-derived MSCs are suggested to have a greater pro-angiogenic potential for therapeutic angiogenesis in ischemia when compared to bone marrow-derived MSCs[222]. Lastly, adipose-derived MSCs are shown to have a higher proliferative capacity than bone-marrow derived MSCs *in vitro*[223,224]. Combining our experience with adipose-derived MSCs and DR preclinical models, statistical modeling, lineage-tracing, immunofluorescent microscopy, and protein and genetic analysis, we will aim to provide valuable

knowledge to the scientific community and push forward more rigorous studies to investigate their therapeutic potential in DR and other ocular diseases.

In Chapter 2, I will describe the development of a statistical software program that tests whether locally delivered MSCs associate greater than random chance with endothelial networks *in vitro* and with angiogenic vessels in murine retinopathy. This project originated out of a Monte Carlo study that explored the random association of diabetic and nondiabetic adipose-derived MSCs to the retinal vasculature in the Akimba DR murine model[191]. Using a Monte Carlo simulation developed in MATLAB (MathWorks, Natick, MA, http://www.mathworks.com) we determined a slightly higher preference of perivascular incorporation for healthy adipose-derived MSCs when intravitreally delivered in the Akimba DR models. However, in this analysis, there was no in-depth statistical validation to determine if there was a statistical difference between the vascular incorporation of healthy and diabetic injected MSCs. Within Chapter 2, we demonstrate a statistical test with higher power and type 1 error to predict if enhanced vascular incorporation occurred within individual samples of biological datasets and between study groups. This statistical software revealed that adipose-derived MSCs had enhanced colocalization with vascular endothelial networks *in vitro* and with retinal blood vessels within ischemic conditions in a preclinical model of DR.

The current work highlighted in Chapter 2 is currently published in *Bioinformatics.*

In Chapter 3, we investigated the bioactivity and cell fate of adipose MSCs derived from vascular smooth muscle cells and pericytes (vSMCs-PCs) using the lineage-tracing murine model *Myh11*-CreER^{T2} [225]. This cell population and its lineage represents a subpopulation of the total cultured SVF cells *in vitro* throughout multiple passages (Figure 1.3), and has been previously assumed to be a putative MSC population. By measuring surface marker expression and tri-

differentiation capability, we demonstrate for the first time that Myh11+ vSMCs-PCs are MSCs according to the ISCT-defined criteria[47]. Interestingly, we further demonstrate that Myh11 lineage negative cells from the adipose SVF are also MSCs, indicating multiple cell sources in which MSCs are derived. MSCs derived from vSMCs-PCs were also intravitreally injected into a preclinical model of DR and shown to improve vascular recovery and re-associate with the retinal vasculature. However, the intravitreal injection of MSCs also induced proliferative vitreoretinopathy (PVR), forming pre-retinal scar through the differentiation of myofibroblast in the vitreous gel. We replicated this finding through severe injury to the eye and demonstrated that endogenous retinal Myh11+ vSMCs-PCs can also induce PVR through myofibroblast differentiation. Remarkably, endogenous retinal vSMCs-PCs remain quiescent for other type of injuries used in this Chapter. Lastly, we used anti-TGFβ strategies to reduce PVR in response to both exogenous delivery of MSCs and to endogenous differentiation of retinal vSMCs-PCs. From the downregulation of TGFβ signaling, we reveal that PVR secondary to exogenous MSC injection is not reduced, while PVR secondary to endogenous vSMCs-PCs is inhibited. The work described in Chapter 3 forms the basis of a paper planned to be submitted to

Journal of Experimental Medicine.

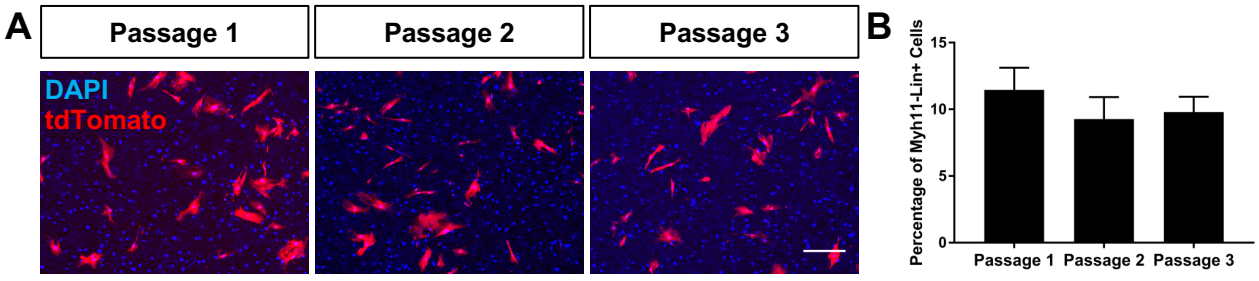

Figure 1.2. Myh11-Lin+ cells are a subpopulation of the cultured SVF over serial passages **(A)** The epididymal adipose tissue of *Myh11*-CreERT2;ROSA STOP FLOX tdTomato+/+ mice were enzymatically digested and the SVF was plated on tissue-treated plastic. The cultured cells were passaged and imaged for tdTomato+ cells at multiple serial passages. **(B)** One-way ANOVA

determined there was no significant difference in the amount of tdTomato+ cells from passage 1-3. Scale bar in (A) represents 100 μm.

In Chapter 4, we discovered in the presence of a Myh11+ subpopulation of cornea endothelial cells in the *Myh11*-CreER^{T2} murine model. To note, the cornea is in the anterior segment of the eye, and the cornea serves as a barrier for protection for the eye. The cornea is argued to control the homeostatic flow of fluid in the anterior chamber to allow for light to be transmitted to the retina. We are the first to report the presence of Myh11 in this part of the cornea, and within this chapter, we examine the fate of these cells with aging. Building off the work in Chapter 3, we also determine if MSCs derived from Myh11+ vSMCs-PCs could differentiate into cornea endothelial cells *in vitro*. We demonstrate that there is evidence to suggest these cells can somewhat differentiate into an endothelial cell lineage and may represent another cell source to replace damaged cornea endothelial cells. These findings in Chapter 4 are being prepared for submission to the scientific journal *Investigate Ophthalmology and Visual Science.*

In Chapter 5, I will conclude with discussing the primary focus of the work, which is to explore the fate of MSCs within the context of ocular disease, particularly DR. Within this chapter, I will begin by discussing the key contributions that this work has provided to the field, and will end the chapter by describing some future work that will expand on the findings of this thesis.

CHAPTER 2

CIRCOAST: A Statistical Hypothesis Test for Cellular Colocalization with Network Structures

Acknowledgements: Bruce A. Corliss[1,*,†], H. Clifton Ray[1,†], James T. Patrie[2], Jennifer Mansour[3], Sam Kesting[1], Janice H. Park[3] , Gustavo Rohde[1] , Paul A. Yates[4] , Kevin A. Janes[1] and Shayn M. Peirce[1]

[1]Department of Biomedical Engineering, University of Virginia
[2]Department of Public Health Sciences, University of Virginia
[3]Department of Biology, University of Virginia
[4]Department of Ophthalmology, University of Virginia

The text included in this chapter has been published: Corliss, B.A.*, Ray, H.C.*, Patrie, J., Mansour, J., Kesting, S., Park, J., Rohde, G., Yates, P.A., Janes, K., Peirce, S.M. and Wren, J., 2018. CIRCOAST: A Statistical Hypothesis Test for Cellular Colocalization with Network Structures. Bioinformatics. *Both authors contributed equally.

Abstract

Motivation: Colocalization of structures in biomedical images can lead to insights into biological behaviors. One class of colocalization problems is examining an annular structure (disk-shaped such as a cell, vesicle, or molecule) interacting with a network structure (vascular, neuronal, cytoskeletal, organellar). Examining colocalization events across conditions is often complicated by changes in density of both structure types, confounding traditional statistical approaches since colocalization cannot be normalized to the density of both structure types simultaneously. We have developed a technique to measure colocalization independent of structure density and applied it to characterizing intercellular colocation with blood vessel networks. This technique could be used to analyze colocalization of any annular structure with an arbitrarily shaped network structure.

Results: We present the circular colocalization affinity with network structures test (CIRCOAST), a novel statistical hypothesis test to probe for enriched network colocalization in 2D z-projected multichannel images by using agent-based Monte Carlo modeling and image processing to generate the pseudo-null distribution of random cell placement unique to each image. This hypothesis test was validated by confirming that adipose-derived stem cells (ASCs) exhibit enriched colocalization with endothelial cells forming arborized networks in culture and then applied to show that locally-delivered ASCs have enriched colocalization with murine retinal microvasculature in a model of diabetic retinopathy. We demonstrate that the CIRCOAST test provides superior power and type I error rates in characterizing intercellular colocalization compared to generic approaches that are confounded by changes in cell or vessel density.

Availability: CIRCOAST source code available at: https://github.com/uva-peirce-cottler-lab/ARCAS.

Supplementary information: Supplementary data are available at *Bioinformatics* online and within the Appendix of this thesis.

Key Abbreviations

ASC: Adipose-derived Mesenchymal Stem Cell

BMRP: Binomial Model of Random Placement

CDNF: Cell-Dilated Network Fraction

COI: Cell-of-Interest

HMRP: Hypergeometric Model of Random Placement

CIRCOAST: Circular Colocalization Affinity with Structures Test

ICA: Intercellular Colocalization Affinity

ICF: Intercellular Colocalization Fraction

MCMRP: Monte Carlo Model of Random Placement

Introduction

Interactions between vascular endothelial cells, which are arranged in arborized networks throughout all tissues of the body, and other cell types are instrumental in the initiation and perpetuation of a wide range of diseases, including diabetes mellitus[226]. Interacting cell types with vascular endothelial cells include immune cells[227], perivascular cells[228,229], and stem cells[230]. Modulating intercellular interactions associated with disease progression is seen as a therapeutic target for preventing or ameliorating the associated pathology[231].

A key imaging-based measure of cell-cell interactions is intercellular colocalization, the frequency that two cell populations reside immediately adjacent to each other. Changes in intercellular colocalization suggest changes in cell-cell interactions and cellular behaviors that influence the interaction, including altered migrational capabilities, cytokine sensing, and other chemotactic behaviors. Most research in cellular colocalization has focused on intracellular interactions with point-based features, specifically whether two molecular probes codistribute (dispersed in a spatially related fashion) or associate with a particular organelle[232]. The statistics are often limited to a pixel-by-pixel analysis of correlation using Pearson's Correlation Coefficient or Mander's Overlap Coefficient[233], or more advanced analysis techniques such as spatial point pattern analysis[234,235] or protein-protein interaction models[236]. By contrast, there is a lack of statistical techniques to study cell-cell interactions[237] where point-based analysis is less pertinent.

Cell populations are known to change dramatically in disease[238], which can confound metrics of colocalization. Intercellular colocalization events depend on the prevalence of the two interacting cell populations, and generic statistics cannot ascertain changes in colocalization because the data cannot be normalized to both cell populations simultaneously. This is especially problematic when there are substantial changes in vascular or cellular density between study groups or high variance between biological replicates. Here, we present an image analysis tool that statistically assesses intercellular colocalization independent of cell and network density by testing against a pseudo null distribution for random intercellular colocalization events unique to each image. By comparing the intercellular colocalization fraction (ICF), the fraction of cells colocalizing with network structures, between an experiment image compared to the distribution of ICF values derived from modeling random cell placement in the same image, changes in colocalization can be ascertained relative to random behavior. Using additional statistics to combine data across images from a single biological replicate and compare between study groups yields a process that can characterize changes in intercellular colocalization affinity (ICA), which we define as the *frequency of colocation events between two cell populations corrected for changes in cell density, cell size, and network density across study groups*.

An example where large changes in cellular density are observed is diabetic retinopathy, a disease that is marked by progressive damage to the retina[239]. Decreases in the densities of both blood vessels[238] and pericytes[240], a cell type that colocalizes with and stabilizes the microvasculature, have been observed in early diabetes and are thought to initiate the degradation of the retina[241]. Toward cell-based therapies, previous work has shown that injecting adipose-derived mesenchymal stem cells (ASCs) can ameliorate microvessel loss when ASCs colocalize with blood vessels and adopt a pericyte-like morphology in the retina and other tissues[93,230].

However, it was difficult to conclude whether or not ASC colocalization with the retinal microvasculature occurred at a rate greater than random chance without a validated statistical method.

We developed and validated CIRCOAST as a tool to measure intercellular colocalization by testing for a known enriched colocalization between ASCs and the arborized networks that endothelial cells form in culture. Then, we applied CIRCOAST to determine that locally delivered ASCs significantly colocalize with the retinal microvasculature in a murine model of diabetic retinopathy. By providing a robust method for evaluating the statistical significance of cell-cell colocalization, CIRCOAST provides insight into putative mechanisms of and potential therapies for a wide range of pathologies. This method naturally extends to the colocalization analysis of any annular shaped structure (disk-shaped such as a cell, vesicle, or molecule) with any arbitrary background network structure within tissues or cells.

Methods

2.1 Codebase

CIRCOAST was written in MATLAB 2016b using the image processing toolbox and can be run either as source code or as compiled code with the MATLAB runtime environment version 9.1. The source code and compiled executable are available as a part of the Automated Random Cell Association Simulator (ARCAS) code repository (https://github.com/uva-peirce-cottler-lab/ARCAS). The user interface is designed with MATLAB's graphical user interface development environment (guide), which allows the user to analyze a dataset of two or more color images, one marking the vasculature, and the others marking one or more cell types to be examined individually for enriched vascular colocalization. In this study, a confocal microscope was used to acquire a z-stack at approximately Nyquist sampling. The 3D images were then flattened with a

max projection in the z axis dimension to produce a 2D RGB image.

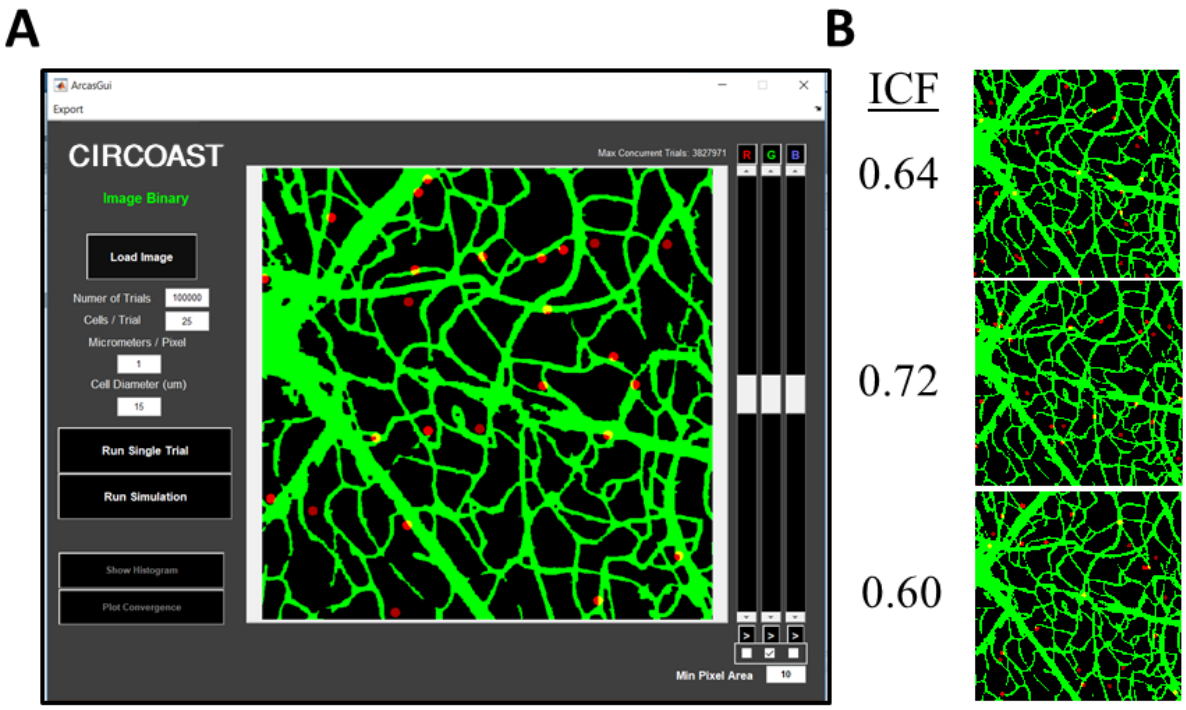

Figure 2.1. CIRCOAST GUI for Analyzing Cellular Colocalization
(A) GUI for CIRCOAST that imports a thresholded vasculature and predicts the random cell colocalization fraction (ICF) (B), through a series of trials from a Monte Carlo Model of Random Placement (MCMRP).

2.2 Monte Carlo Model Development (MCMRP)

An initial Monte Carlo model of Random Placement (MCMRP) was created to simulate randomly placed cells. An input image of the network is imported into the CIRCOAST GUI, and segmented via an adjustable global threshold (Figure 2.1A). Image resolution, cell size, and number of cells are set by the user, and a series of Monte Carlo simulations are performed with an agent-based model that stochastically spawns cells in an image, in which under the random cell placement paradigm, every location within the input image region has an equal chance of being selected as a site of cell placement; and once placed, the fraction of cells overlapping with the vasculature network is calculated (Figure 2.1A, intercellular colocalization fraction, ICF). A probability

distribution for the ICF in a given image is approximated based on the thousands of Monte Carlo simulation repetitions of the random cell placement process (Detailed outline of algorithm in Appendix-Supplementary Note 1).

Probing of the key parameters that influence cellular colocalization with the vasculature was undertaken via a simple program created to stochastically create a network structure resembling blood vessels in a controlled manner (Appendix-Supplemental Figure 1). Dense microvascular networks have been described as having structural characteristics of interconnected wires [242]. The stochastically-generated networks were created by defining a randomly seeded point cloud with an enforced minimum distance between points, and using the watershed algorithm to create a network of line segments bisecting all points. Line segments were then iteratively removed until the desired vessel network was obtained, mimicking the range of vessel density found in vascularized tissues (Extended explanation of algorithm in Appendix-Supplementary Note 2).

A set of parameters defining the network structure and the cell of interest (COI) were identified (Appendix-Supplementary Figure 2), including: 1) network fraction: the fraction of pixels in an image that comprise the network, 2) network length density: the length of the centerline for all network structures divided by the area of the image, 3) network radius: thickness of network orthogonal to the network centerline, 4) cell number, 5) cell diameter, 6) and cell dilated network fraction (CDNF). CDNF defines the area of the image where if the center of a COI is within that area, the COI overlaps with the network by at least one pixel and is counted as being a colocalized cell, which is captured by morphologically dilating the segmented network with the length of the radius of the COI. Therefore, with a fixed network structure, as cell diameter increases so will the value for CDNF.

The relation between each system parameter and the ICF predicted by the MCMRP was

examined over a wide range of parameter values (Appendix-Supplemental Figure 3). All parameters correlated with the MCMRP derived mean ICF; except for cell number, suggesting many variables influence mean of ICF distribution under the random cell placement paradigm, but give little insight to what parameter(s) directly dictate network colocalization.

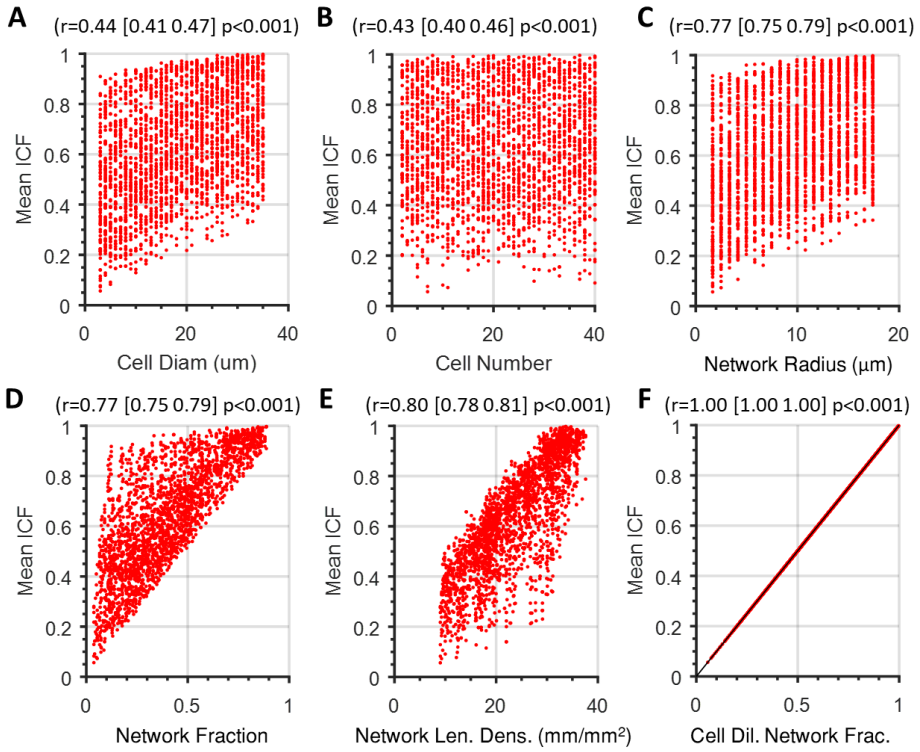

Figure 2.2. Network area fraction dilated by cell radius determines the random cell colocalization fraction.
The mean ICF was calculated with the MCMRP over 10,000 trials with randomly selected parameters and displayed as a function of **(A)** cell diameter, **(B)** cell number, **(C)** network radius, **(D)** network fraction, **(E)** network length density, and **(F)** cell dilated network fraction (CDNF, N=2,500 images). Pearson correlation coefficient and associated 95% confidence interval and p-value are provided at the top of each scatterplot.

To determine if any of the parameters can directly predict mean ICF under the random cell placement paradigm, a dataset of 2500 simulated experiments were generated using the vessel network generator with randomly assigned parameters. The means of ICF distributions derived from the 2500 experiments were correlated with the individual parameters (Figure 2.2). While

most parameters correlated with mean ICF, only CDNF had a correlation coefficient (r) of 1 (rounded to within 6 decimal places), suggesting that CDNF correlates almost perfectly with the MCMRP derived mean ICF (Figure 2.2F). Note that in Fig. 2.2F; that for all intended purposes, the relationship between the CDNF values and mean ICF values is deterministic (points fall on a 45° line).

To further examine if CDNF is a unique predictor of ICF, a multivariable linear regression (MVLR) analysis was conducted with all input parameters as predictor variables and mean ICF as the response variable. Input parameter values and mean ICF values were converted to z-scores so that all of the multivariate regression model coefficients shared the same scale of measure while still preserving the underlying multivariate relationships that exist on the non-z-score scale. All predictors had insignificant p-values except for CDNF (Table 2.1). Furthermore, since the regression coefficients of all predictors other than CDNF were essentially equal to zero, CDNF is the only input parameter that was given any weight in the MVLR in terms of predicting the mean ICF z-score. Given that the MVLR model multiple coefficient of determination (R^2) was equal to 1, we conclude that CDNF is highly and uniquely correlated with the predicted mean ICF of the MCMRP. Although the ICF in given MCMRP trial can differ from CDNF due stochasticity, and the ICF from an acquired image may differ from CDNF from stochasticity or non-random cell placement, the CDNF can be used to calculate the mean ICF *from random behavior* in both cases.

Table 2.1. Multivariable regression of z-scored input parameters versus the z-score of the ICF predicted by Monte Carlo Model of Random Placement (R2 =1.00).
Note that the z-score transformation preserves the underlying multivariate relationships.

Predictor	Coefficient	SE	F-	P-value
Intercept	-9.54E-16	1.20E-05		
Cell Diameter	-1.96E-05	2.56E-05	-0.76	0.444
Cell Number	-5.57E-06	1.20E-05	-0.46	0.642
Network Rad.	-2.59E-05	4.34E-05	-0.60	0.551
Network Frac.	5.01E-06	5.74E-05	0.09	0.931
Network. Len.	-3.24E-05	4.67E-05	-0.69	0.489
CDNF	**1.000**	**5.00E-05**	**2.00E4**	**<0.000**
Model			1.16E9	<0.000

2.3 Binomial Model Development and Validation (BMRP)

Based on the aforementioned Monte Carlo findings, CDNF was used to develop a binomial model of random placement (BMRP) for a more mechanistic and exact representation of cell colocalization under the random placement paradigm. By defining CDNF as the probability of success for a randomly placed cell colocalizing with the vasculature within an image, intercellular colocation can be modeled as a binomial stochastic process using Eq. 1 [243];

$$f(c; n, p) = \binom{n}{c} p^c (1-p)^{n-c}, \quad (1)$$

where p is the cell dilated network fraction (CDNF), c is the number of cells colocalizing, and n is the total number of cells in the image. The mean (μ) and standard deviation (σ) of the distribution can be directly calculated using the formulas listed in Eq. 2 [243], as opposed to approximating the values based on successive MCMRP trials.

$$\mu = n \times p, \quad \sigma = \sqrt{n \times p \times (1-p)} \quad (2)$$

To evaluate the BMRP, the predicted mean ICF from random cell placement was compared to the MCMRP predicted mean ICF (10,000 trials/image) across the same dataset of 2500 simulated experiments that were used to produce Figure 2. The discrepancies between the predicted mean

ICFs of the BMRP and the MCMRP are shown as a function of the predicted mean ICF in Figure 2.3.

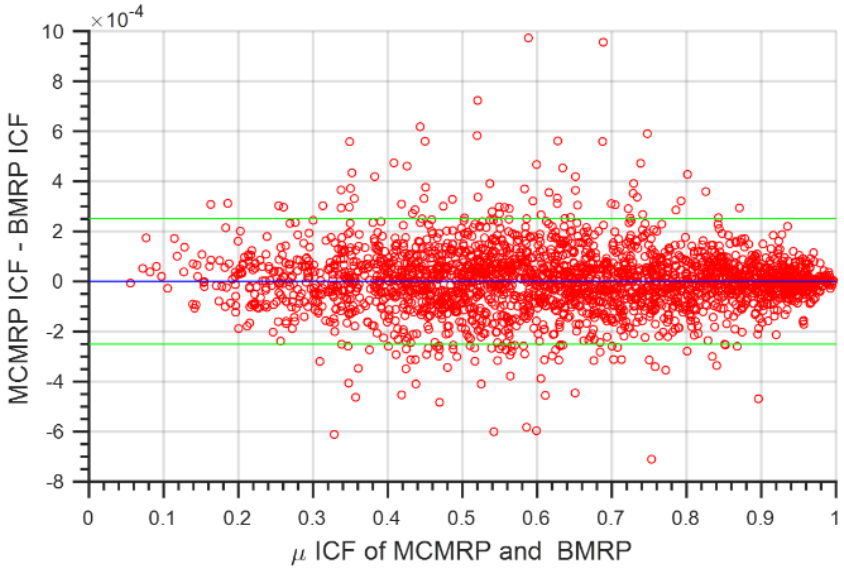

Figure 2.3. Discrepancy between BMRP predicted mean ICF and MCMRP predicted mean ICF.
Bland Altman plot of the 2500 pairs of BMRP and MCMRP predicted mean ICF values, with the difference in paired values plotted against the average. Note that the blue horizontal line identifies the mean discrepancy between the 2500 pairs of BMRP and MCMRP predicted mean ICF values (mean: 1.05E-7), and the green horizontal lines identify the lower and upper 95% confidence limits [-0.00025, 0.00026] for the discrepancy between any pair of BMRP and MCMRP mean ICF values.

A paired two-tailed *Student's* t-test revealed no difference between the predicted mean ICFs of the BMRP and the MCMRP ($p=0.850$, $\alpha=0.05$). Furthermore, no systematic relationship could be detected between the discrepancy between the predicted mean ICFs of the BMRP and the MCMRP as a function the mean of predicted model ICFs ($p=0.248$, Pearson Correlation), nor were any of the input parameters individually systematically related to the discrepancy between the predicted mean ICFs of the BMPR and the MCMRP (Fig. 2.4 A-F). When the z-scores of the input parameters were used as predictor variables in a MVLR model to predict the z-score scaled values for the discrepancies between the predicted mean ICFs of BMPR and MCMRP, neither the MVLR

model nor any of the input parameters individually were significant predictor(s) of the ICF discrepancy z-score (Table 2).

With no significant difference seen between the mean ICF values predicted by the BMRP and the MCMRP, and no systematic relationships seen in the discrepancies between the predicted mean ICFs of the BMPR and the MCMPR across the input parameter space, we concluded that the BMRP accurately represents the MCMRP, and that random cell placement can be modeled as a binomial stochastic process using Equation 1-2.

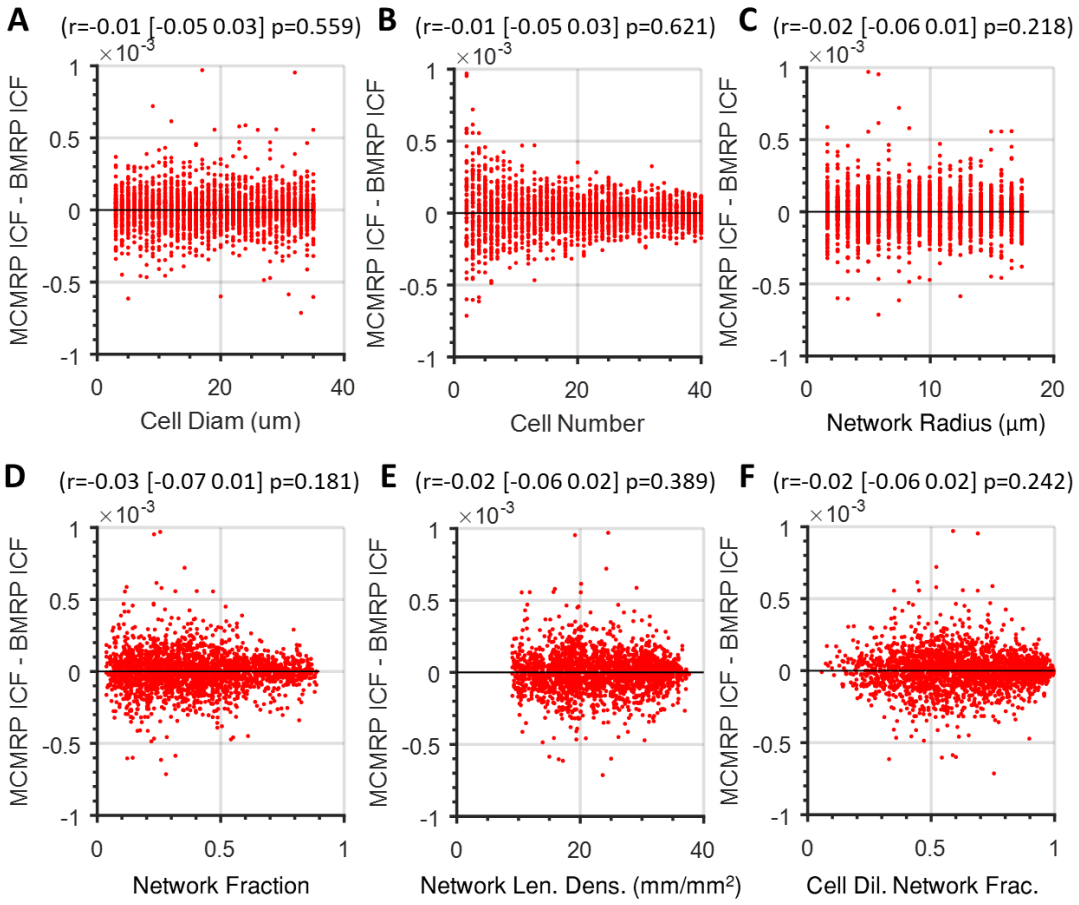

Figure 2.4. Discrepancy between BMRP predicted mean ICF and MCMRP predicted mean ICF.
(A-F) Relationship between each input parameter and the discrepancy between the BMRP predicted mean ICF values and the MCMRP predicted mean ICF values. Pearson correlation coefficient and associated 95% confidence interval and p-value are provided at the top of each scatterplot.

Table 2.2. Multivariable linear regression of z-scored input parameters versus the z-score of the difference in mean ICF predicted by MCMRP and BMRP (R2 <0.00).

Predictor	Coeffici	SE	F-	P-value
Intercept	-0.013	0.017		
Cell Diameter	-0.023	0.036	0.40	0.526
Cell Number	0.017	0.017	1.05	0.305
Network Rad.	-0.100	0.060	2.74	0.098
Network Frac.	0.100	0.799	1.55	0.213
Net. Len.	0.048	0.065	0.54	0.462
CDNF	-0.004	0.070	0.00	0.968
Model			1.38	0.217

2.4 Hypergeometric model and Validation (HMRP)

The binomial model assumes that the random placement of cells are completely independent events, that each successive COI placed in an image can be placed anywhere. However, in practice, COIs cannot overlap because they would be counted as a single cell. Thus, at higher cell densities, there are less locations for additional cells to be added and still counted as additional cells in the image, suggesting that placement of cells are related events and there exists a maximum number of placed cells, possibly suggesting that a hypergeometric model of random placement (HMRP) could be more suitable to model this process:

$$h(k|N,n,K) = \frac{\binom{K}{k}\binom{N-K}{n-k}}{\binom{N}{n}} \quad (3)$$

Where k is the number of colocalizing cells, n is the total observed number of cells in the image, N is the max number of cells that can exist in the image, K is number of colocalizing cells of the max population of cells placed in the image. The mean (μ) and standard deviation (σ) of the distribution can be directly calculated using the formulas listed in Equation 4[243]:

$$u = \frac{n \times k}{N} \qquad \sigma = \sqrt{\frac{n \times k \times (N-k) \times (N-n)}{N^2 \times (N-1)}} \quad (4)$$

Theoretically, the max number of non-overlapping cells that can be found in an image is defined by the hexagonal packing of circles, which previous research has shown to have a packing ratio of 0.901 (fraction of image area covered by circles), demonstrated to be invariant to the size of the circle and bounding area[244]. Yet this packing assumes perfect placement of all circles. Randomly placed non-overlapping pixelated cells may have a much lower packing ratio than this scheme, and may not be invariant to cell size since the shape of a cell is approximated in a pixelated fashion. Moreover, cells must be fully contained in the image area to contribute to the packing ratio for possibly colocalizing cells; cells that exceed the border of the image are not counted because their colocalization state with the network outside of the image cannot be determined.

We designed a Monte Carlo model of random cell placement without replacement that iteratively places cells until no more can fit in the image and then calculates the final packing ratio. Doing this for a range of cell pixel diameters reveals that the packing ratio of randomly placed fully contained non-overlapping pixelated circles changes with cell size (p=0, Kruskal Wallis, N=100 trials, Appendix-Supplemental Figure 4A) and image dimensions (p=0, Kruskal Wallis, N=100 trials, Appendix-Supplemental Figure 4B). For cell diameters less than 5 pixels, distinct cells cannot be discerned at the highest density, so experiment data with that low cellular resolution is considered invalid. For cell diameters above 5 pixels in diameter, a look up table is provided (Appendix-Supplemental Table 1) for 512 by 512 image dimensions and is used for calculating the N parameter in a hypergeometric distribution:

$$N = \frac{A * \eta}{\pi r^2} \quad (5)$$

Where A is the pixel area of image, η is the packing ratio from the look up table, and r is the pixel radius of the cell (Equation 5). The CDNF of each image is used to approximate the number of cells colocalizing (k) from the max population of cells (N), since it represents the fraction of the image where colocalization occurs:

$$k = Np \quad (6)$$

Where p is the CDNF, used also in the binomial distribution from Equation 1.

The mean ICF from the BMRP was compared to HMRP with the same dataset in Figure 3. No difference was seen in mean ICF values (p=0.194, paired t-test, N=2500, Appendix-Supplemental Figure 5A). Multiple variable linear regression revealed a marginally significant relationship between cell diameter and CDNF (Appendix-Supplemental Figure 5B-H), but the magnitude of the discrepancy between the models was negligible (mean difference: 4.26E-6), on par with difference between the MCMRP and BMRP models. The BMRP was selected for experimental use since its discrepancy with the HMRP mean ICF was negligible. Furthermore, with the HMRP, the parameter N changes with both cell size and image size: the computational demand of running simulations to approximate the max cell number in a given image makes it impractical to present as a general method until these parameters can be calculated in a more efficient and parameter invariant fashion.

Related to the issue that placement of cells are dependent events is whether homotypic interactions of the COI (cells migrating based on the position of other cells of the same type to form clumps) would alter the ICF. Encouragingly, we found that there is no difference in mean ICF from random placement of individually placed cells compared to cells placed in non-overlapping or overlapping clumps, suggesting that colocalization with the network structure is independent of self-colocalization with the COI (Appendix-Supplemental Figure 6).

2.5 Statistical Pipeline

Statistical processes were created to test for: **(1)** enriched intercellular colocalization affinity (ICA) of a cell type with the network structure within a single image, **(2)** enriched ICA for a study group of images, and **(3)** unique ICA between two study groups. All three of these tests were conducted by examining where the observed value of the random variable is located along the null probability distribution (Appendix-Supplemental Figure 7).

2.5.1 CIRCOAST Test: Testing Colocalization for Single Image

To test for enriched colocalization affinity in a given image, the network structure in the image is thresholded and segmented, dilated by the radius of the COI, and the fraction of white pixels defines the cell dilated network fraction for that image. Under the binomial stochastic model, the CDNF and cell number is used to calculate the probability of observing colocalization with the network to an equal or greater extent than what is observed in the image if colocalization occurs under random placement (Appendix-Supplemental Figure 7A). Equation 3 is utilized to derive the p values for a one-tailed binomial hypothesis test:

$$\text{CIRCOAST } p = 1 - \sum_{c}^{n} \binom{n}{c} p^{c} (1-p)^{n-c} \quad (3)$$

where c is the observed number of cells colocalizing in the image, n is the total number of cells in the image and p the cell dilated network fraction (CDNF) for that image. The null hypothesis that the image exhibits a degree of colocalization no greater than what would be expected by chance is rejected if CIRCOAST p is less than or equal to 0.05.

Since intercellular colocalization is modeled as a binomial process, sufficient sampling is determined by the quantity of each cell population sampled rather than fields of view imaged. In order to ensure that sufficient sampling can be obtained for each biological replicate, the data from multiple images is pooled together by calculating the combined CDNF across images and summing

total COIs found in each image. This technique was validated by comparing the CDNF and CIRCOAST p-value calculated from a test image compared to splitting it into four sub images. No difference was seen between the test images and original image, confirming the validity of this technique to join colocalization information across images (Appendix-Supplemental Figure 8). Notably, while this process can probe for enriched colocalization affinity in an image, it fails to directly test for enriched colocalization for a study group of multiple biological replicates (animals, culture well plates, etc.).

2.5.2 One-sample CIRCOAST Test: Testing Colocalization for a Single Study Group

We asserted that a statistical test that probes for enriched colocalization within one or more study groups requires a random variable that acts as a metric of colocalization and is scaled to reflect the degree of colocalization beyond what would be expected purely by chance. The p-value from the CIRCOAST calculated from the binomial hypothesis test in Equation 3 satisfied both of the aforementioned criteria. P-values are known to be reliable random variables suitable for hypothesis testing [245]. The mean CIRCOAST p-value is calculated across the joined images of each animal or subject (Appendix-Supplemental Figure 7B). The null distribution of the mean CIRCOAST p-value is simulated by assuming the null hypothesis is true and approximating what the distribution of the mean CIRCOAST p-value would be under the random placement paradigm (i.e. the *pseudo* null distribution). When the null hypothesis is true, the p-value of a hypothesis test is a uniform (0, 1) random variable. Therefore, to generate a pseudo null distribution for the mean binomial p-value, sets of N p-values are generated from a uniform (0, 1) distribution to match the N number of biological replicates in the experiment data, and the mean of the distribution of generated p-values is calculated. Repeating this process (10,000,000 trials) yielded the *pseudo* null distribution of the mean CIRCOAST p-value under the random cell placement paradigm. The percentile at

which the observed mean p-value falls along the distribution of simulated mean p-values yielded a *one-sample cellular colocalization affinity with network structures* (1-sample CIRCOAST) p-value for enriched colocalization across the entire study group by combining the information from the unique binomial distributions found in each image.

2.5.3 Two-sample CIRCOAST Test: Testing Colocalization between 2 Study Groups

To determine if two study groups differ with respect to the frequency of cell-cell colocalization, the CIRCOAST p-values are calculated for all the images from each group and subjected to a two-sample parametric (e.g. Student's t-test) or non-parametric (e.g. Wilcoxon Rank Sum test) test to yield an "observed" p-value (Appendix-Supplemental Figure 7C). This p-value is then compared to the pseudo null distribution of p-values that are generated under the null hypothesis scenario. The pseudo null distribution is generated by way of a large number of permutations of the study group identifications; i.e. the original study group identifications are randomly assigned to the sample identification numbers and the same parametric or non-parametric two-sample test is conducted using these random study group assignments. The fraction of the two-sample permuted test p-values less than or equal to the "observed" two-sample test p-value yields the *two-sample cellular colocalization affinity with network structures* p-value (2-sample CIRCOAST).

2.6 Experimental Validation

In Silico Validation: a dataset of images was created to represent healthy and diseased tissue, with one study group with high injected cell and endothelial cell density to mimic healthy conditions, and the another with low vascular and injected cell density for the dropout seen in diabetes (Appendix-Supplemental Figure 9). Vessels were created with the vessel network generator program and cells randomly placed with a single run of the Monte Carlo Model of Random

Placement. Correct statistical analysis should reveal no changes between study groups since the cells were randomly placed. While generic statistics revealed a change in intercellular colocalization affinity (colocalization per field of view: p=2.46e-09; colocalization per 1 mm vessel length: p=1.12e-02; fraction of injected cells colocalizing: p=6.68e-07; unpaired t-test), CIRCOAST correctly revealed no changes in colocalization between study groups (p=0.494). This dataset reveals that false a positive conclusion can be generated by generic statistics tests that confound changes in vascular and cell density when examining intracellular colocalization.

Imaged cells have a range of phenotypes in both size and shape that depart from the idealized uniform disk shape used in the MCMRP. We determined that a collection of cells with heterogeneous diameters can be approximated as cells with diameter equal to the mean diameter, yielding mean ICF values that are not identical, but have close agreement and negligible effect sizes (Appendix-Supplemental Figure 10). While the shape used to represent a cell can alter the ICF from random cell placement, representing cells as disk whose area is equal to the mean cell area sampled from a collection of imaged cells minimizes inaccuracies from altered geometry (Appendix-Supplemental Figure 11).

Errors in analyzing experimental images, such as failing to identify all cells in an image or discerning individual cells from cell clumps, could potentially throw off results of the CIRCOAST test. To examine the consequence of input error, we created a dataset of 2,000 simulated images, split into 50 study groups with 20 images each, to see how errors in quantification alter mean ICF, CIRCOAST 1-sample P, and statistical outcome. Simulated images had uniform vascular density and elevated cell density to induce a high degree of cell overlap with randomly placed cells.

With highly erroneous quantification represented by cell count quantified by connected components (any overlap between cells leads to them being counted as a single cell, roughly 20%

of cells miscounted), CIRCOAST 1-sample p values were significantly reduced, leading to an elevated false positive rate (Appendix-Supplemental Figure 12A-E). However, this effect was mitigated by calculating the input cell area using the diameter approximated circle method. Therefore, the error caused by incorrectly quantified cell clumps can be minimized by accounting for how the cell clusters change the mean cell area, although high emphasis should be placed on correct cell counting in experiment images. If cells are randomly missed and not counted in the quantification process, mean ICF or CIRCOAST 1-samples p values do not change (Appendix-Supplemental Figure 12 F-H), corroborated by the fact that cell density does not change mean ICF with the MCMRP parameter sweeps in Appendix-Supplemental Figure 3.

Cell Sources: See Appendix-Supplemental Note 3.

***In Vitro* and *In Vivo* Validation**: See Appendix-Supplemental Note 4.

Image Acquisition, Thresholding, and Quantification: See Appendix-Supplemental Note 5.

Results

A biologically relevant application of colocalization of annular cells with network structures is cellular colocalization with microvascular networks, which are comprised of branched networks of endothelial cells. ASCs are known to colocalize with vascular endothelial cells *in vitro*[246] and can engraft when injected *in vivo*[93]. Active homing of ASCs to the vasculature is hypothesized to play a role in this intercellular colocalization, but has not been established at a cell population level. The CIRCOAST statistical pipeline is validated by testing for the enriched cellular colocalization known for ASCs and ECs *in vitro* compared to fluorescent microspheres for a negative control, and then used *in vivo* to determine if injected ASCs exhibit greater than random colocalization with the vasculature to give insight to their possible mode of therapeutic action in disease[93].

ASCs cultured with HUVECS were found to have enriched colocalization over random behavior predicted by the BMRP (Figure 2.5 A, B; $p<1e-7$ 1-sample CIRCOAST, $\alpha=0.05$, 1e7 trials, N=6 wells, 3 images/well). For a negative control, fluorescent microspheres cultured with endothelial cells did not exhibit unique colocalization as expected (Figure 5 C, D; $p=0.235$ 1-sample CIRCOAST, $\alpha=0.05$, 1e7 trials, N=6 wells, 3 images/well). There was a significant difference in injected cell density (Figure 5 E, -18.7%, p=2.4E-2 two-sample t-test) and endothelial cell density (Figure 4F, +74.5%, p=3.3E-3 two-sample t-test) between study groups, illustrating the need for statistical tests that are not confounded by cell or vessel density. As demonstrated in Appendix-Supplemental Figure 9, changes in vascular and cell density can confound generic statistics that examine colocalization events, while the CIRCOAST takes into account these changes between study groups and effectively standardizes for both changes in vascular and cell density. Unique colocalization affinity between ASCs and microspheres with endothelial cells was detected (Figure 5G, p=1.3e-6, 2-sample CIRCOAST, $\alpha=0.05$, 1e7 permutations).

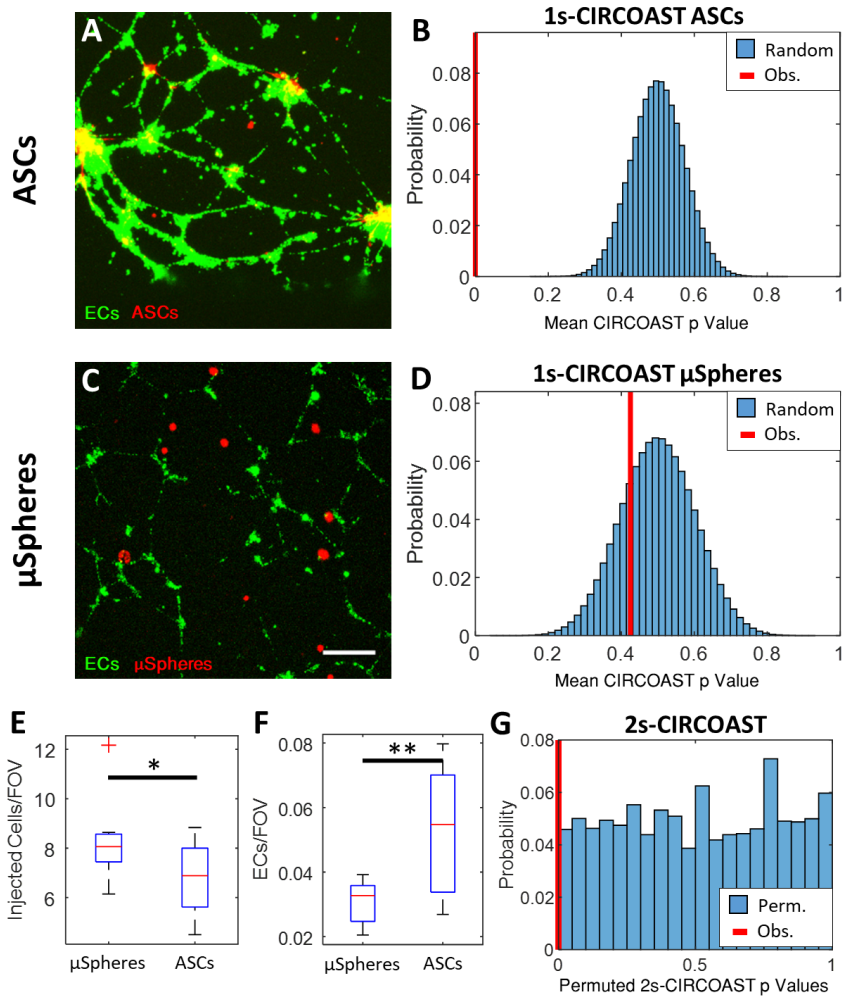

Figure 2.5. ASCs exhibit enriched colocalization with HUVECS, while fluorescent microspheres (µSpheres) do not.
(A) ASCs (red) co-cultured with HUVECS (green). **(B)** Distribution of simulated mean CIRCOAST p values (blue) of random colocalization of ASC group compared to observed mean CIRCOAST p value (red). **(C)** Fluorescent µSpheres seeded on a culture of HUVECs (scale bar 250 um). **(D)** Distribution of simulated mean CIRCOAST p values (blue) of random colocalization from fluorescent µSpheres compared to actual mean p value (red). **(E)** Injected cell density and **(F)** endothelial cell density between groups. **(G)** Distribution of p values (blue) derived from permuting CIRCOAST p values in a Wilcox Sum Rank Test between ASCs and µSpheres, with observed p value (red) (N=6 wells, 3 images/well).

For an *in vivo* validation of the CIRCOAST test, ASCs were injected into the eye in an *in vivo* model of diabetic retinopathy and found to exhibit enriched colocalization with the retinal vasculature (Figure 2.6 A-B, p<2.0e-7 1-sample CIRCOAST, 1e7 trials, N=6 wells). Surprisingly,

injected dead cells also had enriched colocalization with the vasculature (Figure 6 C-D, p<5.2e-4 1-sample CIRCOAST, 1e7 trials, N=6 mice, 3 images/mouse), possibly due to immune cells phagocytosing the injected dead cells while still retaining their fluorescent signal [247,248], and then chemotaxing to the vasculature and reentering the bloodstream [249]. While there was no change in EC density (Figure 6F, 2.24%, p=0.70 two-sample t-test), there was a trend of decreased injected cell density in the dead cell group (Figure 6E, -48.2%, p=0.071 two-sample t-test), and a high degree of variance between biological samples, illustrating the need for statistical tests to correct for high variance with cell densities. No difference was discerned in colocalization affinity between live and dead ASCs (Figure 6G, p=0.53 2-sample CIRCOAST, 1e7 permutations).

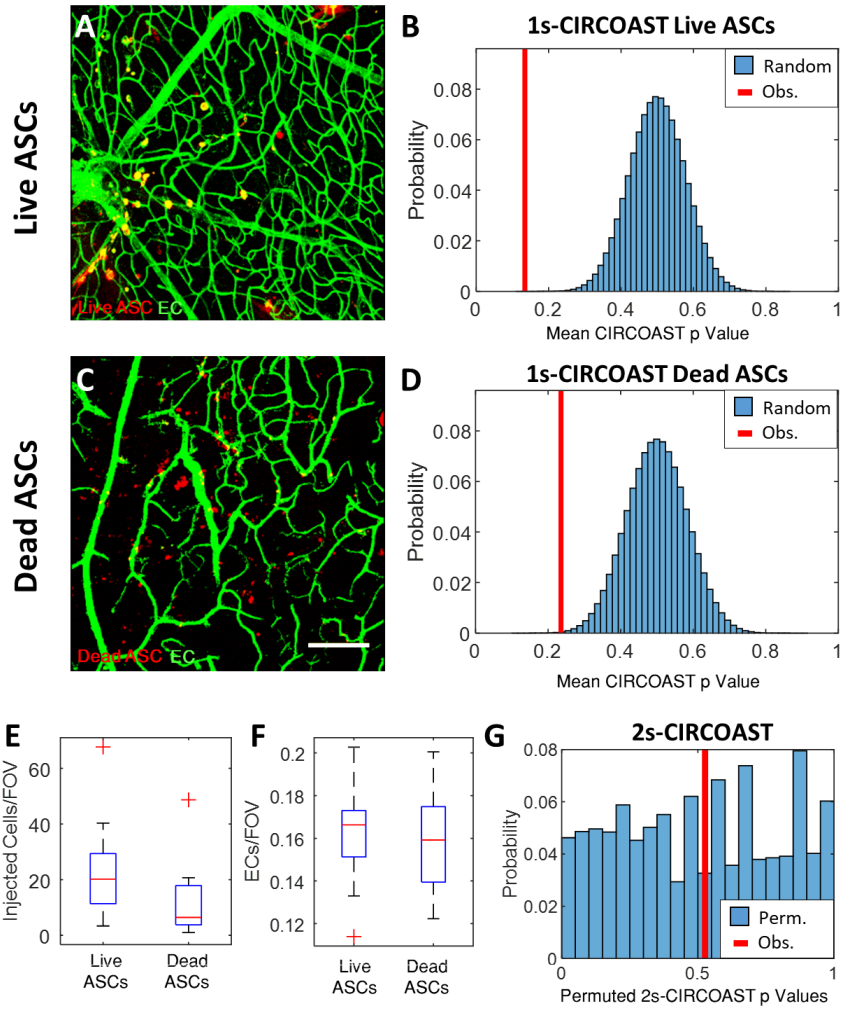

Figure 2.6. Injected live and dead ASCs both exhibit enriched, but unique, intercellular colocalization affinity with the vasculature.
(A) Confocal image of retinal vasculature (green, preprocessed and thresholded) and injected with live DiI-labeled ASCs (red). **(B)** Distribution of simulated mean CIRCOAST p values (blue) of random colocalization of ASC group compared to observed mean binomial p value (red). **(C)** Dead DiI-labeled ASCs in the retinal vasculature (scale bars 150 μm). **(D)** Distribution of simulated mean CIRCOAST p values (blue) of random colocalization from dead cell group, compared to actual mean p value (red). **(E)** Injected cell and **(F)** endothelial cell density between study groups. **(G)** Distribution of permuted p vales of Wilcox sum rank test of CIRCOAST p values between study groups, with observed p value (red) (N=6 mice, 3 images/mouse).

Discussion

In summary, we present CIRCOAST, a tool to characterize intercellular colocalization with network structures independent of the changes in cell and vessel network density found across

study groups from both *in vitro* and *in vivo* experiments. The tool was validated by probing for the previously known colocalization events observed between ASCs and endothelial cells *in vitro,* and used to test for enriched colocalization between these cells *in vivo*.

In the field of immunology, changes in cell density measured via flow cytometry or fluorescence microscopy are used as key metrics to study cell behaviors in disease[250]. These measurements report cell numbers or densities and only indirectly allude to changes in cell-cell interactions. In studies when cellular colocalization is examined more directly using microscopy, changes to cell density of either cell population can confound colocalization metrics analyzed with generic statistics: the method presented here does not have such drawbacks. Additionally, this method could be used to test for changes in colocalization within subpopulations of a single cell type denoted by unique marker expression to implicate marker expression with colocalization behavior.

Although we focused on characterizing the frequency of interactions between cells and microvessels, other static cellular network structures could be analyzed, such as neuron networks, glial cells, and lymphatics. Furthermore, we think that CIRCOAST could be extended beyond cell-vessel associations to study colocalization between two migrating cell populations so as to interrogate putative chemotactic behaviors. Possible applications include the study of interactions between T-cells and B-cells, which are known to be critical for T-cell activation and immune responses to infection[251]. Additionally, T-cell interactions with antigen presenting cells (e.g. macrophages, monocytes, and dendritic cells) play a significant role in homeostatic conditions and in initiating the adaptive immune response during disease[252]. Furthermore, *in vivo* time lapses indicate that macrophages may preferentially interact with pericytes in a juxtacrine fashion and receive instructions for launching innate immune responses[253] and play a role in vascular

remodeling[254]. Analysis of intercellular colocalization could confirm that macrophages are preferentially migrating to pericytes as part of this process. This method could also be extended to intracellular colocalization studies at high resolutions where imaged structures typically approximated as a point cloud are better approximated as an annular shape. Possible intracellular applications would include characterizing vesicle trafficking across cellular cytoskeletal components [255(p)].

Although CIRCOAST serves as a new method for hypothesis testing, additional features could enhance its capability. Future work, for example, could include extending the framework to perform power analyses for experiments, along with measuring the effect sizes between groups. Continued research in using a hypergeometric model of random cell placement could yield more accurate results once the distribution's parameters are better understood for this application. CIRCOAST is also limited to approximating cells as circular shapes, but supporting elongated cell morphologies could facilitate its use in analyzing a greater diversity of cell types and phenotypes. Furthermore, using established methods in characterizing cell morphology[256], simulated cells could be designed to directly represent the heterogeneity in cell size and morphology specific to each image instead of using a single cell shape as an approximation. Currently, CIRCOAST supports the analysis of 2D images that are maximum projections of 3D confocal z-stacks, leading to the issue that cells may appear to colocalize with the projected image but may not be colocalized in the z-dimension. Extending CIRCOAST so that it is capable of analyzing 3D image volumes will allow for more accuracy in determining whether cells of interest are colocalizing in the z-direction, in addition to the x- and y-directions. Usage of a nuclear dye would add greater certainty quantifying structures that correspond to distinct cells, especially in the cases where cell clumps form. Indeed, this test could be extended to characterize colocalization of a cell type with itself to

study homotypic interactions.

Limitations in generic statistical approaches have been implicated as a contributing factor in the crisis of reproducibility in the biomedical sciences [257]. With the development and validation of CIRCOAST, we aim to provide a novel statistical method that is superior to generic hypothesis tests for studying intercellular colocalization, allowing for more robust and repeatable characterization of cell-cell interactions in 2D images of tissues.

CHAPTER 3

Myh11 vascular smooth muscle cells and pericytes give rise to mesenchymal stem cells that precipitate proliferative vitreoretinopathy

Acknowledgements: Bruce A. Corliss[1], Anthony C Bruce[1], Sam Kesting[1], Paromita Dey[2], Jennifer Mansour[3], Scott A Seaman[1], Chris M Smolko[1], Corbin Matthews[1], Bijan Dey[2], Gary K Owens[4,5], Shayn M Peirce[1], Paul A Yates[1,6]

[1]Department of Biomedical Engineering, University of Virginia
[2]The RNA Institute, University at Albany, State University of New York
[3]Department of Biology, University of Virginia
[4]Robert M. Berne Cardiovascular Research Center, University of Virginia
[5]Department of Molecular Physiology and Biological Physics, University of Virginia
[6]Department of Ophthalmology, University of Virginia

Abstract

Adult mesenchymal stem cells (MSCs) offer significant potential for treatment of systemic disease, however multiple patients have been unexpectedly blinded after receiving intraocular injections of adipose-derived MSCs. The cellular origin of harvested MSCs remains unclear, the cell fate of exogenously applied MSCs is unknown, and their propensity to transform to alternate differentiated cell types *in vivo* is controversial. Here we show that adipose-derived, lineage-labeled myosin heavy chain-11 (Myh11) vascular smooth muscles and pericytes (vSMCs-PCs) give rise to definitive MSCs, confirming a perivascular source of MSCs. However, upon culturing and intraocular injection, we find that these cells transform into collagen secreting myofibroblasts, precipitating proliferative vitreoretinopathy. Similarly, in response to a specific type of ocular injury, endogenous retinal Myh11+ vSMCs-PCs detach from the microvasculature and differentiate into myofibroblasts. Inhibition of TGFβR attenuates endogenous retinal Myh11-lineage vSMCs-PC myofibroblast differentiation, but surprisingly does not alter injected adipose Myh11-lineage MSC myofibroblast differentiation, suggesting exogenous MSC-induced fibrosis is regulated by non-TGFβ dependent processes.

Introduction

The perivascular niche in multiple tissues, including bone-marrow[258], lung[259], heart[260], and adipose tissue[261], contains a population of mesenchymal stem cells (MSCs), classically defined by their *in vitro* characteristics of being multi-potent, plastic adherent cells that express a specific surface antigen profile[47]. Much effort has been made towards using this adult stem cell population as a potential therapy for regenerative medicine and wound healing. In particular, adipose-derived MSCs have received significant attention given their ease of accessibility from liposuction aspirates and the abundance of MSCs that can be harvested from this tissue source[262]. A definitive source of cells for adipose-derived MSCs remains to be determined as they are derived from cell culture of the stromal vascular fraction (SVF); a heterogeneous mixture of endothelial cells, immune cells, fibroblasts, and smooth muscle cells and pericytes (vSMCs-PCs) obtained following enzymatic digestion of adipose tissue.

Numerous pre-clinical and human clinical studies have demonstrated potential efficacy for both SVF and MSCs cultured from the SVF for a panoply of conditions including wound healing, bone replacement, inflammatory disease, and erectile dysfunction[263,264]. Despite therapeutic effect, the mechanism is often unclear. The cell fate of these injected cells remains largely unexplored, and at times, the delivered MSCs are not even found after the treated tissue is harvested for analysis[265]. Our limited knowledge of exogenous MSC behavior following delivery *in vivo* has likely contributed to the disastrous and unexpected blinding of multiple patients following injection of autologous SVF into the vitreous as a treatment for age-related macular degeneration[210]. Within days following injection, patients developed proliferative vitreoretinopathy (PVR), with lens subluxation, retinal detachment, and ultimately loss of vision. The exact cause remains unknown.

Within an *in vivo* injury, it is hypothesized that endogenous perivascular cells are activated to a MSC state to replace damaged cells, or to release growth factors, chemokines, and cytokines to remodel the injured tissue[57]. Tracking cell fate with lineage tracing technology has demonstrated that in some cases of injury and disease, perivascular cells appear to differentiate into specialized cells *in vivo*, such as muscle[266,267], follicular dendritic cells[268], osteoblasts [269], beige adipocytes[270], spinal cord scar-forming stromal cells[271], and myofibroblasts[272]. However, these findings were recently challenged by Guimarães-Camboa *et al* demonstrating Tbx18+ perivascular cells failed to exhibit *in vivo* multipotent behavior and were not able to differentiate into adipocytes in aging, into myofibroblasts within trans-aortic constriction, or into neurons after brain injury[273]. It remains unclear if these differences are due to the lineage marker used, the specific model tested, or experimental technique. In addition, the field is further confounded by recent single cell RNAseq data showing the existence of multiple subtypes of pericytes that appear to differ between vascular beds[274].

Definitive lineage analysis has yet to be performed to elucidate the source cell(s) of MSCs cultured *in vitro*, their cell fate once applied exogenously *in vivo*, or even the behavior of endogenous retinal pericytes in the setting of ocular injury, all of which may offer significant clarification of why patients were blinded from these intravitreal injections. To address these outstanding questions, we used the tamoxifen inducible Cre-recombinase, lineage-tracing mouse model, *Myh11*-CreER^{T2} [225], given Myh11 specificity to only vascular smooth muscle cells and at least a subset of pericytes[275].

Methods

Experimental Mouse Models

Myh11-CreER^{T2} mice were crossed with ROSA26-STOP^{FLOX}eYFP+/+ (The Jackson Laboratory, stock number 006148) and ROSA26-STOP^{FLOX}tdTomato+/+ (The Jackson Laboratory, stock number 007914) to generate *Myh11*-CreER^{T2}; ROSA26-STOP^{FLOX}eYFP+/+ (*Myh11*-eYFP+/+) and *Myh11*-CreER^{T2};ROSA26-STOP^{FLOX}tdTomato+/+ (*Myh11*-tdTomato+/+) mice. To induce cre-recombinase activity, 6-8-week-old mice were intraperitoneally injected daily over the course of 10 days with 0.1 mg of tamoxifen (Sigma-Aldrich, Cat#T5648) diluted in 100 µL of peanut oil. All adult male mice received a total of 1 mg of tamoxifen during the course of the 10-day injection period. Adult mice were analyzed or used for experimentation 4 weeks after the last tamoxifen injection to insure proper clearance and rule out the possibility that other unmarked cell types transiently express Myh11 in inflammation and acquire fluorophore expression without being of vSMC-PC lineage.

For OIR experiments, late-stage pregnant C57Bl/6 females (gestational days 11-15) were purchased from The Jackson Laboratory (stock number 00664). At postnatal day 1 (P1) to P3, *Myh11*-tdTomato+/+ pups received intragastric injections of 50 µg tamoxifen in 50 µL peanut oil using the previous protocol[276] to label Myh11-lineage vSMCs-PCs before the start of the OIR model. Once pups were at the age of P7, the mother and pups were both exposed to hyperoxia to induce OIR injury as described below.

Primary Cell Cultures

All primary cells were isolated from white, epididymal adipose tissue and were seeded at an original density of 1.5 x 10^4 cells/cm^2 on tissue, culture-treated plastic. Cells were cultured in

DMEM media supplemented with 10% FBS and 1% antibiotic/antimycotic. Cells were passaged using StemPro Accutase Cell Dissociation Reagent (ThermoFisher, A1110501) after reaching 70%-80% confluency and media was changed every 2-3 days. All cells analyzed throughout the study were between passage 2 and passage 8.

Immunohistochemistry (IHC) and Immunocytochemistry (ICC)

Epididymal white adipose tissue was harvested from tamoxifen-induced male *Myh11*-eYFP+/+ mice and fixed by submersion in 4% paraformaldehyde (PFA) for at least 12 h in 4°C. After fixation, tissue was permeabilized with 0.3% Triton X-100. Tissue was later blocked for 3 h at room temperature with mouse, donkey or goat serum to prevent nonspecific secondary antibody. Retinas, the retinal pigment epithelium layer, and sclera were harvested from enucleated eyes of male *Myh11*-tdTomato+/+ mice and C57Bl/6J pups, and fixed in 4% PFA for 1 h at room temperature. All ocular tissue was then permeabilized with 0.3% Triton X-100 for 1 h at room temperature, and blocked with serum for 1 h at room temperature.

Cultured cells were washed and fixed with 4% PFA for 1 h at room temperature, and permeabilized with 0.3% Triton X-100 for 5 min at room temperature. Following permeabilization, cells were blocked with serum for 1 h at room temperature. After permeabilizaiton and blocking steps, all tissue and cell samples were than washed, and labeled with isolectin GS-IB_4 (ThermoFisher, I32450, 1:200 dilution) or phalloidin (ThermoFisher, A22287, 1:200 dilution) depending on the experimental design. Tissues were stained with primary antibodies for GFP (ThermoFisher, A-21311, 1:200 dilution), Myh11 (Kamiya Biomedical Company, MC-352 1:400 dilution), RFP (Abcam, AB62341, 1:200 dilution), Col-III (Abcam, AB7778, 1:100), Col-IV (Bio-Rad, 134001, 1:200 dilution), CD31 (BioLegend, 102504, 1:200 dilution), and/or αSMA (Sigma-Aldirch, C6198

and F3777, 1:400 dilution). Non-conjugated primary antibodies were labeled with the appropriate secondary antibodies: donkey anti-rabbit Alexa Fluor 546 (ThermoFisher, A10040, 1:650 dilution), anti-rat Alexa Fluor 568 (ThermoFisher, A-11077, 1:650 dilution), donkey anti-goat Alexa Fluor 647 (ThermoFisher, A-21447, 1:650 dilution), and donkey-rabbit Alexa Fluor 647 (ThermoFisher, A-31573, 1:650 dilution). Tissues and cells were preserved and nuclei were stained with VECTASHIELD Antifade Mounting Medium with DAPI (Vector Laboratories, Burlingame, CA). Image acquisition was performed on whole mounted tissue and cultured cells using a Zeiss LSM 880 confocal microscope, and images were processed using ImageJ (NIH).

Flow Cytometry Characterization

White, epididymal adipose tissue from *Myh11*-eYFP+/+ mice was enzymatically digested in 4 units/mL Liberase (Sigma-Aldrich, 5401119001) and 0.74 units/mL of elastase (Worthington, LS002279) within DMEM/F12 media for 1.5 h at 37°C. After enzymatic digestion, mature adipocytes were removed by centrifuging the collected digested mixture at 1100 rpm for 5 min, followed by the discardment of the supernatant. The remaining pellet, or SVF, was washed and red blood cells were removed using red blood cell lysis buffer (ThermoFisher, 00-4333-57). Fc receptors of remaining SVF cells were blocked with antibodies to CD16/CD32 (ThermoFisher, 14-0161-81, 1:500 dilution). After blocking, cells were stained with primary antibodies to CD11b (BD Bioscience, 553309, 1:200 dilution), CD19 (BD Bioscience, 553784, 1:200 dilution), CD31 (eBioscience, 13-0311-811, 1:200 dilution), CD34 (BD Bioscience, 560518, 1:200 dilution), CD45 (BD Bioscience, 553078, 1:200 dilution), CD73 (BD Bioscience, 561543, 1:2000 dilution), CD90 (SouthernBiotech, Birmingham, AL, 1740-09, 1:400 dilution), CD105 (BD Bioscience, 564746, 1:400 dilution), and CD146 (BD Bioscience, 562232, 1:400 dilution). Biotin conjugated

antibodies to mark hematopoietic cell and endothelial cell markers (CD11b, CD19, CD31, CD34, and CD45) were labeled with streptavidin PE-Cy5.5 (ThermoFisher, SA1018, 1:1000 dilution) to establish a "negative dump" and exclude hematopoietic cells and endothelial cells from gating analysis. To determine cell viability, LIVE/DEAD Fixable Aqua Dead Cell Stain Kit (ThermoFisher, L34957) was used according to the manufacturer's protocol. Fluorescence minus one (FMO) controls were used determine correct expression of CD73, CD90, CD105, and CD146. Flow cytometry was performed on FAC-sorted, cultured primary cells, where the FAC-sorting protocol is described in the next methods section. To perform flow cytometry characterization on cultured cells, cells were uplifted with StemPro Accutase Cell Dissociation Reagent (ThermoFisher, A1110501). Fc receptors were blocked with serum, and cells were stained with the above primary antibodies to CD19, CD31, CD45, CD73, CD90, CD105, and CD146. Primary antibodies to CD11b, CD19, CD31, CD34, and CD45 were labeled with goat anti-rat AlexaFluor 546 (ThermoFisher, A-11077, 1:400 dilution). Cells were labeled with DAPI (ThermoFisher, D1306, 1:1000 dilution) to only include viable cells throughout the analysis. Cells were also labeled with isotype control antibodies IgG2a (BioLegend, 400501, 1:200 dilution) IgG2b (BioLegend, 400601, 1:200 dilution), and IgGc (BioLegend, 400701, 1:200 dilution) to serve as negative controls and distinguish between positive and negative gating for CD11b, CD19, CD31, CD34, and CD45. All flow cytometry characterization was performed on a BD LSRFortessa with DIVA 6.0. Flow cytometry data was analyzed in FlowJo v10 and FCS Express 6.0.

Fluorescence Activated Cell Sorting

To extract Myh11+ vSMCs-PCs and lineage-negative ("Lin(-)") population for culturing, white, epididymal adipose tissue from *Myh11*-eYFP+/+ and *Myh11*-tdTomato+/+ mice was

enzymatically digested as previously described [93,277]. Briefly, epididymal adipose tissue was enzymatically digested at 37°C for 1 h in 1 mg/mL in collagenase type I (ThermoFisher, 17100017) digestion buffer consisting of 200 nM adenosine, 2.5% (w/v) bovine serum albumin, 20 mM HEPES (4-(2-hydroxyethyl)-1-piperazineethanesulfonic acid), 1.2 mM monopotassium phosphate, 4.7 mM potassium chloride, 1.2 mM magnesium sulfate heptahydrate, 120 mM sodium chloride, and 1.3 mM calcium chloride dehydrate. After 1 h digesting, mature adipocytes were removed by centrifuging the collected mixture at 1100 rpm at 5 min and discarding the supernatant. The pellet, or SVF, was suspended in red blood cell lysis buffer (ThermoFisher, 00-4333-57) for 5 minutes at room temperature. Next, cells were suspended and washed in DMEM, and filtered through a 70-µm and 40-µm mesh. Collected cells were resupsended in FACS Buffer consisting of DMEM, 50% BSA, 5 mM EDTA, and DAPI (ThermoFisher, D1306, 1:1000 dilution). Myh11+ vSMC-PCs and Lin(-) cells were FAC-sorted using a BD Influx Cell Sorter. Cell populations were immediately sorted into DMEM media supplemented 10% FBS, and 1% antiobiotic/antimycotic and plated and cultured as described above.

In Vitro Tri-Differentiation Assay

For the tri-differentiation assay, cultured cells were introduced to standard low glucose media, adipogenic, chondrogenic, or osteogenic media according to the manufacturer's protocol (R&D Systems, SC010). After 14 days cultured under the appropriate differentiation media, mRNA expression was analyzed using qPCR. Immunocytochemistry was also performed following the steps mentioned above to stain for primary antibodies to FAPB4, Col-II, osteopontin (1:200 dilution) following the manufacturer's protocol (R&D Systems, SC010). Primary antibodies for protein detection were labeled with secondary antibodies donkey anti-rabbit AlexaFluor 647

(ThermoFisher, A31573, 1:400 dilution) and donkey anti-sheep AlexaFluor 647 (ThermoFisher, A21448, 1:400 dilution).

Collection of RNA and qPCR

Before and after tri-differentiation, RNA samples were collected from all cell populations to measure gene expressions of transcription factors and proteins involved in differentiation. RNA was isolated using an RNeasy MicroKit (Qiagen), and cDNA was synthesized using an iScript cDNA Synthesis Kit (Bio-Rad) or Superscript® IV Reverse Transcriptase (ThermoFisher). iQ SYBR Green Supermix (Bio-Rad) and SensiMix II Probe Kit (Bioline) was used as detection kits, and samples were analyzed on a CFX96 Touch (Bio-Rad). GAPDH was used as the housekeeping gene throughout analysis. Primer sequences can be found in Table S1.

Oxygen Induced Retinopathy (OIR)

The OIR model was adapted as previously described [93] and followed the guidelines of the ARVO Statement of the Use of Animals in Ophthalmology and Vision Research. C57Bl/6J mothers and pups were immersed in a closed chamber supplied with 75% oxygen from postnatal day 7 (P7) to postnatal day 12 (P12). Following OIR, eyes of the P12 mice were injected with 10,000 Myh11-Lin(+) MSCs or Lin(-) MSCs in 1.5 μL of PBS. Contralateral eyes were injected with equal volume of 1.5 μL PBS to serve as the appropriate control. To confirm signal in the retinal tissue, cultured MSCs were labeled with Vybrant DiI Cell-Labeling Solution (ThermoFisher) to assist with tracking injected cells. To analyze the retinal vasculature structure and the tissue integration of injected cells, mice were euthanized at P14 and P17 and retinas were harvested and labeled with isolectin GS-IB_4, and primary antibodies to αSMA, Myh11, and Collagen-IV as described earlier

in the above methods section. Tile scan and z-stack confocal images were captured of entire retinas to measure capillary dropout area and retina. Capillary dropout was defined as areas within the retinal tissue lacking tertiary vasculature structures. Capillary dropout area and retina area was calculated using ImageJ (NIH) tracing tool. The capillary dropout area was normalized by the retina area for statistical analysis. To observe the scar formation of Myh11+ MSCs above the superficial vascular plexus, the vitreous gel was also harvested and wholemounted in tandem with the retina and further processed for IHC.

Myh11-Lin(+) MSCs infected with adenovirus vectors as described below were washed with PBS before injection into OIR pups. 10,000 infected Myh11+ MSCs were intravitreally injected into P12 OIR pups in a volume of 1.5 μL of PBS. Five days after injection at P17, retinas and scar tissue were harvested and stained for DAPI, Col-IV, and GFP as described above in the IHC and ICC methods.

Laser Choroidal Neovascularization Model

A laser burn was applied to tamoxifen-induced *Myh11*-tdTomato+/+ mice as previously detailed [278]. Mice were anesthetized with ketamine/xylazine, and the eyes were dilated with tropicamide. Proparacaine hydrochloride ophthalmic drops were applied to the eye as a topical anesthetic. Ophthalmic gel was then applied along with a glass coverslip to serve as a contact lens. Laser photocoagulation (532 nm, 200 mW, 100 μm size, 200 ms) was applied to the fundus where 4 shots were performed in each eye at the 12-, 3-, 6-, and 9-o-clock positions. A successful burn injury was indicated by the formation of a bubble, thus confirming the rupturing of Bruch's membrane. Seven and twenty-one days post-laser injury, eyes were enucleated and the retinal pigment epithelium (RPE) along with the choroid and sclera were separated from the retina to

image the subretinal scar. All optical tissue was wholemounted and stained for DAPI, αSMA, Col-IV, and RFP as described earlier in the IHC and ICC methods.

Sclera Chemical Injury Burn

Silver nitrate burns were applied to the sclera near the boundary of the cornea of anesthetized tamoxifen-induced 12-14-week-old *Myh11*-tdTomato+/+ mice. While mice were under isoflurane anesthesia, proparacaine hydrochloride ophthalmic solution drops were applied to the eyes to serve as a topical anesthetic. After applying the topical anesthetic, the eyes were proptosed, and two silver nitrate burns were placed for approximately 2 seconds within a single 1-2 mm region of the sclera, or the region of the eye directly under the limbal vessels. Buprenex was intraperitoneally injected immediately after the burn injury to serve as an analgesic. Seven days and 21 days post-injury, TGFβR inhibitor, SB431542 (Sigma-Aldrich, S4317), was intravitreally injected into the eye at 100 μM in 1.5 μL of 0.3% (v/v) DMSO in PBS. Contralateral eyes received equal volume of 1.5 μL of 0.3% (v/v) DMSO in PBS to serve as a control for eyes injected with 100 μM SB431542. One month-post silver nitrate, eyes were enucleated, and stereoscope images were captured to determine eye volume measurements. The retinas were harvested, and labelled with phalloidin and stained with primary antibodies targeting αSMA, Col-III, Col-IV, CD31, and RFP as described above in the earlier methods section. Confocal tile scans and z-stack images were captured of the entire retina to calculate retina area and scar area, which was defined as the area of retina that contained off-vessel Myh11+ myofibroblasts (marked by αSMA+ stress fibers) within a Col-IV matrix. The scar area was normalized by retinal area for further statistical analysis.

Adenoviral shRNA Infection of Myh11+ MSCs

The shRNA adenovirus vector Ad-GFP-U6-mSMAD4-shRNA (Cat#ADV-272602) and a non-specific scrambled shRNA adenovirus vector (Cat#1122) was purchased from Vector Biolabs. Both adenovirus vectors contained a GFP reporter gene under control of the U6 promoter, thus we used Myh11-Lin(+) MSCs derived from *Myh11*-tdTomato+/+ male mice. Myh11-Lin(+) MSCs were transfected at 50-3000 MOI for 48 h in standard media culture conditions described above. Infected Myh11+ MSCs were also lysed for quantitative fluorescent immunoblotting as described below.

Immunoblotting

Quantitative fluorescent immunoblotting was performed as previously described[279]. Protein was collected from samples using RIPA lysis buffer and later prepared in 40 µL of dithiothreitol-containing Laemmli sample buffer. Samples were electrophoresed in 10% polyacrcylamide gels with tris-gylcine running buffer (25 mM tris base, 250 mM glycine, and 0.1% SDS) at 130V for 1 h. Proteins were transferred to a PVDF membrane (Millipore) in transfer buffer (25 mM tris, 192 mM glycine, 0.037% SDS, and 10-40% methanol) at 100 V for 1h on ice. PVDF membranes were blocked with 0.5X Odyssey® blocking buffer (LI-COR)+TBS+0.1% Tween-20. Primary antibodies were used to recognize the following proteins: Vinculin (Millipore, #05-386, 1:10,000 dilution), alpha-Tubulin (Abcam, #89884, 1:20,000 dilution), and SMAD4 (Cell Signaling Technology, #46535, 1:10,000 dilution). After incubation in primary antibodies overnight at 4°C, membranes were washed and probed with secondary antibodies diluted with 0.5x Odyssey® blocking buffer. The following secondary antibodies were used to target the above primary antibodies: IRDye® 680LT goat anti-mouse (LI-COR, #926-68020, 1:20,000 dilution), IRDye® 680LT donkey anti-chicken (LI-COR, #926-68028, 1:20,000 dilution), and IRDye® 800CW goat

anti-rabbit (LI-COR #926-32211, 1:20,000 dilution). Membranes were scanned on an Odyssey® infrared scanner (LI-COR) at 169-μm resolution and 0-mm focus offset. The ban intensities of the scanned 16-bit images were quantified by densitometry in ImageJ.

Luminex Analysis

Thirty days post-chemical injury burn described above, the eyes were enucleated from the mice, and the neural retina was harvested and placed in 40 μL of RIPA lysis and extraction buffer (ThermoFisher, 89900). The samples were kept on ice until ultrasonicated for 2 min. Ultrasonicated samples were then centrifuged at 18000g at 4°C for 15 min. The supernatant was collected and analyzed through a custom Luminex MAGPIX bead-based multiplex panel to measure active TGFβ1, CXCL10, IL-1a, IL-2, IL-4, and IL-17.

Statistical Analysis

All statistical tests were performed in GraphPad Prism (GraphPad Softwaree, La Jolla, California, USA, www.graphpad.com). Multiple unpaired t tests were used to compare two mean values of unpaired samples. A ratio paired t test was used to compare the two mean ratio values of paired samples following normal distribution. A Wilcoxon test was used to compare to the two mean values of paired samples that were not normally distributed which was determined by Shapiro-Wilk normality test. Significance for all test was defined as $p < 0.05$. One asterisk represents $p < 0.05$, two asterisks represent $p < 0.01$, three asterisks represent $p < 0.001$, and four asterisks represent $p < 0.0001$.

Results

Myh11 marks vascular smooth muscle cells (vSMCs) and pericytes (PCs) in epididymal, white adipose tissue

MSCs are known to reside in the stromal vascular fraction (SVF) of adipose tissue, but a definitive cell of origin remains elusive, with multiple candidate cells proposed [53,54]. The MSC nature of PCs has been extensively investigated [280], but studies also show that vSMCs exhibit MSC-like *in vivo* behavior, where vSMCs phenotypically switch to macrophage-like and Sca1+ CD106+ cells within atherosclerotic lesions [281–283]. Definitive characterization of a potential MSC phenotype *in vitro* for vSMCs and PCs has yet to be accomplished, as prior studies have not used lineage-tracing analyses that allows cell fate of vSMCs and PCs to be followed.

Myh11 is a contractile protein in the myosin heavy chain family that is classically expressed by vSMCs [225], but we show for the first time that Myh11 is also a marker for the extensive network of PCs in the adipose microvasculature (Figure 3.1A). Immunohistochemical (IHC) analyses of epididymal, white adipose tissue from tamoxifen-induced male *Myh11*-CreER^{T2}; ROSA26-STOP^{FLOX}eYFP+/+ (*Myh11*-eYFP+/+) mice revealed that eYFP marked vSMCs (Figure 3.1B) and PCs (Figures 3.1C), demonstrating that vSMCs and PCs in the adipose microvasculature transcribe Myh11 *in vivo.* IHC similarly confirms that Myh11 continues to be expressed in both vSMCs and PCs (vSMC-PCs) (Figure S3.1A), while in contrast another contractile protein, αSMA, is predominately expressed by vSMCs as compared to PCs (Figure S3.1B). Importantly, we did not find labeling of non-perivascular cells with Myh11 by either immunostaining for Myh11 or expression of eYFP within the adipose tissue.

Cultured Adipose-derived Myh11-Lin(+) vSMCs-PCs are MSCs

The International Society for Cellular Therapy (ISCT) requires an MSC derived *in vitro* [47] at a minimum to be 1) adherent to plastic; 2) to have positive expression for CD73, CD90, CD105, and to have negative expression for CD11b, CD19, CD3, CD34, and CD45; and 3) have the capability to differentiate into adipocytes, chondrocytes, and osteocytes. We initially evaluated the MSC potential of vSMCs-PCs by measuring MSC marker expression of uncultured Myh11-lineage (Myh11-Lin(+)) vSMCs-PCs. Using flow cytometry and gating out hematopoietic and endothelial cells (Figure 3.S2), we found Myh11-Lin(+) vSMCs-PCs lacked expression for CD73 (0.92±0.40% of gated cells), CD90 (13.71±6.19%), and CD105 (3.69±2.25%) (Figure 3.1D). We also measured the expression of CD146 since this marker is regarded by some studies as a potential perivascular and MSC marker [284,285]. From flow cytometry analysis, we found that approximately 45.94±5.49% of Myh11-Lin(+) vSMCs-PCs expressed CD146. Thus, by marker analysis alone, freshly isolated vSMCs-PCs do not meet the ISCT criteria for an MSC phenotype *in vivo,* and CD146 expression within the adipose Myh11+ population is variable.

To characterize the *in vitro* MSC profile of Myh11-Lin(+) vSMCs-PCs from epididymal white adipose tissue, these cells were isolated using FACS (Figure S1C), and then cultured on plastic. FAC-sorted Myh11-Lin(+) vSMCs-PCs sill maintained eYFP expression *in vitro*, as well as αSMA and Myh11 expression measured by IHC (Figure S3.1D). Performing flow cytometry on these serially passaged cells (of at least 2 passages), we find significantly increased expression of the designated MSC markers CD73 (79.75±6.09%), CD90 (82.21±5.47%), CD105 (97.35±0.63%), and CD146 (67.73±2.55%) (Figure 3.1E). Cultured Myh11-Lin(+) vSMCs-PCs also lacked expression (<3%) for hematopoietic and endothelial cell markers, CD11b, CD19, CD34, and CD45, and the endothelial cell maker CD31 (Figure 3.1F). In view of this surface

antigen expression, it seems that vSMC-PCs only acquire a definitive MSC surface marker profile following culture.

We next investigated the tri-differentiation capability of cultured Myh11-Lin(+) vSMCs-PCs, by replacing standard media with adipogenic, chondrogenic, or osteogenic differentiation media. Using immunocytochemistry (ICC) and qPCR, we show that the FAC-sorted, cultured Myh11-Lin(+) vSMCs-PCs undergo adipogenesis, chondrogenesis, and osteogenesis. ICC of cultured cells demonstrated Myh11-Lin(+) vSMCs-PCs increased protein expression of FABP4, Col-II, and Osteopontin after exposure to the adipogenic, chondrogenic, and osteogenic media, respectively (Figures 3.1G-H). During adipogenesis, *PPARγ* and *FABP4* mRNA expression is upregulated when compared to undifferentiated cells. During chondrogenesis, there is upregulation of *ColA1* and *Sox9* mRNA expression, and during osteogenesis, *Osteocalcin* and *Runx2* mRNA expression levels are also increased. Thus, by ISCT criteria Myh11-Lin(+) vSMCs-PCs are MSCs.

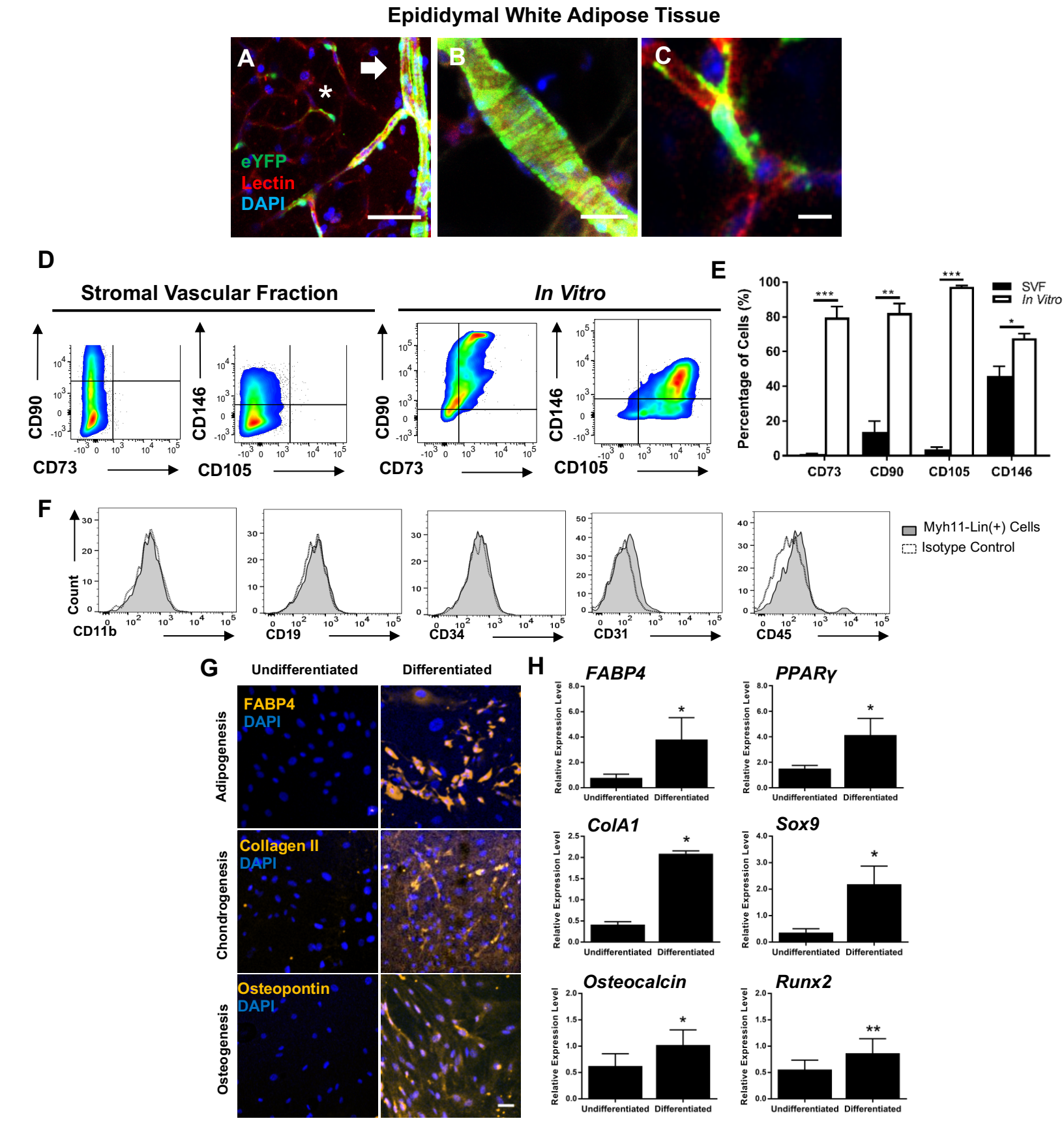
Epididymal White Adipose Tissue
A
B
C
eYFP
Lectin
DAPI
D
Stromal Vascular Fraction
In Vitro
CD90
CD146
CD73
CD105
E
Percentage of Cells (%)
SVF
In Vitro
CD73
CD90
CD105
CD146
F
Count
CD11b
CD19
CD34
CD31
CD45
Myh11-Lin(+) Cells
Isotype Control
G
Undifferentiated
Differentiated
Adipogenesis
Chondrogenesis
Osteogenesis
FABP4
DAPI
Collagen II
DAPI
Osteopontin
DAPI
H
FABP4
PPARγ
ColA1
Sox9
Osteocalcin
Runx2
Relative Expression Level
Undifferentiated
Differentiated

Figure 3.1.: Adipose derived, lineage-marked Myh11+ vascular smooth muscle cells and pericytes (Myh11-Lin(+) vSMCs-PCs) give rise to mesenchymal stem cells (MSCs) during adaptation and growth in vitro.
(A-C) (A) eYFP (green) lineage marker induced by tamoxifen labels Myh11+ cells in epididymal white adipose tissues demonstrating Myh11 is expressed in vascular smooth muscle cells (vSMCs) (arrowhead) and microvascular pericytes (PCs) (asterisk) along lectin+ blood vessels. Scale bar, 50 μm. (B) vSMCs show characteristic "tire tread" pattern on larger arterioles. Scale bar, 25 μm. (C) PCs show characteristic wrapping around adipose capillary microvasculature. Scale bar, 10 μm. **(D-F)** (D) Assessment of markers via flow cytometry to confirm an MSC phenotype shows adipose-derived Myh11-Lin(+) vSMCs-PCs have very low endogenous expression of CD73, CD90, CD105 when collected in the SVF. (E) However, these markers significantly increase once these cells are cultured *in vitro* after isolation via fluorescence activated cell-sorting (FACS) (three independent flow analyses per panel). (F) FAC-sorted and cultured Myh11-Lin(+) vSMCs-PCs lack expression of the hematopoetic, endothelial, and macrophage markers CD11b, CD19, CD34, CD31, and CD45 (three independent flow analyses per panel).**(G-H)** Cultured Myh11-Lin(+) vSMCs-PCs demonstrate requisite tri-differentiation when cultured in adipogeneic, chondrogenic, or osteogenic media for 14 days. (G) Increase in FABP4, Collagen II, and Osteopontin is observed by IHC in Myh11-Lin(+) vSMCs-PCs undergoing tri-differentiation. Scale bar, 50 μm. (H): mRNA expression of protein markers and transcription factors involved in adipogenesis, chondrogenesis, and osteogenesis are also significantly upregulated in Myh11-Lin(+) vSMCs-PCs following tri-differentiation (n=3 biological replicates). Relative expression is normalized to GAPDH expression in each sample. *,$p<0.05$, **,$p<0.01$. Results are represented as mean ± standard error of mean (SEM). Data were analyzed using multiple t unpaired t tests followed by the Holm-Sidak post-hoc comparisons to correct for multiple comparisons (E), or a ratio paired t-test (H).

Adipose-derived Lineage Negative Cells Also Meet ISCT Criteria as MSC

Having confirmed that Myh11-Lin(+) vSMCs-PCs give rise to MSCs *in vitro*, we next examined whether this cell population is the sole contributing source of MSCs within adipose SVF. To do so, we examined surface marker expression of adipose SVF that are eYFP-, which we refer to here as the lineage-negative ("Lin(-)") population. Similar to Myh11-Lin(+) vSMCs-PCs, we find that the Lin(-) population of cells have low expression for CD73 (0.41±0.17%), CD90 (12.33±4.34%), and CD105 (1.62±0.36%) before plating in culture (Figure S3.3A). Unlike the Myh11-Lin(+) vSMCs-PCs found in the SVF, Lin- cells also lacked expression of the perivascular marker CD146 (2.95±1.30%) (Figure S3.3A). However, once FAC-sorted Lin- cells are isolated and cultured on

plastic they significantly increased expression of CD73 (66.29±4.70%), CD90 (83.98±1.32%), CD105 (90.11±3.71%), and CD146 (59.33±2.07%) (Figure S3B). As required by ISCT criteria, this cultured Lin- cell population also lacked expression for hematopoietic and endothelial cell markers CD11b, CD19, CD34, CD31 and CD45 (<3%) (Figure S3.3C).

FAC-sorted and cultured Lin(-) cells are also able to undergo tri-differentiation with FABP4, Col-II, and osteopontin protein expression increasing following exposure to adipogenic, chondrogenic, and osteogenic media, respectively. mRNA differentiation markers are also significantly upregulated in these cells after culture in tri-differentiation media (Figure S3.3D). These results strongly suggest there is no single cellular source from the adipose SVF for MSCs, and a MSC phenotype is a direct result of being cultured, given that isolated cells directly from the adipose tissue do not appear to endogenously express MSC surface markers.

Myh11 lineage-traced MSCs Derived from Adipose vSMCs-PCs Integrate with and Accelerate Recovery of Retinal Vasculature in Oxygen-Induced Retinopathy

The injection of adipose-derived MSCs are considered a therapeutic for regenerative medicine due to their pro-angiogenic paracrine profile and their ability to provide juxtacrine support for endothelial cell angiogenic networks [85,286]. We and others have demonstrated that locally-delivered, adipose-derived MSCs are able to prevent capillary loss and remodel retinal vasculature in murine models of retinal vascular disease [93,189,287]. We next sought to determine if intravitreally delivered MSCs derived solely from adipose Myh11-Lin(+) vSMCs-PCs ("Myh11-Lin(+) MSCs") could accelerate retinal vasculature recovery following oxygen-induced retinopathy (OIR). In the OIR model, the central retinal microvasculature is ablated by exposure to hyperoxia from post-natal day 7 to 12 (P7 to P12) (Figure 3.2A) [288]. After hyperoxic exposure, 10,000 cultured Myh11-

Lin(+) MSCs were intravitreally injected into the eyes of P12 mice, and at P14 and P17, the retinas were harvested and stained with lectin and Col-IV to quantify retinal capillary dropout and examine the integration of Myh11-Lin(+) MSCs into the retinal vasculature. At P14, eyes that were injected with Myh11-Lin(+) MSCs had a significant 18.4% reduction in avascular area compared to PBS-injected contralateral eyes. By P17, there was a significant 22.6% reduction in retinal capillary dropout compared to PBS-injected contralateral eyes (Figure 3.2B). Intravitreal injection of the Lin(-) MSC population similarly accelerates retinal vasculature growth after hyperoxia injury with no significant difference as compared to Myh11-Lin(+) MSCs (Figure S3.4A). These results indicate that adipose derived Myh11-Lin(+) and Lin- MSCs are both supportive for vascular regrowth in models of retinal vascular injury.

We next assessed the ability of injected Myh11-Lin(+) MSCs to associate and integrate with the recovering retinal vasculature. Confocal analysis demonstrates injected Myh11-Lin(+) MSCs are found in perivascular positions, with a typical phenotypic appearance as endogenous retinal pericytes (Figure 3.2C). At P14, 1.54±0.34% of Myh11-Lin(+) MSCs were integrated into the retinal tissue, with 38.14±16.06% of these cells adopting a perivascular position. At P17, there was an increase in both the number of integrated cells (2.91±0.96%) as well as their propensity to adopt a perivascular position (58.24±8.46%) (Figure 3.2C). These results suggest injected Myh11-Lin(+) MSCs can re-adopt a perivascular position consistent with their vSMC-PC perivascular cell origin. However, the majority of intravitreally injected Myh11-Lin(+) MSCs do not invest within the retina tissue.

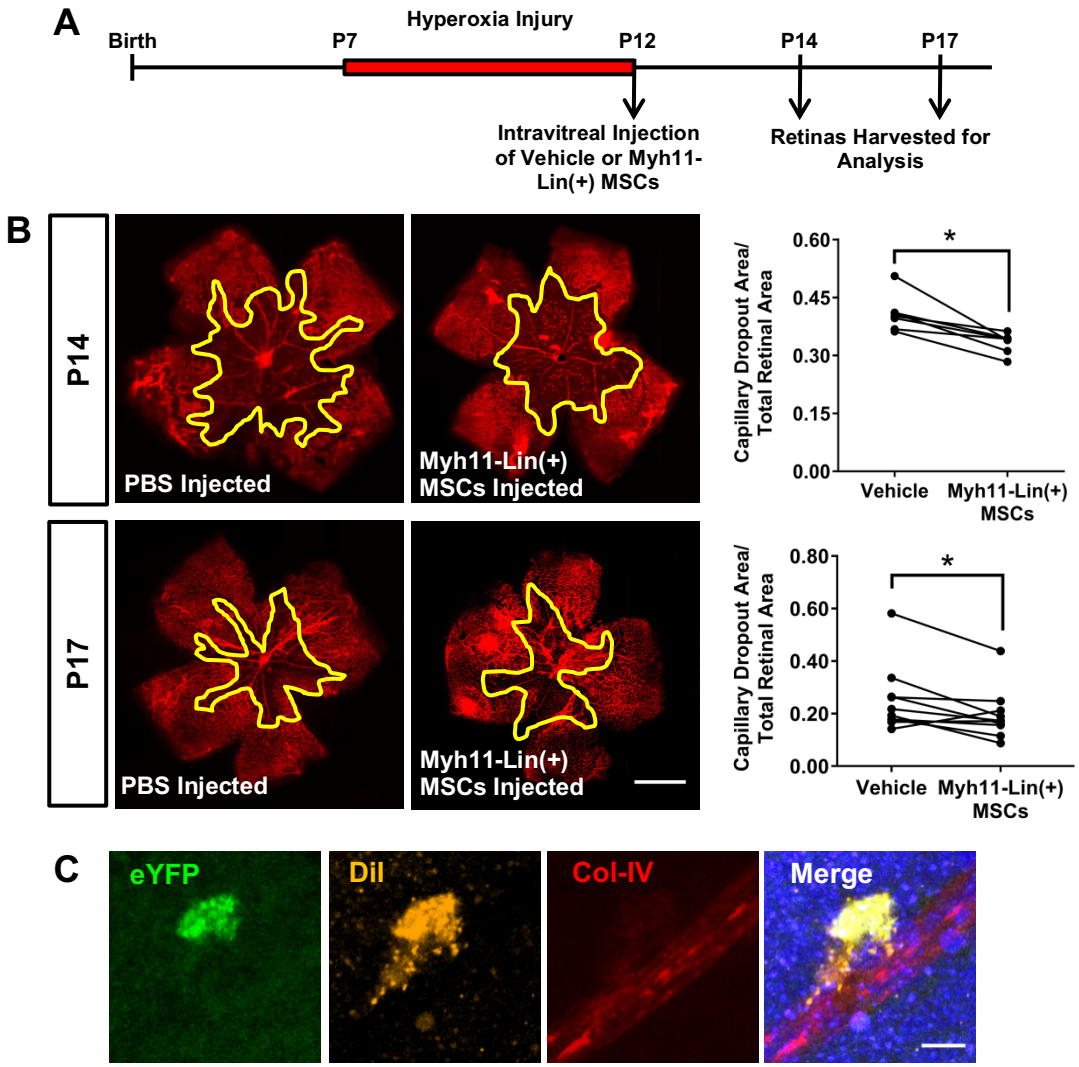

Figure 3.2: Intravitreally injected Myh11-Lin(+) MSCs accelerate microvasculature recovery and adopt a perivascular position during murine oxygen-induced retinopathy (OIR).

(A) Diagram illustrating the timeline of the murine OIR model and intravitreal injection of Myh11-Lin(+) MSCs. After hyperoxia injury from P7 to P12, pup eyes were intravitreally injected with PBS-vehicle or 10,000 cultured Myh11-Lin(+) MSCs and analyzed at P14 and P17 post-injection. **(B)** When compared to the contralateral PBS vehicle control eyes, eyes with intravitreally injected lineage-traced vSMCs-PCs experienced a significant 18.4% reduction (n=7 paired eyes) in capillary dropout area at P14, and, at P17 a significant 22.6% reduction (n=10 paired eyes) in capillary dropout area between the eyes injected with the PBS vehicle control and Myh11-Lin(+) MSCs. Retinal flatmounts are shown with outlined area (yellow) representing capillary dropout region caused by OIR. Retinal blood vessels are immunostained with lectin (red). Scale bar, 1000 µm. **(C)** At P14 and P17, intravitreally injected cultured Myh11-Lin(+) vSMCs-PCs (DiI+/eYFP+) were able to integrate into the retinal tissue and associate with Col-IV+ retinal vasculature Scale bar, 10 µm. *,($p<0.05$). All data were analyzed using a Wilcoxon test.

Myh11-Lin(+) MSCs Derived from Adipose vSMCs-PCs Also Precipitate Proliferative Vitreoretinopathy (PVR)

Although Myh11-Lin(+) MSCs can successfully reintegrate with the retina as putative retinal vSMCs-PCs, the question remains as to the cell fate of the remaining unincorporated cells. Prior to intravitreal injection, cultured Myh11-Lin(+) MSCs are positive for both Myh11 and αSMA stress fibers (Figure S3.1C), but low expression for Col-IV (Figure 3.3A). Unfortunately, after injection Col-IV labeling reveals a substantial increase in extracellular matrix production of the injected cells remaining in the vitreous, with formation of a fibrotic pre-retinal membrane characteristic of PVR (Figure 3.3A-B). We also find that injected Myh11-Lin(+) MSCs remaining in the vitreous exhibit αSMA stress fibers but have decreased Myh11 expression as compared to endogenous, retinal vSMCs-PCs (Figure 3.3C-D). Fibrotic pre-retinal membranes are similarly observed in eyes injected with the Lin(-) population, where this cell population also expresses αSMA+ stress fibers and substantial Col-IV staining (Figure S3.4B). The presence of aSMA+ stress fibers, disassociation from the retinal vasculature in a diseased environment, and Col-IV expression [289,290] suggests that MSCs adopt a default myofibroblast phenotype when injected within the vitreous cavity.

Endogenous Retinal Myh11-Lin(+) vSMCs-PCs Do Not Differentiate Into Myofibroblasts in OIR

Given that the intravitreal injection of Myh11-Lin(+) MSCs precipitates differentiation to a myofibroblast phenotype in the murine OIR model, we next examined if there were similar differentiation of endogenous, retinal Myh11-Lin(+) vSMCs-PCs following OIR injury. To explore this hypothesis, we induced cre-recombinase in P1 to P3 *Myh11*-CreER^{T2};ROSA26-STOP^{FLOX}tdTomato+/+ (*Myh11*-tdTomato+/+) pups using intragastric tamoxifen injections. From

P7 to P12, the induced *Myh11*-tdTomato+/+ pups were introduced to hyperoxia, and at P12 these mice were returned to normoxia and retinas analyzed at P17 (Figure 3.3E). As indicated by the tdTomato expression, we find no endogenous, retinal Myh11-Lin(+) vSMCs-PCs off-vessel with Col-IV+ matrix production and/or an obvious myofibroblast morphological phenotype directly above or within the retinal vascular plane (Figures 3.3F). In the area of central retinal capillary dropout, Myh11-Lin(+) vSMCs-PCs remain directly in contact with CD31+ blood vessels and tip cells extending towards the interstitial space of the retina (Figures 33.G-H). Taken together, the data indicates that Myh11-Lin(+) MSCs can promote retinal vasculature growth and reintegrate with the retinal vasculature to likely serve as functional vSMCs or PCs. However, Myh11-Lin(+) MSCs remaining off vessel by default appear to differentiate into myofibroblasts with copious production of Col-IV matrix characteristic of PVR. For endogenous vSMCs-PCs, this differentiation is not observed within the same retinal injury model. It remains unclear the cause of this distinct difference in behavior, though it is tempting to speculate that association with and integration into the retinal vasculature may fundamentally modulate cell behavior away from myofibroblast differentiation.

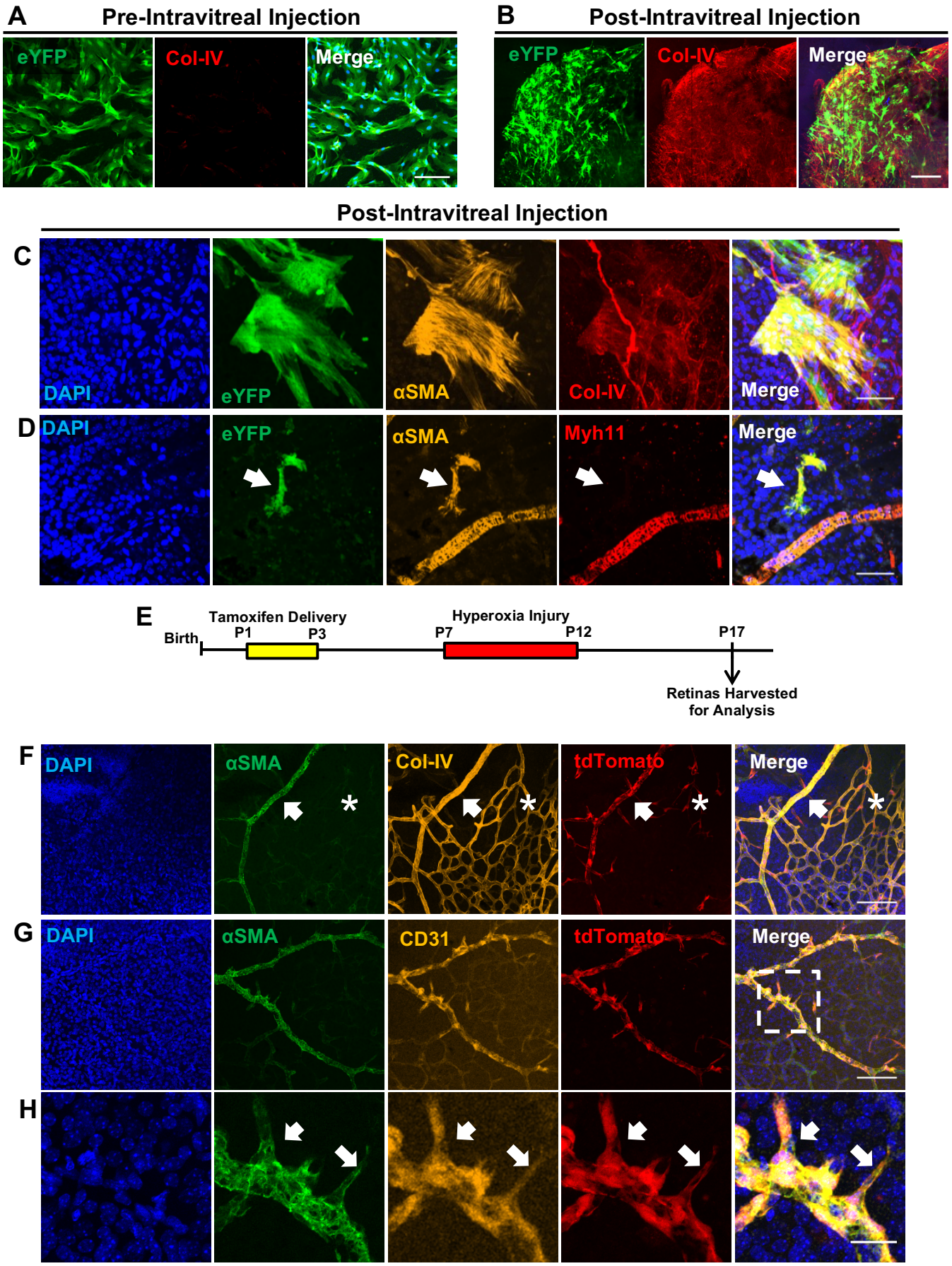
A
Pre-Intravitreal Injection
eYFP
Col-IV
Merge
B
Post-Intravitreal Injection
eYFP
Col-IV
Merge
Post-Intravitreal Injection
C
DAPI
eYFP
αSMA
Col-IV
Merge
D
DAPI
eYFP
αSMA
Myh11
Merge
E
Tamoxifen Delivery
Birth
P1
P3
Hyperoxia Injury
P7
P12
P17
Retinas Harvested
for Analysis
F
DAPI
αSMA
Col-IV
tdTomato
Merge
G
DAPI
αSMA
CD31
tdTomato
Merge
H

Figure 3.3. Within the murine OIR model, intravitreal injected Myh11-Lin(+) MSCs in the vitreous gel exhibit a myofibroblast phenotype, while endogenous, retinal Myh11-Lin(+) vSMCs-PCs remain in a perivascular position.
(A-B) (A) Myh11-Lin(+) MSCs lack expression of Col-IV *in vitro,* however, (B) intravitreal injected Myh11-Lin(+) MSCs produce Col-IV in the vitreous gel, forming a dense, fibrotic pre-retinal membrane in murine OIR eyes. Scale bars, 200 μm.
(C-D) (C) Intravitreal injected Myh11-Lin(+) MSCs demonstrate a myofibroblast phenotype with expression of αSMA+ stress fibers and Col-IV. (D) However, they surprisingly lose their expression of Myh11 following injection (arrow). Note retinal capillaries have Col-IV expression but lack αSMA (asterisk), while arterioles maintain αSMA and Myh11 expression (arrow). DAPI stains nuclei of underlying retinal ganglion cells in addition to injected MSCs. Scale bars, 25 μm (B), 100 μm (C).
(E) Experimental design where tamoxifen is delivered postnatal day 1 to 3 *Myh11*-tdTomato+/+ mice to induce expression of tdTomato in Myh11+ vSMCs-PCs. Induced mice are then exposed to hyperoxia from postnatal day 7 to 12 to cause OIR injury, with retinas harvested at P17 to determine cell fate of endogenous, retinal Myh11-Lin(+) vSMCs-PCs.
(F-H) (F) At P17, endogenous, retinal Myh11-Lin(+) vSMCs-PCs still reside on Col-IV+/CD31+ vessels, with αSMA expression higher in vSMCs (arrow) than PCs (asterisk). Scale bar, 100 μm. (G) Myh11-Lin(+) vSMCs-PCs remain on vessel with no vSMCs-PCs found off vessel. Scale bar, 100 μm. (H) vSMCs-PCs do extend processes from CD31 tip cells (arrow) at the leading front of the regenerating retinal microvasculature. Scale bar, 25 μm. All immunohistochemistry data representative of at least three animals.

Endogenous Myh11-Lin(+) vSMCs-PCs Do Not Contribute to Fibrotic Scar Formation in Laser-induced Choroidal Neovascularization

Given the observed myofibroblast differentiation of intravitreally injected Myh11-Lin(+) MSCs, it raises the possibility that endogenous retinal vSMCs-PCs may similarly differentiate into myofibroblasts to contribute to fibrosis associated with age-related macular degeneration. There are no tissue-resident fibroblasts and no αSMA+/F-actin+ cells are found in the interstitial space of healthy murine retina (Figure S3.6). It is unknown whether and to what extent endogenous retinal or choroidal mural cells contribute to the scar region in sub-retinal fibrosis. To test this hypothesis, laser induced rupture of Bruch's membrane [291] was performed in the lineage tracing *Myh11*-tdTomato+/+ mouse model, generating a choroidal neovascular membrane with associated subretinal fibrosis (Figure 3.4A). We specifically chose to use a tdTomato fluorescent protein

lineage marker with this injury model to avoid confounding green wavelength autofluorescent signals generated by the fibrotic scar and general ocular inflammation accompanying the laser burn. Seven days post-rupture, laser treated eyes were harvested, and we found as expected laser-induced Col-IV+ subretinal fibrosis (Figure 3.4B). Surprisingly, no Myh11-Lin(+) vSMCs-PCs were found within or surrounding the induced scar, despite the presence of cells with clear myofibroblast morphology and characteristic αSMA stress fibers (Figures 4B). Twenty-one days post-rupture of Bruch's membrane, we still observed that no Myh11-Lin(+) vSMCs-PCs had differentiated into myofibroblasts within the scar tissue itself (Figure 3.4C). However, we did find Myh11-Lin(+) vSMCs-PCs were by now fully associated with the induced neovessels that traversed through this fibrotic scar tissue (Figure S3.4A). Myh11-Lin(+) vSMCs-PCs were also seen enveloping the retinal vasculature just above this scar region, but again with no labeled cells off vessel (Figure S3.4B). These results unexpectedly indicate that Myh11-Lin(+) vSMCs-PCs do not appear to contribute to the subretinal fibrotic tissue after laser photocoagulation of the choroid, and by extension are likely not a major contributor to fibrotic scar associated with macular degeneration.

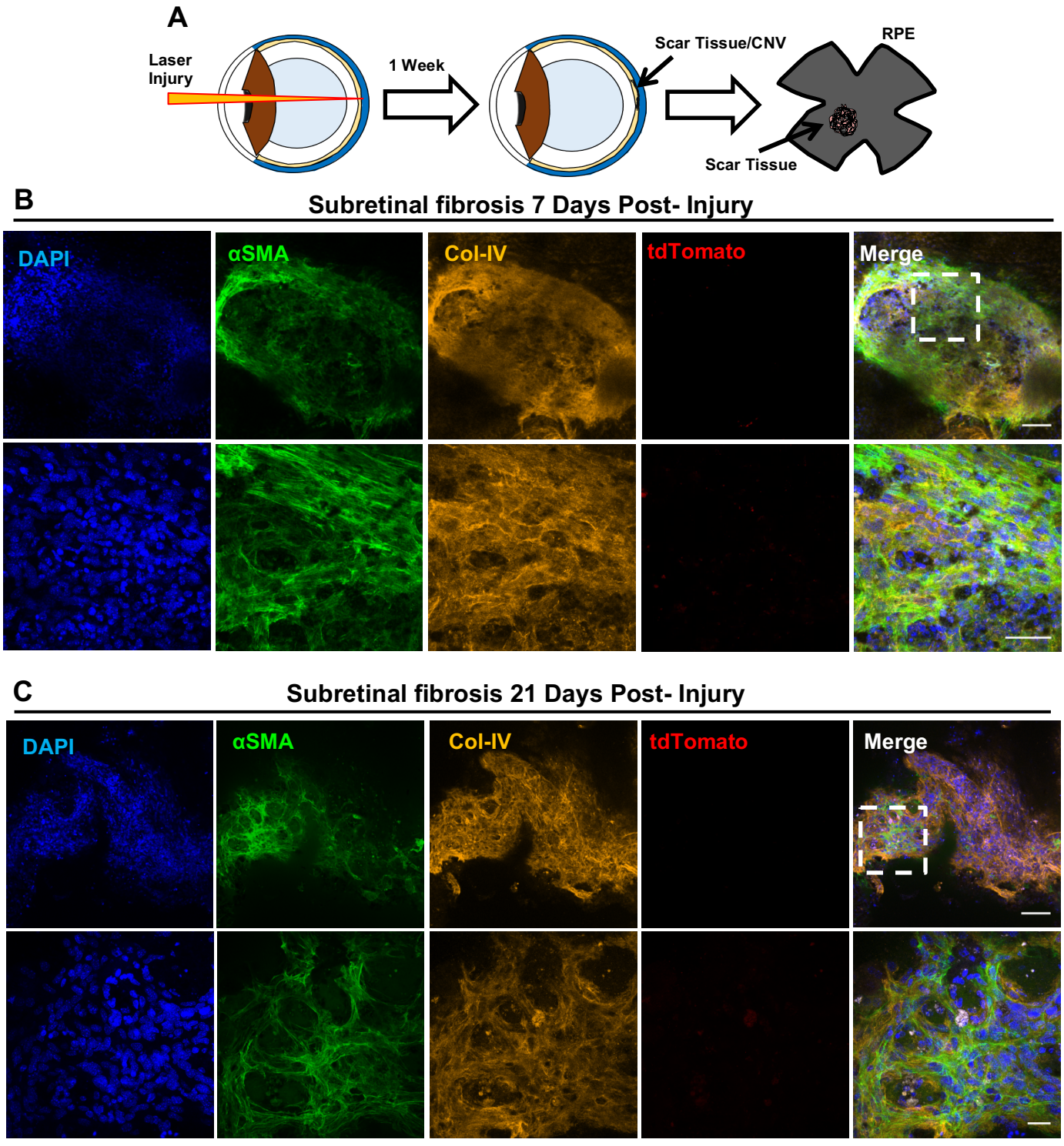
A
Laser Injury
1 Week
Scar Tissue/CNV
RPE
Scar Tissue
B
Subretinal fibrosis 7 Days Post- Injury
DAPI
αSMA
Col-IV
tdTomato
Merge
C
Subretinal fibrosis 21 Days Post- Injury
DAPI
αSMA
Col-IV
tdTomato
Merge

Figure 3.4. Myh11-Lin(+) vSMCs-PCs do not contribute to subretinal scar formation in a murine laser-induced choroidal neovascularization (CNV) model.
(A) Laser injury is introduced to adult Myh11-Lin(+) mice, where vSMCs-PCs are lineage marked with tdTomato. Laser burn ruptures Bruch's membrane, inducing characteristic subretinal neovascularization and fibrotic scar. Scale bars, 100 μm (top), 25 μm (bottom).
(B) Seven days post laser-injury, the subretinal scar labels for both αSMA and Col-IV. However, no tdTomato lineage marked Myh11-Lin(+) vSMCs-PCs are found within this neovascular membrane. Myh11-Lin(+) vSMCs-PCs do not exhibit a myofibroblast phenotype in laser-induced subretinal fibrosis. Scale bars, 100 μm (top), 25 μm (bottom).
(C) Twenty-one days post-laser injury, there are again no observed Myh11-Lin(+) vSMCs-PCs (tdTomato+) myofibroblasts (αSMA+/Col-IV+) in the subretinal scar.
Animals were tested 10-12 weeks of age and immunohistochemistry is representative of three animals per condition.

Chemical Burn Induces Myofibroblast Differentiation of Endogenous, Retinal Myh11+ vSMCs-PCs

We next sought to determine whether endogenous, retinal Myh11-Lin(+) vSMCs-PCs in adult murine eyes contribute to proliferative vitreoretinopathy (PVR), often seen with ocular trauma, retinal detachment, and diabetic retinopathy. We induced PVR using a chemical silver-nitrate burn to the sclera (Figure 3.5A), resulting in formation of substantial pre-retinal fibrosis in retinas harvested 1-month post-burn. We find in this model that Myh11-Lin(+) vSMCs-PCs dissociated from their underlying CD31+ retinal vasculature and exhibit a myofibroblast morphology. Dissociated Myh11-Lin(+) vSMCs-PCs are found amidst pre-retinal fibrotic scar tissue with upregulated expression of αSMA, Col-III, Col-IV, and F-actin (denoted by the staining of phalloidin) (Figures 3.5D-F). No such differentiation is seen in the uninjured eye (Figure 3.5B) or even in the injured eye at retinal locations far from the burn site (Figure S3.6). Myh11-Lin(+) vSMCs (Figure S3.6A) and PCs (Figure S3.6B) remain on CD31+/Col-IV+ retinal microvasculature with seemingly normal vSMC and PC morphology. In these quiescent retinal regions, Myh11-Lin(+) vSMCs-PCs show no significant change in αSMA expression (Figure S3.6A) as compared to the unburned eye. Quiescent vSMCs-PCs also express Myh11, F-actin,

and Col-III, with no indication of change in cellular morphology and no migration off the retinal vasculature (Figures S3.6C-D). These observations demonstrate a traumatic ocular injury such as a chemical burn is sufficient to induce endogenous Myh11-Lin(+) vSMCs-PCs local migration off retinal vessels, with differentiation into myofibroblasts and subsequent profuse production of Col-IV fibrotic pre-retinal scar tissue characteristic of PVR.

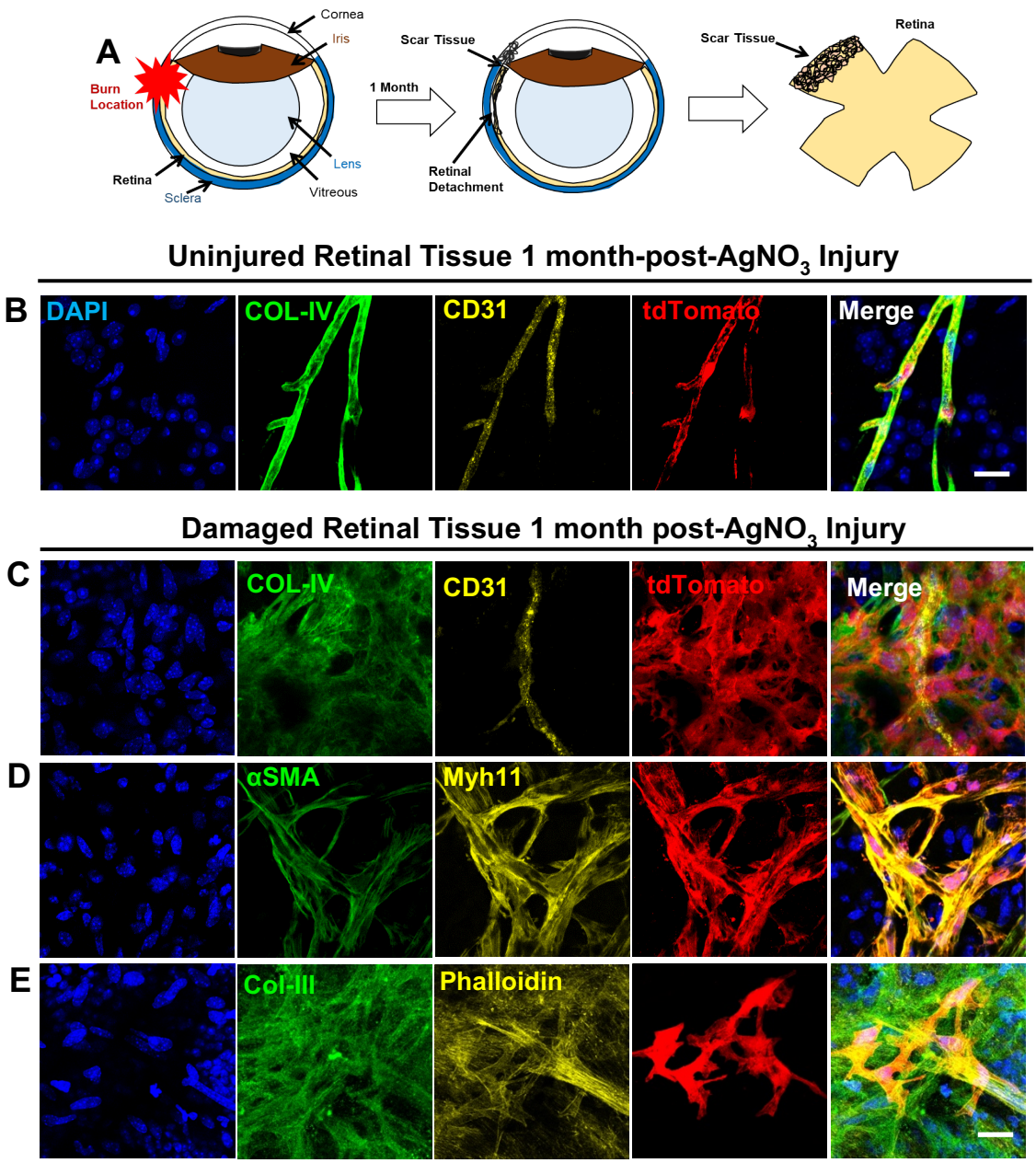

Figure 3.5. Endogenous Myh11-Lin(+) vSMCs-PCs on the retinal vasculature exhibit a myofibroblast phenotype after a chemical burn to the murine sclera.
(A) Model demonstrating that silver-nitrate-burn injury to the sclera induces retinal detachment and formation of retinal fibrotic scar tissue. **(B)** Myh11-Lin(+) vSMCs-PCs, labeled by tdTomato, are found only on the CD31+ retinal vasculature in a normal uninjured eye. Col-IV is expressed but only in the basement membrane of the vasculature. Scale bar, 15 µm. **(C-E)** (C) One-month post-burn injury, fibrotic scar tissue is clearly evident within superficial retina overlying the burn site. Within this induced fibrotic scar, multiple off-vessel Myh11-Lin(+) vSMCs-PCs (tdTomato+) are seen as indicated by lack of overlap with CD31. (D-E) These cells display a myofibroblast phenotype as indicated by αSMA stress fibers and positivity for Col-IV, Col-III, and F-actin as shown by fluorescently labeled phalloidin. Scale bar, 15 µm. Animals were tested 10-12 weeks of age. Immunohistochemistry images are representative of three uninjured and injured eyes.

Chemical Burn Upregulates TGFβ and CXCL10, and Downregulates Multiple Interleukins in Neural Retina

The sequence of molecular and cellular events that precipitate PVR remain very poorly understood and there are currently no approved molecular therapies for treating this condition [292] . Thus, we next sought to investigate the chemokines and cytokines that may initiate the molecular environment leading to Myh11-Lin(+) vSMCs-PCs migration off vessel and differentiation into myofibroblasts. Lysing the neural retina and using a Luminex Bead-based Multiplex Assay, we find that there is a significant upregulation of TGFβ1 and CXCL10, with a corresponding significant reduction in the interleukins IL-1a, IL-2, IL-4, and IL-17 (Figure 3.6A). TGFβ1 has a well described role in activating profibrotic responses and initiating the pathways to promote the increase of stress fibers and collagen secretion [289], however, its role in limiting Myh11-Lin(+) vSMCs-PCs myofibroblast differentiation has not been explored. To validate the potential contribution of TGFβ1 to our observed phenotype, we next inhibited the TGFβR pathway with the small molecule, SB431542, which specifically inhibits the activin type 1 receptors ALK4, ALK5, and ALK7 [293]. Following intravitreal delivery of 100 μM of SB431542 1-week and 3-weeks post-injury (Figure 6B), we find that there is a significant reduction (~20%) in the area of retinal scar when compared to burned eyes intravitreally injected with vehicle control (Figure 3.6C-D). Thus, TGFβ appears to play a direct role in formation of PVR by promoting off-vessel migration of Myh11+ vSMCs-PCs and their subsequent differentiation into matrix producing myofibroblasts.

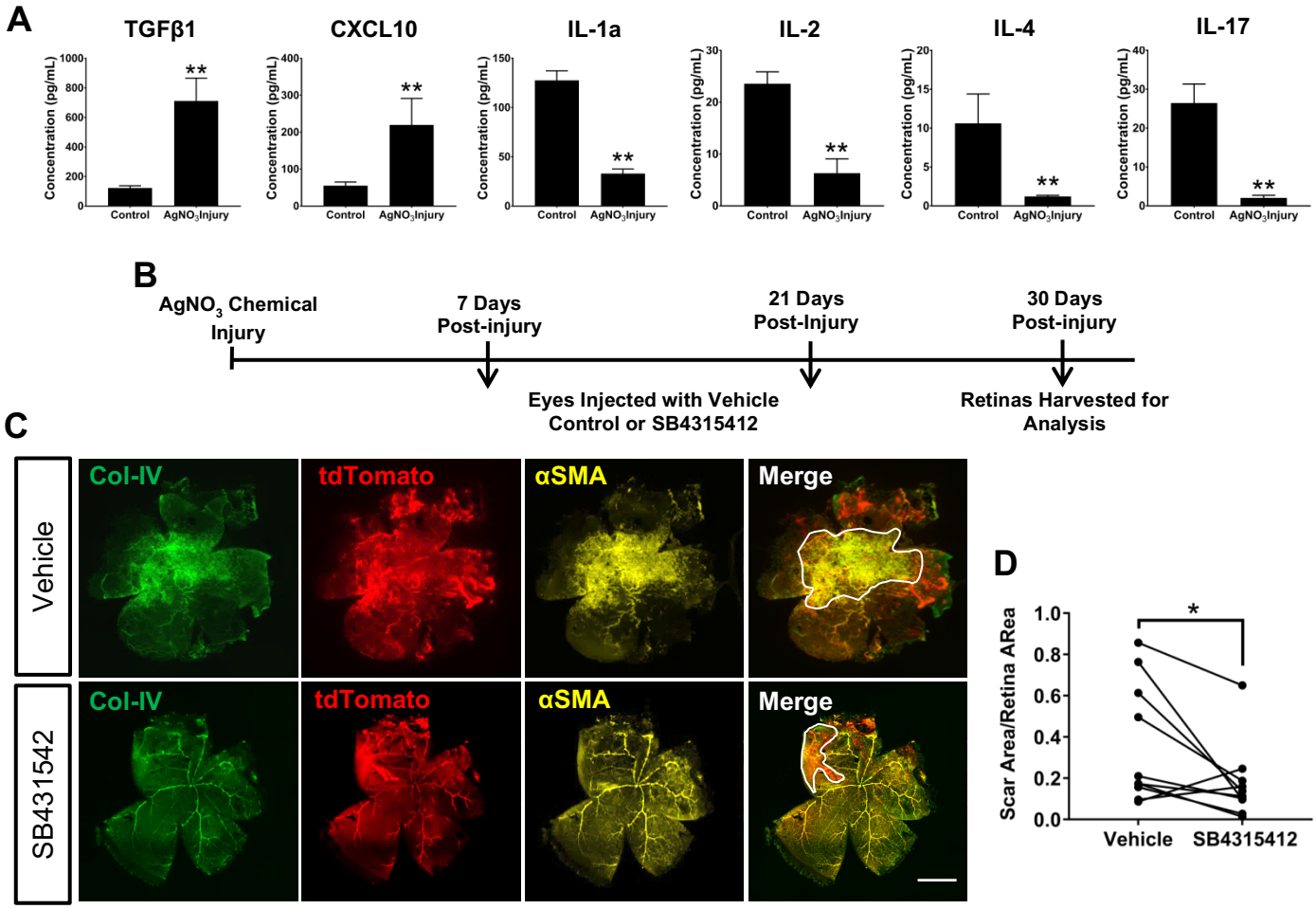

Figure 3.6. Intravitreal injection of the TGFβR inhibitor, SB4315412, reduces retinal scar formation in Myh11-tdTomato+/+ mice one-month post chemical burn injury.

(A) TGFβR and CXCL10 concentrations were significantly increased, while multiple interleukin concentrations were significantly decreased in the neural retina of one-month-post chemical burned eyes as compared to the contralateral uninjured eyes (n=4 paired eyes). Data are represented as mean ± standard error of mean (SEM).

(B) Experimental design for global inhibition of the TGFβ pathway in the eye after chemical-burn injury with burned eyes receiving intravitreal injection of either SB4315412 or carrier control at both 7 and 21 days post injury.

(C) Representative images of wholemount retinas harvested 30 days-post injury from eyes intravitreally injected with vehicle control or 100 μm SB4314212. Retinal scar formation as revealed by the extent and pattern of Col-IV and αSMA IHC is notably diminished in eyes in which TGFβR is inhibited. Scale bar, 1000 μm.

(D): Quantification of scar area (white outline in (C)) generated by the chemical burn shows SB4314212 significantly decreases retinal fibrosis as compared to contralateral vehicle control injected eyes (n=10 paired eyes). Animals were tested 10-12 weeks of age. *,$p<0.05$. Data were analyzed using a ratio paired t test (A), or Wilcoxon test (D).

Decreasing Smad4 in Myh11+ MSCs Does Not Decrease Col-IV Secretion After Injection Into OIR Pups

We next sought to determine if TGFβ signaling pathway may also regulate differentiation of intravitreally injected Myh11+ MSCs into myofibroblasts. Initially, we measured active TGFβ1 concentration in retina and vitreous samples of age-matched OIR pups and wildtype normoxia C57Bl/6J pups and surprisingly found no significant difference (Figure 3.7A). Despite equivalent levels of TGFβ1 in the retinal microenvironment, it is known the TGFβ pathway can also potentially be activated via mechanotransduction [294], as well as positive feedback loops from other pathways, including the WNT signaling pathway [295]. Thus, we attempted to directly block TGFβ signaling in Myh11-Lin(+) MSCs by cell specific knockdown of Smad4 using shRNA-expressing adenovirus vectors. Our hypothesis was that reduction of Smad4, would lead to a decrease in Col-IV+ matrix production in these cells once intravitreally injected into the OIR model. Two days pre-intravitreal injection, Myh11-Lin(+) MSCs (derived from *Myh11*-tdTomato+/+ mice) were infected at 3000 MOI of Smad4-shRNA or scramble-shRNA adenovirus vectors, with co-expression of GFP indicating successful infection (Figure S3.7A-B). Smad4 knockdown in Myh11-Lin(+) MSCs was confirmed through western blot before intravitreal injection (Figure 3.7B). After two days of culturing with adenovirus vectors, 10,000 Myh11-Lin(+) MSCs were injected in P12 OIR pups and retinas were harvested at P17 to investigate the Col-IV matrix production (Figure 3.7D). Surprisingly, Col-IV matrix expression level was unchanged by Smad4-knockdown as compared to the scramble control (Figure 3.7E). Col-IV matrix area was not found to be significantly affected, however, there was surprisingly a trending increase in the Col-IV matrix area in eyes injected with Smad4-knockdown Myh11-Lin(+) MSCs (Figure 3.7F). These results suggest that while TGFβ signaling appears to be significantly involved in myofibroblast

differentiation of endogenous, retinal Myh11+ vSMCs-PCs, non-TGFβ dependent pathways may be activated during myofibroblast differentiation of Myh11-Lin(+) MSCs following intravitreal injection.

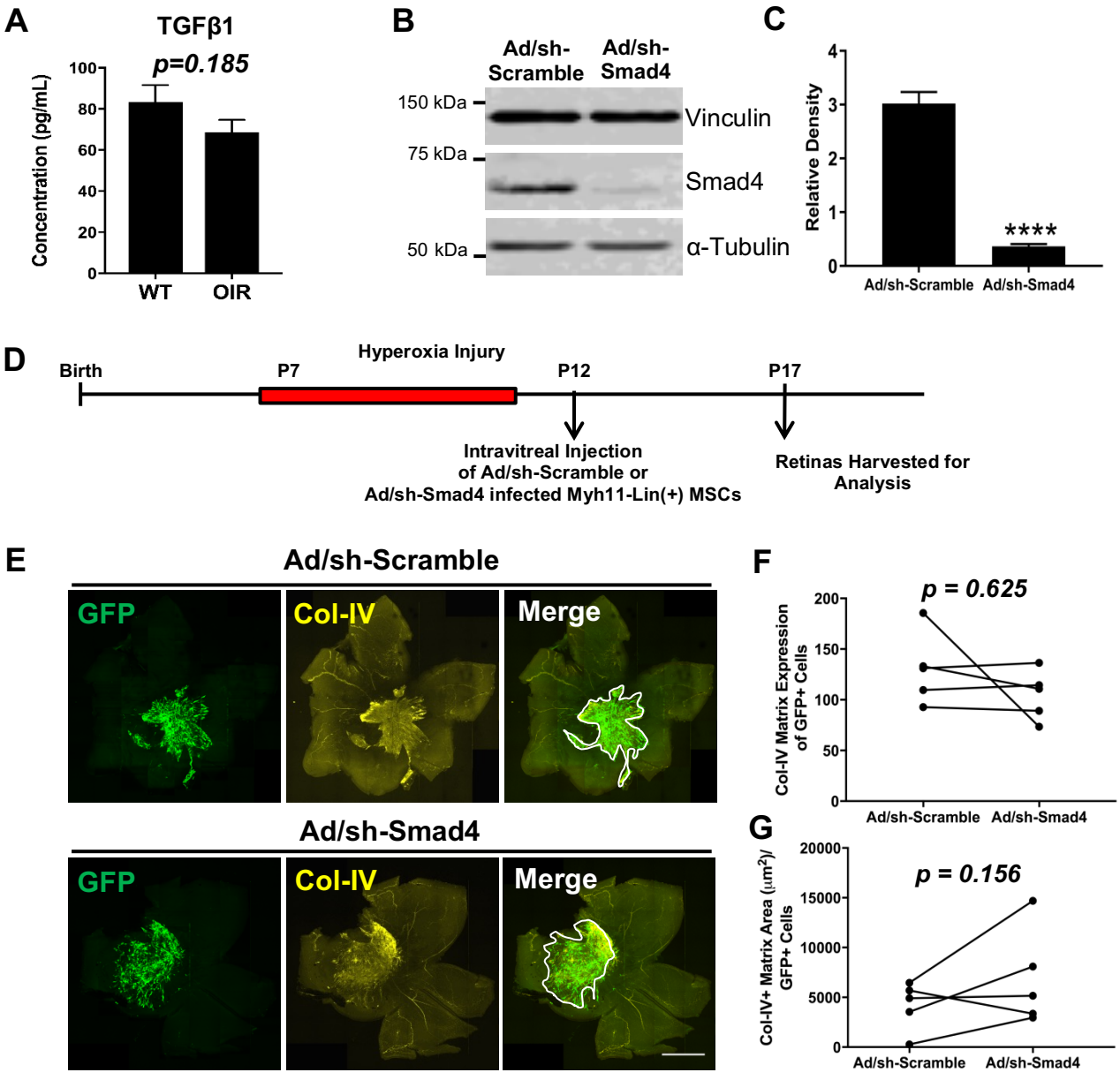

Figure 3.7. Smad4-knockdown within Myh11-Lin(+) MSCs does not abolish induction of proliferative vitreoretinopathy following intravitreal injection of these cells within the murine OIR model.
(A) In contrast to the scleral burn injury model, no significant difference was detected in TGFβ1 protein concentration in neural retina and vitreous of P14 wildtype (WT) pups and pups that underwent OIR (n=5 unpaired eyes).
(B-C) Western blot (B) and densitometry quantification (C) demonstrates significant knockdown of Smad4 in Myh11-Lin(+) MSCs through mSmad4-shRNA adenovirus vectors (n=6 biological replicates). Data are represented as mean ± standard error of mean (SEM).
(D) Experimental design illustrating the intravitreal injection of Smad4-shRNA infected Myh11-Lin(+) MSCs versus Scramble-shRNA infected Myh11-Lin(+) MSCs at P12 following OIR injury, with subsequent harvest of injected retinas at P17.
(E) Representative images of Col-IV pre-retinal matrix production (white outline in Merge panels) in eyes of P17 OIR pups intravitreally injected at P12 with Myh11-Lin(+) MSCs infected with either Ad-GFP-U6-mSmad4-shRNA or with Ad-GFP-U6-scramble. Fibrotic scar is evident in both eyes regardless of Smad4 knockdown. Scale bar, 1000 μm.
(F) No significant difference is found in fibrotic scar Col-IV matrix expression of the eyes intravitreally injected with Myh11-Lin(+) MSCs infected with Ad-GFP-U6-scramble adenovirus vectors (GFP+) as compared to Myh11-Lin(+) MSCs infected with Ad-GFP-U6-mSmad4-shRNA adenovirus vectors (GFP+) (n=6 paired eyes).
(G) Similarly, no significant difference is found in fibrotic scar Col-IV matrix area normalized by the number of GFP+ cells found within this fibrotic scar. However, less GFP+ cells incorporate within the fibrotic scar following Smad4 knockdown, resulting in a paradoxical trend towards increased Col-IV expression per GFP+ cell despite Smad4 knockdown. ***,$p<0.001$. Data were analyzed using unpaired t test (A, C), or Wilcoxon test (F, G).

Discussion

The source cell or cells that comprise mesenchymal stem cells (MSCs) within the adipose stromal vascular fraction (SVF) remains controversial[296]. FAC-sorting based on *in vivo* surface antigen profiles has identified multiple sub-populations of perivascular cells as putative MSCs. The markers used thus far, including NG2, PDGFRβ, αSMA, and CD146 are indiscriminate for pericytes, activated fibroblasts, glial cells, endothelial cells, nerve cells, and other adventitial cells[273,280,297–300]. Unfortunately, sorting on surface marker expression does not eliminate the possibility of a contaminating cell in the cultured SVF that may otherwise confound results when

analyzing MSC behavior. Cell identity also cannot be definitively followed over serial passage in culture given the apparent fluidity of cell surface markers we have shown in the present study.

Using lineage-tracing technology, we have for the first time isolated Myh11-Lin(+) vascular smooth muscle cells and pericytes (vSMCs-PCs) from the adipose microcirculation, and demonstrated that this perivascular cell population meet all specified ISCT criteria required for classification as a mesenchymal stem cell (MSC). Specifically, Myh11-Lin(+) vSMCs-PCs adhere to plastic, upregulate the expression of classically-defined MSC surface markers, and possess the ability to tri-differentiate *in vitro*. We show in adipose tissue that Myh11 expression is found only on vSMCs and PCs, eliminating confounding cell types. We further show cultured Myh11-Lin(+) vSMCs-PCs maintain expression of Myh11 and αSMA, and are capable of being followed thru multiple passages with continued expression of eYFP or tdTomato. Surprisingly, freshly isolated Myh11-Lin(+) vSMCs-PCs have very low expression of the requisite ISCT MSC surface markers. This suggests that culturing itself may cause transformation to an MSC phenotype, or perhaps the ISCT surface markers are only coincidentally induced *in vitro* as a result of the particular culture conditions.

Our results show that the Lin(-) population of cells in adipose tissues also meet the ISCT criteria for classification as an MSC, with demonstrated adherence to plastic, expression of requisite MSC surface antigen markers, and ability to tri-differentiate. These findings would suggest that Myh11+ perivascular cells do not comprise a sole source of MSCs within adipose tissue. We cannot rule out the possibility that all mural cells are perhaps MSCs, as undoubtedly there are other mural cells that are Myh11-. Other cells types could similarly comprise MSCs, given the Lin(-) population also includes tissue-resident fibroblasts, endothelial progenitors, and/or adventitial cells in the adipose tissue [301]. Surprisingly, the Lin(-) population is largely CD146- *in*

vivo, revealing that these cells also do not express this perivascular and putative MSC surface marker *in vivo.* Collectively, our findings indicate that the removal of Lin(-) cells and Myh11-Lin(+) vSMCs-PCs from their natural *in vivo* environment into an artificial culture largely drives cells into an "MSC state". Our results would suggest that the ability to acquire this "MSC state" in culture may be an inherent characteristic of diverse range of cells within adipose SVF, rather than a property limited to a select sub-population of cells.

While differentiation of adipose-derived MSCs to alternate cells types is well established *in vitro*, there has been recent controversy about whether and to what extent this behavior occurs *in vivo*; n multiple injury and aging models, there were no observed transformed or even off vessel lineage-marked Tbx18+ cells [273]. Yet, prior studies demonstrated Myh11+ vSMCs-PCs possess the ability to differentiate *in vivo* into beige adipocytes under cold exposure [270], and into macrophage-like proinflammatory foam cells in atherosclerosis [282,283]. It has been suggested, but not yet demonstrated, that this discrepancy is perhaps the consequence of the chosen lineage marker or injury model used in these studies [302].

Our present results lend direct support to the contention that generation of off-vessel transdifferentiated cells is dependent on the injury model chosen, even within the same end-organ and for the same lineage-marked population. In particular, we show a laser burn consistently produces sub-retinal fibrosis that surprisingly has no contribution from endogenous Myh11-Lin(+) perivascular cells. In fact, Myh11-Lin(+) vSMCs-PCs are directly adjacent to this induced fibrosis surprisingly remain on vessel and with apparently normal cell morphology. In direct contrast, a chemical silver nitrate scleral burn results in substantial transition of Myh11-Lin(+) cells off vessel and differentiation into copious collagen-secreting myofibroblasts synonymous with proliferative vitreoretinopathy (PVR)[303]. Despite this transition, Myh11-Lin(+) cells distant from the injury site

again appear to remain with normal cell morphology attached to their underlying vessel. The fundamental cause for these observed differences remains unclear. One reasonable interpretation is that the injury must be severe enough or the local molecular milieu must have a specific composition to disrupt vSMC-PC connection with their underlying vascular basement membrane and endothelial cells. This may perhaps serve as a protective brake to the end-organ to avoid excessive fibrosis which might otherwise compromise function. We would suggest that presence of a severe stressor is both key and rare *in vivo* for inducing MSC behavior of vSMCs-PCs. While not specifically excluding the contribution to PVR from alternate cell types, these results argue that off-vessel transformation of vSMCs-PCs is perhaps a key and underappreciated step in this process.

We unfortunately demonstrate that a large majority of intravitreally injected adipose-derived MSCs transform to myofibroblasts, with abundant production of Col-IV+ pre-retinal scar tissue. This seems to occur despite their lacking of significant Col-IV expression *in vitro.* In view of the evident PVR in the multiple patients injected with adipose SVF, we suggest this transformation as a likely cause for their resulting blindness [210]. We cannot of course rule out additional contributing factors, including substantial induction of inflammation due to the injected cells, presence of fibroblasts and other inflammatory cell types within the SVF, or digestion of ocular structures from retained collagenase in the SVF. Nevertheless, it is clear that adipose SVF and cultured MSCs appear primed for generating retinal fibrosis and are probably sufficient in of themselves to account for the evident PVR in these patients.

We can only speculate as to the exact cause of this transformation in the eye, but prior studies suggest that a 3D fibril matrix environment is sufficient to initiate myofibroblast activation through mechanotransductive pathways, resulting in the increase of stress fibers and collagen

production[304,305]. Therefore, the 3D collagen matrix of the vitreous body[306], where most of the injected cells reside, is likely a contributing factor in generating the myofibroblast phenotype of the injected adipose-derived MSCs. Although sub-retinal injection of these stem cells is a viable alternate approach for delivery, there remains similar concerns regarding the risk of fibrosis or other adverse side effects[307].

We predict that this fibrotic transition is likely evident in other tissues injected with adipose-derived MSCs. While it may be tolerated, or perhaps even therapeutic in other tissues, it is particularly devastating to the eye. Adipose-derived MSCs are commonly injected into diseased cartilage and skin wounds to enhance repair, with improvements attributed primarily to their paracrine activity [263]. However, our results suggest alternatively that the delivered MSCs differentiate into myofibroblasts and remodel the surrounding connective tissue through the secretion of collagen. In this instance, such transformation in cartilage or within wounds, may in fact help further repair this tissue, rather than be deleterious to function. Our findings argue that future clinical use of adipose-derived MSCs must pay particular attention to the differentiated phenotype of injected adipose MSCs themselves, rather than principally focus on their secondary effects on surrounding tissues.

Despite the aforementioned complications, the opportunity to replace damaged or lost perivascular cells on the microvasculature, or perhaps even facilitate growth of new vessels, using adipose derived MSCs remains an intriguing possibility. For Myh11-Lin(+) cultured cells, we are essentially seeking a re-adoption of their prior *in vivo* function in the adipose tissue as vSMCs-PCs. Our group has previously established that MSCs, cultured from the heterogeneous population of adipose SVF, functionally reintegrate with the retinal vasculature and adopt standard mural cell markers [93,287]. We now demonstrate functional reintegration, morphology, and marker expression

using for the first time using definitive MSCs derived from adipose Myh11-Lin(+) vSMCs-PCs. Our prior work suggests adoption of a perivascular position is an inherent rather than random chance behavior of these injected cells [308]. The key issue remains that functional vascular integration occurs for only a small proportion of injected MSCs, and thus methods must be developed that enhance this phenotype, perhaps by molecularly enhancing their migration to the vasculature, while discouraging myofibroblast transformation of those MSCs remaining off-vessel.

TGFβR appears to be integral in initiating this transition off-vessel, as the small molecule inhibitor SB4315412, is seemingly sufficient to preserve the retinal vasculature and thus attenuate this response. However, once off vessel, myofibroblast differentiation of vSMCs-PCs appears to be their default phenotype. We are surprisingly not able to significantly attenuate myofibroblast differentiation of injected adipose MSCs despite SMAD inhibition and this differentiation notably occurs in an ocular injury environment having relative normal TGFβ levels. Interestingly, SMAD inhibition has produced similar failures in reducing systemic fibrosis, despite the presumed role of TGFβ in regulating this process [309,310]. One possible unifying explanation is that TGFβ may assume a larger role in initiating off vessel transition of vSMCs-PCs, while subsequent fibrotic transformation of vSMCs-PCs once off vessel may be initiated through any number of additional fibrotic regulatory pathways, including YAP/TAZ, BMP, MRTF, and WNT [311].

Although the therapeutic potential for MSCs has been well demonstrated, the present study should serve as a cautionary note on our limited understanding on MSC identity, and more importantly, their behavior once injected *in vivo*. We believe fully leveraging the safe and therapeutic potential of MSCs in regenerative medicine requires a more refined understanding of their response to both culture-related stimuli and injury-related environments. Our results

demonstrate a myofibroblast phenotype is perhaps a common cell fate for injected adipose-derived MSCs. Thus, future studies will require a more systematic approach to regulate the molecular milieu and multiple potential fibrotic signaling pathways of injected MSCs. We believe insights gained by such refined MSC studies can inform our understanding of systemic fibrosis found in any number of disease states, as our results indicate these processes are inextricably intertwined.

Supplemental Information

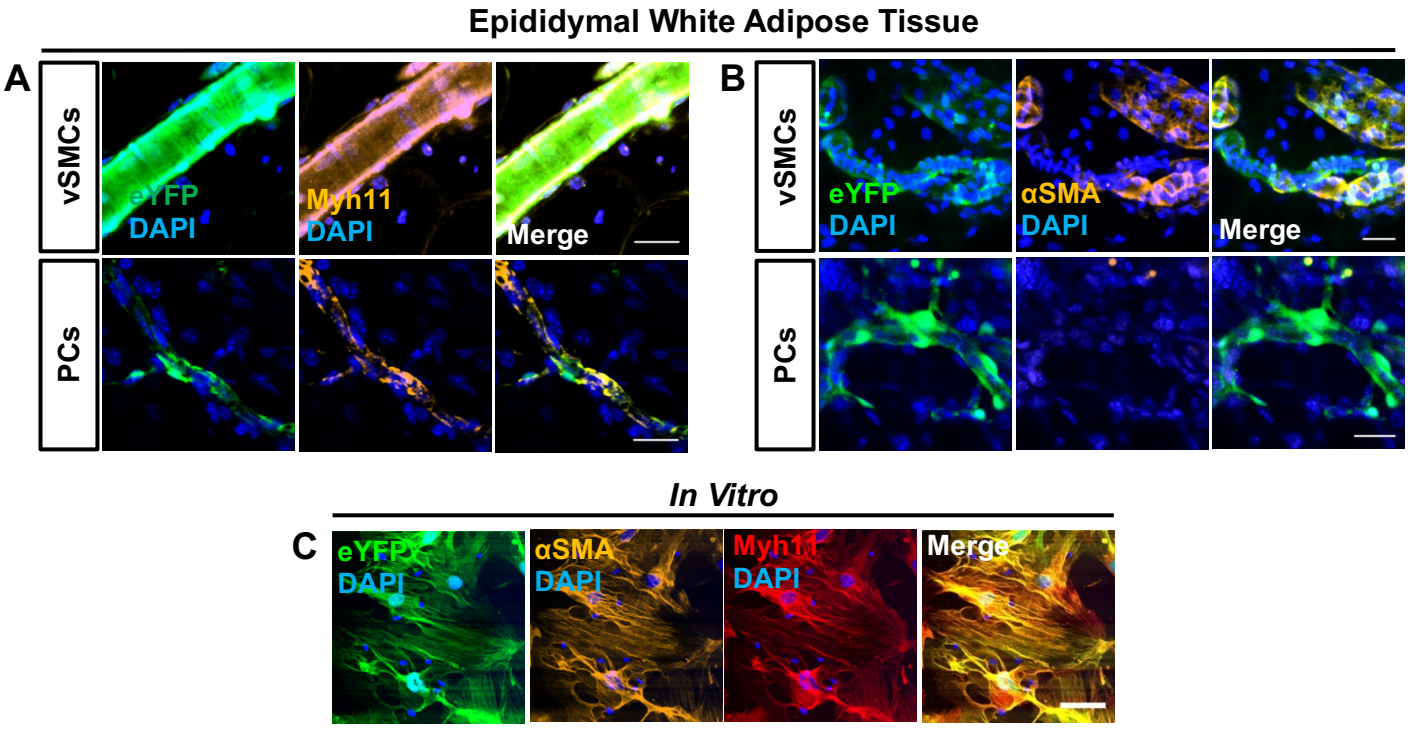

Figure S3.1. In vivo and in vitro expression of αSMA and Myh11 in Myh11-Lin(+) vascular smooth muscle cells and pericytes (vSMCs-PCs)

(A-B) (A) Representative images of epididymal, white adipose tissue from tamoxifen-induced *Myh11*-CreER^{T2}; ROSA26-STOP^{FLOX}eYFP+/+ (*Myh11*-eYFP+/+) mice immunostained for Myh11 and αSMA. Myh11 expression overlaps with but is not entirely coincident with eYFP expression in both vSMCs and PCs. Scale bars, 50 µm (top) and 25 µm (bottom). (B) In contrast, αSMA expression is higher in vSMCs on arterioles. Scale bars, 50 µm (top) and 25 µm (bottom). **(C)** FAC-sorted and cultured Myh11-Lin(+) vSMCs-PCs remain fluorescent for the eYFP lineage marker and express both αSMA and Myh11 *in vitro*. Before culture, Myh11-Lin(+) vSMCs-PCs were found to represent 3.28±0.32% (n=8 biological samples) of cells in the adipose stromal vascular fraction (SVF). Scale bars, 100 µm. Animals were tested 10-12 weeks of age, and immunohistochemistry images are representative of three animals.

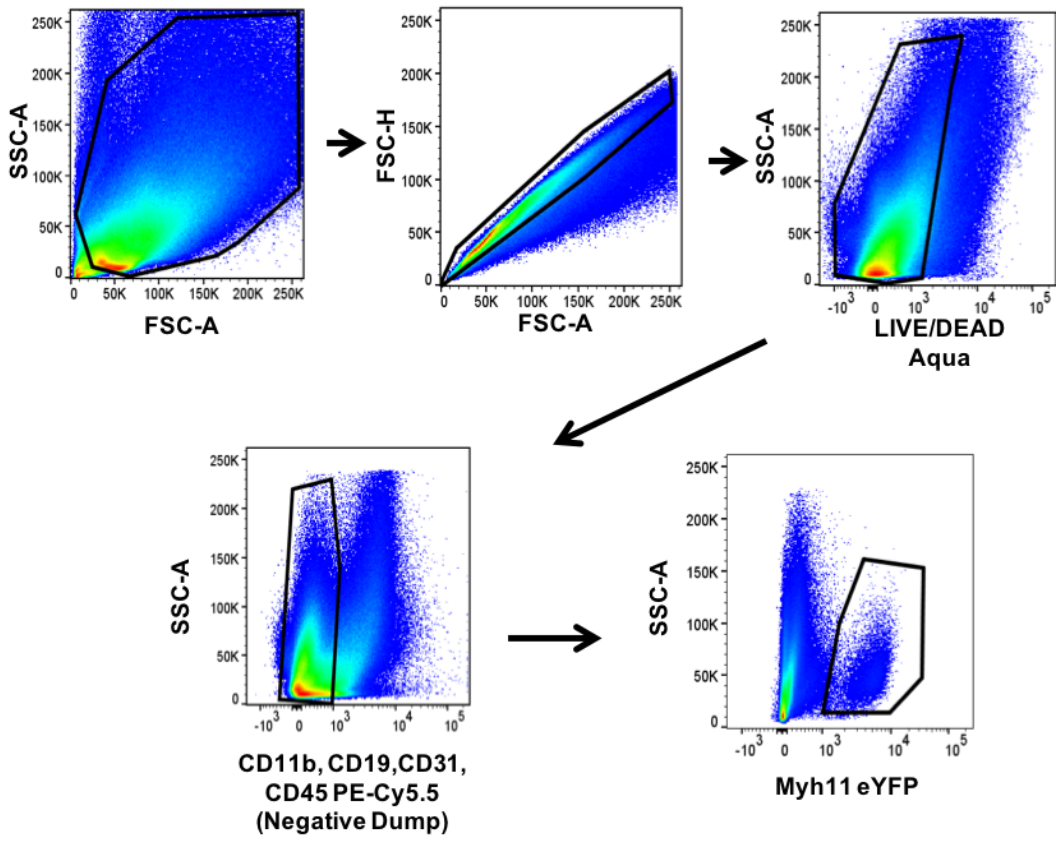

Figure S3.2. Gating for flow cytometry characterization for Myh11-Lin(+) vSMCs-PCs analysis and Lin(-) population.

The stromal vascular fraction (SVF) was enzymatically digested with liberase and elastase, and red blood cells were removed using red blood cell lysis buffer. The remaining cells were strained through 70 μm mesh filter and surface marker expression for this final cell population was analyzed via flow cytometry. Cells were gated on size (FSC-A vs SSC-A), followed by singlets (FSC vs Trigger Pulse Width), and viability (LIVE/DEAD Aqua vs SSC-A). Hematopoietic cells (CD11b, CD19, CD45) and endothelial cells (CD31+) were eliminated using a "negative dump" channel (PE-Cy5.5). The remaining population was used to gate on eYFP expression to separate eYFP+ Myh11-Lin(+) vSMCs-PCs from the eYFP- Lin(-) cell population.

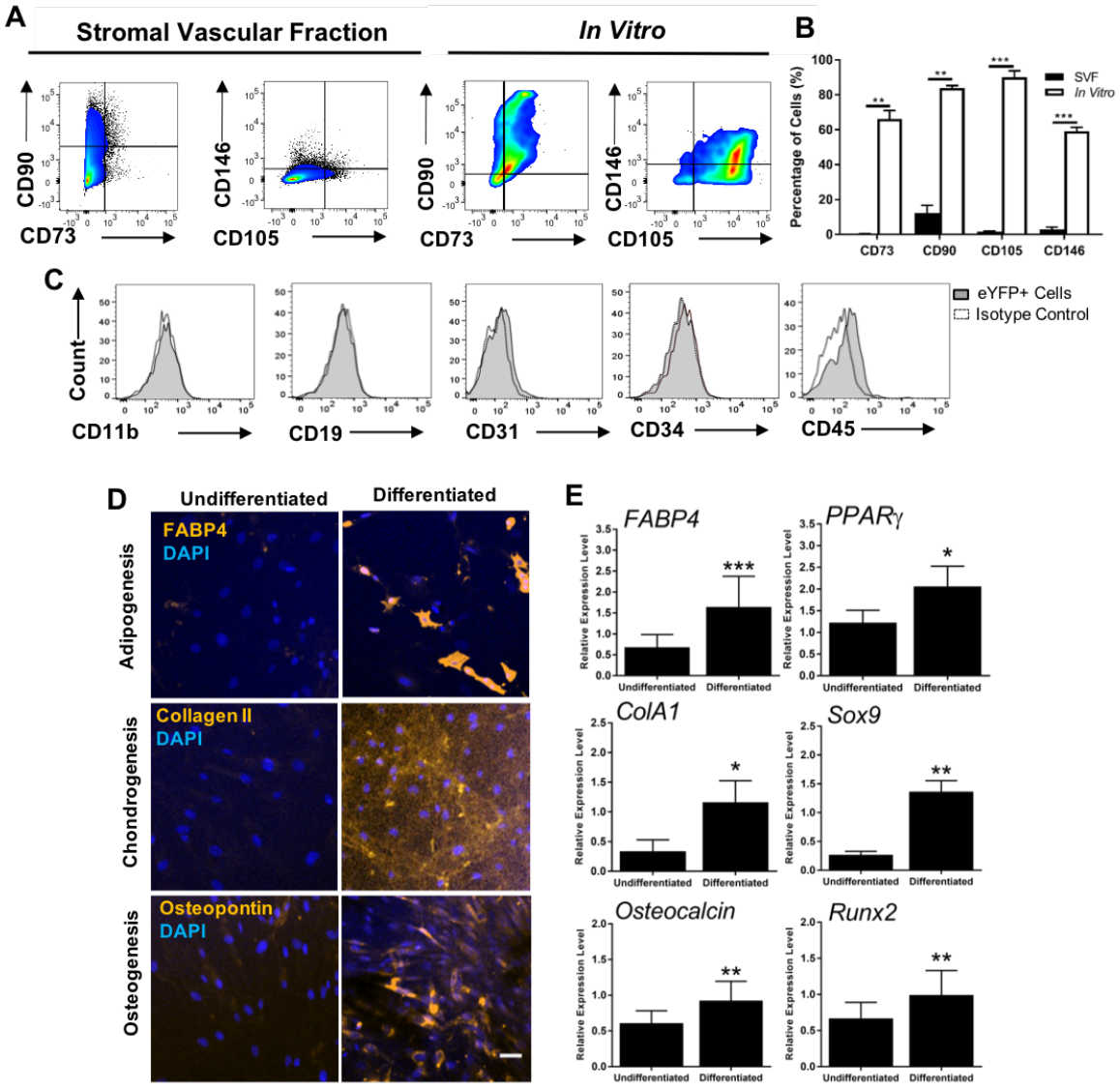

Figure S3. 3The Lin(-) population from the adipose stromal vascular fraction are also mesenchymal stem cells.

(A-C) Flow cytometry reveals freshly isolated Lin(-) population, or eYFP- cells, derived from white epididymal adipose tissue stromal vascular fraction lack expression of putative mesenchymal stem cell markers CD73, CD90, CD105, and CD146, however these surface antigens are markedly increased in this population once cultured *in vitro*. Cultured Lin(-) population also lacks expression of hematopoetic and endothelial cell markers CD11b , CD19, CD31, CD34, and CD45.

(D-E) Tridifferentiation analysis of Lin(-) population when introduced to adipogeneic, chondrogenic, and osteogenic media for 14 days. (D) Representative images show significant increases in FABP4, Collagen II, and Osteopontin expression in Lin(-) cells associated with adipogenic, chondrogenic, and osteogenic differentiation respectively. Scale bar, 50 µm. (E)

Genetic analysis shows significant increases in mRNA expression of protein markers and transcription factors involved in adipogenesis, chondrogenesis, and osteogenesis following differentiation of cultured Lin(-) cells. Experiments were completed in three biological replicates. Relative expression values were generated by normalizing GAPDH expression within the individual sample.*, ($p<0.05$), ** ,($p<0.01$). Results are represented as mean ± standard error of mean (SEM). Data were analyzed using a multiple unpaired t test followed by the Holm-Sidak post-hoc comparisons to correct for multiple comparisons (B), or a ratio paired t-test (H).

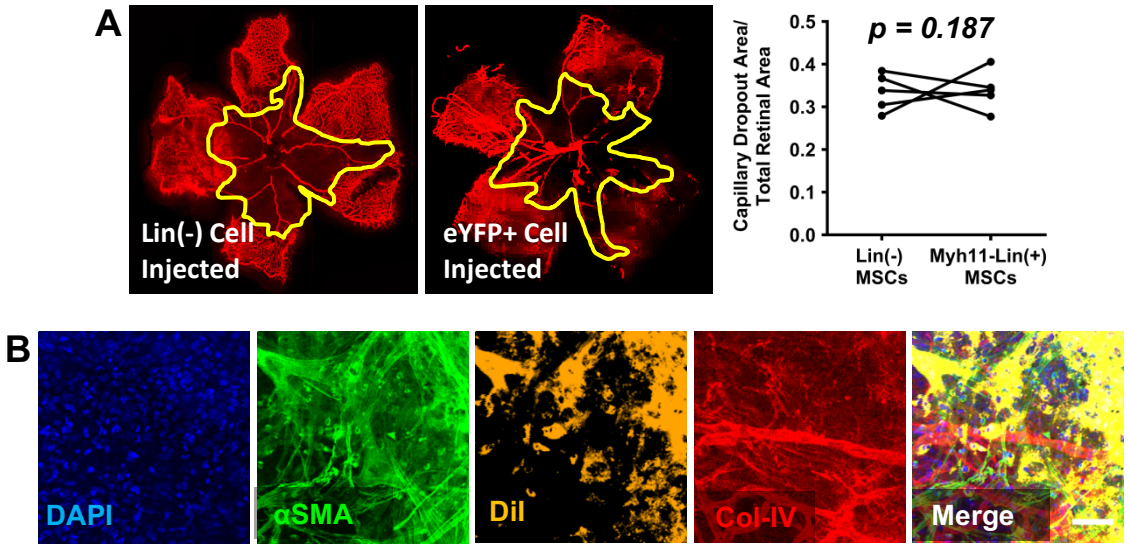

Figure S3.4. Effects of intravitreal injection of of Lin(-) mesenchymal stem cells (MSCs) in murine oxygen induced retinopathy (OIR) eyes are comparable with those following injection of Myh11-Lin(+) MSCs.

(A) At P12, following OIR injury, MSCs derived from the Lin(-) population are injected into one eye, with Myh11-Lin(+) vSMCs-PCs injected into the contralateral eye. At P14, retinal wholemounts show no difference in the area of capillary dropout is observed between paired eyes, suggesting both cell types induce similar acceleration of retinal vasculature recovery (n=5 paired eyes). Retinal vasculature (red) is immunostained by lectin. Yellow outlines area of capillary dropout.

(B) Intravitreal injection of DiI labeled Lin(-) MSC population in the OIR model induces pre-retinal fibrotic scar tissue, with injected cells demonstrating a typical myofibroblast phenotype, with substantial production of Col-IV and expression of αSMA stress fibers. Scale bar, 50 μm. Data are analyzed using a Wilcoxon test (A).

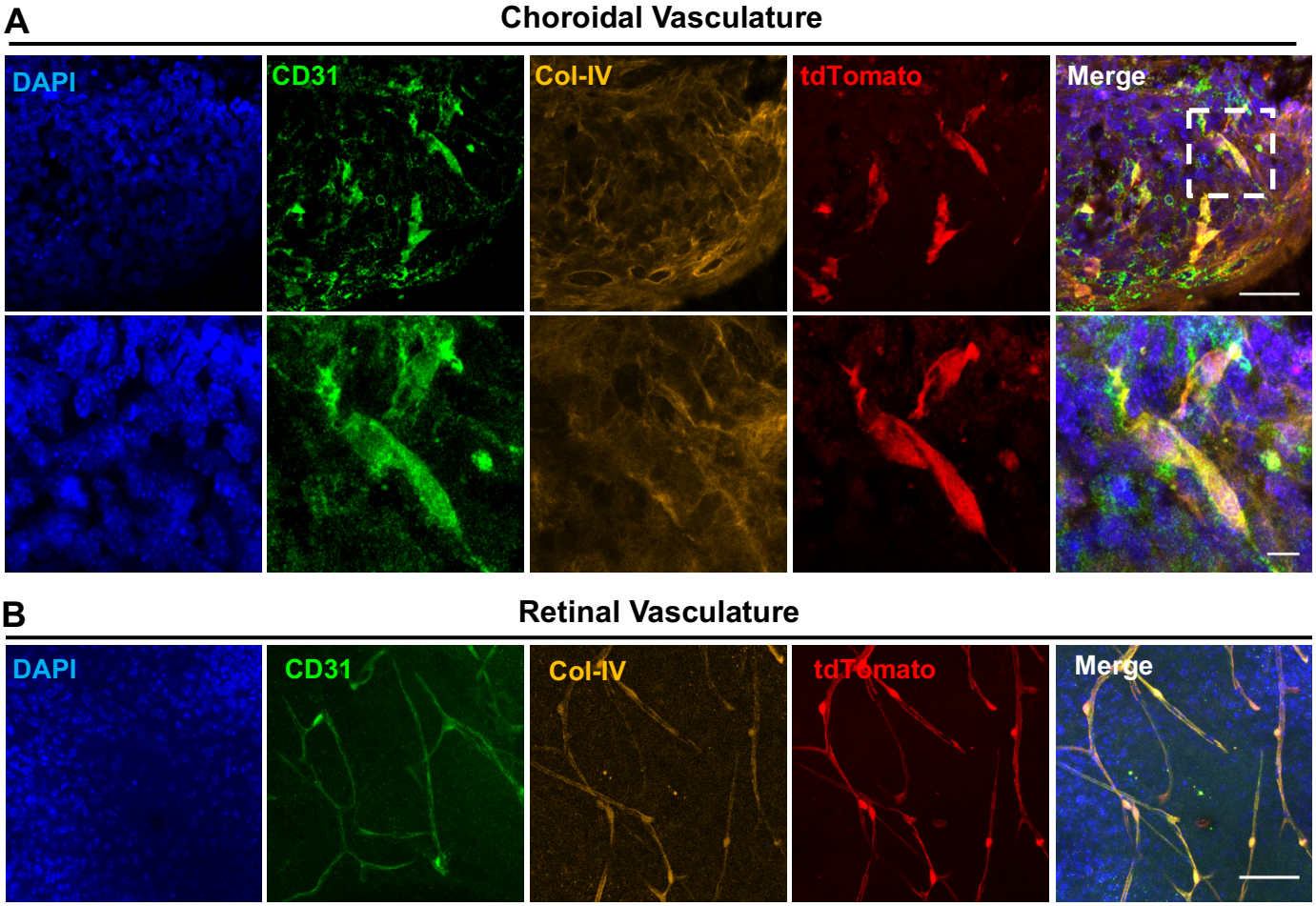

Figure S3.5. Myh11-Lin(+) vSMCs-PCs are fully associated with the vasculature in the area of laser-induced subretinal fibrosis model

(A) A laser burn choroidal neovascularization (CNV) model was used to induce subretinal fibrosis in tamoxifen-induced Myh11-CreER^{T2};ROSA26-STOP^{FLOX}tdTomato+/+ (*Myh11*-tdTomato+/+) adult mice. Myh11-Lin(+) vSMCs-PCs (tdTomato+) are found entirely on the CD31+ (green) choroidal neovasculature in the Col-IV+ (orange) scar region 21-days post laser burn. There are no tdTomato+ cells outside these vessels residing in the fibrotic scar. Inset (dashed lines) represents higher magnification of Myh11-Lin(+) vSMCs-PCs on choroidal neovasculature. Scale bars, 50 µm (top) and 10 µm (bottom).

(B) After laser-induced subretinal fibrosis, Myh11-Lin(+) vSMCs-PCs (tdTomato+) similarly continue to remain invested in the retinal microvasculature (CD31+/Col-IV+) that is directly adjacent to the subretinal scar, with no off-vessel cells observed. Scale bars, 100 µm.

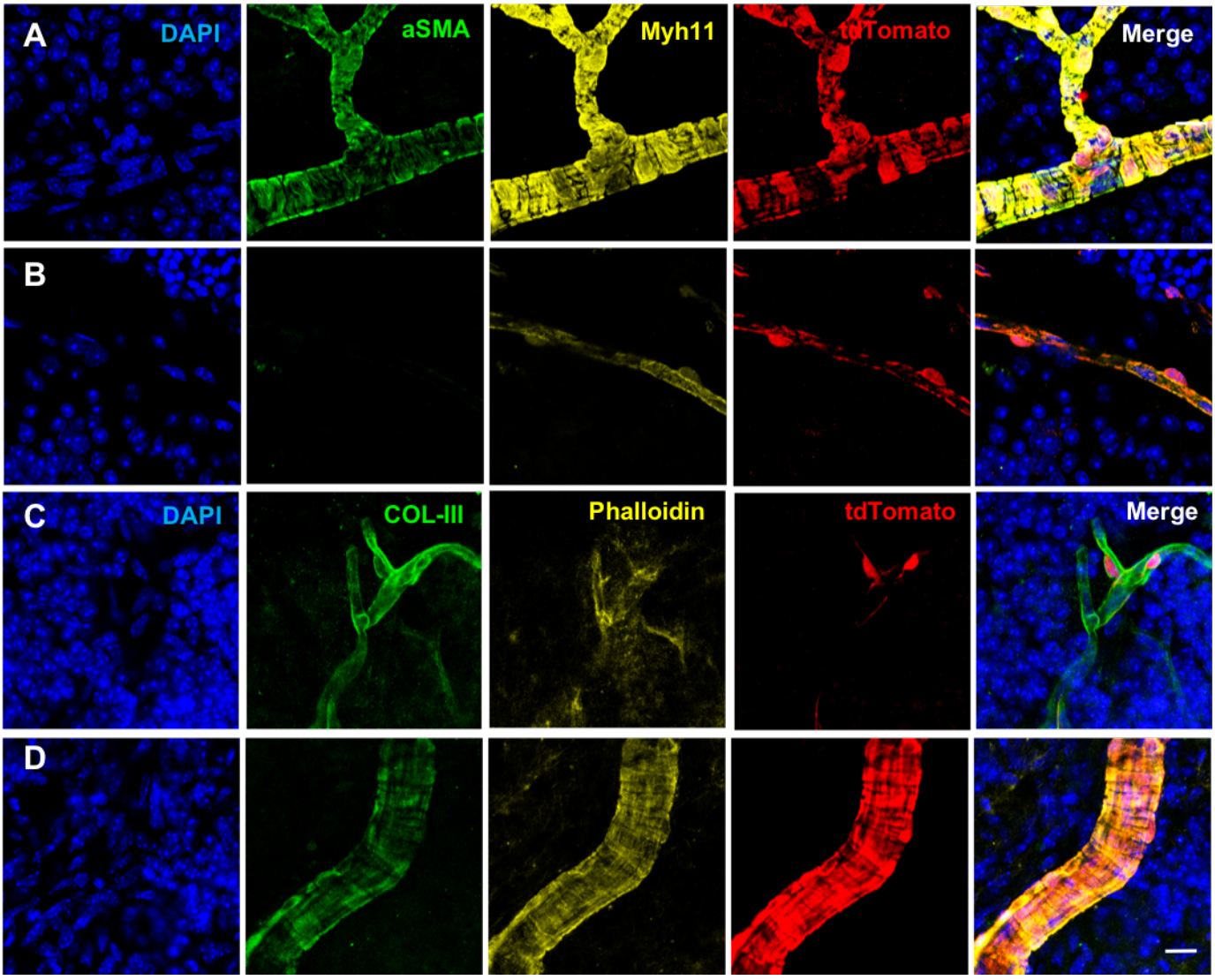

Figure S3.6. Myh11-Lin(+) vSMCs-PCs remain fully associated with retinal microvasculature at retinal locations distant from the scleral burn

(A-D) Myh11-Lin(+) vSMCs and PCs (tdTomato+) cells located in the hemi-retina opposite from the scleral burn site remain fully invested on large retinal arteriolar blood vessels (A) and capillaries (B) and are Myh11+. These quiescent lineage-traced vSMCs are Col-III, F-actin+ (Phalloidin+) and αSMA, while lineage-marked PCs do not express F-actin or αSMA (C-D). Scale bars, 15 μm. Animals were 10-12 weeks of age, and immunohistochemistry images are representative of three animals.

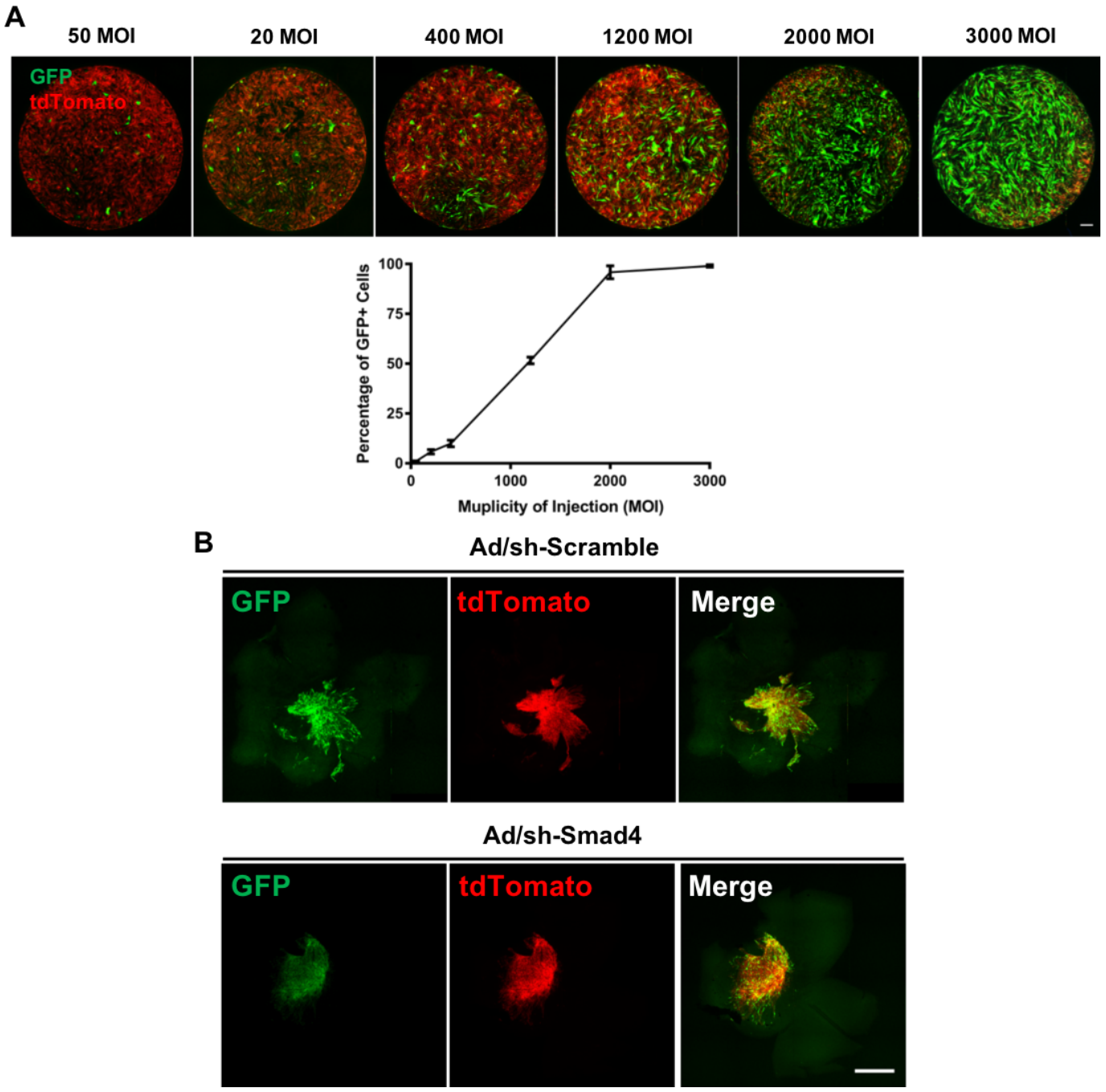

Figure S3.7. Myh11-Lin(+) MSCs are efficiently infected with shRNA adenovirus vectors, resulting in expression of GFP marker.

(A) GFP expression of Myh11-Lin(+) MSCs infected with 50-3000 MOI of Ad-GFP-U6-mSmad4-shRNA. Percentage of GFP+ cells increased with MOI. Data is representative of three independent biological replicates. Scale bar, 500 μm

(B) tdTomato and GFP expression are both maintained in intravitreally injected Myh11-Lin(+) (TdTomato+) MSCs that were prior to injection infected with either Ad-GFP-U6-scramble-shRNA or Ad-GFP-U6-mSmad4-shRNA. Scale bar, 1000 μm.

Table 3.1. List of primers used for qPCR

Gene	Sequence
FABP4	F: AGCTTGTCTCCAGTGAAAACTTCG R: CATTTACGCTGATGATCATGTTGG
PPARγ	F: GGATAAAGCATCAGCCTTCCACT R: TCCGGCAGTTAAGATCACACCTA
COLA1	F: AATGAAGAACTGGACTGTCCCAAC R: GGTCCCTCGACTCCTACATCTTCT
SOX9	F: AAGAAAGACCACCCCGATTACAA R: AGCGCCTTGAAGATAGCATTAGG
Osteocalcin	F: GACTCGGATGAATCTGACGAATCT R: GACCTCAGTCCATAAGCCAAGCTA
Runx2	F: GAACCAAGAAGGCACAGACAGAA R: AGGCGGGACACCTACTCTCATAC

CHAPTER 4

Shared Lineage between Corneal Endothelial Cells and Myh11+ MSCs Reveals Potential for Therapeutic Restoration of Endothelium

Acknowledgements: Bruce A. Corliss[1], Corbin Matthews[1], Kate Fitzgerald[1], Richard Doty[1], Chris M Smolko[1], Hamzah Shariff[1], Shayn M. Peirce[1], Paul Yates[1,2].

[1]Biomedical Engineering, University of Virginia,
[2]Department of Ophthalmology, University of Virginia

Abstract

Purpose: To establish Myh11 as a marker of a subset of corneal endothelial cells (CECs), and to demonstrate the feasibility of restoring the corneal endothelium with *Myh11*-lineage (*Myh11*-Lin(+)) adipose-derived mesenchymal stem cells (MSCs).

Methods: Intraperitoneal administration of tamoxifen and (Z)-4-Hydroxytamoxifen eyedrops were used to trace the lineage of Myh11 expressing cells with the *Myh11*-Cre-ER^{T2}-flox-tdTomato mouse model. Immunostaining and western blot characterized marker expression and spatial distribution of Myh11-Lin(+) cells in the cornea, and administration of 5-ethynyl-2′-deoxyuridine labeled proliferating cells. Adipose-derived MSCs were isolated from Myh11+ vSMCs-PCs and treated with cornea differentiation media to evaluate corneal endothelial differentiation potential. Myh11-Lin(+) MSCs were injected into the anterior chamber to test for incorporation into the cornea endothelium.

Results: A subset of CECs both express and are of Myh11-Lin(+), a marker previously used to trace pericyte, smooth muscle cells, and adipose-derived MSCs. Myh11-Lin(+) CECs marked a stable subpopulation of cells in the cornea endothelium. Myh11-Lin(+) MSCs are capable of some degree of CEC differentiation and incorporation into the cornea endothelium.

Conclusion: Dystrophy and dysfunction of the corneal endothelium accounts for almost half of all corneal transplants, the maintenance of the cornea endothelium is poorly understood, and there is a lack of mouse models to study specific CEC populations. We establish a mouse model that can trace the cell fate of a subpopulation of CECs based on Myh11 expression. A subset of adipose-derived MSCs that share this Myh11 lineage are capable of mimicking CEC phenotype and can incorporate into the corneal endothelium when injected, revealing a potential alternative therapy to corneal transplants.

Introduction

The cornea endothelial cell (CEC) layer is the innermost layer of the cornea comprised of a single layer of hexagonal cells connected by tight junctions[312]. CECs serve a critical role in maintaining hydration and exchanging nutrients between the anterior chamber to the outer layers of the cornea, including the outermost epithelium and intermediate layer of stromal cells[313]. Active transport of sodium and potassium ions across the corneal endothelium osmotically drain water from the stromal layer of the cornea to the aqueous humor while maintaining a semipermeable barrier that allows limited passive flow in the reverse direction[314]. This scheme, referred to as a "pump-leak" mechanism[313], leads to the constant cycling of fluid into the outer corneal cell layers that maintains optical transparency for the tissue[315], allowing light to pass through unimpeded to reach the retina, the tissue layer responsible for sight. With the absence of a blood vessel network in the cornea to provide metabolic support, as found in vascularized tissues, the constant fluid cycling directed by the cornea endothelium is responsible for delivering necessary nutrients to the outer tissue layers[313]. Additionally, CECs maintains the Descemet's membrane[312], a collagen rich basement membrane of the cornea implicated in supporting CEC phenotype and function through autocrine extracellular matrix deposition signaling[316].

Taken together, proper function of the corneal endothelium is critical for the homeostatic maintenance and function of the tissue, with too little fluid flux leading to insufficient tissue hydration and improper nutrient supply, while too high fluid flux leading to edema and a reduction in visual acuity[313]. To prevent pathological malfunction, CEC cell populations must remain at sufficient densities to maintain the basement membrane outer tissue layers. However, previous research suggests that the CEC layer cannot be regenerated or repopulated in adult tissue, and

CECs dropout with aging, injury, surgical trauma, and dysfunction[317]. If CEC density falls below a 500 cells/mm^2 the cornea becomes hazy and cornea transplant surgery is often required[318].

Disruption of this cell population can occur with various corneal diseases[319], hypoxia caused by long term wear of contacts[320], and cornea transplant surgery[321]. Paradoxically, corneal transplants are often the only therapeutic option for a depleted cornea endothelium, but the trauma from the surgical procedure can lead to further acute dropout of cornea endothelia cells[322]. Furthermore, over the long term, transplant patients exhibit a 4-fold dropout of the corneal endothelial cell layer compared to uninjured corneas[323]. Without an endogenous cell population to repopulate this tissue layer that is required for basic homeostatic maintenance of the cornea and critical for visual acuity, a clinically relevant exogenous cell population is needed to prevent attrition of this cell layer and preserve its function. Adipose-derived mesenchymal stem cells (MSCs) represent a cell population that can be efficiently harvested in the clinic from readily available adipose tissue, cultured, and reintroduced back into the patient as an autologous stem cell therapy that avoids immune responses associated with use of exogenous tissue sources[324].

We demonstrate that CECs share Myh11 lineage with a subpopulation of MSCs, a marker previously associated with vascular smooth muscle cells[325] and pericytes[275] (vSMCs-PCs), using a lineage tracing mouse model and confirmed with antibody immunofluorescence and western blot. Informed by their shared lineage, we demonstrate that cultured MSCs can differentiate into a phenotype associated with CECs and capable of adhering to the injured adult corneal endothelium when exogenously injected into the anterior chamber after a scratch injury. Whole tissue image analysis of corneas from Myh11 lineage tracing mice indicates that Myh11 exclusively marks a stable subpopulation of corneal endothelial cells and may serve some unknown function in maintenance of the endothelium. We provide the first lineage tracing mouse model for selectively

following a subset of endothelial cells in the cornea that can trace their cell fate in injury and disease, and demonstrate the potential to supplement the corneal endothelium with a clinically relevant and convenient cell source.

Methods

Animals

All experiments were approved by the University of Virginia Institutional Animal Care and Use Committee. We generated *Myh11*-CreER^{T2} mice were crossed with ROSA26-STOP^{FLOX}eYFP+/+ (The Jackson Laboratory, stock number 006148) and ROSA26-STOP^{FLOX}tdTomato+/+ (The Jackson Laboratory, stock number 007914) to generate *Myh11*-CreER^{T2}; ROSA26-STOP^{FLOX}eYFP+/+ (*Myh11*-eYFP) and *Myh11*-CreER^{T2}; ROSA26-STOP^{FLOX}tdTomato+/+ (*Myh11*-RFP) mice. Adult male *Myh11*-RFP mice at 6-8 weeks or 16-18 weeks of age were intraperitoneally injected with 0.1 mg tamoxifen (Sigma, T5648) diluted in 100 µL peanut oil. *Myh11*-eYFP mice between 6-8 weeks of age were intraperitoneally injected with 0.1 mg tamoxifen in 100 uL peanut oil. All *Myh11*-RFP and *Myh11*-eYFP male mice were delivered a total of 10 mg in the span of two weeks regardless of age. For the 24-hour chase eyedrop tamoxifen delivery experiment, *Myh11*-RFP mice were given a single eyedrop of 5 mg/ml (Z)-4-hydroxytamoxifen (Sigma, H7904) in peanut oil 3 times over a 12 hour period, and then imaged 24 hours later. For the day 2 and day 21 chase eyedrop tamoxifen delivery experiment, Myh11-RFP mice were given a single eyedrop of 5 mg/mL tamoxifen in peanut oil 3 times daily for 3 days, and then imaged 2 days and 21 days later. Adult C57Bl/6J (stock number 00664) were purchased from The Jackson Laboratories.

Immunohistochemistry and Immunocytochemistry

Eyes were enucleated and corneas were harvested from the eyes and fixed in 1% PFA for 40 minutes. Afterwards, corneas were washed with PBS, and permeabilized with 0.3% Triton X-100 for 1 hour at room temperature. Eyes prepped for cyrosectioning were submerged in 1% PFA for 24 hrs at 4°C, and then placed in 30% (w/v) sucrose in PBS overnight at 4°C. Afterwards, eyes were placed in OCT compound and cut in 8 μm cryosections. The cryosections were permeabilized with 0.3% Triton X-100 for 30 min at room temperature. After permeabilizaiton, all cornea tissue samples were blocked with serum, and stained with primary antibodies to CD31 (Biolegend, 102504, 1:300), CD34 (Biolegend, 119301, 1:200), ZO-1 (ThermoFisher, 61-7300, 1:100), Myh11 (Kamiya Biomedical Company, MC-352, 1:300 dilution), N-Cadherin (Abcam, ab18203, 1:100), αSMA (Invitrogen, 53-9760-82, 1:150), Anti-RFP (Abcam, ab62341, 1:200). Non-conjugated antibodies were labeled with donkey anti-rat Alexa Fluor 568 (ThermoFisher, A-11077, 1:650 dilution), donkey anti-rat Alexa Flour 488 (Invitrogen, A-21208, 1:600), donkey anti-rabbit Alexa Flour 546 (Invitrogen, A10040, 1:600), donkey anti-rabbit Alexa Flour 647 (ThermoFisher, A-31573, 1:600), donkey anti-rat Alexa flour 647 (Abcam, Ab150155, 1:600). Tissues were stained with DAPI (ThermoFisher, D1306, 1:1000) to label nuclei.

Primary cells were fixed with 1% PFA for 30 min at room temperature. Following fixation, cells were washed with PBS and permeabilized with 0.3% Triton X-100 for 5 min at room temperature. Cells were blocked with serum and stained with primary antibodies to N-cadherin (Abcam, ab18203, 1:200 dilution) and eYFP (Abcam, ab6673, 1:200 dilution). All fluorescent images were acquired via confocal microscopy using a Zeiss LSM 880.

5-ethynyl-2'-deoxyuridine (EdU) Assay

5-ethynyl-2'-deoxyuridine (EdU) (ThermoFisher, A10044) and Click-iT® EdU AlexaFluor® 647 Imaging Kit (ThermoFisher, C10340) was used to label proliferating cells in the cornea. Tamoxifen-induced *Myh11*-RFP+/+ adult male mice were intraperitoneally injected with 100 mg/kg of tamoxifen daily at 6-8 weeks of age. 30 days post injection, corneas were harvested and fixed in 3.7% PFA for 15 min at room temperature. Following fixation, corneas were washed with 3% BSA in PBS, and permeabilized with 0.5% Triton X-100 in PBS for 20 min at room temperature. The permeabilization buffer was removed and tissue was washed in 3% BSA in PBS. Next, corneas were incubated with Click-iT® reaction cocktail (containing reaction buffer, CuSO4, Alexa Fluor® 647 Azide, and reaction buffer additive) for 30 minutes in room temperature, protected from light. Lastly, tissues were washed with 3% BSA for 30 min twice, and afterwards, stained for DAPI and whole-mounted for fluorescent confocal imaging.

Primary Cell Culture

Myh11-Lin(+) vSMCs-PCs from the epididymal adipose tissue was harvested for collection and culturing by previous a previous protocol[277]. Briefly, the eipididymal adipose pads were harvested from tamoxifen-induced male *Myh11*-eYFP+/+ mice, and the adipose pads were enzymatically digested in 1 mg/mL collagenase type 1 (ThermoFisher, 17100017) for 1 hr at 37°C. Next, the digested fat pads were centrifuged at 400 g for 5 min and the pellet, or stromal vascular fraction (SVF), was collected. Red blood cells were removed from the SVF by adding red blood cell lysis buffer (ThermoFisher, 00-4333-57) for 5 min at room temperature. Next, cells were washed with DMEM media and centrifuged to collect the remaining SVF pellet. The remaining SVF was filtered through a 70-µm and 40-µm mesh, and later resuspended in FACS Buffer consisting of DMEM, 50% BSA, 5 mM EDTA, and DAPI (ThermoFisher, D1306, 1:1,000 dilution). Myh11-

Lin(+) vSMC-PCs were FAC-sorted using a BD Influx Cell Sorter, and immediately cultured into wells at an initial density of 1.5e4 cells/cm^2. Cells were cultured in DMEM supplemented with 10% FBS and 1% antibiotic-antimycotic. Once cells reached 70-80% confluency, cells were passaged with 0.05% Trypsin-EDTA. Cells were cultured in 37°C, 5% CO_2, and 95% humidity. All experiments consisted of cells between passages 6-8.

In Vitro Corneal Endothelial Cell Differentiation

Myh11-Lin(+) MSCs were uplifted and cultured on FNC Coating Mix (ThermoFisher, NC9971265). Once *Myh11*-Lin(+) MSCs reached greater than 90% confluency, the standard media was replaced by corneal endothelial differentiation media as previously described[326]. Briefly, *Myh11*-Lin(+) MSCs were exposed for 3 days to dual Smad induction media, which consisted of DMEM/F12 media supplemented with 20% KnockOut serum replacement (ThermoFisher, 10828028), 1% non-essential amino acids (ThermoFisher, 11140076), 500 ng/mL Noggin (Sigma, SRP3227) 10 μM SB431542 (Sigma, S4317), 1 mM L-glutamine (ThermoFisher, 25030081), 0.1 mM betamercaptoethanol (ThermoFisher, 21985023), and 8 ng/ml recombinant murine FGF-2 (Peprotech, 450-33). On day 3, the dual Smad induction media was replaced with dual Smad induction media now supplemented with 0.1X B27 supplement (ThermoFisher, 17504044), 10 ng/ml recombinant mouse Dkk-2 (R&D Systems, 2435-DKB/CF), and 10 ng/ml recombinant murine PDGF-BB (Peprotech, 315-18). This media solution was changed every 3 days over the course of 14 days. After the course of 14 days, cells were fixed and stained using methods described above.

CEC In Vivo Injury Model

We adopted a previous animal procedure to introduce injury to the CEC layer, followed by local delivery of Myh11-Lin(+) MSCs cultured in CEC differentiated media for 14 days[327]. Briefly, adult C57Bl/6J mice were placed under isoflurane anesthesia, and proparacaine hydrochloride ophthalmic solution was applied to the eyes as a topical anesthetic. Next, a small entry in the peripheral cornea was caused by a 33-gauge needle. To cause the injury and removal of CECs, a 36-gauge needle was used to scrape along the bottom most layer of the cornea, while taking great care to avoid the iris and lens. 5,000 *Myh11*-Lin(+) cells cultured in CEC differentiation media were delivered in 3 μL of DMEM media supplemented with 100 μM Rho Kinase (ROCK) inhibitor Y-27632 (Sigma, Y0503) and 100 μM TGFβR inhibitor SB4314542 (Sigma, S4317). After the local delivery of cells into the aqueous humor, the mice were immediately overturned on their backs to allow the injected cells to fall down toward the CEC layer and adhere. The mice were kept in isoflurane anesthesia for 3 h to allow for cells to potentially adhere to the CEC layer. Seven days post-delivery of *Myh11*-CEC differentiated cells, eyes were enucleated and stained for confocal microscopy as described above.

Immunoblotting

Quantitative fluorescent immunoblotting was performed as previously described[279]. Protein was collected from the cornea and sclera using RIPA lysis buffer (Sigma, R0278) supplemented with proteinase inhibitor (Sigma, 11836170001). Sample were kept on ice until ultrasonication. After ultrasonication, the samples were centrifuged at 18000g for 15 min at 4°C. Similarly, protein from cultured primary cells was collected using RIPA lysis buffer supplemented with proteinase inhibitor. Next, samples were centrifuged at 16,000 g for 15 min at 4°C. All sample protein

concentration was measured using a BCA assay for equal loading in gels. Protein was later prepared in 40 μL of dithiothreitol-containing Laemmli sample buffer. Samples were electrophoresed in 10% polyacrcylamide gels with tris-gylcine running buffer (25 mM tris base, 250 mM glycine, and 0.1% SDS) at 130V for 1 h. Proteins were transferred to a PVDF membrane (Millipore) in transfer buffer (25 mM tris, 192 mM glycine, 0.037% SDS, and 10-40% methanol) at 100 V for 1h on ice. PVDF membranes were blocked with 0.5X Odyssey® blocking buffer (LI-COR)+TBS+0.1% Tween-20. Primary antibodies were used to recognize the following proteins: Myh11 (Kamiya Biomedical, MC-352, 1:10,000 dilution), CD31 (Cell Signaling Technology, #77699, 1:10,000 dilution), Vinculin (Millipore, #05-386, 1:10,000 dilution), HSP90 (Santa Cruz, sc-7947, 1:10,000 dilution), and αSMA (Cell Signaling Technology, #19245, 1:10,000 dilution). After incubation in primary antibodies overnight at 4°C, membranes were washed and probed with secondary antibodies diluted with 0.5x Odyssey® blocking buffer. The following secondary antibodies were used to target the above primary antibodies: IRDye® 680LT goat anti-mouse (LI-COR #926-68020, 1:20,000 dilution), IRDye® 680LT goat anti-rat (LI-COR #926-68029, 1:20,000 dilution), and IRDye® 800CW goat anti-rabbit (LI-COR #926-32211, 1:20,000 dilution). Membranes were scanned on an Odyssey® infrared scanner (LI-COR) at 169-μm resolution and 0-mm focus offset. The ban intensities of the scanned 16-bit images were quantified by densitometry in ImageJ.

Whole Cornea Endothelium Image Processing

Confocal tiles of up to 1.5 GB in size were imported into MATLAB with two channels, one for DAPI and one for RFP. The goal for the analysis was to capture all of the DAPI cell nuclei from the cornea endothelial cell layer, and quantify the total RFP+ nuclei cell count and the fraction of

RFP+ nuclei as a function of binned radial distance from the edge of the cornea to the center. To accomplish this, a surface z projection was performed on the image, where a z-max projection was computed on the z-stack that only captures the bottommost layer of the cornea. The resulting 2D image was segmented for individual nuclei and each nuclei's RFP expression state determined in a binary fashion. The ROI of the corneal endothelial cell layer was manually defined, and thresholded Euclidean distance was used to separate the cornea radially into five bins. The fraction of RFP+ DAPI nuclei was calculated for each bin.

For the surface z-projection of the cornea, (Supplementary Figure 2A, B), the DAPI channel tile underwent a first pass local adaptive segmentation in 3D, where the images were blurred and processed with a min and max filter with the approximate dimension of a cell nuclei (xx μm, xx pix). Foreground was segmented based on where the max filtered image was at least 25 grey values above the background min filtered image. Each of the layers were segmented, and then the bottommost layer was found by finding the bottommost z-slice index of each positive thresholded pixel to create a 2D elevation image, where the pixel value denoted the bottommost z index for that pixel (Supplementary Figure 2C, D). After passing the elevation image through a max filter (xx μm, xx pix) to find the local surface height of the tissue, an *initial surface z projection* was performed that projected the maximum intensity pixel value (in this case from the binary 3D threshold of the tissue) in the z-direction that included the slices above the tissue all the way through the bottom of the tissue represent an *initial surface z-projection*. This yielded a reasonable accurate surface projection of the segmented cell nuclei in the lateral dimensions (x and y), but the highly sensitive threshold was not accurate in z: often the nuclei were segmented in the z-slices above where the nuclei were located in the z-stack. To find a more accurate z-index for the surface projection, the local z slice height from the 2D *initial surface z projection* image

was refined by finding the z-slice with the max local contrast between segmented nuclei and background existed, with the assumption that the z-slice with this max contrast was at the center of the nucleus in the z-dimension (Supplementary Figure 2D). These new z-coordinates were again used as a second 2D elevation image to calculate a *refined surface z-projection* (Supplementary Figure 2E, F). The nuclei were then thresholded and a watershed algorithm applied to split touching nuclei that were above minimum the area of (300 pixels, μm^2) · Some nuclei were split incorrectly into many small components, these were reunited base on the components being below 100 pixels in area (Supplementary Figure 2G-I). The red RFP channels were thresholded based on a global threshold (Supplementary Figure 2J) and the state of every DAPI nuclei was determined if it had at least 65% of its area segmented as positive for RFP (Supplementary Figure 2K). Comparing automated cell counts to manually results in a sample dataset of 12 images demonstrated high accuracy and agreement between the counting methods (Supplementary Figure 2L-O).

To examine the radial distribution of RFP labeled cell nuclei, ROIs were manually defined in a blinded fashion encompassing the lateral border of the CEC layer. Within the circular ROI the, radial distance was calculated with a Euclidean distance transform of the ROI and divided by the max distance so that radial distance was normalized from 0 to 1. Pixels were split into 5 bins based on radial distance. Cell nuclei were separated into each of the bins based on their center of mass, and the fraction of RFP+ cell nuclei in each bin was calculated.

Image Analysis and Statistical Analysis

All data was processed using MATLAB and ImageJ. Please see Supplementary Methods 2 for details. For plots, one star denotes $p<0.05$, two stars $p<0.01$, and three stars $p<0.001$. Source code and data available at: https://github.com/bacorliss/public_cornea_endothelial.git

Results

Myh11-Lin(+) Cells are Exclusively Detected in the Cornea Endothelial Cell Layer

In the male corneas of the *Myh11*-RFP lineage tracing mouse model, a subset of cells was RFP+ throughout the cornea endothelium after 2 weeks of intraperitoneal administration of tamoxifen and 4 weeks of chase (Figure 4.1A). Male mice administered with vehicle control did not have any RFP expressing cells in the cornea, demonstrating that the RFP expression was not due to leaky cre-recombinase with the mouse model, but from tamoxifen treatment (Figure S4.1A). The same RFP+ cells, albeit at a lower concentration, were observed in the cornea with 2 days of local of administration of eyedrops containing 4-hydroxytamoxifen with 21 days of chase, suggesting these RFP+ cells were labeled locally and did not originate from the circulatory system (Figure S4.1B, C).

Confocal imaging of the sagittal sectioned layers of the cornea revealed that RFP expressing cells localized with the bottommost cell layer of the cornea, the cornea endothelium (Figure 4.1B). A high-resolution confocal z-stack visualized with a lateral projection (Figure 4.1C), 3D segmentation (Fig. 4.1D-G), and tissue layer specific z-projections confirmed that RFP expression was exclusively found at the base of the cornea. The RFP expression was found within a homogeneously spaced and highly organized cobblestone arrangement of cell nuclei at the base of the tissue consistent with previous characterizations of the cornea endothelium.

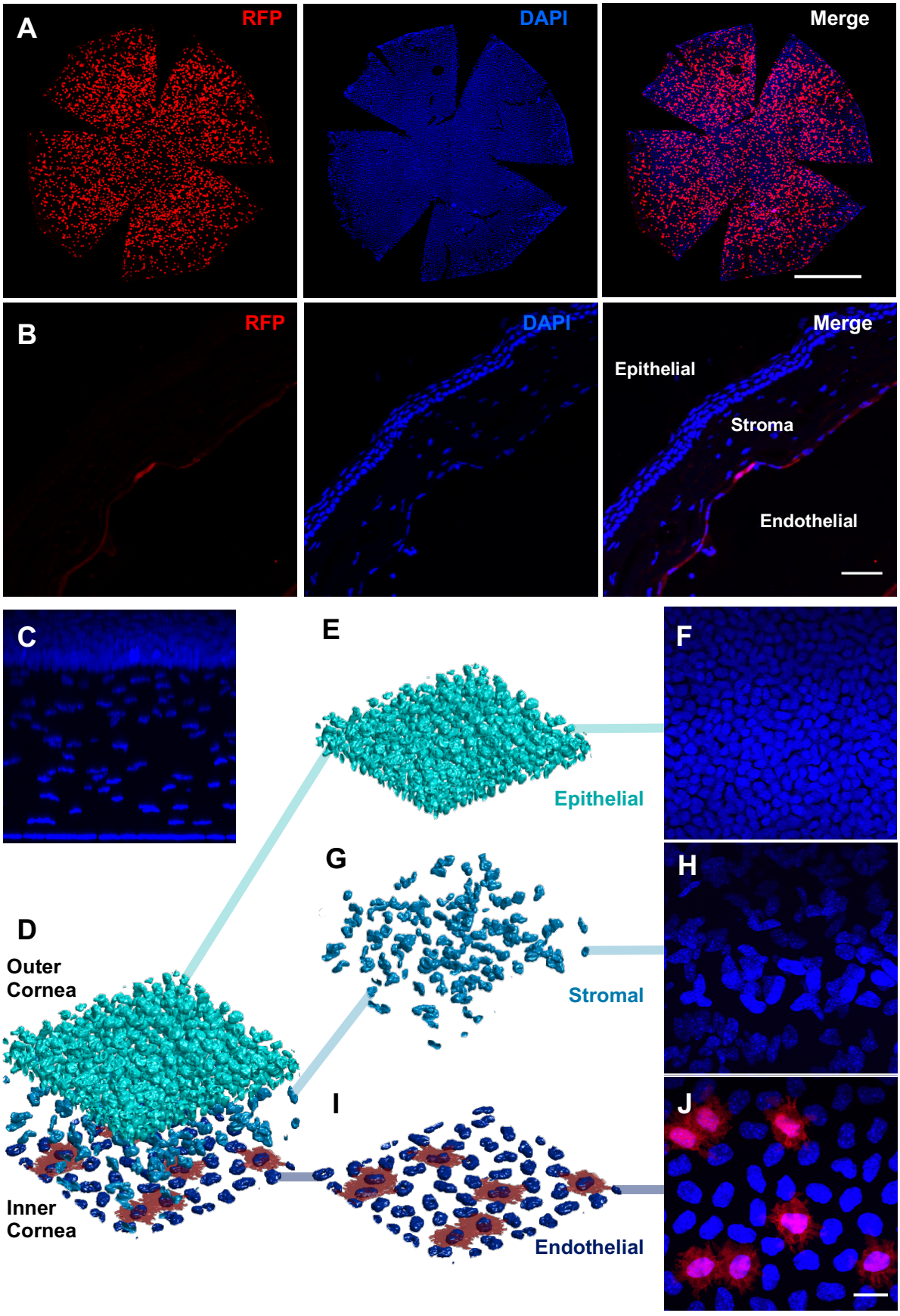
A
RFP
DAPI
Merge
B
RFP
DAPI
Merge
Epithelial
Stroma
Endothelial
C
D
Outer
Cornea
Inner
Cornea
E
Epithelial
F
G
Stromal
H
I
Endothelial
J

Figure 4.1. Myh11 lineage tracing marks a subpopulation of cells on the basal surface of the cornea.
(**A**) Confocal tile of the cornea of *Myh11*-RFP+ male mice treated with 2 weeks of tamoxifen intraperitoneal injections with a four-week chase, with RFP (red) and DAPI (blue) (scale bar 1 mm). (**B**) Cryo-sectioned fluorescent image with epithelial cell layer, stroma, and endothelial layer annotated from cell nuclei structure, with lineage cells restricted to base endothelial layer (scale bar 50 μm). (**C**) Lateral maximum intensity projection of high-resolution confocal z-stack through cornea (scale bar 25 μm). (**D**) 3D reconstruction of cell nuclei, with clear separation of (**E, F**) epithelial, (**G, H**) stromal, and (**I, J**) endothelial cell layers delineated by cell nuclei structure and morphology (scale bar 25 μm).

Myh11-Lin(+) Cells in the Cornea Express Myh11 and Known CEC Markers

After establishing the existence of Myh11-lineage cells (Myh11-Lin(+)) in the CEC layer of adult *Myh11*-RFP mice, immunofluorescence and immunoblotting was used to characterize the marker expression of Myh11-Lin(+) CECs and determine if the Myh11 protein was actively produced and not merely the *Myh11* transcript. Immunofluorescence revealed Myh11 staining not only marked the smooth muscle cells and pericytes in the corneal limbal vessels as expected, but also cells in the avascular CEC layer (Fig 4.2A, B). Expression of Myh11 protein in the cornea was confirmed with surgical isolation of avascular cornea from the vascularized limbal vessels and sclera through immunoblotting for Myh11 and CD31, an endothelial cell adhesion receptor marker. As expected from a vascularized tissue, the samples from the sclera had detectable levels of Myh11 and CD31 (Figure 4.2C). Isolated cornea samples lacked CD31 expression since, no blood vessels exist in the tissue (Figure 4.2D, t-test, $p = 0.0062$), but expressed Myh11 at comparable levels to the sclera when normalized to Viniculin expression (Figure 4.2E, t-test, $p= 0.357$). Corneal *Myh11*-Lin(+) cells, labeled with RFP, were confirmed to exhibit the same marker expression as corneal endothelial cells[328], being positively marked with the junctional proteins N-cadherin and ZO-1, while lacking expression in CD31, CD34, and αSMA (Figure 4.2F-H). The lack of vascular (CD31, CD34) and perivascular (αSMA) markers lend further evidence that these corneal Myh11-

Lin(+) cells are not associated with any vascular structures and represent a distinct cell type from pericytes and smooth muscle cells.

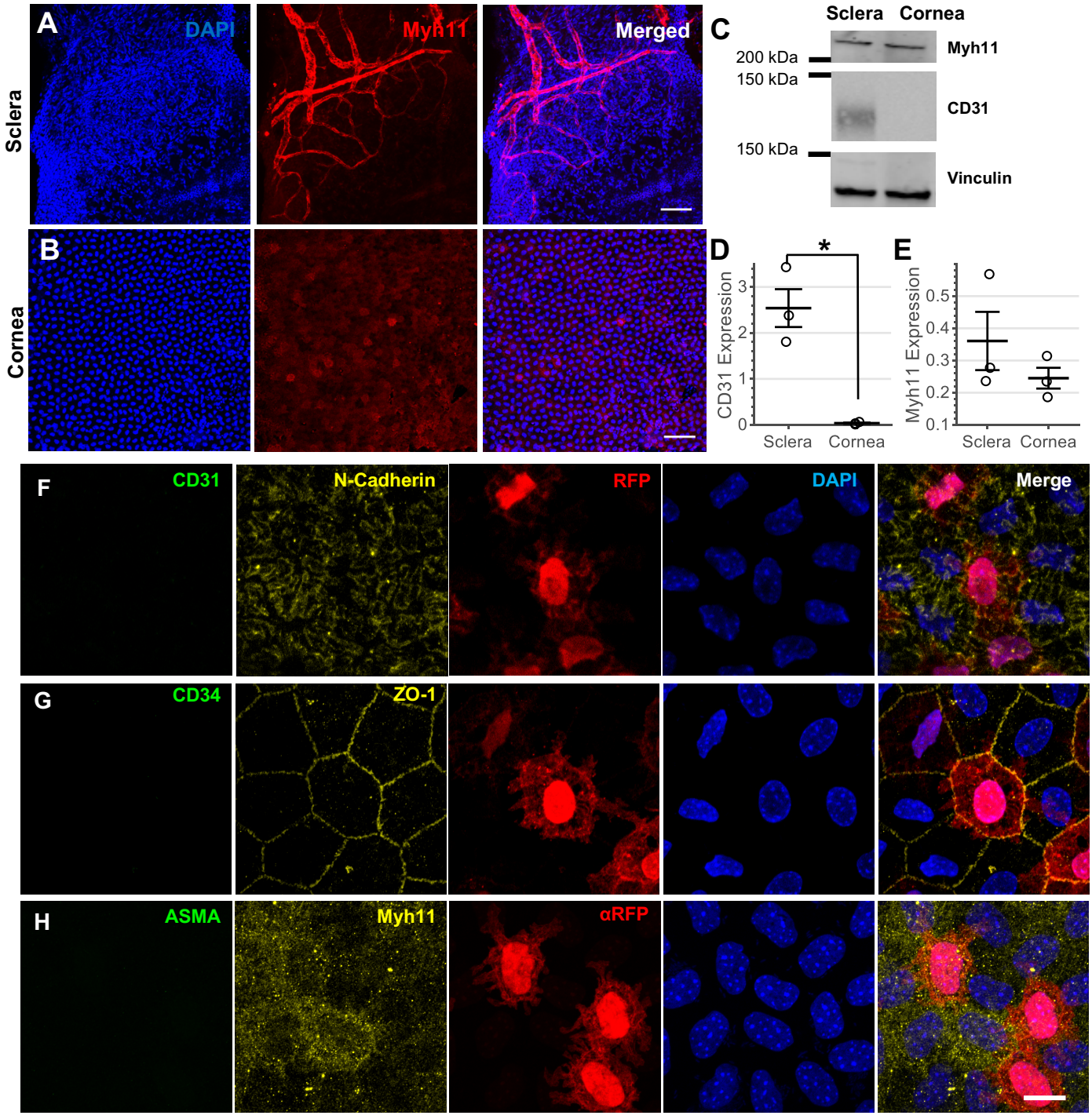

Figure 4.2. Myh11 protein is found in the avascular cornea, and Myh11 lineage cells of the cornea express markers for corneal endothelial cells
Immunostaining of anti-Myh11 antibody in the (**A**) sclera limbal vessels and (**B**) cornea endothelium (scale bar 100 μm). (**C, D**) Confirmation of Myh11 protein expression with western blot of surgically isolated sclera and avascular cornea. (**E**) Immunostained fluorescent images of *Myh1*1-Lin(+) cells in basal layer of cornea with anti-CD31 (green), anti-N-cadherin (yellow), anti-RFP (red), and DAPI (blue). (**F**) *Myh11-RFP* cells labeled with CD34 (green), Zo-1 (yellow). (**G**) *Myh11*-Lin(+) cells immunostained with anti-aSMA (green) and anti-Myh11 (yellow) (scale bar 15 μm).

There is no Evidence for Peripheral Migration of Myh11-Lin(+) CECs Into the Central CEC Layer

While these Myh11-Lin(+) cells in the corneal endothelial cell layer express the Myh11 transcript and protein, and exhibit a cornea endothelial cell phenotype, there remains the possibility that a portion of these cells are perivascular in origin and migrating from the peripheral vascular networks in the limbal vessels and the sclera. If the cells are indeed migrating from the peripheral cornea, then cell migration densities should be skewed with radial position relative to the center of the cornea, with outer portions of the cornea having higher Myh11-Lin(+) cell densities at earlier timepoints. We examine multiple timepoints with both acute tamoxifen treatment from eyedrops to more sustained induction with intraperitoneal injections. Entire corneas were imaged with high resolution tiles and the nuclei of the cornea endothelial cell layer were automatically detected along with their expression for RFP (Figure S4.2).

After a triple dose of tamoxifen eyedrops over a 12-hour period, followed by a short term 12-hour chase to represent an early timepoint, the fraction of RFP positive cells over the radial distance to the center of the cornea had did not have a negative slope, indicating that Myh11-Lin(+) cells were not migrating from the edge of the cornea (radial value of 0) to the center (radial, 1) (Figure S4.2A-C, 95% confidence interval of slope with best fit of linear model). Eye drop induction of three times a day for three days with a 2 day or 21 day chase revealed no difference in the total number of Myh1l-Lin(+) cells (Figure 4.3A, t-test, p=0.411), and both timepoints

showed a slightly positive relation between radial distance of fraction of cornea endothelial cells marked (Figure 4.3B, C) processed from whole cornea tiles (Figure 4.3D, E).

The same trends were seen with lineage tracing mice treated with 2 weeks of intraperitoneal injections of tamoxifen for 2 weeks at 6 weeks of age and 16 weeks of age, both with 4 weeks of chase time after induction. There was no change in total Myh11-Lin(+) cells, and both timepoints had a positive relation between fraction of marked cells and radial distance to center of the cornea (Figure 4.4A-F), suggesting the age of mouse for these two timepoints did not alter what subsets of CECs were marked for Myh11 lineage. There was roughly a 10-fold difference between RFP+ cell density between eyedrop of 4-hydroxytamoxifen and intraperitoneal injection of tamoxifen, which we attribute to differences of tamoxifen delivery to the cornea and duration of treatment.

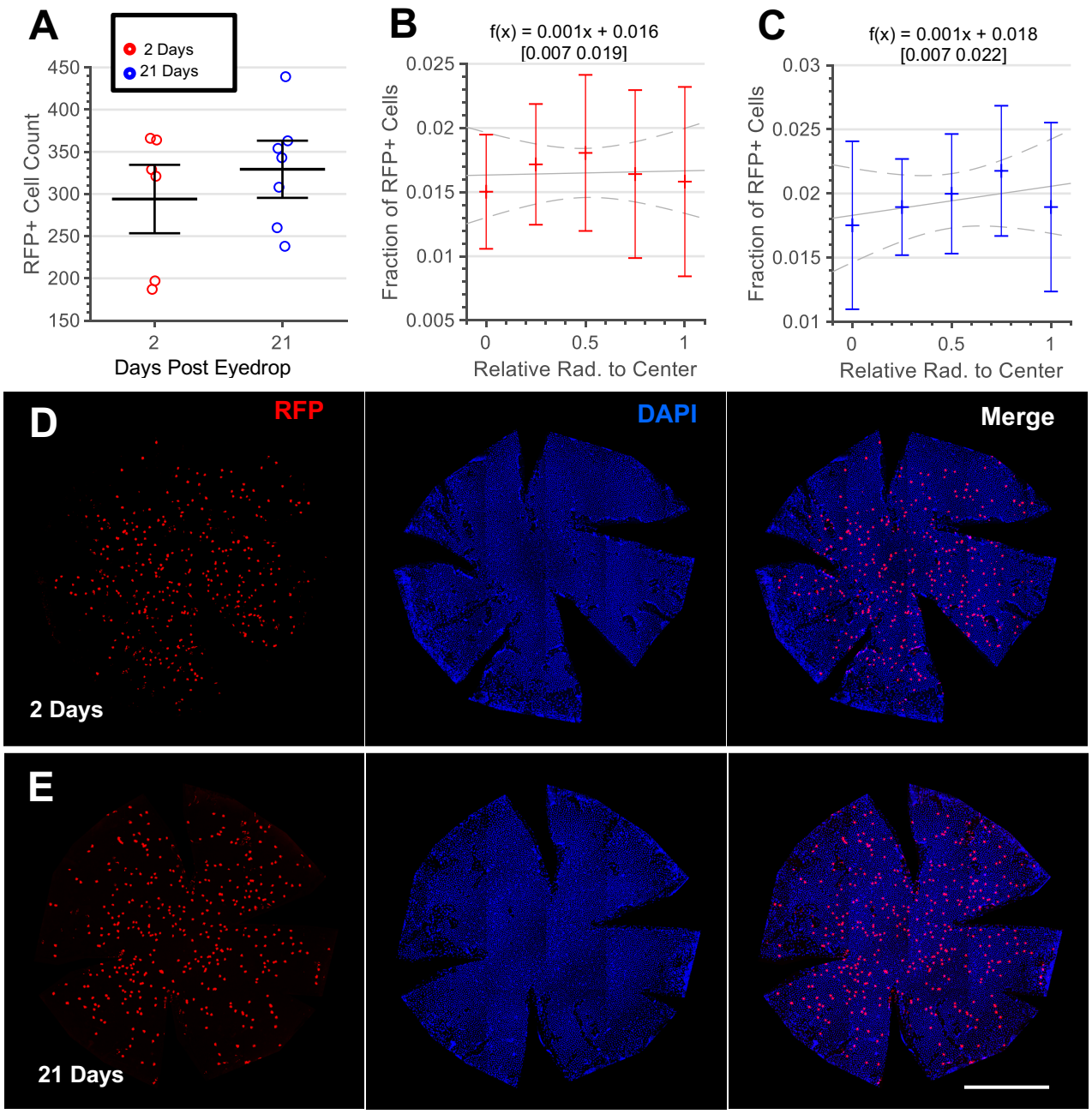

Figure 4.3. Myh11 lineage tracing through eyedrop delivery and differing chase times reveals no change in cell labeling and a positive relationship with radial distribution.
(**A**) Cell count of *Myl1*-Lin(+) RFP expressing cells in cornea with 2 and 21 days chase post-tamoxifen induction. (**B**) Radial distribution of density of *Myh11*-Lin(+) cells to center of cornea with 2 days of chase with fitted line (95% confidence interval of slope in brackets). (**C**) Radial distribution of density of *Myh11*-Lin(+) cells to center of cornea with fitted linear model with 95% confidence interval (solid and hyphened gray line, 95% confidence interval of slope in brackets) for (**B**) 2 days and (**C**) 21 days post-tamoxifen induction. Representative images from (**D**) 2 days

and (**E**) 21 days of chase post-tamoxifen induction with RFP (red) and DAPI (blue) (sale bar 1 mm).

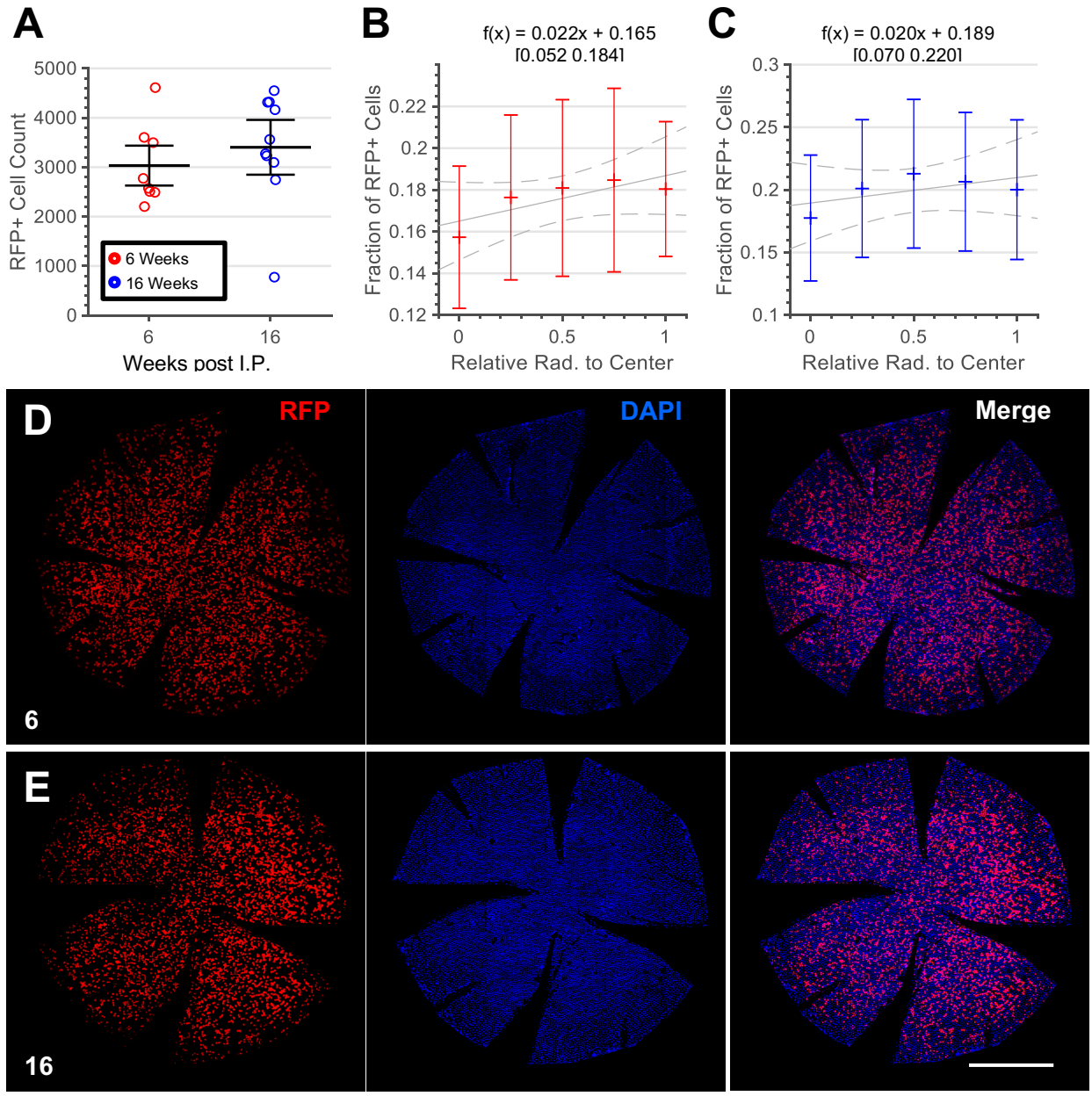

Figure 4.4. Myh11 lineage tracing through intraperitoneal administration of tamoxifen with differing induction start times reveals no change in RFP+ cell density and a positive relationship with radial density towards center

(**A**) Cell count of RFP+ cell nuclei in cornea endothelium with induction starting at 6 and 16 weeks. Radial distribution of density of Myh11 lineage cells to center of cornea with tamoxifen induction starting at (**B**) 6 weeks and (**C**) 16 weeks with fitted linear model with 95% confidence interval (solid and hyphened gray line, 95% confidence interval of slope in brackets).

Representative images from mice with tamoxifen induction starting at (**D**) 6 weeks and (**E**) 16 weeks (scale bar 1 mm).

Myh11-Lin(+) CECs are Non-proliferative

There is little evidence to suggest that CECs proliferate *in vivo*, however one report has suggested that human adult corneas may contain proliferating CECs in the extreme periphery, or the transition zone, of the cornea[329]. We next determined if Myh11-Lin(+) CECs exhibited proliferation by detecting the incorporation of the thymidine analogue 5–ethynyl–2′–deoxyuridine (EdU). Adult tamoxifen-induced *Myh11*-RFP mice were intraperitoneally injected with 200 mg/kg of EdU, and after 30 days, we harvested the cornea tissue to investigate the proliferation of Myh11-Lin(+) CECs. As expected, EdU was detected in the proliferating cornea epithelial cells[330], however, we did not find positive expression of EdU in Myh11-Lin(+) CECs or any other CECs (Fig S4.1). Unlike what has been observed in other preclinical models[331], our work suggests that in adult murine tissue CECs are non-proliferating cells.

Cultured Adipose-derived Myh11-Lin(+) MSCs Differentiate into CEC-like Cells

Restoration of the cornea endothelium have been supplied by exogenous cell sources. We explored the potential of using adipose-derived mesenchymal stem cells (MSCs), a readily available *in vitro* multipotent cell source for autologous procedures. In fact, adipose Myh11+ vSMCs-PCs are suggested to be putative MSCs, thus, the shared Myh11 lineage may be favorable in restoring the corneal endothelium. Myh11-Lin(+) cells from the epididymal fat pad were isolated with enzymatic digestion and cultured using a previously established protocol for CEC differentiation of human embryonic stem cells using Smad inhibitors [326]. After 3 days of differentiation media treatment, western blots (Figure 4.5A) revealed a reduction in expression of the fibroblast marker

HSP90[332] in cultured Myh11-Lin(+) cells (Figure 4.5B, unpaired t-test, p=0.0396), along with a trend of lower αSMA expression (Figure 4.5C, paired t-test, p=0.298). Myh11-Lin(+) MSCs do not initially express N-cadherin prior to treatment with CEC differentiation media (Figure 4.5D), but acquire expression after 14 days of treatment (Figure 4.5B, E). Myh11-Lin(+) MSCs underwent morphological changes from an elongated, spindle-shaped fibroblast shape to a smaller, more round shape.

Local Delivery of Differentiated Myh11-Lin(+) MSCs into Injured CEC Layer

We next tested whether differentiated Myh11-Lin(+) CECs *in vitro* could be delivered into the CEC layer and exhibit a CEC phenotype. After introducing mechanical injury to the CEC layer of C57Bl/6J mice using a previous protocol[333], we injected 5,000 CEC differentiated Myh11-Lin(+) MSCs to anterior chamber with the addition of 100 μM of Rho Kinase (ROCK) inhibitor, Y-27632, and 100 μM TGFβR inhibitor, SB4314542. Immediately after injection, mice were overturned with anterior segment of the eye facing downwards to promote the adherence of injected cells to the CEC layer. One week after local delivery to the CEC layer, immunofluorescence showed that there was a low percentage (<1% of total delivered cells) of CEC differentiated Myh11+ MSCs that adhered to the CEC layer and acquired expression of N-cadherin. However morphological structure was not fully consistent with the endogenous CECs (Figure 4.5G, H).

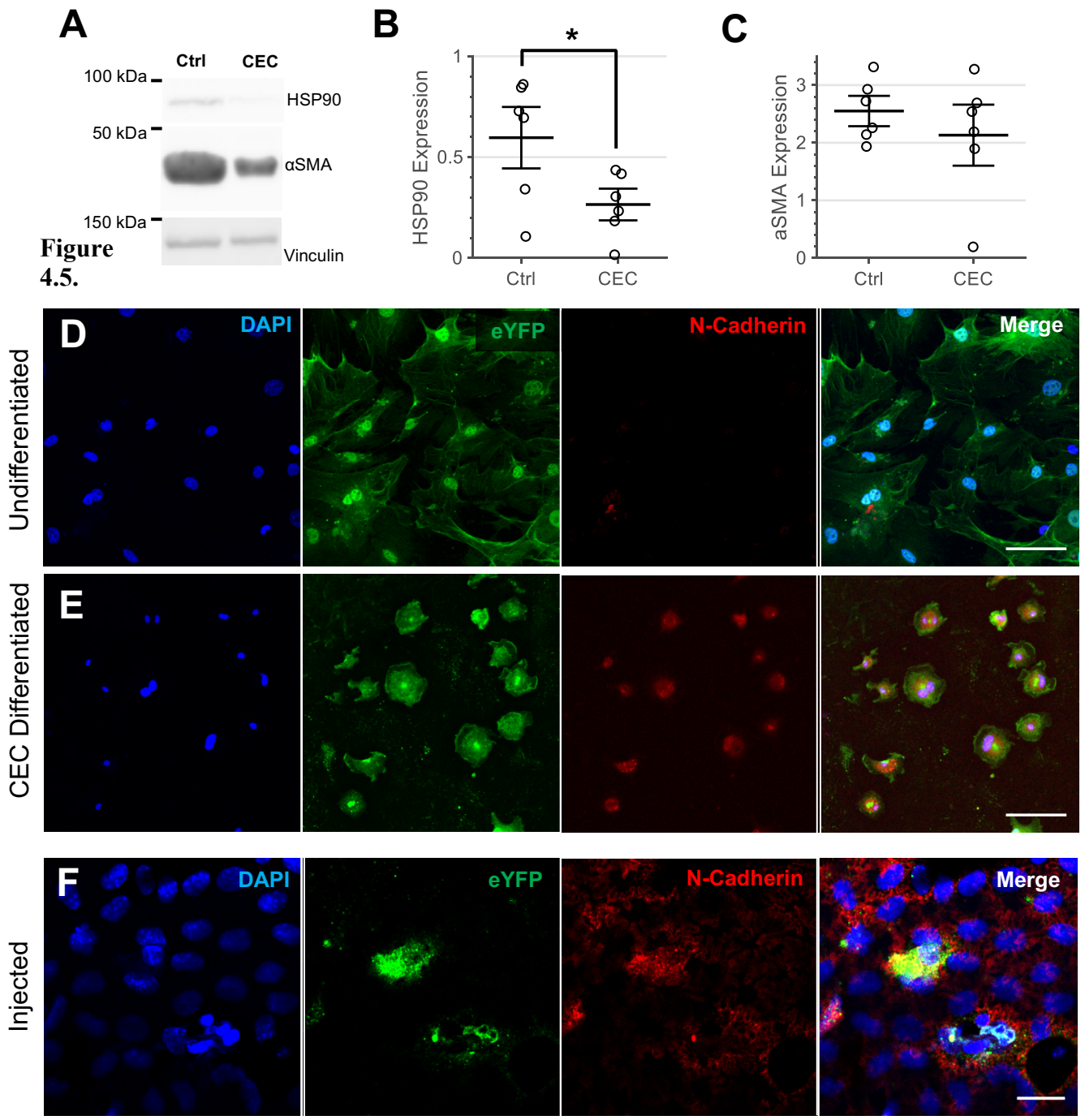
A
Ctrl
CEC
100 kDa
50 kDa
150 kDa
HSP90
αSMA
Vinculin
B
HSP90 Expression
1
0.5
0
*
Ctrl
CEC
C
aSMA Expression
3
2
1
0
Ctrl
CEC
D
DAPI
eYFP
N-Cadherin
Merge
Undifferentiated
E
CEC Differentiated
F
DAPI
eYFP
N-Cadherin
Merge
Injected

Figure 4.5.

Myh11 isolated ASCs can differentiate into a cornea endothelial cell phenotype and adhere to the corneal endothelium after delivery into the anterior chamber
(A-C) Western blot from cells treated with endothelial differentiation media compared to untreated cells, with comparison of (**B**) HSP90 and (**C**) αSMA normalized to viniculin. **(D-E)** Undifferentiated *Myh11*-Lin(+) MSCs stained with anti-eYFP (green), anti-N-cadherin (red), and DAPI (blue), and (**D**) after 14 days treatment with cornea endothelial differentiation media **(E)** (scale bar 100 μm). Data is representative of three biological replicates. (**F**) Representative image (n=3) of exogenous Myh11 lineage ASC adhering to corneal endothelial basal surface 14 days post injection to anterior chamber following a scratch wound (scale bar 25 μm).

Discussion

The cornea endothelium is responsible for maintaining optical transparency and nutrient transport for the entire cornea[334]. Compared to the epithelial and stromal layers, it is the cell layer with the least demonstrated regenerative capacity, with substantial evidence pointing to a complete lack of cell turnover, even in the case of acute injury[335]. Accelerated degeneration of the cornea endothelium remains a substantial risk for any of the annual worldwide 185,000 corneal transplants[336], although cornea transplantation remains the only successful option to partially restore the cornea endothelium. Transplant procedures involve either the replacement of all cornea layers or just the cornea endothelial cell layer and the adjacent basement membrane[321]. These partial transplants use donor CECs in DMEK/DSEAK grafts to replace loss and damaged CECs[337]. However, exogenous cell sources are known to illicit a host immune response, possibly leading to graft rejection or impaired recovery, or lack of visual acuity improvement[338]. With only 1 in 70 patients in need of corneal transplants actually receiving a graft[336], there is a chronic shortage of donor tissue to meet global demands. The use of autologous cell sources for these procedures have the possibility of providing superior clinical outcomes than exogenous transplants independent of a donor tissue supply[339]. Mesenchymal stem cells (MSCs) have the potential to differentiate into a variety of cell types *in vitro*, and previous work has shown that human umbilical cord-derived stem cells can differentiate into corneal endothelial cells *in vitro* using differentiation media that alter

TGFβ and BMP signaling[340,341]. Yet this stem cell source cannot be harvested from adult patients, limiting its utility for large scale use in the clinic. MSCs can be harvested from adult adipose tissue, a readily available adult tissue source[342]. MSCs have been shown to have similar *in vitro* differentiation capability as umbilical cord-stem cells, and there is evidence to suggest that MSCs have the ability to differentiate into endothelial cells[343].

However, adipose-derived MSCs are suggested to have diverse cell lineages[53,54], presenting a confounding factor that could lead to inconsistent therapeutic efficacy. We investigate a specific subpopulation of MSCs, those that express Myh11, that we demonstrate is shared with a subpopulation of CECs. The adherence of Myh11-Lin(+) MSCs to the corneal endothelium surface demonstrates the concept of using an autologous stem cell therapy to regenerate the corneal endothelium in contrast to current therapies that depend on donor tissue allografts. While Myh11-Lin(+) MSCs were able to adhere to the CEC layer after local delivery, these cells did not exhibit a complete CEC phenotype after 14 day differentiation, in contrast with cultured and *in vivo* CECs exhibiting a hexagonal shape connected by tight junctions such as ZO-1. Future work needs to address how to successfully differentiate this population into a more differentiated CEC cell.

Myh11 is considered a lineage marker of vascular smooth muscle cells and pericytes (vSMC-PCs), cells that enwrap and regulate the macro and microvasculature through contraction, juxtracrine, and paracrine signaling. However, My11-Lin(+) CECs exhibited a unique phenotype marker expression compare to vSMCs-PCs with their expression of N-cadherin, ZO-1, and lack of αSMA, along with no association with blood vessels. Cytoskeletal complexes and other actomyosin proteins, primarily actomyosin 2, are heavily concentrated at the apical tight junctions and adherent junctions that form CEC barrier[344], and are implicated in the maintenance of CEC barrier integrity[345–348]. Myh11 may also play a role with in maintaining CEC permeability that are

critical for corneal homeostasis. While our results corroborate previous studies that show lack of cell proliferation, the cell fate of CECs in disease is unknown, and the possibility that this cell layer can endogenously be partially restored from another tissue layer has not been ruled out. The Myh11 lineage tracing mouse model can be used to not only examine cell fate of CECs in disease and injury, but also probe for any signs of contributions from other tissues. We anticipate that using Myh11 lineage tracing will provide a novel model for investigating future corneal endothelium research and have provided proof of concept for autologous adipose-derived MSC restoration of the corneal endothelium.

Supplemental Information

Supplemental Methods 1: Primary Cell Culture

Briefly, the eipididymal adipose pads were harvested from tamoxifen-induced male *Myh11*-eYFP+/+ mice, and the adipose pads were enzymatically digested in 1 mg/mL collagenase type 1 (ThermoFisher, 17100017) for 1 hr at 37°C. Next, the digested fat pads were centrifuged at 400 g for 5 min and the pellet, or stromal vascular fraction (SVF), was collected. Red blood cells were removed from the SVF by adding red blood cell lysis buffer (ThermoFisher, 00-4333-57) for 5 min at room temperature. Next, cells were washed with DMEM media and centrifuged to collect the remaining SVF pellet. The remaining SVF was filtered through a 70-µm and 40-µm mesh, and later resuspended in FACS Buffer consisting of DMEM, 50% BSA, 5 mM EDTA, and DAPI (ThermoFisher, D1306, 1:1,000 dilution). Myh11-Lin(+) vSMC-PCs were FAC-sorted using a BD Influx Cell Sorter, and immediately cultured into wells at an initial density of 1.5e4 cells/cm^2. Cells were cultured in DMEM supplemented with 10% FBS and 1% antibiotic-antimycotic. Once cells reached 70-80% confluency, cells were passaged with 0.05% Trypsin-EDTA. Cells were cultured in 37°C, 5% CO_2, and 95% humidity. All experiments consisted of cells between passages 6-8.

Supplemental Methods 2: Whole Cornea Endothelium Image Processing

Confocal tiles of up to 1.5 GB in size were imported into MATLAB with two channels, one for DAPI and one for RFP. The goal for the analysis was to capture all of the DAPI cell nuclei from the cornea endothelial cell layer, and quantify the total RFP+ nuclei cell count and the fraction of RFP+ nuclei as a function of binned radial distance from the edge of the cornea to the center. To accomplish this, a surface z projection was performed on the image, where a z-max projection was computed on the z-stack that only captures the bottommost layer of the cornea. The resulting 2D

image was segmented for individual nuclei and each nuclei's RFP expression state determined in a binary fashion. The ROI of the corneal endothelial cell layer was manually defined, and thresholded Euclidean distance was used to separate the cornea radially into five bins. The fraction of RFP+ DAPI nuclei was calculated for each bin.

For the surface z-projection of the cornea, (Supplementary Figure 2A, B), the DAPI channel tile underwent a first pass local adaptive segmentation in 3D, where the images were blurred and processed with a min and max filter with the approximate dimension of a cell nuclei (xx μm, xx pix). Foreground was segmented based on where the max filtered image was at least 25 grey values above the background min filtered image. Each of the layers were segmented, and then the bottommost layer was found by finding the bottommost z-slice index of each positive thresholded pixel to create a 2D elevation image, where the pixel value denoted the bottommost z index for that pixel (Supplementary Figure 2C, D). After passing the elevation image through a max filter (xx μm, xx pix) to find the local surface height of the tissue, an *initial surface z projection* was performed that projected the maximum intensity pixel value (in this case from the binary 3D threshold of the tissue) in the z-direction that included the slices above the tissue all the way through the bottom of the tissue represent an *initial surface z-projection*. This yielded a reasonable accurate surface projection of the segmented cell nuclei in the lateral dimensions (x and y), but the highly sensitive threshold was not accurate in z: often the nuclei were segmented in the z-slices above where the nuclei were located in the z-stack. To find a more accurate z-index for the surface projection, the local z slice height from the 2D *initial surface z projection* image was refined by finding the z-slice with the max local contrast between segmented nuclei and background existed, with the assumption that the z-slice with this max contrast was at the center of the nucleus in the z-dimension (Supplementary Figure 2E). These new z-coordinates were again

used as a second 2D elevation image to calculate a *refined surface z-projection* (Supplementary Figure 2F, G). The nuclei were then thresholded and a watershed algorithm applied to split touching nuclei that were above minimum the area of (300 pixels, μm^2). Some nuclei were split incorrectly into many small components, these were reunited base on the components being below 100 pixels in area (Supplementary Figure 2H-J). The red RFP channels were thresholded based on a global threshold (Supplementary Figure 2K) and the state of every DAPI nuclei was determined if it had at least 65% of its area segmented as positive for RFP (Supplementary Figure 2L). Comparing automated cell counts to manually results in a sample dataset of 12 images demonstrated in a pairwise fashion and through Bland-Altman plots reveal high accuracy and agreement between the counting methods (Supplementary Figure 2M-P).

To examine the radial distribution of RFP labeled cell nuclei, ROIs were manually defined in a blinded fashion encompassing the lateral border of the CEC layer. Within the circular ROI the, radial distance was calculated with a Euclidean distance transform of the ROI and divided by the max distance so that radial distance was normalized from 0 to 1. Pixels were split into 5 bins based on radial distance. Cell nuclei were separated into each of the bins based on their center of mass, and the fraction of RFP+ cell nuclei in each bin was calculated.

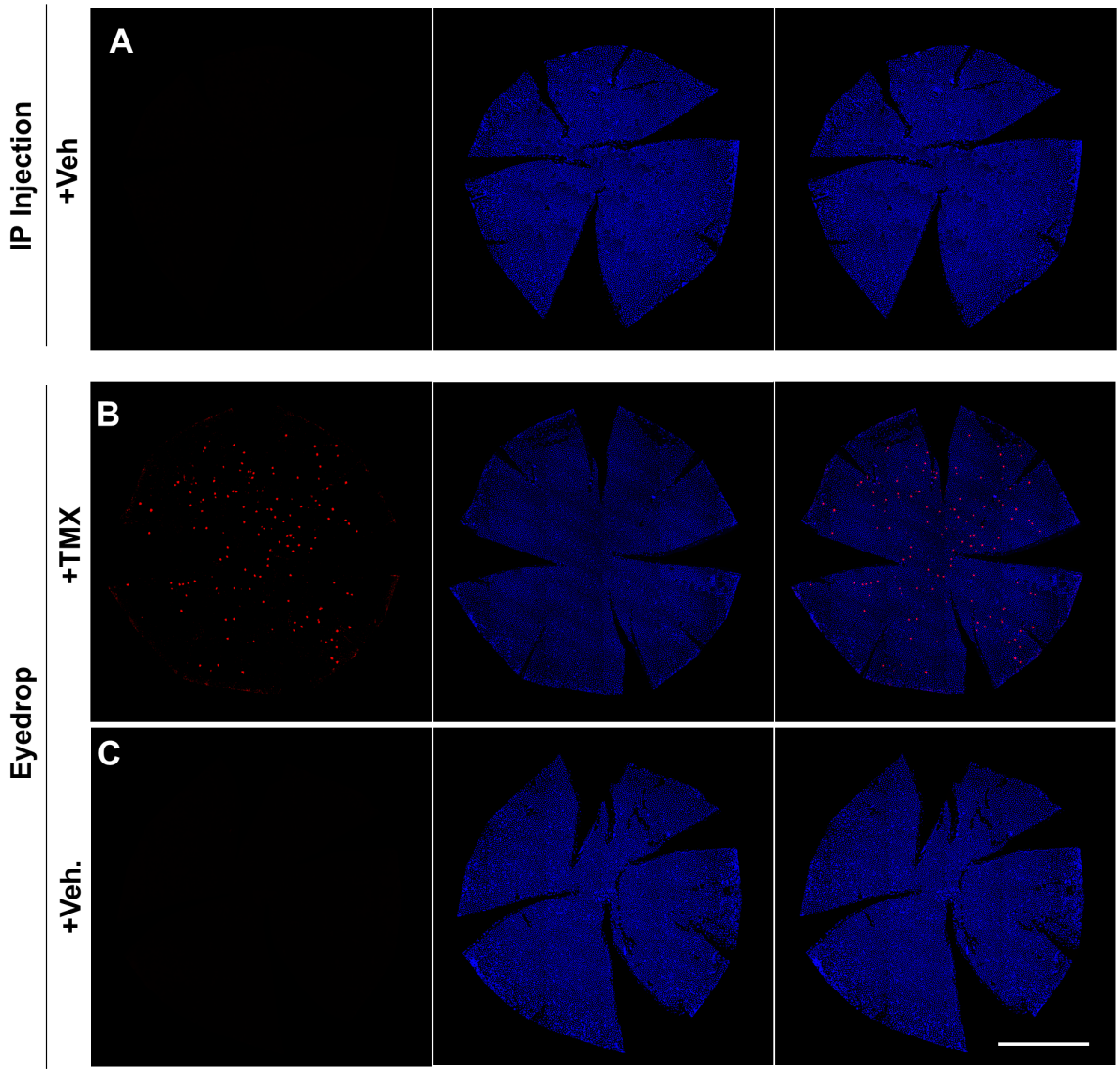

Figure S4.1. Eyedrop induction also yields Myh11-Lin (+) cells, while no cells are marked with vehicle

(**A**) Confocal tile of mouse treated with IP injection of peanut oil as vehicle with RFP (red) and DAPI cell nuclei (blue). Representative image of cornea of *Myh11*-RFP mouse treated with activated (B) tamoxifen eye drops (4-hydroxytomaxifen) for 2 days with 3-week chase, compared with (**C**) vehicle (scale bar 1mm).

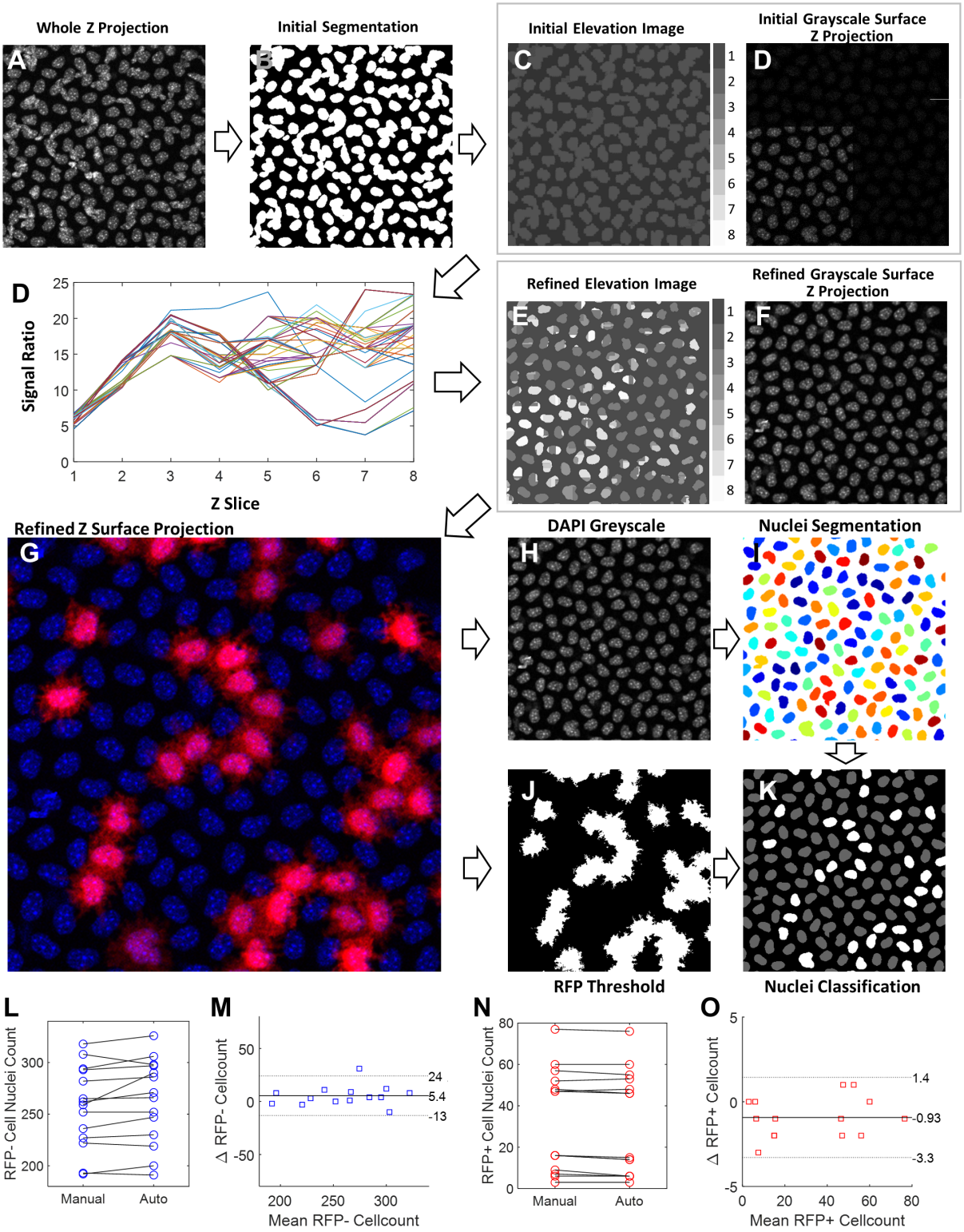
Whole Z Projection
Initial Segmentation
Initial Elevation Image
Initial Grayscale Surface Z Projection
A
B
C
D
Signal Ratio
Z Slice
Refined Elevation Image
Refined Grayscale Surface Z Projection
E
F
Refined Z Surface Projection
DAPI Greyscale
Nuclei Segmentation
G
H
J
K
RFP Threshold
Nuclei Classification
L
M
N
O
RFP- Cell Nuclei Count
Manual
Auto
Δ RFP- Cellcount
Mean RFP- Cellcount
RFP+ Cell Nuclei Count
Δ RFP+ Cellcount
Mean RFP+ Cellcount

Figure S4.2. Whole-mounted cornea endothelial image processing pipeline
Whole-mounted cornea labeled with DAPI and RFP was tiled with confocal microscopy, and the z-projection of the surface cells that comprise the endothelial was obtained and analyzed. (**A**) Representative image of a z-projection through an entire z-stack, which was acquired from imaging cells from the stroma and endothelium. **(B)** Initial segmentation of DAPI nuclei, (**C, D**) with an initial attempt to locate where in Z the surface of the tissue is located that did not always capture the topmost layer of cells. The surface project was refined by (**D**) finding the z slice with the max contrast between foreground and background, yielding a (**E, F**) refined z projection of the surface cell layer. (**G**) The refined surface z projection was then obtained from the original image from both channels, and both (**H, I**) DAPI (blue) and (**J**) RFP labeling was segmented. (**K**) The marked state of each DAPI cell was determine based on the thresholded overlap with RFP. (**L, M**) Paired and Bland-Altman plots comparing manual and automated counting of RFP- cells show close agreement. (**N, O**) Paired and Bland-Altman plots comparing manual and automated counting of RFP+ cells show close agreement.

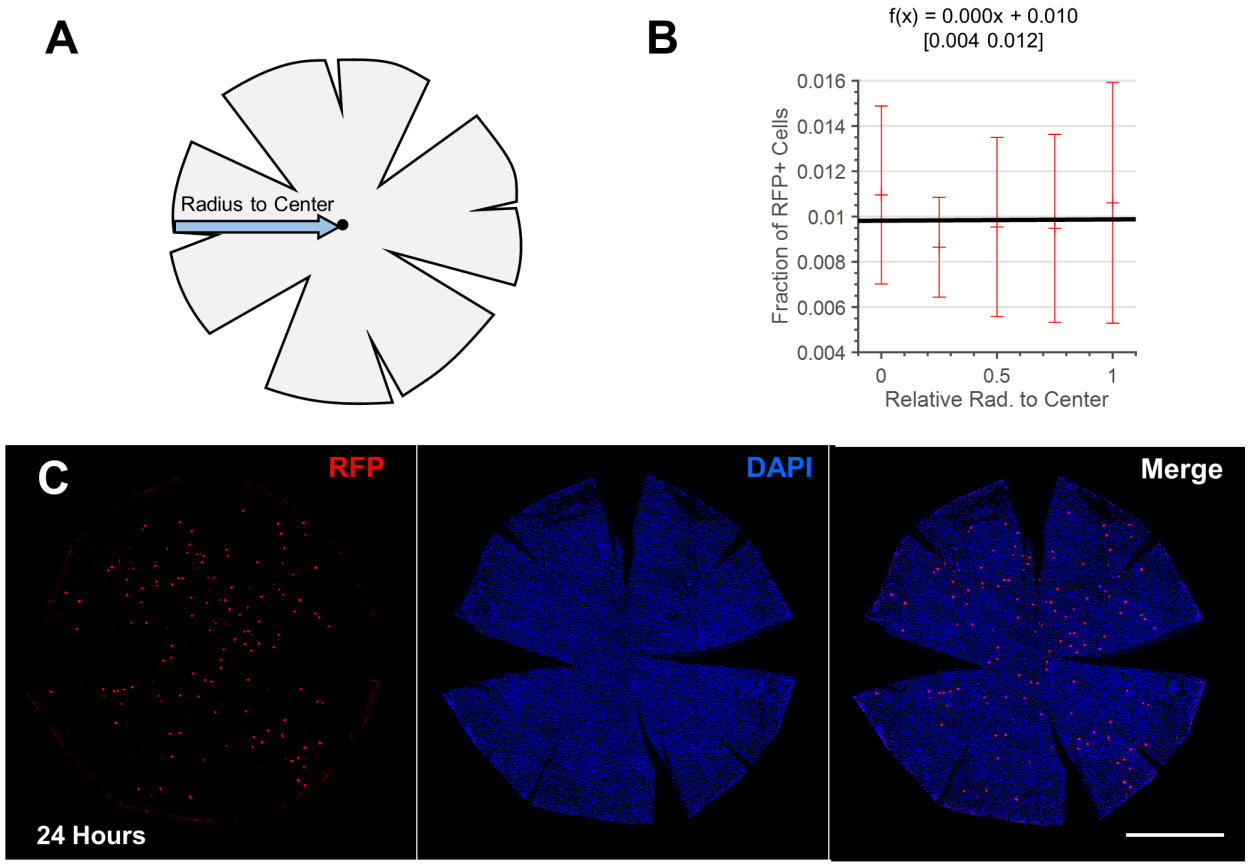

Figure S4.3. Single day treatment of tamoxifen eyedrops with 1 day of chase reveals no sign of Myh11-Lin(+) cells migrating in from peripheral cornea

(**A**) Schematic of how the cornea was radially partitioned between regions. (**B**) Radial distribution of density of *Myh11*-Lin(+) cells to center of cornea with fitted line shows small positive relationship between cell density and radial distribution. A negative slope of the fitted line would indicate a sign of migration from periphery (95% confidence interval of slope in brackets). (**C**) Representative image with RFP (red) and DAPI (blue) (sale bar 1 mm).

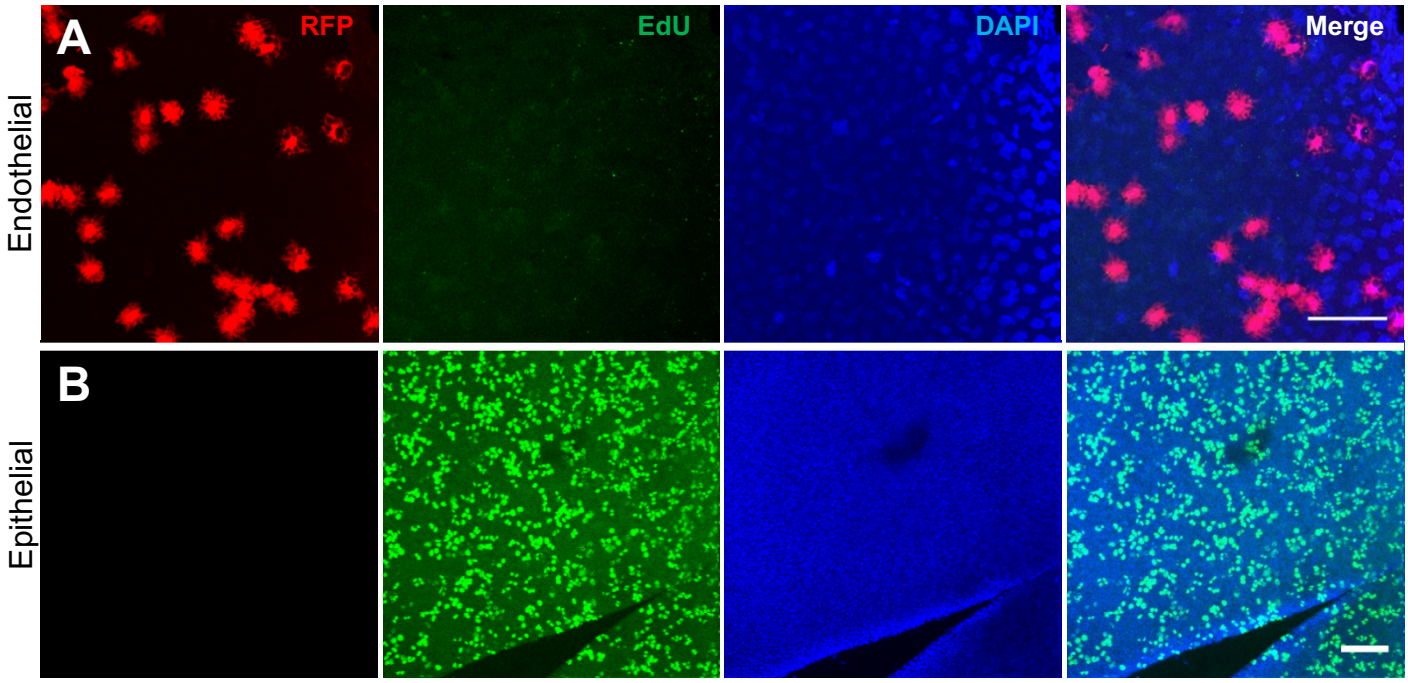

Figure S4.4. Myh11 lineage corneal endothelial cells are non-proliferative
Myh11 lineage cells in the cornea after injection of Edu, with RFP (red), EdU (green), and DAPI (blue) in the (**A**) endothelial cell layer, and (**B**) epithelial cell layer of the cornea (scale bar 100 μm).

CHAPTER 5

DISCUSSSION AND FUTURE DIRECTIONS

Overview

The unifying goal of this thesis was to reestablish a healthy ocular tissue environment within ocular disease through the local delivery of mesenchymal stem cells (MSCs). MSCs are derived from the perivascular region of tissue, and thus we also investigated whether the endogenous population of perivascular cells, namely the retinal vascular smooth muscle cells and pericytes (vSMCs-PCs) were able to differentiate into MSCs and contribute to restoring the ocular tissue in disease.

In diabetic retinopathy (DR), this ocular disease is underlined by retinal vasculature destruction caused by chronic diabetes and inflammation in the retinal tissue. Past studies show MSCs can remodel vasculature through paracrine and juxtacrine methods, thus we examined if intraviteally delivered MSCs could incorporate into the retinal vasculature at a greater than random chance (Chapter 2) and promote retinal vasculature growth (Chapter 3) in a preclinical model of ischemic DR. We also explored within the context of ischemic retinopathy and other ocular injury if the resident vSMCs-PCs could display an MSC phenotype and differentiate into another cell type to participate in the retinal wound healing process (Chapter 3). Lastly, we investigated the ability of MSCs derived from vSMCs-PCs to differentiate into endothelial cells to replace damaged corneal endothelial cells in a cornea injury model (Chapter 4). Taken together, our meticulously investigation of the *in vitro* and *in vivo* bioactivity of MSCs provides insight into the potential therapeutic mechanisms of MSCs once delivered in clinical ocular diseases.

In this final chapter, I will discuss the main outcomes of the data presented in the preceding chapters and discuss future experimental work. The discussion will largely consist of topics of how MSC research should be conducted to reassure safe and comprehensive scientific work for future research studying MSC therapy for ocular diseases.

Key Contributions and Extended Applications

Statistical Analysis on MSC Incorporation to the Retinal Vasculature

Past reports have only demonstrated the ability of adipose-derived MSCs to become pericyte-like cells in neovascularization[93,230,246], but have not systematically measured the frequency at which MSCs incorporate into the endothelial networks or *in vivo* microvasculature. Here, we examine the proclivity of adipose-derived MSCs to become pericyte-like cells in endothelial network formation *in vitro* and murine ischemia retinopathy. The publicly available MatLab® statistical tool described in Chapter 2 measures the enriched colocalization of adipose-derived MSCs with *in vitro* endothelial cell networks and retinal vasculature in ischemic retinopathy. Using novel statistical testing, we are the first group to demonstrate adipose-derived MSCs colocalize with *in vitro* endothelial cell networks and the *in vivo* retinal microvasculature greater than random chance. This confirms MSCs engrafted within the retinal tissue have a predisposition to migrate towards the retinal vasculature, however, it is still unclear on what molecular signaling mechanisms are driving MSCs toward the vasculature endothelium. Regardless, this type of analysis is beneficial to compare the colocalization of a variety of biological structures within individual data sets and multiple sample groups, which benefits multiple research groups that explore strategies to enhance colocalization between cells, proteins, and other organelles.

MSCs Are Derived From Multiple Origins From Adipose Tissue

No other study has used lineage-tracing to perform a thorough investigation of the MSC characterization and behavior of perivascular cells. Because of this, there has been no definitive proof of a specific cell population or populations being a possible source of MSCs. Other reports have commonly used surface marker expression to isolate and derive presumed MSCs from the

stromal vascular fraction of tissue. However, this method does not guarantee the extraction of a specific putative MSC population since the surface marker profiles overlap between different perivascular cells. With the use of a lineage-tracing model in Chapter 3, adipose Myh11+ vSMCs-PCs were isolated, cultured, and analyzed for surface marker expression and tri-differentiation ability. We show that this cell population does meet the criteria to for a MSC *in vitro* defined by the International Society for Cellular Therapy (ISCT)[47]. Furthermore, extracting the lineage-negative population, it was shown that cells not of Myh11+ vSMCs-PCs were also MSCs *in vitro.* Together, this convergence of adipose stromal cells to an *in vitro* MSC phenotype may suggest that there are no particular source of MSC, and the MSC phenotype may be fundamentally dependent on the artificial culture conditions. However, it is still essential that future work use lineage-tracing to study a specific cell population as a MSC, which may reveal that certain putative MSCs may have different cell behaviors and characteristics that are outside of the criteria defined by ISCT. Establishing rigor with lineage-tracing promotes consistency when studying the basic science behind MSC function and therapy, as examining a designated cell population most likely limits biological variation across studies.

MSCs Not Incorporated to Retinal Vasculature Adopt Myofibroblast Phenotype

Considering we desired to develop a MSC therapy for DR, we intravitreally injected the MSCs derived from Myh11+ vSMCs-PCs into a model of retinopathy and showed that from the intravitreal injections blood vessel growth was accelerated. Similar to our previous reports[93,191], the injected MSCs from Myh11-lineaged vSMCs-PCs incorporated to retinal blood vessels at a low percentage, which indicates the paracrine profile of the MSCs essentially induced retinal vasculature growth. Most notably, the delivered MSCs that were located in the vitreous body of

the injected eyes exhibited a myofibroblast phenotype. This was exhibited by the expression of αSMA stress fibers and the presence of Col-IV secretion. The prominent collagen matrix is identical to the epiretinal membrane formed in proliferative vitreoretinopathy, and this vision-deterring membrane formation is occasionally found in PDR and retinal detachment surgeries. This collagen matrix was also present in the vitreous gel after the delivery of MSCs not derived from the lineage of Myh11+ vSMCs-PCs; we demonstrate that the lineage-negative cells (termed "Lin(-)" in Chapter 3) are able to comparably accelerate the retinal vasculature growth in a preclinical retinopathy model, and adopt a myofibroblast phenotype contributing to epiretinal membrane formation.

Because of the myofibroblast differentiation of injected MSCs derived from Myh11+ vSMCs-PCs, the *in vivo* MSC behavior of retinal Myh11+ vSMCs-PCs was also investigated. We analyzed three different models of injury, and only from a severe chemical burn injury to the sclera of the eye, the retinal Myh11+ vSMCs-PCs were able to detach from the vasculature and differentiate into myofibroblasts.

Both the exogenous and endogenous phenotype of Myh11+ vSMCs-PCs displayed a myofibroblast phenotype after complete detachment from the vasculature endothelium, which suggests that Myh11+ vSMCs-PCs may have a preferred propensity to differentiate into myofibroblasts. There is some evidence to suggest that vSMCs-PCs can perhaps differentiate into other cell types after injury to replace damaged cells[270], however, the data presented in this thesis indicates that myofibroblast differentiation is perhaps favored. Given this observation of scar formation, MSC therapy for the eye appears to be an arduous feat, but, the results presented in this thesis still elucidate a fibrotic source of cells in the eye, which had not been previously reported. Targeting retinal Myh11+ vSMCs-PCs and preventing their myofibroblast differentiation may lead

to a novel therapy for proliferative vitreoretinopathy, which currently is only clinically treated through surgery.

MSC Myofibroblast Differentiation is Controlled by Complex Cellular Signaling

As discussed, myofibroblast differentiation can occur in the cell population of Myh11+ vSMCs-PCs. In Chapter 3, we attempted to regulate the myofibroblast differentiation of both exogenous and endogenous Myh11+ vSMCs-PCs by inhibiting the TGFβ signaling pathway. From the global inhibition of TGFβ after chemical injury to the eye, we see a reduction in myofibroblast differentiation and retinal scar formation. In contrast, myofibroblast differentiation of MSCs derived from Myh11 + vSMCs-PCs delivered in ischemic retinopathy is not changed from the inhibition of TGFβ signaling pathway. This suggests that other signaling pathways are sufficient and perhaps necessary to induce myofibroblast differentiation in exogenous MSCs. This is important to consider in future work that attempts to use MSCs as a therapy, as there is risk of unwanted collagen and scar production from the delivery or engraftment of MSCs.

The strategy of reducing MSC myofibroblast differentiation was further explored in Chapter 4. We investigated whether MSCs derived from adipose Myh11+ vSMCs-PCs could serve as a replacement cell source of cornea endothelial cells. Previous studies have used human embryonic stem cells to differentiate into cornea endothelial cells, but we are the first group to investigate this differentiation using MSCs derived from Myh11+ vSMCs-PCs. Corneal endothelial cell *in vitro* differentiation largely is dependent on inhibiting both TGFβ and BMP signaling pathways through inactivation of Smad proteins. From the inhibition of these morphogenetic pathways, we observe a drastic morphological change in MSCs and the typical fibroblast-like culture morphology found in standard culture conditions. This change was not able

to result in a successful differentiation into mature endothelial cells, but there was no observed myofibroblast phenotype of the delivered MSCs into the aqueous humor below the cornea. Notably, inhibition of Smad proteins resulted in a decrease in HSP90, which is an important chaperone molecule in regulating fibrosis[332,349–351]. This suggests that simultaneously targeting TGFβ and BMP signaling, and inhibiting HSP90 activation, may be an alternate strategy in limiting the myofibroblast differentiation of Myh11+ MSCs. Overall, research should avoid a reductionist approach in altering the potential myofibroblast behavior of MSCs, and perhaps by targeting multiple signaling pathways, MSC differentiation into other cell types may be possible.

Future Directions

Stimulating a Pericyte Phenotype of Delivered Adipose-derived MSCs

In Chapter 2 and Chapter 3, we demonstrate that adipose-derived MSCs are able to migrate and towards the retinal vasculature and adopt a pericyte-like position. However, there is still a considerable amount of delivered MSCs (>90% of total injected cells) that do not reach the retinal tissue. The low retinal integration and vasculature incorporation of the total delivered MSCs could be contributed to the MSCs being trapped in the vitreous gel of the eye, the loss of MSCs from the efflux of the injection, or even cell death of the injected MSCs.

There are several practical strategies to consider to determine if vascular integration of MSCs can be improved in preclinical models of DR. First, future work could inject lineage-traced vSMCs-PCs immediately following enzymetic digestion and fluorescent activated cell-sorting (FACS) of the adipose stromal vascular fraction. This approach would ultimately avoid the artificial conditions in culturing, which may preserve the *in vivo* "vSMC-PC cell memory" to the vasculature endothelium. Furthermore, vSMCs or PCs alone could be isolated and sorted based on CD146 expression to further explore if intravitreally injected vSMCs or PCs leads to an increase

in retinal vasculature integration, as the morphology of cell may be a factor in migration to the retinal tissue and vasculature. There is some concern of the difficulty of this strategy, however, as this type of approach is dependent on time constraints on scheduling the use of FACS equipment with the experimentation on preclinical models of a certain age. Also, sorting enough cells for direct intravitreal injection would be challenging, as vSMCs-PCs represent approximately 3% of the estimated 1 million total cells isolated from the stromal vasculature fraction of one murine adipose tissue pad. Dividing this subpopulation even further may not provide an adequate number of cells for experiments. Lastly, another approach could be to lower the total number of MSCs delivered into the vitreous gel of murine preclinical models. Currently, we inject 10,000 cells per 1.5 μL of vehicle solution, and decreasing the number of cells delivered may reduce cell aggregation, which in turn, would increase greater migration to the retinal tissue.

Future experiments should also explore the role of molecular and cellular pathways that are potentially involved in MSCs migrating and attaching to the retinal vasculature. As demonstrated in development and postnatal angiogenesis studies, the recruitment of PCs to vascular endothelium is dependent on several ligand-receptor complexes[70], including the sonic hedgehog (Shh)/Shh receptor Patched (Ptc); stromal-derived factor 1-a (SDF-1α)/CXCR4; heparin-binding epidermal growth factor (HB-EGF)/ErbB; PDGF-B/PDGFRβ ; Angiopoietin-1 (Ang-1)/Tie-2. In regards to neovascularization found in DR, most of the ligands that are responsible for pericyte migration and recruitment are also upregulated in the vitreous and retinal tissue[352–356]. Therefore, the molecular environment is somewhat conditioned for delivered MSCs to adopt a perivascular position on the newly formed retinal vasculature.

Because the retinal molecular environment seems to favor MSC adoption into PCs, or perhaps even vSMCs, future work should analyze the expression levels of the above-mentioned

ligand-receptor complexes on the injected MSCs within the ischemic retinal tissue. To accomplish this, a multitude of protein and genetic markers of injected MSCs, both on- and off retinal blood vessels, need be measured. This analysis can be conducted by harvesting the retinal tissue and using a combination of immunohistochemistry and fluorescent *in situ* hybridization (FISH) to detect several targets in the delivered MSCs. These targets should include receptors and downstream signaling complexes of PC migratory and recruitment ligand-receptor pathways, as well as other vSMC-PC markers, such as aMyh11, αSMA, Vinculin, NG2, CD146, PDGFRβ, RGS5, and angiopoietin-1. Furthermore, it would be critical to detect the presence of integrin connections, such α5β1, α3β1, α6β1, and α1β1[70], to determine successfully connection with the basal lamina and vascular endothelium.

Comparably, another technique to use in detecting the mentioned targets is imaging mass cytometry[357], which is an imaging extension of mass cytometry and allows for the detection of approximately 30 markers within one biological sample. This state-of-the-art technique is advantageous over traditional fluorescent microscopy as it performs high-throughput measurements of multiple tissue samples, and the collected can also be analyzed statistically with clustering algorithms. Currently, this imaging technique is limited to a few institutions, and would most likely serve as a tool for investigations several years later.

Lastly, another option would be to enzymatically digest the vitreous and retinal tissue, inhibit DNA replication through dactinomycin or other agents, and sort the lineage-labeled injected MSCs for single-cell sequencing, such as RNAseq and TAGseq. This experimental technique would probably be the most technically challenging of the three options presented due to the relatively low number of MSCs that may be collected from the digested tissue. To avoid this dilemma, an *in vitro* high-throughput system could be developed to more efficiently examine the

protein and genetic profile of MSCs within the presence of proliferating and tube-forming endothelial cells.

Performing these probing experiments may reveal that certain molecular and cellular pathways are upregulated or downregulated in MSCs within the retinal tissue. Genetic engineering through retroviral, lentiviral, or CRISPR/Cas9 techniques could be used to promote the overexpression or the suppression of select pathways in the attempt to promote a more vSMC/PC phenotype after delivery into the vitreous. For instance, the notch signaling pathway is also suggested to play a role in MSC migration and adhesion to retinal vasculature, as it was recently demonstrated that the juxtacrine connection of adipose-derived MSCs to endothelial cells in ischemic retina, and consequently, endothelial network formation was dependent on NOTCH2 expression[357]. By engineering an overexpression of NOTCH receptors in MSCs, there may be an improved level of MSC retinal vasculature integration, which could be verified using the statistical software of CIRCOAST, as explained in Chapter 2.

Finally, intravitreally delivered MSCs may gradually migrate towards the retinal vasculature and upregulate a pericyte-like phenotype in a time-dependent manner. Surprisingly, we did not find significant expression of Myh11—a marker that only marks vSMCs-PCs in vasculature tissue—on injected MSCs that were engrafted into the retinal tissue, however, this was only analyzed in the retinal tissue samples 2 days and 5 days post-injection. The expression of this defined smooth muscle cell and pericyte marker may increase as the injected MSCs are fully in contact through integrin connections with endothelial cells and the vascular basement membrane. Thus, future work should explore analyzing preclinical models throughout different time points, to determine if MSCs have an improved incorporation with the retinal vasculature compared to a few days post-injection.

Engraftment of Isolated vSMCs-PCs and MSCs into Retinal Grafts

MSC delivery into diseased tissue results in the repair of blood vessels through paracrine and juxtacrine mechanisms. However, the ability of MSCs to reach the retinal tissue and the retinal vasculature after intravitreal injection may not be the best clinical procedure for a potential MSC-based DR therapy. Some researchers are using cell transplantation or retinal graft implants to restore damaged retinal tissue in end-stage retinitis pigmentosa—a genetic disorder where photoreceptor cells break down in the retina, causing vision loss. This type of approach could be adopted to repair the healthy retinal vasculature, as the engineered microvasculature grafts could be inserted subretinally to perhaps replace damaged tissue in end-stage DR patients.

Currently, human embryonic stem cells and induced pluripotent stem cells are differentiated *in vitro* into self-organized 3D neural retina and optic cups through defined protocols[358,359]. After differentiation, these cell structures are transplanted subretinally in preclinical models of retinal degeneration with the expectation to regenerate damaged neural retina. Several weeks after transplantation, these cells integrate into the damaged retinal space and express mature photoreceptor markers[360–363], however, the functional capacity of these grafts still remain unexplored.

A similar approach could be taken in restoring the damaged retinal area where MSCs or isolated vSMCs-PCs are cultured with other parenchymal cells to engineer vasculature grafts *in vitro*. 3D-printing techniques could also be adopted within this approach to leverage the control of engineering the vasculature grafts, in which endothelial cells, extracellular matrix networks, and MSCs/vSMCs-PCs are printed in the same 3D patterns that resemble the microvasculature retinal structure. Once grafts are optimized for stability and differentiation *in vitro,* the grafts could be delivered subretinally in ischemic retinal areas of DR to add a healthy vasculature network within

the tissue. Transplanting the vasculature grafts in the peripheral space of end-stage DR patients would perhaps be the most suitable, as this is least likely to interfere with the macula and potentially cause vision loss. The surgical procedure must be carried out with great care as there have been reports of pre-retinal membrane formation and retinal wrinkling after cellular transplantation in the subretinal space[364,365]. With successful surgery and graft acceptance, it is expected that vasculature grafts may integrate with the surrounding retinal vasculature and form a healthy retinal microvasculature complex, as demonstrated in microvasculature engineered grafts delivered to other tissue[366–368]. As with previous graft studies, it is important to provide appropriate characteristic and functional tests before and after transplantation. Fluorescent angiography, optical coherence tomography, and electroretinograms would assess maturation and biological activity of the retina microvasculature and surrounding tissue to determine if the inserted grafts improved the overall health of the diseased tissue. By supplying the DR retina with a healthy vasculature construct, there may be a decrease in peripheral vision loss, and the decrease risk of leaky blood vessels due to the replacement with healthy and mature blood vessels in the tissue.

Furthermore, future experiments could implement the idea of engineered vascular grafts into the current versions of the neural retina and optic cups 3D implants. The current neural engineered grafts were developed without the presence of vasculature structures, and it is unknown if these engineered cells are optimally healthy without any surrounding blood vessels to supply nutrients and oxygen. Complementing neural grafts with vasculature grafts or perivascular cells may be the most optimal design in replacing the entirety of damaged retinal tissue in DR. This type of complex graft may not only enhance vasculature function after transplantation, but also supply the retina with functional photoreceptor cells, which may lead to the restoration of vision in DR patients.

Using MSC-Derived Microvesicles and Exosomes to Repair Retinal Vasculature in DR

Non-cell based MSC therapy is becoming of more interest in clinical investigations because of potential safety issues, low engraftment of MSCs, and the theory that most of the therapeutic benefit is due to the paracrine factors of the engrafted MSCs[79,369]. For the eye, a non-cell-based therapy is even more meaningful because of our results showing myofibroblast differentiation of intravitreally injected MSCs, which results in vision-impairing scar above the retina. However, the intravitreal injection of MSCs still accelerates retinal vasculature growth in ischemic retinopathy, creating a conundrum around MSC cell-based or non-cell based therapeutic efficacy. This warrants future work to compare MSC delivery to the delivery of MSC secreted microvesicles (MVs) and exosomes (EVs) to repair the state of the retinal vasculature in DR.

MVs (>200 μm) and EVs (40-100 nm) are both phospholipid membrane-bound vesicles that contain proteins, DNA fragments, mRNA, and miRNA. MVs/EVs are mediators of intracellular communication in both physiology and pathophysiology environments, controlling a multitude of signaling cascades around cell proliferation, differentiation, and survival. Because of the phospholipid membrane, the macromolecule contents within MVs/EVs are protected from degradation. Once the MVs/EVs are created and loaded within the cytoplasm of the cell, binding of MVs/EVs to the target cell is thought to occur through juxtacrine signaling, fusion, or endocytosis[370]. MVs/EVs derived from MSCs are considered a potential therapy for DR since it has been demonstrated that MVs/EVs regulate inflammation, apoptosis, and are considered both pro- and anti-angiogenesis[371–375].

There are a few reports to examine the bioactivity and therapeutic potential of MVs/EVs derived from MSCs in eye disease. After laser-induced retinal injury, the intravitreal delivery of EVs from murine adipose-derived MSCs reduced damage in rod and cone bioelectrical signaling,

apoptosis measured by TUNEL staining, and inflammation measured by the downregulation MCP-1, TNF-α, and ICAM-1[376]. Mead and colleagues have demonstrated that the neuroprotective effect from the intravitreal delivery of EVs derived from bone marrow MSCs in a rat optic nerve crush model, a model that results in significant retinal ganglion cell death and axon degeneration[377]. Twenty-one days after intravitreal injection of EVs, the thickness of the nerve fiber layer of optic nerve crushed was significantly preserved when compared to the untreated control. The injection of EVs was also found to reduce the loss of retinal ganglion cells by 30%, as well as preserve the bioelectrical function (measured by ERG) of retinal ganglion cells. Lastly, the work of Mead and colleagues suggested that miRNA were most likely the active component in mediating the retinal ganglion cell neuroprotection since the knockdown of miRNA quantity in exosomes through the siRNA silencing of Ago2 resulted in the suppression of therapeutic effects.

There are currently no reports that have examined the effect of MSC-derived MVs/EVs on restoring the health of the retinal vasculature in DR. Our research group has previously reported that the intravitreal injection of conditioned media derived from MSCs (which contains MVs/EVs and the non-membrane bound macromolecules secreted by MSCs) is not sufficient to provide retinal vasoprotection seen from the injection of adipose-derived MSCs in the ischemic retina of Akimba mice[287]. This result may be explained by the insufficient concentration of pro-angiogenic molecules, or the paracrine profile of the cultured MSCs was not adequate in composition to induce a retinal vasoproliferative response. Exploring the use of MSC-derived MVs/EVs as a therapy for DR may reveal that the contents within the MVs/EVs may be more favorable than MSC-conditioned media in restoring the health of the diabetic retinal vasculature and surrounding tissue.

Therapeutic studies mostly show that MVs/EVs carry macromolecule contents, particularly miRNA, that regulate the transcription of immunosuppressive and anti-inflammatory genes[378–381].

The advantage of MVs/EVs as a therapeutic agent is that there is that there is a phospholipid membrane surrounding the macromolecules, specifically the nucleotides, from degradation. Isolating MVs/EVs can be achieved through a variety of different techniques: 1) differential centrifugation (200-100,00 x g centrifugal force), 2) flotation density gradient centrifugation, 3) monoclonal antibody detection, 4) ultrafiltration, and 5) high performance liquid chromatography[382]. To properly examine MSC-derived MV/EV therapy for DR, the macromolecule contents of MV/EV should be meticulously examined through high-throughput screening kits and traditional laboratory techniques, such as miRNA PCR profiling kits, immunofluorescence antibody detection, western blots. If the macromolecule content of MVs/EVs is found not to be ideal, the macromolecule content could be theoretically altered through pretreatment or genetic engineering of MSCs, which may lead to a more desirable MV/EV profile for targeting specific pathways and damaged cells in ocular disease. For instance, culturing MSCs in hypoxia may change their MV/EV macromolecule contents to a more pro-angiogenic profile, which may benefit the restoration of healthy retinal vasculature in an ischemic DR environment. However, attempting to formulate a correct macromolecule content may be too difficult because of the many interacting variables of transcribing, packing, and loading proteins and nucleotides within membrane-bounded vesicles.

When planning for the injection of MVs/EVs it is important to consider both the tracking and binding specificity of these vesicles. MVs/EVs can be labeled with lyophilic dyes before injection, where fluorescent imaging can be used to detect the location of the MVs/EVs within the retina. Future work should also explore if some sort of transgene or genetic construct can be loaded into the MVs/EVs to test whether the loading contents were successfully integrated into the targeted cells. For instance, similar to how viral transfections occur in host cells, the MVs/EVs

could be loading with a nucleotide construct that could transcribe a fluorescent reporter molecule. Regardless, it is suspected without any sort of manipulation pre-delivery that intravitreally delivered MVs/EVs would have a random dispersion across the retina after delivery. The statistical software CIRCOAST described in Chapter 2 could address whether MVs/EVs associated with certain cell types greater than random chance or between other experimental variables. This would open up further investigation to explore if MV/EV surface protein composition could be modified to improve the biodistribution within the retina or so that binding could occur to a specific retinal cell type. Considering that we have focused on restoring healthy retinal vasculature in DR, target specificity could be enhanced by modifying the MV/EV surface expression to selectively bind to retinal endothelial cells or vSMCs-PCs surface protein receptors.

Computational Modeling of MSCs

Our understanding of MSCs and their therapeutic potential can be advanced through multi-scale computational modeling, or the use of a variety of *in silico* methods to study complex behaviors and systems. Previous studies have been dependent on experiments that only are capable of examining limited MSC behaviors, such as a few selected protein or genetic markers, after the manipulation of a single variable. These types of experiments have been valuable to establishing a fundamental understanding of MSCs, however, there are still aspects of MSCs that are not explored that are very difficult and time-consuming to understand with traditional laboratory techniques.

With computational modeling, thousands of simulations can be conducted in order to predict the complex cell behavior of MSCs. These computational models are based on a variety of omics data, and when appropriately designed can provide substantial insight into behaviors that

are difficult to capture with current experimental methods. Thus, there first needs to be a coordination between labs to collect and share bioinformatics on MSCs to construct effective models. This type of shared data includes data collected from high-throughput assays such as 1) Luminex Multiplex Bead Assays that measures cytokines, chemokines, and growth factors; 2) sequencing technology such as single-cell RNAseq and DNAseq that detects genomic information of individual cells; and 3) flow cytometry and mass cytof that detects the protein expression of individual cells. Realistically, with any model, there is likely to be bioinformatics data missing to build an ideal model, thus, accurate assumptions can be made based on sensitivity analysis and parameter estimation models to compensate for missing data.

In the context of DR and MSC therapy, a multi-scale computational model could be built that explore MSC bioactivity impacted from both mechanical and chemical cues in the diseased retinal tissue environment. To start, a signaling or gene regulatory network model could be developed to model how mechanical and chemical cues in a DR environment impacts the single MSC that is delivered into a replicated DR environment. The signaling network could be based on ODES, a decision tree model, or mixed-effects model systems that simulate multiple molecular signaling pathways that are upregulated, downregulated, or unchanged by local cues found in a typical DR environment. Theoretically, the input of cues in the model would be based on diversity of reports accumulated from DR patients[120,125,383,384]. Implementing this type of collected patient data in a signaling network pathway model, we can explore the expression of molecules, proteins, and genes that control for MSC differentiation, metabolism, survival, and proliferation.

Next, an agent-based model (ABM) could be developed to predict the emergent micro and macro behavior of multiple MSCs that are modeled from the described, theoretical signaling network model. An ABM would be designed similar to the signaling network model, with a set

of rules governing the MSCs (agents) and their interaction with one another and the simulated DR tissue environment that includes damaged retinal neural and/or vascular cells. By creating simple rules, it is expected that future ABM simulations would provide simulations to predict micro MSC behaviors such as the migration, apoptosis, blood vessel attachment, collagen secretion, and paracrine secretion. In turn, macro behaviors could also be observed in the ABM simulations, including those that explain the degree of inflammation, the total neuronal function, and blood vessel complex within the simulated retinal tissue.

Using these multi-scale models will ultimately conserve resources, particularly time, to explain the complex behaviors of MSCs. Furthermore, computational modeling could explain other potential detrimental or unwanted MSC bioactivity, as the case of myofibroblast differentiation explained in Chapter 3. Therefore, computational modeling could possibly prevent additional harm to preclinical and clinical patients, as the *in silico* predicted dangerous MSC bioactivity could be perturbed prior to delivery and engraftment. Also, with further experimental validation, these purposed multi-scale models can be further improved for accuracy and perhaps expanded to other research groups that examine MSC bioactivity and therapeutic potential for other diseased tissue.

Is There a Difference Between vSMCs-PCs, MSCs, and (Myo)Fibroblasts?

Historical Classification of vSMCs-PCs, MSCs, and (Myo)Fibroblasts

The first observations of vSMCs-PCs, MSCs, and (myo)fibroblasts were based on microscopy and chemical analysis of animal tissue (including human) and cultured cells. The anatomical positions of these cell populations have been somewhat distinct, however, reviewing the classical studies reveals overlap in cellular phenotype in these different cell populations, particularly when analyzed

in vitro. In the late nineteenth century, vSMCs were described as muscular fibre cells in the tunica media of human arteries[385], and were later identified in 1957 by electron microscopy enseathed and connected to the vascular endothelium of extending arterioles[386]. Relatedly, PCs, were first described in 1871 by Eberth and Rouget as contractile cells surrounding the endothelial capillaries[387,388]. Approximately 60 years later, in 1923, these contractile and perivascular cells were officially termed "pericyte" by Zimmermann[389]. In 1906, fibroblasts were identified in the connective tissue of animals, and in the 1970s, myofibroblasts were first described in as "wound fibroblast" in skin wound healing of parabiotic rats[390], which was later conferred through electron microscopy[391]. Interestingly, the time period at which the function of fibroblasts was described, corresponds around the same date as the discovery of the "MSC" by Friedenstein and colleagues[42–44]. In fact, within the first described *in vitro* cultured conditions, fibroblasts were described as structurally and functionally similar to smooth muscle cells[391]. When defining MSCs, reports largely describe these cells as being perivascular cells, and once cultured these perivascular cells form CFU-Fs under several passages. Under distinct media conditions, these same cells exhibit some form of mulitpotency *in vitro*. Similarly, cultured "fibroblasts" also display multipotent differentiation[392,393] and paracrine bioactivity that is similar to *in vitro* "MSCs"[394–396].

As reported in Chapter 3, there is strong evidence to suggest a significant overlap in the cell types of vSMCs-PCs, MSCs, and fibroblasts/myofibroblasts in the case of culturing and *in vivo* wound healing. When harvested from adipose stromal vascular fraction, these cell populations seem to all converge a "MSC" phenotype that is defined by the ISCT. In addition, these cells appear to exhibit a similar *in vitro* paracrine profile when cultured, as the cultured Myh11-Lin(-) population and cultured Myh11+ vSMCs-PCs exhibit similar concentrations of proteins in their respected conditioned media (Figure 5.1).

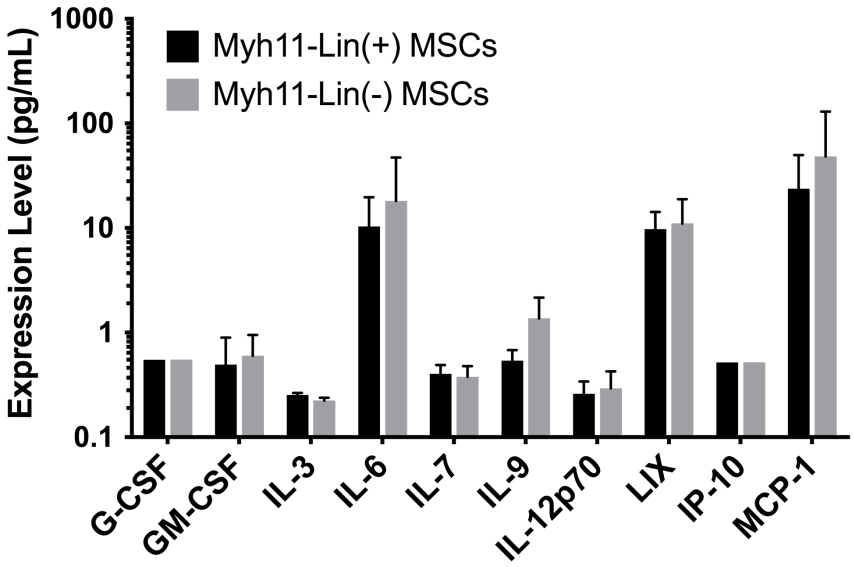

Figure 5.1. Conditioned media from MSCs derived from Myh11+ vSMCs-PCs ("Myh11-Lin(+)") and Myh11- stromal vascular cells ("Myh11-Lin(-)")
MSCs were cultured for 24 hrs without the addition of FBS in standard media and culture conditions. After 24 hrs, media was collected and analyzed through Luminex Bead-based Multiplex Assay. No significance was detected between detected growth factors, chemokines, and cytokines.The data presented here is representative of three biological replicates. A Holm-Sidak t-test was used to determine statistical significance.

Taking into account the phenotype of a MSC *in vitro*, the "MSC" state most likely represents a cell-state in which vSMCs-PCs and other perivascular cells, are readily inclined to be pushed towards a myofibroblast state. In wound healing and tissue injury repair, there is a coordination of communication between epithelial cells, fibroblasts, vSMCs-PCs, and leukocytes to prompt the repair of the surrounding environment. The inflammatory cells are largely responsible for releasing cytokines and chemokines to successively induce the differentiation of the surrounding fibroblasts, perivascular, and epithelial cells into myofibroblasts[290,397]. We show under traumatic injury in Chapter 3, that vSMCs-PCs migrate off-vessel and differentiate to a myofibroblast. Collectitvely, the cell lineage of a vSMC-PC, MSC, and (myo)fibroblast seems to

be connected to the health of the adult tissue, where these cell populations can display a convergence to a myofibroblast or wound-healing cell in certain types of injury.

Vasoconstriction and the Activation of vSMCs-PCs Toward a Myofibroblast State

It is currently unclear the time point at which microvascular vSMCs-PCs are required to migrate off-vessel and contribute to the myofibroblast pool in the wound healing process, especially considering that tissue-resident fibroblasts are present in most tissue to aid in the remodeling of connective tissue. The work in this thesis suggests that the vSMCs-PCs differentiate into myofibroblasts only in severe injury of the eye, in which there is extreme inflammation and blood vessel damage. In our models of eye injury in Chapter 3, we measured the amount of TGFβ1 expression levels in the models of oxygen-induced retinopathy, laser-induced chorodial neovascularization, and sclera chemical burn injury. We observed that the TGFβ1 expression levels were significantly higher than the control tissues only in the chemical injury burn model. TGFβ1 has different mechanisms of action depending on the cell type and the tissue environment, but has been demonstrated to increase the activation of contractile pathways in vSMCs-PCs[398,399]. Dunfield and colleagues have suggested that the increased and sustained levels of vasoconstriction cause microvasculature vSMCs-PCs to differentiate into myofibroblasts and contribute to the fibrotic cell pool. In a recent report, this group revealed Fibroblast growth factor-inducible 14 (Fn14) is increased on PCs in chronic kidney disease[400]. The authors suggest the ligand for Fn14, TNF-related weak-inducer of apoptosis (TWEAK) maintains the fibrosis process through pericyte contraction to their subsequent activation and persistence myofibroblast persistence. In the kidney disease environment, it is implied that TWEAK is secreted by the surrounding macrophages

and fibrogenic activation is induced by canonical and noncanonical NF-kB, IFN regulatory factors (IRF), and ERK signaling.

This finding alludes that chronic and consistent activation of vasoconstrictive pathways are perhaps sufficient to provoke retinal vSMCs-PCs to migrate off-vessel and differentiate into myofibroblasts. Interestingly, TGFβ1 and TGFβ2 are upregulated in the vitreous and contractile pretinal fibrous membranes of PDR and PVR patients[401]. Other vasoconstrictive molecules, such as Angiotensin-II is also found in higher levels in the vitreous samples of PDR patients[384], and is suspected to contribute to retinal vasculature dysfunction by increasing inflammation and VEGF signaling[402].

As there is no current small molecule therapy for fibrosis in the eye, we show in Chapter 3 a global knockdown of TGFβ signaling after chemical injury burn does indeed downregulate vSMC-PC myofibroblast differentiation and the succeeding retinal fibrosis. Although differentiation was impeded, we did not explore the specific knockdown of TGFβ signaling in retinal vSMCs-PCs. To follow-up on this finding, impending experiments should use immunohistochemistry to measure if TGFβR1 is upregulated in retinal vSMCs-PCs, or a subset of vSMCs-PCs, shortly after the onset of the chemical burn injury. By detecting which vSMCs-PCs are highly expressive of TGFβR1, we may reveal the state at which vSMCs-PCs are positioned to differentiate into myofibroblasts. The literature currently hints to functionally different classes of vSMCs-PCs[274,403], and there is a possibility that only specific vSMCs-PCs are required or primed to contribute to the fibrotic pool in injury. Given enough samples of chemically injured retinal tissue, vSMCs-PCs with supposedly high expression TGFβR1 could be isolated, sorted, and analyzed through genomic sequencing techniques. By analyzing the genetic data of these isolated cells novel molecular pathways could be further investigated to target the downregulation of

fibrosis in PVR and PDR. Furthermore, genetic models of conditional knockdown of TGFβ could be developed and crossed with the Myh11-CreER^{T2} model to further demonstrate the cell-specific knockdown of TGFβ downregulates vSMC-PC myofibroblast differention after chemical injury burn.

Impact of Diabetic Environment on Delivered MSCs

One limitation of the presented work is the use of nondiabetic animal models to phenotypically replicate the retinal vasculature dysfunction of DR. We have conducted preliminary work to show that injecting MSCs derived from Myh11+ vSMCs-PCs leads to a slight decrease in retinal vasculature dropout of Akimba mice[185] (Figure 5.2), a murine model that phenotypically replicates PDR in the presence of hyperglycemia. Although the preliminary results are based on a small sample size, it seems that MSCs may possess some ability to improve the health of the retinal vasculature in the long-term exposure of a diabetic environment. However, there is still concern about how chronic hyperglycemia will impact the state of the long-term health of the injected MSCs, and consequently, the effectiveness of MSC therapy. Thus, it is critical for future work to explore the cell behavior and viability of MSCs, particularly those derived from Myh11+ vSMCs-PCs, in diabetic preclinical models, including adult DR preclinical mouse models such as the non-obese diabetic (NOD) mice[404], leptin receptor-deficient (db/db) mice[405], Akita mice[178], and the mentioned Akimba mice.

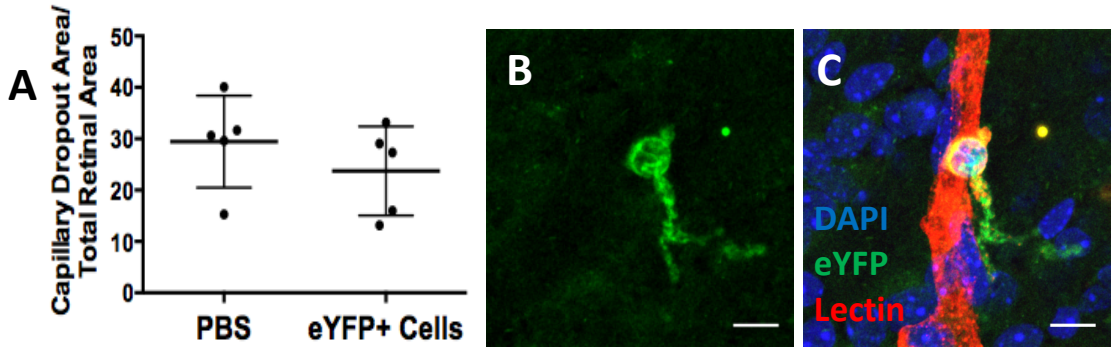

Figure 5.2. Local deliver of MSCs derived from Myh11+ vSMCs-PCs in Akimba model
(A) Intravitreal injection (5,000 cells/1.5 μL PBS) of MSCs derived from vSMCs-PCs in postnatal day 9 Akimba pups slightly diminishes retinal capillary dropout 4 weeks post injection (n=5, $p>0.05$). Wilcoxon rank sum test was used to test statistical significance. **(B,C)** MSCs (green) were able to adopt a pericyte-like position on the lectin+ retinal vasculature (red). Scale bar represents 10 μm.

Previous work suggests that chronic hyperglycemia and exposure to short-term high glucose levels is detrimental to the cell survival, differentiation, and pro-angiogenic function of MSCs. This observation is particularly important to consider when exploring autologous MSC treatment of diabetic patients. We have already shown that adipose-derived MSCs harvested from diabetic mice have impaired pro-angiogenic paracrine signaling and slightly lower vasculature integration when compared to MSCs harvested from non-diabetic mice[191]. Others show similar results, where MSCs derived from type 2 diabetic mice exhibit decreased adhesion and migration *in* vitro through the suppression of the PI3K-Akt pathway[406], and transplanted MSCs fail to increase neovascularization in hindlimb ischemia due to hyperinsulinemia-induced, Nox4-generated oxidant stress[406]. Outside of the direct context of glucose, Yang et al. found that rat bone-marrow MSCs were also impacted negatively by AGEs[407], which is abnormally increased in retinal diabetic conditions. Within this study, AGEs inhibited the proliferation and migration via the ROS-p38 MAPK-mediated pathway of MSCs, which also led to the release of pro-inflammatory factors.

Given that diabetes impairs the therapeutic potential of MSCs, there is some evidence to suggest that MSC viability and therapeutic function may be protected through a combined treatment of small molecules and organic compounds. It was reported that AGE mediated-apoptosis in adipose-derived MSCs was inhibited by antioxidants N-acetylcysteine (NAC) and ascorbic acid 2-phosphate (AAP)[408]. Also, within this follow-up study, miR-223 upregulation was found in NAC and AAP treated adipose-derived MSCs, and miR-223 inhibition combined with the presence of antioxidants amplified the protection of AGE-mediated apoptosis. Other reports have shown that antioxidants melatonin, polyphenols, epigallocatechin-3-gallate, curcumin, and 17β-estradiol protect MSCs from reactive oxidative stress-induced apoptosis[409–411]. To counteract the negative impacts of a diabetic environment on MSCs, using these types of approaches in future studies may help prevent and amplify the therapeutic benefits of MSCs once delivered in the diseased environment of DR.

Utilizing Lineage-Tracing of MSCs in Human Clinical Studies

One of the advantages of the work described in Chapter 3 and Chapter 4 is the use of the *Myh11*-CreER^{T2} mouse model[225] to continuous fluorescent lineage-tracing of Myh11+ vSMCs-PCs. With this technology, we followed the Myh11+ vSMCs-PCs population and its progeny in all the environments of experimental preclinical analyses. In Chapter 2 of this thesis and other work[93,191], we have used lipophilic dyes to label MSCs for cell-tracing in injected eyes, however, this technique is less inadequate when compared to lineage-tracing using an endogenous reporter. Lipophilic dye is reported to transfer between cells, particularly macrophages[412], which makes it difficult for MSCs to be accurately followed. Likewise, for *in vivo* detection of delivered MSCs in clinical trials, MSCs are labeled after isolation and cultured *in vitro* with fluorescent reporter

genes, radiotracers, and nanoparticles. Throughout clinical testing, the labeled MSCs are then detected using ultrasound, MRI, and nuclear medicine (SPECT, PET)[412,413].

Although MSCs can be traced *in vivo* within human patients, there is no report that has labelled a select population of putative MSCs (i.e. Myh11+ vSMCs-PCs) from the stromal vascular fraction before culture or delivery into the desired tissue. To establish rigor in human MSC basic science and therapy, future work should use methods similar to what we present in this thesis to study a specific subset of putative MSCs. Using technology to label only Myh11+ vSMCs-PCs would establish a scientific control on MSC clinical therapy by standardizing the desired MSC population harvested across several human patients. If this type of technology was developed, there would be an exact putative MSC population that was injected across multiple studies, allowing for a more significant cross-comparison between clinical reports. Lastly, when considering a MSC therapy to replace loss vSMCs-PCs in DR, selecting for only Myh11+ vSMCs-PCs in patient tissue may be beneficial, as we previously mention that this cell population may be more inclined to readopt a vSMC-PC position than the other putative MSCs found throughout the stromal vascular fraction of harvested tissue.

Traditionally, cell populations that are regarded as putative MSCs are harvested, isolated, and sorted based on surface marker expression, which makes it difficult to solely select for any cell population due to the overlap of surface markers with other cell types in the stromal vascular fraction. To address this issue, Millipore, Inc. has aided in the development of a product to label cell populations based on mRNA expression without damage of the cell. This technology, coined "SmartFlare™ Live Cell RNA Detection"[414] , is based on NanoFlare detection published by Mirkin and collegaues[415–417]. This system works by having antisense DNA for a specific recognition sequence adsorbed to the surface of a gold nanoparticle, and with the binding of the target mRNA,

the "reporter flare" is released and a fluorescent signal is scattered throughout the cell cytoplasm. The original work of this technology was developed for the detection of cancer cells in whole blood, but this type of technology would also be well-suited for isolating vSMCs-PCs based on *Myh11* mRNA expression. Interestingly, the efficacy of NanoFlare has been questioned by the science community[418], and the SmartFlare™ product line was recently discontinued. Still, by using this described method or another similar approach, specific cell populations could be studied in future preclinical and clinical work, thus strengthening the rigor of MSC clinical therapy investigation. A follow-up study for the work presented in Chapter 3 would be to use Myh11 SmartFlare probes to isolate human vSMCs-PCs and explore the MSC behavior and bioactivity of this isolated cell population after delivery into preclinical models of DR. The results of this study could be further compared to the preclinical results described in this thesis.

Using MSCs Effectively and Safely in Other Ocular Diseases

Chapter 3 results underline the possible danger of MSC-cell based therapies for retinal diseases such as DR. According to our work in this chapter, intravitreally injected MSCs have the propensity to differentiate into a fibrotic phenotype within the vitreous gel of the eye. Also, in Chapter 4, we demonstrate the difficulty of differentiating and delivering MSCs into a non-myofibroblast cell within the cornea endothelial cell layer. Because of these results, it is imperative that future work explore injecting MSCs into ocular tissue that could benefit from the production and remodeling of connective tissue.

For instance, the cornea stroma intrinsically contains fibroblasts (also referred to as keratocytes) and a dense collagen network. This layer is located in the middle of the cornea between the epithelial and endothelial layer, and the stroma fibroblasts secrete collagen fibers and other extracellular components to maintain corneal transparency. In disease and injury, these

fibroblasts activate into myofibroblasts to remodel the connective tissue, and these cells eventually undergo apoptosis after the completion of the wound healing process[419]. The resident fibroblasts are eventually replaced through mitosis, but in some cornea diseases, including keratoconus, the resident fibroblasts are impaired by mechanisms largely unknown[420]. In the case of keratoconus, the cornea stroma layer is abnormally thinner and apoptosis is upregulated in the fibroblast population[421,422]. Within diseased cornea stroma, a MSC cell-based therapy could serve to replace damaged fibroblasts, and perhaps increase or restore the extracellular matrix to preserve the health of the cornea stroma.

In a preliminary study, MSCs derived from Myh11+ vSMCs-PCS were injected into the cornea stroma of healthy mice, and the MSCs were found to exhibit a myofibroblast phenotype 7 days post-injection (Figure 5.3). This myofibroblast phenotype was equivalent to the myofibroblast phenotype of delivered MSCs in the vitreous, as both engrafted MSC populations exhibited a myofibroblast morphology with expression of αSMA stress fibers and Col-IV. It is unclear how long the MSC myofibroblast phenotype will persist post-injection, however, myofibroblast activation of the resident fibroblasts can be inhibited through IL-1α and the reduction of TGFβ2 following the conclusion of wound healing[419].

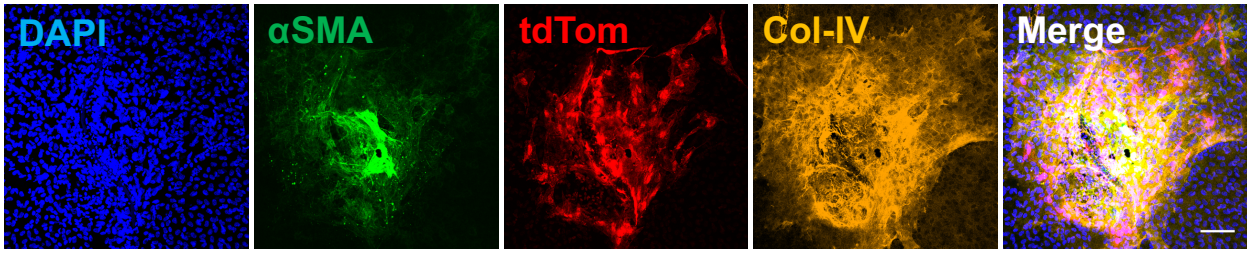

Figure 5.3. Injection of MSCs derived from Myh11+ vSMCs-PCs into the cornea stroma results in myofibroblast differentiation
A cornea pocket was performed in adult C57Bl/6J mice to locally deliver 5,000 cells per 3 μL in PBS to the cornea stroma. Locally delivered MSCs (red) were found to exhibit a myofibroblast phenotype that includes the presence of αSMA stress fibers and copious Col-IV production. Scale bar represents 100 μm.

Unfortunately, there is a caveat with injecting MSCs as a cell source of myofibroblasts; opaque collagen can potentially be secreted from myofibroblasts that can lead to haziness in the cornea, and consequently, the impairment of vision[423]. Therefore, research work that investigates MSC delivery in the cornea should be cautious around the production of the levels and types of collagen secreted by the engrafted MSCs. As mentioned throughout this current chapter in the above sections, genetic engineering of MSCs may be ideal to control for prolonged myofibroblast activation and the secretion of dense collagen. In fact, crystallins are suggested to control for the level of haziness in the cornea. Specifically, crystallins transketolase (TKT) and aldehyde dehydrogenase class 1 (ALDH1) are higher in healthy, transparent corneas[424]. This suggests that MSCs could be engineered to express constant water-soluble, crystallins to reduce the possibility of haze formation after delivery and engraftment into the stroma.

Another strategy for a MSC cell-based therapy for the cornea would be to integrate MSCs into decellularized 3D-engineered grafts developed for clinical cornea replacement surgery. Combining synthetic grafts and 3D-printing technology would further control more for the construction of a more organized cornea stroma structure. Notably, using aspects of 3D-printing

would allow for the direct placement of MSCs within the grafts, and would be more advantageous to the design of the artificial tissue to match the natural formation of the cornea stroma. Simply locally delivering MSCs would most likely result in the random assortment of MSCs in the cornea stroma and may lead to unwanted collage formation in certain areas of the stroma. Currently, human corneal stromal cells are isolated for integration into engineered stromal grafts[382], however, these cells are perhaps more difficult to isolate from patients when compared to MSCs harvested from larger tissue such as adipose tissue. Also, considering the abundance of MSCs that are harvested from adipose tissue and expanded *in vitro*, MSCs are more practical to use as a potential cornea stroma fibroblast cell source than isolated human stromal cells. As with most of the future work discussed in this chapter, investigating MSC differentiation and viability after placement into 3D-grafts, and subsequently, after the placement in preclinical models, can be investigated by analyzing surface and intercellular markers with several imaging and protein and genetic screening techniques mentioned above. The engrafted engineered constructs could also be imaged *in vivo* by corneal topography and tomography.

The Future of MSCs – Name Change, Policy, and Therapy

With the current work that I have presented in this thesis, I recommend a referendum to remove the "stem cell" term from "mesenchymal stem cells", especially in regards to adipose-derived MSCs. Some researchers have used and suggested the name "mesenchymal stromal cells", which may be more appropriate given the lack of the "stem cell" aspect these cells display *in vivo*. Throughout the years, Arnold Caplan, who is regarded as the "father of MSCs" has also suggested a name change to MSCs, where he has recommended the term "medicinal signaling cells" to describe MSCs[425]. I argue that both the term "stem cell" and "medicinal signaling cells" introduces bias into the scientific community, as both terms suggest that these cells are assumed to grant a

therapeutic outcome in all types of experimentation. This is especially true when considering how MSCs have been advertised to the public, as it is suspected that patients would assume "medicinal signaling cells" and "stem cell" presents a somewhat miraculous treatment for their illnesses.

The work of this thesis and others demonstrate that *in vitro* MSCs somewhat meets the classical definition of a stem cell, which is as a population of unspecialized cells that can self-renew and potentially give rise to specialized cell types under certain conditions. The differentiation of MSCs is particularly questioned because several of the differentiation observations captured *in vitro* has not been able to be replicated *in vivo*. We show in this thesis, as well as others, the ability of the putative MSC *in vivo*, lacks the ability to directly differentiate into another tissue or organ specific cell after injury, other than a myofibroblast. Only through the introduction of a particular media conditions *in vitro*, these cells are able to display differentiation towards multiple cell types. As with induced pluripotent stem cells, there seems to be a need to completely reprogram the cell in order for MSCs to adopt a more traditional stem cell phenotype. This reprogramming does not seem to occur under physiological and pathophysiological conditions, which again warrants an elimination of the term "stem cell". Furthermore, it is unclear the degree MSCs are "unspecialized", as the stem cell genetic profile has not been fully explored, particularly the pluripotent stem cell factors and Yamanaka factors Oct4, Sox2, KLF4, c-Myc, Lin28, and Nanog. With lab technical variation across research groups, including the isolation and culture of MSCs, it is difficult to conclude the true "stem cell" behavior of MSCs. Because of this, I recommend the scientific community and governing agency make a proposal to culture and analyze putative MSCs in consistent, agreed-upon established conditions.

Given that MSCs are more likely more of a fibroblast in nature *in vitro*, and our lack of cell-engineering of MSCs, the introduction of these cells for diseases is perhaps best for skin and

cartilage-based injury. This eliminates the risk of developing unwanted extracellular matrix in unwanted tissue spaces, such as the eye. Therefore, delivering MSCs into dense intrinsic collagen tissue that is damaged would provide both extracellular matrix support with a smaller risk in losing organ function. Also, there may be the additional therapeutic benefit from MSCs adopting pericyte-like vascular coverage for damaged vessels and immunomodulation to induce an anti-inflammatory environment.

Concluding Remarks

DR and other ocular diseases are expected to continue impacting the vision of millions of individuals around the world, and a MSC-based therapy represents an opportunity to regenerate healthy tissue in a systematic fashion. Regardless of the thousands of publications on MSCs, the work around MSC therapy is still nascent, as there are still elements of MSC behavior that are still unknown. As with the recent injections of the stromal vascular cells and "adipose-derived stem cells" into patients, it is imperative that the scientific community takes the initiative to not only establish scientific rigor and innovation, but also establish safety around any element of MSC therapy. There is still much to learn about this cell population and using their biological activity for therapeutic use is still promising. In closing, there needs to be a synchronized effort from stem cell biologists, statisticians, geneticists, engineers, physicians, and other healthcare professionals to generate fruitful outcomes in MSC basic science research and clinical studies.

REFERENCES

1. Rowley WR, Bezold C, Arikan Y, Byrne E, Krohe S. Diabetes 2030: Insights from Yesterday, Today, and Future Trends. *Popul Health Manag*. 2017;20(1):6-12. doi:10.1089/pop.2015.0181
2. Cefalu WT, Petersen MP, Ratner RE. The Alarming and Rising Costs of Diabetes and Prediabetes: A Call for Action! *Diabetes Care*. 2014;37(12):3137-3138. doi:10.2337/dc14-2329
3. Guariguata L, Whiting DR, Hambleton I, Beagley J, Linnenkamp U, Shaw JE. Global estimates of diabetes prevalence for 2013 and projections for 2035. *Diabetes Res Clin Pract*. 2014;103(2):137-149. doi:10.1016/j.diabres.2013.11.002
4. Bommer C, Sagalova V, Heesemann E, et al. Global economic burden of diabetes in adults: Projections from 2015 to 2030. *Diabetes Care*. 2018;41(5):963-970. doi:10.2337/dc17-1962/-/DC1
5. Singh R, Kishore L, Kaur N. Diabetic peripheral neuropathy: Current perspective and future directions. *Pharmacol Res*. 2014;80:21-35. doi:10.1016/j.phrs.2013.12.005
6. Fowler MJ. Microvascular and Macrovascular Complications of Diabetes. 2014;26(2):77-82. doi:10.2337/diaclin.26.2.77
7. Sabanayagam C, Banu R, Chee ML, et al. Incidence and progression of diabetic retinopathy: a systematic review. *Lancet Diabetes Endocrinol*. 2018;8587(18):1-10. doi:10.1016/S2213-8587(18)30128-1
8. Flaxman SR, Bourne RRA, Resnikoff S, et al. Global causes of blindness and distance vision impairment 1990–2020: a systematic review and meta-analysis. *Lancet Glob Heal*. 2017;5(12):e1221-e1234. doi:10.1016/S2214-109X(17)30393-5
9. Lee R, Wong TY, Sabanayagam C. Epidemiology of diabetic retinopathy, diabetic macular edema and related vision loss. *Eye Vis*. 2015;2(1):17. doi:10.1186/s40662-015-0026-2
10. Yau JWY, Rogers SL, Kawasaki R, et al. Global prevalence and major risk factors of diabetic retinopathy. *Diabetes Care*. 2012;35:556-564. doi:10.2337/dc11-1909
11. Ting DSW, Cheung GCM, Wong TY. Diabetic retinopathy: global prevalence, major risk factors, screening practices and public health challenges: a review. *Clin Experiment Ophthalmol*. 2015;(July 2015):n/a-n/a. doi:10.1111/ceo.12696
12. Giacco F. Oxidative stress and diabetic complications. *Circ Res*. 2011;107(9):1058-1070. doi:10.1161/CIRCRESAHA.110.223545.Oxidative
13. Hammes H-P, Feng Y, Pfister F, Brownlee M. Diabetic Retinopathy: Targeting Vasoregression. *Diabetes*. 2011;60(1):9-16. doi:10.2337/db10-0454
14. Tarr J, Tarr JM, Kaul K, Chopra M, Kohner EM, Chibber R. Pathophysiology of Diabetic Retinopathy Pathophysiology of Diabetic Retinopathy. 2013;2013(January). doi:10.1155/2013/343560
15. Das A. Diabetic retinopathy: Battling the global epidemic. *Investig Ophthalmol Vis Sci*. 2016;57(15):6669-6682. doi:10.1167/iovs.16-21031
16. Brownlee M. The pathobiology of diabetic complications: A unifying mechanism. *Diabetes*. 2005;54(6):1615-1625. doi:10.2337/diabetes.54.6.1615
17. Aiello LM. Perspectives on diabetic retinopathy. *Am J Ophthalmol*. 2003;136(1):122-135. doi:10.1016/S0002-9394(03)00219-8
18. Diabetes Control and Complications Trial Research Group, Nathan DM, Genuth S, et al.

The effect of intensive treatment of diabetes on the development and progression of long-term complications in insulin-dependent diabetes mellitus. *N Engl J Med*. 1993;329(14):977-986. doi:10.1056/NEJM199309303291401
19. Kohner EM, Aldington SJ, Stratton IM, et al. United Kingdom Prospective Diabetes Study, 30: diabetic retinopathy at diagnosis of non-insulin-dependent diabetes mellitus and associated risk factors. *Arch Ophthalmol (Chicago, Ill 1960)*. 1998;116(3):297-303. http://www.ncbi.nlm.nih.gov/pubmed/9514482.
20. Klein R, Klein BE, Moss SE, Davis MD, DeMets DL. The Wisconsin epidemiologic study of diabetic retinopathy. III. Prevalence and risk of diabetic retinopathy when age at diagnosis is 30 or more years. *Arch Ophthalmol (Chicago, Ill 1960)*. 1984;102(4):527-532. http://www.ncbi.nlm.nih.gov/pubmed/6367725.
21. Stratton IM, Adler AI, Neil HA, et al. Association of glycaemia with macrovascular and microvascular complications of type 2 diabetes (UKPDS 35): prospective observational study. *BMJ*. 2000;321(7258):405-412. http://www.ncbi.nlm.nih.gov/pubmed/10938048.
22. Klein R, Klein BE, Moss SE, Davis MD, DeMets DL. The Wisconsin epidemiologic study of diabetic retinopathy. IV. Diabetic macular edema. *Ophthalmology*. 1984;91(12):1464-1474. http://www.ncbi.nlm.nih.gov/pubmed/6521986.
23. Klein R, Klein BE, Moss SE, Davis MD, DeMets DL. The Wisconsin epidemiologic study of diabetic retinopathy. II. Prevalence and risk of diabetic retinopathy when age at diagnosis is less than 30 years. *Arch Ophthalmol (Chicago, Ill 1960)*. 1984;102(4):520-526. http://www.ncbi.nlm.nih.gov/pubmed/6367724.
24. Zhang J, Ma J, Zhou N, Zhang B, An J. Insulin use and risk of diabetic macular edema in diabetes mellitus: a systemic review and meta-analysis of observational studies. *Med Sci Monit*. 2015;21:929-936. doi:10.12659/MSM.892056
25. Early worsening of diabetic retinopathy in the Diabetes Control and Complications Trial. *Arch Ophthalmol (Chicago, Ill 1960)*. 1998;116(7):874-886. http://www.ncbi.nlm.nih.gov/pubmed/9682700.
26. Hu L, Li D-H. Relationship between modified homeostasis model assessment/correlative serum factors and diabetic retinopathy among type 2 diabetics with insulin therapy in Guangzhou, China. *Int J Ophthalmol*. 2014;7(3):463-468. doi:10.3980/j.issn.2222-3959.2014.03.14
27. Jingi AM, Noubiap JJN, Essouma M, et al. Association of insulin treatment versus oral hypoglycaemic agents with diabetic retinopathy and its severity in type 2 diabetes patients in Cameroon, sub-Saharan Africa. *Ann Transl Med*. 2016;4(20):395. doi:10.21037/atm.2016.08.42
28. Kuo JZ, Guo X, Klein R, et al. Association of fasting insulin and C peptide with diabetic retinopathy in Latinos with type 2 diabetes. *BMJ open diabetes Res care*. 2014;2(1):e000027. doi:10.1136/bmjdrc-2014-000027
29. Jingi AM, Tankeu AT, Ateba NA, Noubiap JJ. Mechanism of worsening diabetic retinopathy with rapid lowering of blood glucose: The synergistic hypothesis. *BMC Endocr Disord*. 2017;17(1):1-4. doi:10.1186/s12902-017-0213-3
30. Arnarsson Á, Stefánsson E. Laser treatment and the mechanism of edema reduction in branch retinal vein occlusion. *Investig Ophthalmol Vis Sci*. 2000;41(3):877-879.
31. Ogata N, Tombran-Tink J, Jo N, Mrazek D, Matsumura M. Upregulation of pigment epithelium-derived factor after laser photocoagulation. *Am J Ophthalmol*. 2001;132(3):427-429. http://www.ncbi.nlm.nih.gov/pubmed/11530069.

32. Photocoagulation treatment of proliferative diabetic retinopathy. Clinical application of Diabetic Retinopathy Study (DRS) findings, DRS Report Number 8. The Diabetic Retinopathy Study Research Group. *Ophthalmology*. 1981;88(7):583-600. http://www.ncbi.nlm.nih.gov/pubmed/7196564.
33. Treatment techniques and clinical guidelines for photocoagulation of diabetic macular edema. Early Treatment Diabetic Retinopathy Study Report Number 2. Early Treatment Diabetic Retinopathy Study Research Group. *Ophthalmology*. 1987;94(7):761-774. http://www.ncbi.nlm.nih.gov/pubmed/3658348.
34. Fong DS, Girach A, Boney A. Visual side effects of successful scatter laser photocoagulation surgery for proliferative diabetic retinopathy: a literature review. *Retina*. 2007;27(7):816-824. doi:10.1097/IAE.0b013e318042d32c
35. Boynton GE, Stem MS, Kwark L, Jackson GR, Farsiu S, Gardner TW. Multimodal Characterization of Proliferative Diabetic Retinopathy Reveals Alterations in Outer Retinal Function and Structure. *Ophthalmology*. 2015;122(5):957-967. doi:10.1016/j.ophtha.2014.12.001
36. Heier JS, Korobelnik J-F, Brown DM, et al. Intravitreal Aflibercept for Diabetic Macular Edema: 148-Week Results from the VISTA and VIVID Studies. *Ophthalmology*. 2016;123(11):2376-2385. doi:10.1016/j.ophtha.2016.07.032
37. Diabetic Retinopathy Clinical Research Network, Wells JA, Glassman AR, et al. Aflibercept, bevacizumab, or ranibizumab for diabetic macular edema. *N Engl J Med*. 2015;372(13):1193-1203. doi:10.1056/NEJMoa1414264
38. Sultan MB, Zhou D, Loftus J, Dombi T, Ice KS, Macugen 1013 Study Group. A phase 2/3, multicenter, randomized, double-masked, 2-year trial of pegaptanib sodium for the treatment of diabetic macular edema. *Ophthalmology*. 2011;118(6):1107-1118. doi:10.1016/j.ophtha.2011.02.045
39. Massin P, Bandello F, Garweg JG, et al. Safety and efficacy of ranibizumab in diabetic macular edema (RESOLVE Study): a 12-month, randomized, controlled, double-masked, multicenter phase II study. *Diabetes Care*. 2010;33(11):2399-2405. doi:10.2337/dc10-0493
40. Mitchell P, Bandello F, Schmidt-Erfurth U, et al. The RESTORE study: ranibizumab monotherapy or combined with laser versus laser monotherapy for diabetic macular edema. *Ophthalmology*. 2011;118(4):615-625. doi:10.1016/j.ophtha.2011.01.031
41. Okabe K, Kobayashi S, Yamada T, et al. Neurons limit angiogenesis by titrating VEGF in retina. *Cell*. 2014;159(3):584-596. doi:10.1016/j.cell.2014.09.025
42. Friedenstein AJ. Precursor cells of mechanocytes. *Int Rev Cytol*. 1976;47:327-359. http://www.ncbi.nlm.nih.gov/pubmed/11195.
43. Friedenstein AJ, Chailakhyan RK, Latsinik N V, Panasyuk AF, Keiliss-Borok I V. Stromal cells responsible for transferring the microenvironment of the hemopoietic tissues. Cloning in vitro and retransplantation in vivo. *Transplantation*. 1974;17(4):331-340. http://www.ncbi.nlm.nih.gov/pubmed/4150881.
44. Friedenstein AJ, Chailakhjan RK, Lalykina KS. The development of fibroblast colonies in monolayer cultures of guinea-pig bone marrow and spleen cells. *Cell Tissue Kinet*. 1970;3(4):393-403. http://www.ncbi.nlm.nih.gov/pubmed/5523063.
45. Friedenstein AJ. Osteogenic stem cells in bone marrow. *Heersche JNM, Kanis JA, eds Bone Miner Res Netherlands Elsevier Sci Publ*. 1990:243-272.
46. Caplan AI. Mesenchymal stem cells. *J Orthop Res*. 1991;9(5):641-650.

doi:10.1002/jor.1100090504
47. Dominici M, Le Blanc K, Mueller I, et al. Minimal criteria for defining multipotent mesenchymal stromal cells. The International Society for Cellular Therapy position statement. *Cytotherapy*. 2006;8(4):315-317. doi:10.1080/14653240600855905
48. Ka L, Kong H, Cell S, Shing LK, Surgery O. Concise Review: The Surface Markers and Identity of Human Mesenchymal Stem Cells. *Stem Cells*. 2014;6(32):1408-1419. doi:10.1002/stem.1681
49. Bourin P, Bunnell B a, Casteilla L, et al. NIH Public Access. 2014;15(6):641-648. doi:10.1016/j.jcyt.2013.02.006.Stromal
50. Ullah I, Subbarao RB, Rho GJ. Human mesenchymal stem cells - current trends and future prospective. *Biosci Rep*. 2015;35(2):1-18. doi:10.1042/BSR20150025
51. Beltrami AP, Cesselli D, Bergamin N, et al. Multipotent cells can be generated in vitro from several adult human organs (heart, liver, and bone marrow). *Blood*. 2007;110(9):3438-3446. doi:10.1182/blood-2006-11-055566
52. Crisan M, Chen C-W, Corselli M, Andriolo G, Lazzari L, Péault B. Perivascular Multipotent Progenitor Cells in Human Organs. *Ann N Y Acad Sci*. 2009;1176(1):118-123. doi:10.1111/j.1749-6632.2009.04967.x
53. Zimmerlin L, Donnenberg VS, Rubin JP, Donnenberg AD. Mesenchymal markers on human adipose stem/progenitor cells. *Cytom Part A*. 2013;83A(1):134-140. doi:10.1002/cyto.a.22227
54. Eto H, Ishimine H, Kinoshita K, et al. Characterization of Human Adipose Tissue-Resident Hematopoietic Cell Populations Reveals a Novel Macrophage Subpopulation with CD34 Expression and Mesenchymal Multipotency. *Stem Cells Dev*. 2013;22(6):985-997. doi:10.1089/scd.2012.0442
55. Guimarães-Camboa N, Evans SM. Are Perivascular Adipocyte Progenitors Mural Cells or Adventitial Fibroblasts? *Cell Stem Cell*. 2017;20(5):587-589. doi:10.1016/j.stem.2017.04.010
56. Kramann R, Schneider RK, DiRocco DP, et al. Perivascular Gli1+ Progenitors Are Key Contributors to Injury-Induced Organ Fibrosis. *Cell Stem Cell*. 2014;16(1):51-66. doi:10.1016/j.stem.2014.11.004
57. Murphy MB, Moncivais K, Caplan AI. Mesenchymal stem cells: environmentally responsive therapeutics for regenerative medicine. *Exp Mol Med*. 2013;45(11):e54. doi:10.1038/emm.2013.94
58. Wang Y, Chen X, Cao W, Shi Y. Plasticity of mesenchymal stem cells in immunomodulation: pathological and therapeutic implications. *Nat Immunol*. 2014;15(11):1009-1016. doi:10.1038/ni.3002
59. Connick P, Kolappan M, Crawley C, et al. Autologous mesenchymal stem cells for the treatment of secondary progressive multiple sclerosis: An open-label phase 2a proof-of-concept study. *Lancet Neurol*. 2012;11(2):150-156. doi:10.1016/S1474-4422(11)70305-2
60. Sun L, Akiyama K, Zhang H, et al. Mesenchymal stem cell transplantation reverses multiorgan dysfunction in systemic lupus erythematosus mice and humans. *Stem Cells*. 2009;27(6):1421-1432. doi:10.1002/stem.68
61. Wang D, Zhang H, Liang J, et al. Allogeneic mesenchymal stem cell transplantation in severe and refractory systemic lupus erythematosus: 4 years experience. *Cell Transpl*. 2012;22:2267-2277. doi:ct0877wang [pii]\r10.3727/096368912X658719
62. Wang D, Akiyama K, Zhang H, et al. Double allogenic mesenchymal stem cells

transplantations could not enhance therapeutic effect compared with single transplantation in systemic lupus erythematosus. *Clin Dev Immunol*. 2012;2012. doi:10.1155/2012/273291
63. Jacobs S a, Roobrouck VD, Verfaillie CM, Van Gool SW. Immunological characteristics of human mesenchymal stem cells and multipotent adult progenitor cells. *Immunol Cell Biol*. 2013;91(1):32-39. doi:10.1038/icb.2012.64
64. Spees JL, Lee RH, Gregory CA. Mechanisms of mesenchymal stem/stromal cell function. *Stem Cell Res Ther*. 2016;7(1):125. doi:10.1186/s13287-016-0363-7
65. De Oliveira F. Pericytes in Diabetic Retinopathy. *Br J Ophthalmol*. 1966;50(3):134-144.
66. Vom Hagen F, Feng Y, Hillenbrand A, et al. Early loss of arteriolar smooth muscle cells: More than just a pericyte loss in diabetic retinopathy. *Exp Clin Endocrinol Diabetes*. 2005;113(10):573-576. doi:10.1055/s-2005-872894
67. Hammes H-P, Lin J, Renner O, et al. Pericytes and the Pathogenesis of Diabetic Retinopathy. *Diabetes*. 2002;51(10):3107-3112. doi:10.2337/diabetes.51.10.3107
68. Zeng H, Green WR, Tso MOM. Microglial activation in human diabetic retinopathy. *Arch Ophthalmol (Chicago, Ill 1960)*. 2008;126(2):227-232. doi:10.1001/archophthalmol.2007.65
69. Simpson D a, Murphy GM, Bhaduri T, Gardiner T a, Archer DB, Stitt a W. Expression of the VEGF gene family during retinal vaso-obliteration and hypoxia. *Biochem Biophys Res Commun*. 1999;262(2):333-340. doi:10.1006/bbrc.1999.1201
70. Armulik A, Genové G, Betsholtz C. Pericytes: developmental, physiological, and pathological perspectives, problems, and promises. *Dev Cell*. 2011;21(2):193-215. doi:10.1016/j.devcel.2011.07.001
71. Hofer HR, Tuan RS. Secreted trophic factors of mesenchymal stem cells support neurovascular and musculoskeletal therapies. *Stem Cell Res Ther*. 2016;7(1):1-14. doi:10.1186/s13287-016-0394-0
72. Kim H, Han JW, Lee JY, et al. Diabetic mesenchymal stem cells are ineffective for improving limb ischemia due to their impaired angiogenic capability. *Cell Transplant*. 2015;24(8):1571-1584. doi:10.3727/096368914X682792
73. Xu Y, Meng H, Li C, et al. Umbilical cord-derived mesenchymal stem cells isolated by a novel explantation technique can differentiate into functional endothelial cells and promote revascularization. *Stem Cells Dev*. 2010;19(10):1511-1522. doi:10.1089/scd.2009.0321
74. Bortolotti F, Ukovich L, Razban V, et al. In vivo therapeutic potential of mesenchymal stromal cells depends on the source and the isolation procedure. *Stem Cell Reports*. 2015;4(3):332-339. doi:10.1016/j.stemcr.2015.01.001
75. Mathieu E, Lamirault G, Toquet C, et al. Intramyocardial Delivery of Mesenchymal Stem Cell-Seeded Hydrogel Preserves Cardiac Function and Attenuates Ventricular Remodeling after Myocardial Infarction. Hsieh PC-H, ed. *PLoS One*. 2012;7(12):e51991. doi:10.1371/journal.pone.0051991
76. Miyahara Y, Nagaya N, Kataoka M, et al. Monolayered mesenchymal stem cells repair scarred myocardium after myocardial infarction. *Nat Med*. 2006;12(4):459-465. doi:10.1038/nm1391
77. Nagaya N, Fujii T, Iwase T, et al. Intravenous administration of mesenchymal stem cells improves cardiac function in rats with acute myocardial infarction through angiogenesis and myogenesis. *Am J Physiol Circ Physiol*. 2004;287(6):H2670-H2676.

doi:10.1152/ajpheart.01071.2003
78. Hu X, Wang J, Chen J, et al. Optimal temporal delivery of bone marrow mesenchymal stem cells in rats with myocardial infarction. *Eur J Cardio-Thoracic Surg*. 2007;31(3):438-443. doi:10.1016/j.ejcts.2006.11.057
79. Gnecchi M, Zhang Z, Ni A, Dzau VJ. Paracrine mechanisms in adult stem cell signaling and therapy. *Circ Res*. 2008;103(11):1204-1219. doi:10.1161/CIRCRESAHA.108.176826
80. Rehman J, Traktuev D, Li J, et al. Secretion of Angiogenic and Antiapoptotic Factors by Human Adipose Stromal Cells. *Circulation*. 2004;109(10):1292-1298. doi:10.1161/01.CIR.0000121425.42966.F1
81. Kwon HM, Hur SM, Park KY, et al. Multiple paracrine factors secreted by mesenchymal stem cells contribute to angiogenesis. *Vascul Pharmacol*. 2014;63(1):19-28. doi:10.1016/j.vph.2014.06.004
82. Ejtehadifar M, Shamsasenjan K, Movassaghpour A, et al. The Effect of Hypoxia on Mesenchymal Stem Cell Biology. *Adv Pharm Bull*. 2015;5(2):141-149. doi:10.15171/apb.2015.021
83. Hu X, Yu SP, Fraser JL, et al. Transplantation of hypoxia-preconditioned mesenchymal stem cells improves infarcted heart function via enhanced survival of implanted cells and angiogenesis. *J Thorac Cardiovasc Surg*. 2008;135(4):799-808. doi:10.1016/j.jtcvs.2007.07.071
84. Liu J, Hao H, Xia L, et al. Hypoxia pretreatment of bone marrow mesenchymal stem cells facilitates angiogenesis by improving the function of endothelial cells in diabetic rats with lower ischemia. *PLoS One*. 2015;10(5):e0126715. doi:10.1371/journal.pone.0126715
85. Amos PJ, Mulvey CL, Seaman SA, et al. Hypoxic culture and in vivo inflammatory environments affect the assumption of pericyte characteristics by human adipose and bone marrow progenitor cells. *AJP Cell Physiol*. 2011;301(6):C1378-C1388. doi:10.1152/ajpcell.00460.2010
86. Gong M, Yu B, Wang J, et al. Mesenchymal stem cells release exosomes that transfer miRNAs to endothelial cells and promote angiogenesis. *Oncotarget*. 2017;8(28):45200-45212. doi:10.18632/oncotarget.16778
87. Salomon C, Ryan J, Sobrevia L, et al. Exosomal Signaling during Hypoxia Mediates Microvascular Endothelial Cell Migration and Vasculogenesis. Emanueli C, ed. *PLoS One*. 2013;8(7):e68451. doi:10.1371/journal.pone.0068451
88. Shabbir A, Cox A, Rodriguez-Menocal L, Salgado M, Van Badiavas E. Mesenchymal Stem Cell Exosomes Induce Proliferation and Migration of Normal and Chronic Wound Fibroblasts, and Enhance Angiogenesis In Vitro. *Stem Cells Dev*. 2015;24(14):1635-1647. doi:10.1089/scd.2014.0316
89. Stratman AN, Malotte KM, Mahan RD, Davis MJ, Davis GE. Pericyte recruitment during vasculogenic tube assembly stimulates endothelial basement membrane matrix formation. *Blood*. 2009;114(24):5091-5101. doi:10.1182/blood-2009-05-222364
90. Sorrell JM, Baber MA, Caplan AI. Influence of adult mesenchymal stem cells on in vitro vascular formation. *Tissue Eng Part A*. 2009;15(7):1751-1761. doi:10.1089/ten.tea.2008.0254
91. Au P, Tam J, Fukumura D, Jain RK, Dc W. Bone marrow − derived mesenchymal stem cells facilitate engineering of long-lasting functional vasculature Bone marrow – derived mesenchymal stem cells facilitate engineering of long-lasting functional vasculature. 2013;111(9):4551-4558. doi:10.1182/blood-2007-10-118273

92. Boyd NL, Nunes SS, Jokinen JD, et al. Microvascular mural cell functionality of human embryonic stem cell-derived mesenchymal cells. *Tissue Eng Part A*. 2011;17(11-12):1537-1548. doi:10.1089/ten.TEA.2010.0397
93. Mendel TA, Clabough EBD, Kao DS, et al. Pericytes derived from adipose-derived stem cells protect against retinal vasculopathy. *PLoS One*. 2013;8(5):e65691. doi:10.1371/journal.pone.0065691
94. Park WS, Heo SC, Jeon ES, et al. Functional expression of smooth muscle-specific ion channels in TGF-β1-treated human adipose-derived mesenchymal stem cells. *Am J Physiol - Cell Physiol*. 2013;305(4):C377-C391. doi:10.1152/ajpcell.00404.2012
95. Liu C, Fan Y, Zhou L, et al. Pretreatment of mesenchymal stem cells with angiotensin II enhances paracrine effects, angiogenesis, gap junction formation and therapeutic efficacy for myocardial infarction. *Int J Cardiol*. 2015;188:22-32. doi:10.1016/j.ijcard.2015.03.425
96. Xu X-P, He H-L, Hu S-L, et al. Ang II-AT2R increases mesenchymal stem cell migration by signaling through the FAK and RhoA/Cdc42 pathways in vitro. *Stem Cell Res Ther*. 2017;8(1):164. doi:10.1186/s13287-017-0617-z
97. Kadlubowska J, Malaguarnera L, Waz P, Zorena K. Neurodegeneration and Neuroinflammation in Diabetic Retinopathy: Potential Approaches to Delay Neuronal Loss. *Curr Neuropharmacol*. 2016;14(8):831-839. doi:10.2174/1570159X14666160614095559
98. Lieth E, Barber AJ, Xu B, et al. Glial reactivity and impaired glutamate metabolism in short-term experimental diabetic retinopathy. Penn State Retina Research Group. *Diabetes*. 1998;47(5):815-820. http://www.ncbi.nlm.nih.gov/pubmed/9588455.
99. Mandal LK, Choudhuri S, Dutta D, et al. Oxidative stress-associated neuroretinal dysfunction and nitrosative stress in diabetic retinopathy. *Can J Diabetes*. 2013;37(6):401-407. doi:10.1016/j.jcjd.2013.05.004
100. Huang X-T, Li C, Peng X-P, et al. An excessive increase in glutamate contributes to glucose-toxicity in β-cells via activation of pancreatic NMDA receptors in rodent diabetes. *Sci Rep*. 2017;7:44120. doi:10.1038/srep44120
101. Abu El-Asrar AM, Dralands L, Missotten L, Geboes K. Expression of antiapoptotic and proapoptotic molecules in diabetic retinas. *Eye*. 2007;21(2):238-245. doi:10.1038/sj.eye.6702225
102. Voulgari-Kokota A, Fairless R, Karamita M, et al. Mesenchymal stem cells protect CNS neurons against glutamate excitotoxicity by inhibiting glutamate receptor expression and function. *Exp Neurol*. 2012;236(1):161-170. doi:10.1016/j.expneurol.2012.04.011
103. Hao P, Liang Z, Piao H, et al. Conditioned medium of human adipose-derived mesenchymal stem cells mediates protection in neurons following glutamate excitotoxicity by regulating energy metabolism and GAP-43 expression. *Metab Brain Dis*. 2014;29(1):193-205. doi:10.1007/s11011-014-9490-y
104. Pease ME, Zack DJ, Berlinicke C, et al. Effect of CNTF on retinal ganglion cell survival in experimental glaucoma. *Invest Ophthalmol Vis Sci*. 2009;50(5):2194-2200. doi:10.1167/iovs.08-3013
105. Zhang C-W, Lu Q, You S-W, et al. CNTF and BDNF have similar effects on retinal ganglion cell survival but differential effects on nitric oxide synthase expression soon after optic nerve injury. *Invest Ophthalmol Vis Sci*. 2005;46(4):1497-1503. doi:10.1167/iovs.04-0664
106. Wen R, Tao W, Li Y, Sieving PA. CNTF and retina. *Prog Retin Eye Res*. 2012;31(2):136-

151. doi:10.1016/j.preteyeres.2011.11.005
107. Wang L, Deng Q-Q, Wu X-H, Yu J, Yang X-L, Zhong Y-M. Upregulation of glutamate-aspartate transporter by glial cell line-derived neurotrophic factor ameliorates cell apoptosis in neural retina in streptozotocin-induced diabetic rats. *CNS Neurosci Ther*. 2013;19(12):945-953. doi:10.1111/cns.12150
108. Boss JD, Singh PK, Pandya HK, et al. Assessment of Neurotrophins and Inflammatory Mediators in Vitreous of Patients With Diabetic Retinopathy. *Invest Ophthalmol Vis Sci*. 2017;58(12):5594-5603. doi:10.1167/iovs.17-21973
109. Mysona BA, Shanab AY, Elshaer SL, El-Remessy AB. Nerve growth factor in diabetic retinopathy: beyond neurons. *Expert Rev Ophthalmol*. 2014;9(2):99-107. doi:10.1586/17469899.2014.903157
110. Guo Z-Y, Sun X, Xu X-L, Zhao Q, Peng J, Wang Y. Human umbilical cord mesenchymal stem cells promote peripheral nerve repair via paracrine mechanisms. *Neural Regen Res*. 2015;10(4):651-658. doi:10.4103/1673-5374.155442
111. Hsieh JY, Wang HW, Chang SJ, et al. Mesenchymal Stem Cells from Human Umbilical Cord Express Preferentially Secreted Factors Related to Neuroprotection, Neurogenesis, and Angiogenesis. *PLoS One*. 2013;8(8):1-11. doi:10.1371/journal.pone.0072604
112. Yu S, Tanabe T, Dezawa M, Ishikawa H, Yoshimura N. Effects of bone marrow stromal cell injection in an experimental glaucoma model. *Biochem Biophys Res Commun*. 2006;344(4):1071-1079. doi:10.1016/j.bbrc.2006.03.231
113. Johnson T V., Bull ND, Hunt DP, Marina N, Tomarev SI, Martin KR. Neuroprotective effects of intravitreal mesenchymal stem cell transplantation in experimental glaucoma. *Investig Ophthalmol Vis Sci*. 2010;51(4):2051-2059. doi:10.1167/iovs.09-4509
114. Mesentier-Louro LA, Zaverucha-do-Valle C, da Silva-Junior AJ, et al. Distribution of mesenchymal stem cells and effects on neuronal survival and axon regeneration after optic nerve crush and cell therapy. Câmara NOS, ed. *PLoS One*. 2014;9(10):e110722. doi:10.1371/journal.pone.0110722
115. Mead B, Logan A, Berry M, Leadbeater W, Scheven BA. Intravitreally Transplanted Dental Pulp Stem Cells Promote Neuroprotection and Axon Regeneration of Retinal Ganglion Cells After Optic Nerve Injury. *Investig Opthalmology Vis Sci*. 2013;54(12):7544. doi:10.1167/iovs.13-13045
116. Mead B, Logan A, Berry M, Leadbeater W, Scheven BA. Dental pulp stem cells, a paracrine-mediated therapy for the retina. *Neural Regen Res*. 2014;9(6):577-578. doi:10.4103/1673-5374.130089
117. Wang W, Lo ACY. Diabetic retinopathy: Pathophysiology and treatments. *Int J Mol Sci*. 2018;19(6). doi:10.3390/ijms19061816
118. Zhang W, Liu H, Al-Shabrawey M, Caldwell RW, Caldwell RB. Inflammation and diabetic retinal microvascular complications. *J Cardiovasc Dis Res*. 2011;2(2):96-103. doi:10.4103/0975-3583.83035
119. Joussen A. Aspirin prevents early diabetic changes in the retina through inhibition of TNF-a. 2002.
120. Demircan N, Safran BG, Soylu M, Ozcan a a, Sizmaz S. Determination of vitreous interleukin-1 (IL-1) and tumour necrosis factor (TNF) levels in proliferative diabetic retinopathy. *Eye (Lond)*. 2006;20(12):1366-1369. doi:10.1038/sj.eye.6702138
121. Limb GA, Chignell AH, Green W, LeRoy F, Dumonde DC. Distribution of TNF alpha and its reactive vascular adhesion molecules in fibrovascular membranes of proliferative

diabetic retinopathy. *BrJOphthalmol*. 1996;80(0007-1161 (Print)):168-173.
122. Vincent JA, Mohr S. Inhibition of caspase-1/interleukin-1?? signaling prevents degeneration of retinal capillaries in diabetes and galactosemia. *Diabetes*. 2007;56(1):224-230. doi:10.2337/db06-0427
123. Kowluru RA, Odenbach S. Role of interleukin-1β in the development of retinopathy in rats: Effect of antioxidants. *Investig Ophthalmol Vis Sci*. 2004;45(11):4161-4166. doi:10.1167/iovs.04-0633
124. MURUGESWARI P, SHUKLA D, RAJENDRAN A, KIM R, NAMPERUMALSAMY P, MUTHUKKARUPPAN V. Proinflammatory Cytokines and Angiogenic and Anti-Angiogenic Factors in Vitreous of Patients With Proliferative Diabetic Retinopathy and Eales' Disease. *Retina*. 2008;28(6):817-824. doi:10.1097/IAE.0b013e31816576d5
125. Maier R, Weger M, Haller-Schober E-M, et al. Multiplex bead analysis of vitreous and serum concentrations of inflammatory and proangiogenic factors in diabetic patients. *Mol Vis*. 2008;14(December 2007):637-643. http://www.pubmedcentral.nih.gov/articlerender.fcgi?artid=2276180&tool=pmcentrez&rendertype=abstract.
126. Mocan MC, Kadayifcilar S, Eldem B. Interleukin-6 in diabetic eyes—Mocan et al Elevated intravitreal interleukin-6 levels in patients with proliferative diabetic retinopathy. *Can J Ophthalmol*. 2006;41(JANUARY):747-752. doi:10.3129/i06-070
127. Funatsu H, Yamashita H, Ikeda T, Mimura T, Eguchi S, Hori S. Vitreous levels of interleukin-6 and vascular endothelial growth factor are related to diabetic macular edema. *Ophthalmology*. 2003;110(9):1690-1696. doi:10.1016/S0161-6420(03)00568-2
128. Meleth AD, Agrón E, Chan CC, et al. Serum inflammatory markers in diabetic retinopathy. *Investig Ophthalmol Vis Sci*. 2005;46(11):4295-4301. doi:10.1167/iovs.04-1057
129. Adamiec-Mroczek J, Oficjalska-Młyńczak J. Assessment of selected adhesion molecule and proinflammatory cytokine levels in the vitreous body of patients with type 2 diabetes - Role of the inflammatory-immune process in the pathogenesis of proliferative diabetic retinopathy. *Graefe's Arch Clin Exp Ophthalmol*. 2008;246(12):1665-1670. doi:10.1007/s00417-008-0868-6
130. Aveleira A, Lin C, Abcouwer SF, Ambro F, Antonetti DA. TNF- ⎵ Signals Through PKC /NF- B to Alter the Tight Junction Complex and Increase Retinal Endothelial Cell Permeability. *Diabetes*. 2010;59(November):2872-2882. doi:10.2337/db09-1606.
131. Joussen AM, Murata T, Tsujikawa A, Kirchhof B, Bursell SE, Adamis AP. Leukocyte-mediated endothelial cell injury and death in the diabetic retina. *Am J Pathol*. 2001;158(1):147-152. doi:10.1016/S0002-9440(10)63952-1
132. Joussen AM, Poulaki V, Mitsiades N, Cai W, Adamis AP, Aiello LP. Diabetic leukocytes mediate vascular endothelial cell apoptosis via a Fas – Fas-L mediated pathway. 2002.
133. Rasmusson I, Ringdén O, Sundberg B, Le Blanc K. Mesenchymal stem cells inhibit the formation of cytotoxic T lymphocytes, but not activated cytotoxic T lymphocytes or natural killer cells. *Transplantation*. 2003;76(8):1208-1213. doi:10.1097/01.TP.0000082540.43730.80
134. Ren G, Zhang L, Zhao X, et al. Mesenchymal stem cell-mediated immunosuppression occurs via concerted action of chemokines and nitric oxide. *Cell Stem Cell*. 2008;2(2):141-150. doi:10.1016/j.stem.2007.11.014
135. Krampera M, Cosmi L, Angeli R, et al. Role for interferon-gamma in the

immunomodulatory activity of human bone marrow mesenchymal stem cells. *Stem Cells*. 2006;24(2):386-398. doi:10.1634/stemcells.2005-0008
136. Ryan JM, Barry F, Murphy JM, Mahon BP. Interferon-gamma does not break, but promotes the immunosuppressive capacity of adult human mesenchymal stem cells. *Clin Exp Immunol*. 2007;149(2):353-363. doi:10.1111/j.1365-2249.2007.03422.x
137. DelaRosa O, Lombardo E, Beraza A, et al. Requirement of IFN-gamma-mediated indoleamine 2,3-dioxygenase expression in the modulation of lymphocyte proliferation by human adipose-derived stem cells. *Tissue Eng Part A*. 2009;15(10):2795-2806. doi:10.1089/ten.TEA.2008.0630
138. Groh ME, Maitra B, Szekely E, Koç ON. Human mesenchymal stem cells require monocyte-mediated activation to suppress alloreactive T cells. *Exp Hematol*. 2005;33(8):928-934. doi:10.1016/j.exphem.2005.05.002
139. Cuerquis J, Romieu-Mourez R, François M, et al. Human mesenchymal stromal cells transiently increase cytokine production by activated T cells before suppressing T-cell proliferation: effect of interferon-γ and tumor necrosis factor-α stimulation. *Cytotherapy*. 2014;16(2):191-202. doi:10.1016/j.jcyt.2013.11.008
140. Aggarwal S, Pittenger MF. Human mesenchymal stem cells modulate allogeneic immune cell responses. *Transplantation*. 2009;105(4):1815-1822. doi:10.1182/blood-2004-04-1559.Supported
141. Cao YL, Zhang FQ, Hao FQ. Th1/Th2 cytokine expression in diabetic retinopathy. *Genet Mol Res*. 2016;15(3). doi:10.4238/gmr.15037311
142. Karlstetter M, Scholz R, Rutar M, Wong WT, Provis JM, Langmann T. Retinal microglia: just bystander or target for therapy? *Prog Retin Eye Res*. 2015;45:30-57. doi:10.1016/j.preteyeres.2014.11.004
143. Xu C, Fu F, Li X, Zhang S. Mesenchymal stem cells maintain the microenvironment of central nervous system by regulating the polarization of macrophages/microglia after traumatic brain injury. *Int J Neurosci*. 2017;127(12):1124-1135. doi:10.1080/00207454.2017.1325884
144. Hegyi B, Környei Z, Ferenczi S, et al. Regulation of mouse microglia activation and effector functions by bone marrow-derived mesenchymal stem cells. *Stem Cells Dev*. 2014;23(21):2600-2612. doi:10.1089/scd.2014.0088
145. Liu Y, Zhang R, Yan K, et al. Mesenchymal stem cells inhibit lipopolysaccharide-induced inflammatory responses of BV2 microglial cells through TSG-6. *J Neuroinflammation*. 2014;11:135. doi:10.1186/1742-2094-11-135
146. Luu NT, Mcgettrick HM, Buckley CD, et al. Crosstalk between mesenchymal stem cells and endothelial cells leads to downregulation of cytokine-induced leukocyte recruitment. *Stem Cells*. 2013;31(12):2690-2702. doi:10.1002/stem.1511
147. Zhang L, Zheng H, Shao H, et al. Long-term therapeutic effects of mesenchymal stem cells compared to dexamethasone on recurrent experimental autoimmune uveitis of rats. *Investig Ophthalmol Vis Sci*. 2014;55(9):5561-5571. doi:10.1167/iovs.14-14788
148. Oh JY, Kim TW, Jeong HJ, et al. Intraperitoneal infusion of mesenchymal stem/stromal cells prevents experimental autoimmune uveitis in mice. *Mediators Inflamm*. 2014;2014. doi:10.1155/2014/624640
149. Ko JH, Lee HJ, Jeong HJ, et al. Mesenchymal stem/stromal cells precondition lung monocytes/macrophages to produce tolerance against allo- and autoimmunity in the eye. *Proc Natl Acad Sci*. 2016;113(1):158-163. doi:10.1073/pnas.1522905113

150. Davatchi F, Nikbin B, Shams H, Sadeghi Abdollahi B, Mohyeddin M, Shahram F. Mesenchymal stem cell therapy unable to rescue the vision from advanced Behcet's disease retinal vasculitis: Report of three patients. *Int J Rheum Dis*. 2013;16(2):139-147. doi:10.1111/1756-185X.12068
151. Lecaudé S, Wolf-schnurrbusch UEK, Abdullahi H, Enzmann V. Bone marrow-derived stem cells differentiate into retinal pigment epithelium-like cells in vitro but are not able to repair retinal degeneration in vivo. *Stem Cell Transl Investig*. 2015:1-10. doi:10.14800/scti.1017
152. Machalińska A, Kłos P, Baumert B, et al. Stem Cells are mobilized from the bone marrow into the peripheral circulation in response to retinal pigment epithelium damage--a pathophysiological attempt to induce endogenous regeneration. *Curr Eye Res*. 2011;36(7):663-672. doi:10.3109/02713683.2011.576796
153. Gong L, Wu Q, Song B, Lu B, Zhang Y. Differentiation of rat mesenchymal stem cells transplanted into the subretinal space of sodium iodate-injected rats. *Clin Exp Ophthalmol*. 2008;36(7):666-671. doi:10.1111/j.1442-9071.2008.01857.x
154. Duan P, Xu H, Zeng Y, Wang Y, Yin ZQ. Human bone marrow stromal cells can differentiate to a retinal pigment epithelial phenotype when co-cultured with pig retinal pigment epithelium using a transwell system. *Cell Physiol Biochem*. 2013;31(4-5):601-613. doi:10.1159/000350080
155. Vossmerbaeumer U, Ohnesorge S, Kuehl S, et al. Retinal pigment epithelial phenotype induced in human adipose tissue-derived mesenchymal stromal cells. *Cytotherapy*. 2009;11(2):177-188. doi:10.1080/14653240802714819
156. Huang C, Zhang J, Ao M, et al. Combination of retinal pigment epithelium cell-conditioned medium and photoreceptor outer segments stimulate mesenchymal stem cell differentiation toward a functional retinal pigment epithelium cell phenotype. *J Cell Biochem*. 2012;113(2):590-598. doi:10.1002/jcb.23383
157. Li Y, Atmaca-Sonmez P, Schanie CL, Ildstad ST, Kaplan HJ, Enzmann V. Endogenous bone marrow-derived cells express retinal pigment epithelium cell markers and migrate to focal areas of RPE damage. *Investig Ophthalmol Vis Sci*. 2007;48(9):4321-4327. doi:10.1167/iovs.06-1015
158. Harris JR, Brown GAJ, Jorgensen M, et al. Bone marrow-derived cells home to and regenerate retinal pigment epithelium after injury. *Investig Ophthalmol Vis Sci*. 2006;47(5):2108-2113. doi:10.1167/iovs.05-0928
159. Arnhold S, Absenger Y, Klein H, Addicks K, Schraermeyer U. Transplantation of bone marrow-derived mesenchymal stem cells rescue photoreceptor cells in the dystrophic retina of the rhodopsin knockout mouse. *Graefe's Arch Clin Exp Ophthalmol*. 2007;245(3):414-422. doi:10.1007/s00417-006-0382-7
160. Castanheira P, Torquetti L, Nehemy MB, Goes AM. Retinal incorporation and differentiation of mesenchymal stem cells intravitreally injected in the injured retina of rats. *Arq Bras Oftalmol*. 2008;71(5):644-650. doi:10.1590/S0004-27492008000500007
161. Chiou SH, Kao CL, Peng CH, et al. A novel in vitro retinal differentiation model by co-culturing adult human bone marrow stem cells with retinal pigmented epithelium cells. *Biochem Biophys Res Commun*. 2005;326(3):578-585. doi:10.1016/j.bbrc.2004.11.061
162. Nadri S, Yazdani S, Arefian E, et al. Mesenchymal stem cells from trabecular meshwork become photoreceptor-like cells on amniotic membrane. *Neurosci Lett*. 2013;541:43-48. doi:10.1016/j.neulet.2012.12.055

163. Kicic A, Shen W, Wilson AS, Constable IJ, Robertson T, Rakoczy PE. Differentiation of Marrow Stromal Cells into Photoreceptors in the Rat Eye. 2003;23(21):7742-7749.
164. Nadri S, Kazemi B, Eeslaminejad MB, Yazdani S, Soleimani M. High yield of cells committed to the photoreceptor-like cells from conjunctiva mesenchymal stem cells on nanofibrous scaffolds. *Mol Biol Rep*. 2013;40(6):3883-3890. doi:10.1007/s11033-012-2360-y
165. Oswald J, Boxberger S, Jørgensen B, et al. Mesenchymal stem cells can be differentiated into endothelial cells in vitro. *Stem Cells*. 2004;22(3):377-384. doi:10.1634/stemcells.22-3-377
166. Janeczek Portalska K, Leferink A, Groen N, et al. Endothelial Differentiation of Mesenchymal Stromal Cells. *PLoS One*. 2012;7(10). doi:10.1371/journal.pone.0046842
167. Silva G V., Litovsky S, Assad JAR, et al. Mesenchymal stem cells differentiate into an endothelial phenotype, enhance vascular density, and improve heart function in a canine chronic ischemia model. *Circulation*. 2005;111(2):150-156. doi:10.1161/01.CIR.0000151812.86142.45
168. Liu JW, Dunoyer-Geindre S, Serre-Beinier V, et al. Characterization of endothelial-like cells derived from human mesenchymal stem cells. *J Thromb Haemost*. 2007;5(4):826-834. doi:10.1111/j.1538-7836.2007.02381.x
169. Dong J, Gu Y, Li C, et al. Response of mesenchymal stem cells to shear stress in tissue-engineered vascular grafts. *Acta Pharmacol Sin*. 2009;30(5):530-536. doi:10.1038/aps.2009.40
170. Yue W-M, Liu W, Bi Y-W, et al. Mesenchymal stem cells differentiate into an endothelial phenotype, reduce neointimal formation, and enhance endothelial function in a rat vein grafting model. *Stem Cells Dev*. 2008;17(4):785-793. doi:10.1089/scd.2007.0243
171. Bahat-Stroomza M, Barhum Y, Levy YS, et al. Induction of adult human bone marrow mesenchymal stromal cells into functional astrocyte-like cells: potential for restorative treatment in Parkinson's disease. *J Mol Neurosci*. 2009;39(1-2):199-210. doi:10.1007/s12031-008-9166-3
172. Lim JY, Park SI, Kim SM, et al. Neural differentiation of brain-derived neurotrophic factor-expressing human umbilical cord blood-derived mesenchymal stem cells in culture via TrkB-mediated ERK and ??-catenin phosphorylation and following transplantation into the developing brain. *Cell Transplant*. 2011;20(11-12):1855-1866. doi:10.3727/096368910X557236
173. Kopen GC, Prockop DJ, Phinney DG. Marrow stromal cells migrate throughout forebrain and cerebellum, and they differentiate into astrocytes after injection into neonatal mouse brains. *Proc Natl Acad Sci U S A*. 1999;96(19):10711-10716. doi:10.1073/pnas.96.19.10711
174. Sanchez-Ramos J, Song S, Cardozo-Pelaez F, et al. Adult bone marrow stromal cells differentiate into neural cells in vitro. *Exp Neurol*. 2000;164(2):247-256. doi:10.1006/exnr.2000.7389
175. Eglitis MA, Dawson D, Park KW, Mouradian MM. Targeting of marrow-derived astrocytes to the ischemic brain. *Neuroreport*. 1999;10(6):1289-1292. papers3://publication/uuid/A16CE43B-3CF8-4FCB-AD83-FF3E00D9EB25.
176. Portmann-Lanz CB, Schoeberlein A, Portmann R, et al. Turning placenta into brain: placental mesenchymal stem cells differentiate into neurons and oligodendrocytes. *Am J Obstet Gynecol*. 2010;202(3):294.e1-294.e11. doi:10.1016/j.ajog.2009.10.893

177. Jo DH, Cho CS, Kim JH, Jun HO, Kim JH. Animal models of diabetic retinopathy: doors to investigate pathogenesis and potential therapeutics. *J Biomed Sci*. 2013;20(1):38. doi:10.1186/1423-0127-20-38
178. Barber AJ, Antonetti DA, Kern TS, et al. The Ins2Akita mouse as a model of early retinal complications in diabetes. *Investig Ophthalmol Vis Sci*. 2005;46(6):2210-2218. doi:10.1167/iovs.04-1340
179. Gastinger MJ, Singh RSJ, Barber AJ. Loss of cholinergic and dopaminergic amacrine cells in streptozotocin- diabetic rat and Ins2Akita-diabetic mouse retinas. *Investig Ophthalmol Vis Sci*. 2006;47(7):3143-3150. doi:10.1167/iovs.05-1376
180. Han Z, Guo J, Conley SM, Naash MI. Retinal angiogenesis in the Ins2Akita mouse model of diabetic retinopathy. *Investig Ophthalmol Vis Sci*. 2013;54(1):574-584. doi:10.1167/iovs.12-10959
181. Martin PM, Roon P, Van Ells TK, Ganapathy V, Smith SB. Death of retinal neurons in streptozotocin-induced diabetic mice. *Invest Ophthalmol Vis Sci*. 2004;45(9):3330-3336. doi:10.1167/iovs.04-0247
182. Articles O. Basement Thickening Capillaries Layers. *Vascular*. 1995:1120-1123.
183. Ganda OP, Rossini AA, Like AA. Studies on streptozotocin diabetes. *Diabetes*. 1976;25(7):595-603. doi:10.2337/diabetes.25.7.595
184. Kim J-H, Kim JH, Yu YS, Min BH, Kim K-W. Protective effect of clusterin on blood-retinal barrier breakdown in diabetic retinopathy. *Invest Ophthalmol Vis Sci*. 2010;51(3):1659-1665. doi:10.1167/iovs.09-3615
185. Rakoczy EP, Ali Rahman IS, Binz N, et al. Characterization of a mouse model of hyperglycemia and retinal neovascularization. *Am J Pathol*. 2010;177(5):2659-2670. doi:10.2353/ajpath.2010.090883
186. Wisniewska-Kruk J, Klaassen I, Vogels IMC, et al. Molecular analysis of blood-retinal barrier loss in the Akimba mouse, a model of advanced diabetic retinopathy. *Exp Eye Res*. 2014;122:123-131. doi:10.1016/j.exer.2014.03.005
187. Tee LBG, Penrose M a, O'Shea JE, Lai C-M, Rakoczy EP, Dunlop S a. VEGF-induced choroidal damage in a murine model of retinal neovascularisation. *Br J Ophthalmol*. 2008;92(6):832-838. doi:10.1136/bjo.2007.130898
188. Binz N, Ali Rahman IS, Chinnery HR, et al. Effect of vascular endothelial growth factor upregulation on retinal gene expression in the Kimba mouse. *Clin Experiment Ophthalmol*. 2013;41(3):251-262. doi:10.1111/j.1442-9071.2012.02845.x
189. Rajashekhar G, Ramadan A, Abburi C, et al. Regenerative therapeutic potential of adipose stromal cells in early stage diabetic retinopathy. *PLoS One*. 2014;9(1). doi:10.1371/journal.pone.0084671
190. Yang Z, Li K, Yan X, Dong F, Zhao C. Amelioration of diabetic retinopathy by engrafted human adipose-derived mesenchymal stem cells in streptozotocin diabetic rats. *Graefe's Arch Clin Exp Ophthalmol*. 2010;248(10):1415-1422. doi:10.1007/s00417-010-1384-z
191. Cronk SM, Kelly-Goss MR, Ray HC, et al. Adipose-Derived Stem Cells From Diabetic Mice Show Impaired Vascular Stabilization in a Murine Model of Diabetic Retinopathy. *Stem Cells Transl Med*. 2015;4(5):459-467. doi:10.5966/sctm.2014-0108
192. Ezquer M, Urzua CA, Montecino S, Leal K, Conget P, Ezquer F. Intravitreal administration of multipotent mesenchymal stromal cells triggers a cytoprotective microenvironment in the retina of diabetic mice. *Stem Cell Res Ther*. 2016;7(1):42. doi:10.1186/s13287-016-0299-y

193. Cao W, Li F, Steinberg RH, Lavail MM. Development of normal and injury-induced gene expression of aFGF, bFGF, CNTF, BDNF, GFAP and IGF-I in the rat retina. *Exp Eye Res*. 2001;72(5):591-604. doi:10.1006/exer.2001.0990
194. Sapieha PS, Peltier M, Rendahl KG, Manning WC, Di Polo A. Fibroblast growth factor-2 gene delivery stimulates axon growth by adult retinal ganglion cells after acute optic nerve injury. *Mol Cell Neurosci*. 2003;24(3):656-672. doi:10.1016/S1044-7431(03)00228-8
195. Johnson T V., Bull ND, Martin KR. Identification of barriers to retinal engraftment of transplanted stem cells. *Investig Ophthalmol Vis Sci*. 2010;51(2):960-970. doi:10.1167/iovs.09-3884
196. Crigler L, Robey RC, Asawachaicharn A, Gaupp D, Phinney DG. Human mesenchymal stem cell subpopulations express a variety of neuro-regulatory molecules and promote neuronal cell survival and neuritogenesis. *Exp Neurol*. 2006;198(1):54-64. doi:10.1016/j.expneurol.2005.10.029
197. Emre E, Yüksel N, Duruksu G, et al. Neuroprotective effects of intravitreally transplanted adipose tissue and bone marrow–derived mesenchymal stem cells in an experimental ocular hypertension model. *Cytotherapy*. 2015;17(5):543-559. doi:10.1016/j.jcyt.2014.12.005
198. Zhang X, Ren X, Li G, et al. Mesenchymal stem cells ameliorate experimental autoimmune uveoretinitis by comprehensive modulation of systemic autoimmunity. *Investig Ophthalmol Vis Sci*. 2011;52(6):3143-3152. doi:10.1167/iovs.10-6334
199. Li G, Yuan L, Ren X, et al. The effect of mesenchymal stem cells on dynamic changes of T cell subsets in experimental autoimmune uveoretinitis. *Clin Exp Immunol*. 2013;173(1):28-37. doi:10.1111/cei.12080
200. Zhang L, Coulson-Thomas VJ, Ferreira TG, Kao WWY. Mesenchymal stem cells for treating ocular surface diseases. *BMC Ophthalmol*. 2015;15 Suppl 1:155. doi:10.1186/s12886-015-0138-4
201. Liu H, Zhang J, Liu C-Y, et al. Cell therapy of congenital corneal diseases with umbilical mesenchymal stem cells: lumican null mice. *PLoS One*. 2010;5(5):e10707. doi:10.1371/journal.pone.0010707
202. Coulson-Thomas VJ, Caterson B, Kao WW-Y. Transplantation of human umbilical mesenchymal stem cells cures the corneal defects of mucopolysaccharidosis VII mice. *Stem Cells*. 2013;31(10):2116-2126. doi:10.1002/stem.1481
203. Gu S, Xing C, Han J, Tso MOM, Hong J. Differentiation of rabbit bone marrow mesenchymal stem cells into corneal epithelial cells in vivo and ex vivo. *Mol Vis*. 2009;15:99-107. http://www.ncbi.nlm.nih.gov/pubmed/19156227.
204. Jiang T-S, Cai L, Ji W-Y, et al. Reconstruction of the corneal epithelium with induced marrow mesenchymal stem cells in rats. *Mol Vis*. 2010;16:1304-1316. http://www.ncbi.nlm.nih.gov/pubmed/20664793.
205. Ma Y, Xu Y, Xiao Z, et al. Reconstruction of chemically burned rat corneal surface by bone marrow-derived human mesenchymal stem cells. *Stem Cells*. 2006;24(2):315-321. doi:10.1634/stemcells.2005-0046
206. Oh JY, Kim MK, Shin MS, et al. The anti-inflammatory and anti-angiogenic role of mesenchymal stem cells in corneal wound healing following chemical injury. *Stem Cells*. 2008;26(4):1047-1055. doi:10.1634/stemcells.2007-0737
207. Uccelli A, Prockop DJ. Why should mesenchymal stem cells (MSCs) cure autoimmune diseases? *Curr Opin Immunol*. 2010;22(6):768-774. doi:10.1016/j.coi.2010.10.012

208. Huang Y, Enzmann V, Ildstad ST. Stem Cell-Based Therapeutic Applications in Retinal Degenerative Diseases. *Stem Cell Rev Reports*. 2011;7(2):434-445. doi:10.1007/s12015-010-9192-8
209. Leow SN, Luu CD, Hairul Nizam MH, et al. Safety and Efficacy of Human Wharton's Jelly-Derived Mesenchymal Stem Cells Therapy for Retinal Degeneration. Almeida-Porada GD, ed. *PLoS One*. 2015;10(6):e0128973. doi:10.1371/journal.pone.0128973
210. Kuriyan AE, Albini TA, Townsend JH, et al. Vision Loss after Intravitreal Injection of Autologous "Stem Cells" for AMD. *N Engl J Med*. 2017;376(11):1047-1053. doi:10.1056/NEJMoa1609583
211. Park SS. Cell Therapy Applications for Retinal Vascular Diseases: Diabetic Retinopathy and Retinal Vein Occlusion. *Invest Ophthalmol Vis Sci*. 2016;57(5):ORSFj1-ORSFj10. doi:10.1167/iovs.15-17594
212. Murdoch B, Zarzeczny A, Caulfield T. Exploiting science? A systematic analysis of complementary and alternative medicine clinic websites' marketing of stem cell therapies. *BMJ Open*. 2018;8(2):e019414. doi:10.1136/bmjopen-2017-019414
213. Grand View Research. *Stem Cells Market Analysis By Product (Adult Stem Cells, HESC, Induced Pluripotent Stem Cells), By Application (Regenerative Medicine, Drug Discovery), By Technology, By Therapy, And Segment Forecasts, 2018 - 2025*. https://www.grandviewresearch.com/industry-analysis/stem-cells-market.
214. Gottlieb S. *Statement from FDA Commissioner Scott Gottlieb, M.D. on the FDA's New Policy Steps and Enforcement Efforts to Ensure Proper Oversight of Stem Cell Therapies and Regenerative Medicine*. https://www.fda.gov/NewsEvents/Newsroom/PressAnnouncements/ucm573443.htm.
215. Sacchetti B, Funari A, Remoli C, et al. No identical "mesenchymal stem cells" at different times and sites: Human committed progenitors of distinct origin and differentiation potential are incorporated as adventitial cells in microvessels. *Stem Cell Reports*. 2016;6(6):897-913. doi:10.1016/j.stemcr.2016.05.011
216. Amos PJ, Kapur SK, Stapor PC, et al. Human Adipose-Derived Stromal Cells Accelerate Diabetic Wound Healing: Impact of Cell Formulation and Delivery. *Tissue Eng Part A*. 2010;16(5):1595-1606. doi:10.1089/ten.TEA.2009.0616
217. Hsu Y-C. Theory and Practice of Lineage Tracing. *Stem Cells*. 2015;33(11):3197-3204. doi:10.1002/stem.2123
218. Kretzschmar K, Watt FM. Lineage Tracing. *Cell*. 2012;148(1-2):33-45. doi:10.1016/j.cell.2012.01.002
219. Caplan AI. Adult Mesenchymal Stem Cells: When, Where, and How. *Stem Cells Int*. 2015;2015:1-6. doi:10.1155/2015/628767
220. Singer NG, Caplan AI. Mesenchymal stem cells: mechanisms of inflammation. *Annu Rev Pathol*. 2011;6:457-478. doi:10.1146/annurev-pathol-011110-130230
221. Strem BM, Hicok KC, Zhu M, et al. Multipotential differentiation of adipose tissue-derived stem cells. *Keio JMed*. 2005;54(0022-9717 (Print)):132-141. doi:10.2302/kjm.54.132
222. Kim Y, Kim H, Cho H, Bae Y, Suh K, Jung J. Direct comparison of human mesenchymal stem cells derived from adipose tissues and bone marrow in mediating neovascularization in response to vascular ischemia. *Cell Physiol Biochem*. 2007;20(6):867-876. doi:10.1159/000110447
223. Kern S, Eichler H, Stoeve J, Klüter H, Bieback K. Comparative analysis of mesenchymal

stem cells from bone marrow, umbilical cord blood, or adipose tissue. *Stem Cells*. 2006;24(5):1294-1301. doi:10.1634/stemcells.2005-0342
224. Izadpanah R, Trygg C, Patel B, et al. Biologic properties of mesenchymal stem cells derived from bone marrow and adipose tissue. *J Cell Biochem*. 2006;99(5):1285-1297. doi:10.1002/jcb.20904.Biologic
225. Gomez D, Shankman LS, Nguyen AT, Owens GK. Detection of histone modifications at specific gene loci in single cells in histological sections. *Nat Methods*. 2013;10(2):171-177. doi:10.1038/nmeth.2332
226. Ruggiero D, Lecomte M, Michoud E, Lagarde M, Wiernsperger N. Involvement of cell-cell interactions in the pathogenesis of diabetic retinopathy. *Diabetes Metab*. 1997;23(1):30-42.
227. Gerhardt T, Ley K. Monocyte trafficking across the vessel wall. *Cardiovasc Res*. 2015;107(3):321-330. doi:10.1093/cvr/cvv147
228. Sheets AR, Durham JT, Herman IM. Quantitative Imaging-Based Examination of Pericytes Controlling Endothelial Growth Dynamics and Angiogenesis. *Methods Mol Biol*. 2016;1430:221-229. doi:10.1007/978-1-4939-3628-1_15
229. Motherwell JM, Azimi MS, Spicer K, et al. Evaluation of Arteriolar Smooth Muscle Cell Function in an Ex Vivo Microvascular Network Model. *Sci Rep*. 2017;7(1):2195. doi:10.1038/s41598-017-02272-4
230. Amos PJ, Shang H, Bailey AM, Taylor A, Katz AJ, Peirce SM. IFATS collection: The role of human adipose-derived stromal cells in inflammatory microvascular remodeling and evidence of a perivascular phenotype. *Stem Cells*. 2008;26(10):2682-2690. doi:10.1634/stemcells.2008-0030
231. Gartner ZJ, Prescher JA, Lavis LD. Unraveling cell-to-cell signaling networks with chemical biology. *Nat Chem Biol*. 2017;13(6):564-568. doi:10.1038/nchembio.2391
232. Dunn KW, Kamocka MM, McDonald JH. A practical guide to evaluating colocalization in biological microscopy. *Am J Physiol - Cell Physiol*. 2011;300(4):C723-C742. doi:10.1152/ajpcell.00462.2010
233. Zinchuk V, Zinchuk O. Quantitative colocalization analysis of confocal fluorescence microscopy images. *Curr Protoc Cell Biol*. 2008;Chapter 4:Unit 4.19. doi:10.1002/0471143030.cb0419s39
234. Helmuth JA, Paul G, Sbalzarini IF. Beyond co-localization: inferring spatial interactions between sub-cellular structures from microscopy images. *BMC Bioinformatics*. 2010;11:372. doi:10.1186/1471-2105-11-372
235. Burguet J, Andrey P. Statistical Comparison of Spatial Point Patterns in Biological Imaging. *PLoS One*. 2014;9(2):e87759. doi:10.1371/journal.pone.0087759
236. Johnson GR, Li J, Shariff A, Rohde GK, Murphy RF. Automated Learning of Subcellular Variation among Punctate Protein Patterns and a Generative Model of Their Relation to Microtubules. *PLOS Comput Biol*. 2015;11(12):e1004614. doi:10.1371/journal.pcbi.1004614
237. Payés C, Rodríguez JA, Friend S, Helguera G. Cell Interaction Analysis by Imaging Flow Cytometry. 2012. doi:10.5772/51147
238. Kowluru RA, Chan P-S. Capillary Dropout in Diabetic Retinopathy. In: MD EJD, ed. *Diabetic Retinopathy*. Contemporary Diabetes. Humana Press; 2008:265-282.
239. Wong TY, Cheung CMG, Larsen M, Sharma S, Simó R. Diabetic retinopathy. *Nat Rev Dis Prim*. 2016;2:16012. doi:10.1038/nrdp.2016.12

240. Ejaz S, Chekarova I, Ejaz A, Sohail A, Lim CW. Importance of pericytes and mechanisms of pericyte loss during diabetic retinopathy. *Diabetes, Obes Metab*. 2008;10(1):53-63. doi:10.1111/j.1463-1326.2007.00795.x
241. Beltramo E, Porta M. Pericyte loss in diabetic retinopathy: mechanisms and consequences. *Curr Med Chem*. 2013;20(26):3218-3225.
242. Longden TA, Dabertrand F, Koide M, et al. Capillary K+-sensing initiates retrograde hyperpolarization to increase local cerebral blood flow. *Nat Neurosci*. 2017;advance on. doi:10.1038/nn.4533
243. Sokal RR, Rohlf FJ. *Biometry: The Principles and Practice of Statistics in Biological Research*. [Extensive. New York: W.H. Freeman; 2012.
244. Steinhaus H. *Mathematical Snapshots*. 3rd ed. New York: Dover; 1999.
245. Sackrowitz H, Samuel-Cahn E. P Values as Random Variables-Expected P Values. *Am Stat*. 1999;53(4):326-331. doi:10.2307/2686051
246. Merfeld-Clauss S, Gollahalli N, March KL, Traktuev DO. Adipose tissue progenitor cells directly interact with endothelial cells to induce vascular network formation. *Tissue Eng Part A*. 2010;16(9):2953-2966. doi:10.1089/ten.TEA.2009.0635
247. Sutton EJ, Henning TD, Pichler BJ, Bremer C, Daldrup-Link HE. Cell tracking with optical imaging. *Eur Radiol*. 2008;18(10):2021-2032. doi:10.1007/s00330-008-0984-z
248. Kang S-W, Lee S, Na JH, et al. Cell Labeling and Tracking Method without Distorted Signals by Phagocytosis of Macrophages. *Theranostics*. 2014;4(4):420-431. doi:10.7150/thno.7265
249. Cortez-Retamozo V, Etzrodt M, Pittet MJ. Regulation of macrophage and dendritic cell responses by their lineage precursors. *J Innate Immun*. 2012;4(5-6):411-423. doi:10.1159/000335733
250. Krummel MF, Bartumeus F, Gérard A. T cell migration, search strategies and mechanisms. *Nat Rev Immunol*. 2016;16(3):193-201. doi:10.1038/nri.2015.16
251. Janeway JCA, Travers P, Walport M, Shlomchik MJ. B-cell activation by armed helper T cells. 2001.
252. Mahnke K, Ring S, Bedke T, Karakhanova S, Enk AH. Interaction of regulatory T cells with antigen-presenting cells in health and disease. *Chem Immunol Allergy*. 2008;94:29-39. doi:10.1159/000154854
253. Stark K, Eckart A, Haidari S, et al. Capillary and arteriolar pericytes attract innate leukocytes exiting through venules and “instruct” them with pattern-recognition and motility programs. *Nat Immunol*. 2012;14(1):41-51. doi:10.1038/ni.2477
254. Corliss BA, Azimi MS, Munson JM, Peirce SM, Murfee WL. Macrophages: An Inflammatory Link Between Angiogenesis and Lymphangiogenesis. *Microcirc (New York, NY 1994)*. 2016;23(2):95-121. doi:10.1111/micc.12259
255. Schuh M. An actin-dependent mechanism for long range vesicle transport. *Nat Cell Biol*. 2011;13(12):1431-1436. doi:10.1038/ncb2353
256. Pincus Z, Theriot JA. Comparison of quantitative methods for cell-shape analysis. *J Microsc*. 2007;227(Pt 2):140-156. doi:10.1111/j.1365-2818.2007.01799.x
257. Nuzzo R. Scientific method: Statistical errors. *Nat News*. 2014;506(7487):150. doi:10.1038/506150a
258. Caplan A. Mesenchymal stem cells. *J Orthop Res*. 1991;9(5):641-650. doi:10.1002/jor.1100090504
259. Griffiths MJD, Bonnet D, Janes SM. Stem cells of the alveolar epithelium. *Lancet*.

2005;366(9481):249-260. doi:10.1016/S0140-6736(05)66916-4
260. Beltrami AP, Barlucchi L, Torella D, et al. Adult cardiac stem cells are multipotent and support myocardial regeneration. *Cell*. 2003;114(6):763-776. doi:10.1016/S0092-8674(03)00687-1
261. Zuk PA, Zhu M, Mizuno H, et al. Multilineage Cells from Human Adipose Tissue: Implications for Cell-Based Therapies. *Tissue Eng*. 2001;7(2):211-228. doi:10.1089/107632701300062859
262. Zhu X, Shi W, Tai W, Liu F. The comparition of biological characteristics and multilineage differentiation of bone marrow and adipose derived Mesenchymal stem cells. *Cell Tissue Res*. 2012;350(2):277-287. doi:10.1007/s00441-012-1453-1
263. Bateman ME, Strong AL, Gimble JM, Bunnell BA. Using Fat to Fight Disease: A Systematic Review of Non-Homologous Adipose-Derived Stromal/Stem Cell Therapies. *Stem Cells*. 2018. doi:10.1002/stem.2847
264. Reed-Maldonado AB, Lue TF. The Current Status of Stem-Cell Therapy in Erectile Dysfunction: A Review. *World J Mens Health*. 2016;34(3):155. doi:10.5534/wjmh.2016.34.3.155
265. Brooks A, Futrega K, Liang X, et al. Concise Review: Quantitative Detection and Modeling the In Vivo Kinetics of Therapeutic Mesenchymal Stem/Stromal Cells. *Stem Cells Transl Med*. 2018;7(1):78-86. doi:10.1002/sctm.17-0209
266. Dellavalle a, Maroli G, Covarello D, et al. Pericytes resident in postnatal skeletal muscle differentiate into muscle fibres and generate satellite cells. *Nat Commun*. 2011;2:499. doi:10.1038/ncomms1508
267. Dellavalle A, Sampaolesi M, Tonlorenzi R, et al. Pericytes of human skeletal muscle are myogenic precursors distinct from satellite cells. *Nat Cell Biol*. 2007;9(3):255-267. doi:10.1038/ncb1542
268. Krautler NJ, Kana V, Kranich J, et al. Follicular dendritic cells emerge from ubiquitous perivascular precursors. *Cell*. 2012;150(1):194-206. doi:10.1016/j.cell.2012.05.032
269. Park D, Spencer JA, Koh BI, et al. Endogenous bone marrow MSCs are dynamic, fate-restricted participants in bone maintenance and regeneration. *Cell Stem Cell*. 2012;10(3):259-272. doi:10.1016/j.stem.2012.02.003
270. Long JZ, Svensson KJ, Tsai L, et al. A smooth muscle-like origin for beige adipocytes. *Cell Metab*. 2014;19(5):810-820. doi:10.1016/j.cmet.2014.03.025
271. Goritz C, Dias DO, Tomilin N, Barbacid M, Shupliakov O, Frisen J. A Pericyte Origin of Spinal Cord Scar Tissue. *Science (80-)*. 2011;333(6039):238-242. doi:10.1126/science.1203165
272. Humphreys BD, Lin S-L, Kobayashi A, et al. Fate tracing reveals the pericyte and not epithelial origin of myofibroblasts in kidney fibrosis. *Am J Pathol*. 2010;176(1):85-97. doi:10.2353/ajpath.2010.090517
273. Guimarães-Camboa N, Cattaneo P, Sun Y, et al. Pericytes of Multiple Organs Do Not Behave as Mesenchymal Stem Cells In Vivo. *Cell Stem Cell*. 2017;20(3):345-359.e5. doi:10.1016/j.stem.2016.12.006
274. He L, Vanlandewijck M, Mäe MA, et al. Single-cell RNA sequencing of mouse brain and lung vascular and vessel-associated cell types. *Sci Data*. 2018;5:180160. doi:10.1038/sdata.2018.160
275. Berthiaume A-A, Grant RI, McDowell KP, et al. Dynamic Remodeling of Pericytes In Vivo Maintains Capillary Coverage in the Adult Mouse Brain. *Cell Rep*. 2018;22(1):8-16.

doi:10.1016/j.celrep.2017.12.016
276. Pitulescu ME, Schmidt I, Benedito R, Adams RH. Inducible gene targeting in the neonatal vasculature and analysis of retinal angiogenesis in mice. *Nat Protoc*. 2010;5(9):1518-1534. doi:10.1038/nprot.2010.113
277. Seaman S a., Tannan SC, Cao Y, Peirce SM, Lin KY. Differential Effects of Processing Time and Duration of Collagenase Digestion on Human and Murine Fat Grafts. *Plast Reconstr Surg*. 2015;136(2):189e-99e. doi:10.1097/PRS.0000000000001446
278. Lambert V, Lecomte J, Hansen S, et al. Laser-induced choroidal neovascularization model to study age-related macular degeneration in mice. *Nat Protoc*. 2013;8(11):2197-2211. doi:10.1038/nprot.2013.135
279. Janes KA. An analysis of critical factors for quantitative immunoblotting. *Sci Signal*. 2015;8(371):1-12. doi:10.1126/scisignal.2005966
280. Kelly-Goss MR, Sweat RS, Stapor PC, Peirce SM, Murfee WL. Targeting Pericytes for Angiogenic Therapies. *Microcirculation*. 2014;21(4):345-357. doi:10.1111/micc.12107
281. Gomez D, Owens GK. Smooth muscle cell phenotypic switching in atherosclerosis. *Cardiovasc Res*. 2012;95(2):156-164. doi:10.1093/cvr/cvs115
282. Shankman LS, Gomez D, Cherepanova OA, et al. KLF4-dependent phenotypic modulation of smooth muscle cells has a key role in atherosclerotic plaque pathogenesis. *Nat Med*. 2015;21(6):628-637. doi:10.1038/nm.3866
283. Cherepanova OA, Gomez D, Shankman LS, et al. Activation of the pluripotency factor OCT4 in smooth muscle cells is atheroprotective. *Nat Med*. 2016;22(October 2015):1-12. doi:10.1038/nm.4109
284. Crisan M, Yap S, Casteilla L, et al. A perivascular origin for mesenchymal stem cells in multiple human organs. *Cell Stem Cell*. 2008;3(3):301-313. doi:10.1016/j.stem.2008.07.003
285. Espagnolle N, Guilloton F, Deschaseaux F, Gadelorge M, Sensébé L, Bourin P. CD146 expression on mesenchymal stem cells is associated with their vascular smooth muscle commitment. *J Cell Mol Med*. 2014;18(1):104-114. doi:10.1111/jcmm.12168
286. Amos PJ, Shang H, Bailey AM, Taylor A, Katz AJ, Peirce SM. IFATS Collection: The Role of Human Adipose-Derived Stromal Cells in Inflammatory Microvascular Remodeling and Evidence of a Perivascular Phenotype. *Stem Cells*. 2008;26(10):2682-2690. doi:10.1634/stemcells.2008-0030
287. Cronk SM, Kelly-Goss MR, Ray HC, et al. Adipose-Derived Stem Cells From Diabetic Mice Show Impaired Vascular Stabilization in a Murine Model of Diabetic Retinopathy. *Stem Cells Transl Med*. 2015;4(5):459-467. doi:10.5966/sctm.2014-0108
288. Scott a, Fruttiger M. Oxygen-induced retinopathy: a model for vascular pathology in the retina. *Eye (Lond)*. 2010;24(3):416-421. doi:10.1038/eye.2009.306
289. Hinz B, Phan SH, Thannickal VJ, Galli A, Bochaton-Piallat ML, Gabbiani G. The myofibroblast: One function, multiple origins. *Am J Pathol*. 2007;170(6):1807-1816. doi:10.2353/ajpath.2007.070112
290. El Agha E, Kramann R, Schneider RK, et al. Mesenchymal Stem Cells in Fibrotic Disease. *Cell Stem Cell*. 2017;21(2):166-177. doi:10.1016/j.stem.2017.07.011
291. Grossniklaus HE, Kang SJ, Berglin L. Animal models of choroidal and retinal neovascularization. *Prog Retin Eye Res*. 2010;29(6):500-519. doi:10.1016/j.preteyeres.2010.05.003
292. Tosi GM, Marigliani D, Romeo N, Toti P. Disease Pathways in Proliferative

Vitreoretinopathy: An Ongoing Challenge. *J Cell Physiol*. 2014;229(11):1577-1583. doi:10.1002/jcp.24606
293. Inman GJ. SB-431542 Is a Potent and Specific Inhibitor of Transforming Growth Factor-beta Superfamily Type I Activin Receptor-Like Kinase (ALK) Receptors ALK4, ALK5, and ALK7. *Mol Pharmacol*. 2002;62(1):65-74. doi:10.1124/mol.62.1.65
294. Sakata R, Ueno T, Nakamura T, Ueno H, Sata M. Mechanical stretch induces TGF-beta synthesis in hepatic stellate cells. *Eur J Clin Invest*. 2004;34(2):129-136. doi:10.1111/j.1365-2362.2004.01302.x
295. Carthy JM, Garmaroudi FS, Luo Z, McManus BM. Wnt3a induces myofibroblast differentiation by upregulating TGF-β signaling through SMAD2 in a β-catenin-dependent manner. *PLoS One*. 2011;6(5). doi:10.1371/journal.pone.0019809
296. Murray IR, Péault B. Q&A: Mesenchymal stem cells - where do they come from and is it important? *BMC Biol*. 2015;13(1):99. doi:10.1186/s12915-015-0212-7
297. Nishiyama A, Komitova M, Suzuki R, Zhu X. Polydendrocytes (NG2 cells): multifunctional cells with lineage plasticity. *Nat Rev Neurosci*. 2009;10(1):9-22. doi:10.1038/nrn2495
298. Corselli M, Chen CW, Sun B, Yap S, Rubin JP, Peault B. The tunica adventitia of human arteries and veins as a source of mesenchymal stem cells. *Stem Cells Dev*. 2012;21(8):1299-1308. doi:10.1089/scd.2011.0200
299. Wynn T a, Yugandhar VG, Clark M a. Cellular and molecular mechanisms of fibrosis. *J Pathol*. 2013;46(2):26-32. doi:10.1002/path.2277.Cellular
300. Bardin N, Anfosso F, Massé JM, et al. Identification of CD146 as a component of the endothelial junction involved in the control of cell-cell cohesion. *Blood*. 2001;98(13):3677-3684. doi:10.1182/blood.V98.13.3677
301. Dykstra JA, Facile T, Patrick RJ, et al. Concise review: Fat and furious: Harnessing the full potential of adipose-derived stromal vascular fraction. *Stem Cells Transl Med*. 2017;6(4):1096-1108. doi:10.1002/sctm.16-0337
302. Vishvanath L, Long JZ, Spiegelman BM, Gupta RK. Do Adipocytes Emerge from Mural Progenitors? *Cell Stem Cell*. 2017;20(5):585-586. doi:10.1016/j.stem.2017.03.013
303. Garweg JG, Tappeiner C, Halberstadt M. Pathophysiology of Proliferative Vitreoretinopathy in Retinal Detachment. *Surv Ophthalmol*. 2013;58(4):321-329. doi:10.1016/j.survophthal.2012.12.004
304. Rhee S. Fibroblasts in three dimensional matrices: Cell migration and matrix remodeling. *Exp Mol Med*. 2009;41(12):858-865. doi:10.3858/emm.2009.41.12.096
305. Aarabi S, Bhatt KA, Shi Y, et al. Mechanical load initiates hypertrophic scar formation through decreased cellular apoptosis. *FASEB J*. 2007;21(12):3250-3261. doi:10.1096/fj.07-8218com
306. Ihanamäki T, Pelliniemi LJ, Vuorio E. Collagens and collagen-related matrix components in the human and mouse eye. *Prog Retin Eye Res*. 2004;23(4):403-434. doi:10.1016/j.preteyeres.2004.04.002
307. Da Cruz L, Fynes K, Georgiadis O, et al. Phase 1 clinical study of an embryonic stem cell-derived retinal pigment epithelium patch in age-related macular degeneration. *Nat Biotechnol*. 2018;36(4):1-10. doi:10.1038/nbt.4114
308. Corliss BA, Ray HC, Patrie J, et al. CIRCOAST: A Statistical Hypothesis Test for Cellular Colocalization with Network Structures. *Bioinformatics*. 2018;(July):1-9. doi:10.1093/bioinformatics/bty638

309. Neelisetty S, Alford C, Reynolds K, et al. Renal fibrosis is not reduced by blocking transforming growth factor-β signaling in matrix-producing interstitial cells. *Kidney Int*. 2015;88(3):503-514. doi:10.1038/ki.2015.51
310. Duan WJ, Yu X, Huang XR, Yu JW, Lan HY. Opposing roles for Smad2 and Smad3 in peritoneal fibrosis in vivo and in vitro. *Am J Pathol*. 2014;184(8):2275-2284. doi:10.1016/j.ajpath.2014.04.014
311. Piersma B, Bank RA, Boersema M. Signaling in Fibrosis: TGF-β, WNT, and YAP/TAZ Converge. *Front Med*. 2015;2(September):1-14. doi:10.3389/fmed.2015.00059
312. Doughty MJ. Concerning the symmetry of the "hexagonal" cells of the corneal endothelium. *Exp Eye Res*. 1992;55(1):145-154.
313. Bonanno JA. "Molecular Mechanisms Underlying the Corneal Endothelial Pump." *Exp Eye Res*. 2012;95(1):2-7. doi:10.1016/j.exer.2011.06.004
314. Miller WL. Cornea: Fundamentals, Diagnosis and Management, 4th ed. *Optom Vis Sci*. 2018;95(7):625. doi:10.1097/OPX.0000000000001247
315. Zavala J, López Jaime GR, Rodríguez Barrientos CA, Valdez-Garcia J. Corneal endothelium: developmental strategies for regeneration. *Eye*. 2013;27(5):579-588. doi:10.1038/eye.2013.15
316. Chen J, Li Z, Zhang L, et al. Descemet's Membrane Supports Corneal Endothelial Cell Regeneration in Rabbits. *Sci Rep*. 2017;7(1):6983. doi:10.1038/s41598-017-07557-2
317. Nucci P, Brancato R, Mets MB, Shevell SK. Normal endothelial cell density range in childhood. *Arch Ophthalmol (Chicago, Ill 1960)*. 1990;108(2):247-248. http://www.ncbi.nlm.nih.gov/pubmed/2302110.
318. Agarwal A, Jacob S, Agarwal A, Agarwal S, Kumar M A. Iatrogenic descemetorhexis as a complication of phacoemulsification. *J Cataract Refract Surg*. 2006;32(5):895-897. doi:10.1016/j.jcrs.2006.01.070
319. Bourne WM. Biology of the corneal endothelium in health and disease. *Eye*. 2003;17(8):912-918. doi:10.1038/sj.eye.6700559
320. Carlson KH, Ilstrup DM, Bourne WM, Dyer JA. Effect of silicone elastomer contact lens wear on endothelial cell morphology in aphakic eyes. *Cornea*. 1990;9(1):45-47.
321. Boynton GE, Woodward MA. Evolving Techniques in Corneal Transplantation. *Curr Surg reports*. 2015;3(2). doi:10.1007/s40137-014-0079-5
322. Bourne WM, Brubaker RF, O'Fallon WM. Use of air to decrease endothelial cell loss during intraocular lens implantation. *Arch Ophthalmol (Chicago, Ill 1960)*. 1979;97(8):1473-1475.
323. Bourne WM, Nelson LR, Hodge DO. Continued endothelial cell loss ten years after lens implantation. *Ophthalmology*. 1994;101(6):1014-1022; discussion 1022-1023.
324. Alagesan S, Griffin MD. Autologous and allogeneic mesenchymal stem cells in organ transplantation: what do we know about their safety and efficacy? *Curr Opin Organ Transplant*. 2014;19(1):65-72. doi:10.1097/MOT.0000000000000043
325. Chasseigneaux S, Moraca Y, Cochois-Guégan V, et al. Isolation and differential transcriptome of vascular smooth muscle cells and mid-capillary pericytes from the rat brain. *Sci Rep*. 2018;8(1):12272. doi:10.1038/s41598-018-30739-5
326. McCabe KL, Kunzevitzky NJ, Chiswell BP, Xia X, Goldberg JL, Lanza R. Efficient generation of human embryonic stem cell-derived corneal endothelial cells by directed differentiation. *PLoS One*. 2015;10(12):1-24. doi:10.1371/journal.pone.0145266
327. Okumura N, Sakamoto Y, Fujii K, et al. Rho kinase inhibitor enables cell-based therapy

for corneal endothelial dysfunction. *Sci Rep*. 2016;6(1):26113. doi:10.1038/srep26113
328. He Z, Forest F, Gain P, et al. 3D map of the human corneal endothelial cell. *Sci Rep*. 2016;6:29047. doi:10.1038/srep29047
329. Espana EM, Sun M, Birk DE. Existence of corneal endothelial slow-cycling cells. *Investig Ophthalmol Vis Sci*. 2015;56(6):3827-3837. doi:10.1167/iovs.14-16030
330. Fabiani C, Barabino S, Rashid S, Dana MR. Corneal epithelial proliferation and thickness in a mouse model of dry eye. *Exp Eye Res*. 2009;89(2):166-171. doi:10.1016/j.exer.2009.03.003
331. Patel SP, Bourne WM. Corneal Endothelial Cell Proliferation: A Function of Cell Density. *Invest Ophthalmol Vis Sci*. 2009;50(6):2742-2746. doi:10.1167/iovs.08-3002
332. Sontake V, Wang Y, Kasam RK, et al. Hsp90 regulation of fibroblast activation in pulmonary fibrosis. *JCI insight*. 2017;2(4):e91454. doi:10.1172/jci.insight.91454
333. Chen J, Li Z, Zhang L, et al. Descemet's Membrane Supports Corneal Endothelial Cell Regeneration in Rabbits. *Sci Rep*. 2017;7(1):6983. doi:10.1038/s41598-017-07557-2
334. Fischbarg J. Mechanism of fluid transport across corneal endothelium and other epithelial layers: a possible explanation based on cyclic cell volume regulatory changes. *Br J Ophthalmol*. 1997;81(1):85-89. doi:10.1136/bjo.81.1.85
335. Oie Y, Nishida K. Corneal regenerative medicine. *Regen Ther*. 2016;5:40-45. doi:10.1016/j.reth.2016.06.002
336. Gain P, Jullienne R, He Z, et al. Global Survey of Corneal Transplantation and Eye Banking. *JAMA Ophthalmol*. 2016;134(2):167-173. doi:10.1001/jamaophthalmol.2015.4776
337. Gorovoy MS. Descemet-Stripping Automated Endothelial Keratoplasty. *Cornea*. 2006;25(8):886. doi:10.1097/01.ico.0000214224.90743.01
338. Maguire MG, Stark WJ, Gottsch JD, et al. Risk Factors for Corneal Graft Failure and Rejection in the Collaborative Corneal Transplantation Studies. *Ophthalmology*. 1994;101(9):1536-1547. doi:10.1016/S0161-6420(94)31138-9
339. Saba N, Abraham R, Keating A. Overview of autologous stem cell transplantation. *Crit Rev Oncol Hematol*. 2000;36(1):27-48.
340. Yamashita K, Inagaki E, Hatou S, et al. Corneal Endothelial Regeneration Using Mesenchymal Stem Cells Derived from Human Umbilical Cord. *Stem Cells Dev*. 2018;27(16):1097-1108. doi:10.1089/scd.2017.0297
341. Joyce NC, Harris DL, Markov V, Zhang Z, Saitta B. Potential of human umbilical cord blood mesenchymal stem cells to heal damaged corneal endothelium. *Mol Vis*. 2012;18:547-564.
342. Minteer D, Marra KG, Rubin JP. Adipose-Derived Mesenchymal Stem Cells: Biology and Potential Applications. In: Weyand B, Dominici M, Hass R, Jacobs R, Kasper C, eds. *Mesenchymal Stem Cells - Basics and Clinical Application I*. Advances in Biochemical Engineering/Biotechnology. Berlin, Heidelberg: Springer Berlin Heidelberg; 2013:59-71.
343. Joddar B, Kumar SA, Kumar A. A Contact-Based Method for Differentiation of Human Mesenchymal Stem Cells into an Endothelial Cell-Phenotype. *Cell Biochem Biophys*. 2018;76(1-2):187-195. doi:10.1007/s12013-017-0828-z
344. Srinivas SP. Dynamic regulation of barrier integrity of the corneal endothelium. *Optom Vis Sci*. 2010;87(4):E239-54. doi:10.1097/OPX.0b013e3181d39464
345. Ponsaerts R, D'hondt C, Bultynck G, Srinivas SP, Vereecke J, Himpens B. The myosin II ATPase inhibitor blebbistatin prevents thrombin-induced inhibition of intercellular

calcium wave propagation in corneal endothelial cells. *Invest Ophthalmol Vis Sci*. 2008;49(11):4816-4827. doi:10.1167/iovs.07-1533
346. Satpathy M, Gallagher P, Lizotte-Waniewski M, Srinivas SP. Thrombin-induced phosphorylation of the regulatory light chain of myosin II in cultured bovine corneal endothelial cells. *Exp Eye Res*. 2004;79(4):477-486. doi:10.1016/j.exer.2004.06.018
347. Srinivas SP, Satpathy M, Gallagher P, Larivière E, Van Driessche W. Adenosine induces dephosphorylation of myosin II regulatory light chain in cultured bovine corneal endothelial cells. *Exp Eye Res*. 2004;79(4):543-551. doi:10.1016/j.exer.2004.06.027
348. Srinivas SP, Satpathy M, Guo Y, Anandan V. Histamine-induced phosphorylation of the regulatory light chain of myosin II disrupts the barrier integrity of corneal endothelial cells. *Invest Ophthalmol Vis Sci*. 2006;47(9):4011-4018. doi:10.1167/iovs.05-1127
349. Yun IS, Lee MH, Rah DK, Lew DH, Park J-C, Lee WJ. Heat Shock Protein 90 Inhibitor (17-AAG) Induces Apoptosis and Decreases Cell Migration/Motility of Keloid Fibroblasts. *Plast Reconstr Surg*. 2015;136(1):44e-53e. doi:10.1097/PRS.0000000000001362
350. Tomcik M, Zerr P, Pitkowski J, et al. Heat shock protein 90 (Hsp90) inhibition targets canonical TGF-β signalling to prevent fibrosis. *Ann Rheum Dis*. 2014;73(6):1215-1222. doi:10.1136/annrheumdis-2012-203095
351. Datta R, Bansal T, Rana S, et al. Hsp90/Cdc37 assembly modulates TGFβ receptor-II to act as a profibrotic regulator of TGFβ signaling during cardiac hypertrophy. *Cell Signal*. 2015;27(12):2410-2424. doi:10.1016/j.cellsig.2015.09.005
352. Butler JM, Guthrie SM, Koc M, et al. SDF-1 is both necessary and sufficient to promote proliferative retinopathy. *J Clin Invest*. 2005;115(1):86-93. doi:10.1172/JCI22869
353. Szigeti A, Ecsedy M, Schneider M, et al. Stromal Cell-Derived Factor 1 Polymorphism in Retinal Vein Occlusion. *PLoS One*. 2016;11(11):e0166544. doi:10.1371/journal.pone.0166544
354. Ball SG, Shuttleworth CA, Kielty CM. Vascular endothelial growth factor can signal through platelet-derived growth factor receptors. *J Cell Biol*. 2007;177(3):489-500. doi:10.1083/jcb.200608093
355. Sugimoto M, Cutler A, Shen B, et al. Inhibition of EGF signaling protects the diabetic retina from insulin-induced vascular leakage. *Am J Pathol*. 2013;183(3):987-995. doi:10.1016/j.ajpath.2013.05.017
356. Gerhardinger C, Dagher Z, Sebastiani P, Park YS, Lorenzi M. The transforming growth factor-beta pathway is a common target of drugs that prevent experimental diabetic retinopathy. *Diabetes*. 2009;58(7):1659-1667. doi:10.2337/db08-1008
357. Giesen C, Wang HAO, Schapiro D, et al. Highly multiplexed imaging of tumor tissues with subcellular resolution by mass cytometry. *Nat Methods*. 2014;11(4):417-422. doi:10.1038/nmeth.2869
358. Kuwahara A, Ozone C, Nakano T, Saito K, Eiraku M, Sasai Y. Generation of a ciliary margin-like stem cell niche from self-organizing human retinal tissue. *Nat Commun*. 2015;6(1):6286. doi:10.1038/ncomms7286
359. Zhong X, Gutierrez C, Xue T, et al. Generation of three-dimensional retinal tissue with functional photoreceptors from human iPSCs. *Nat Commun*. 2014;5(1):4047. doi:10.1038/ncomms5047
360. McLelland BT, Lin B, Mathur A, et al. Transplanted hESC-Derived Retina Organoid Sheets Differentiate, Integrate, and Improve Visual Function in Retinal Degenerate Rats.

Invest Ophthalmol Vis Sci. 2018;59(6):2586-2603. doi:10.1167/iovs.17-23646
361. Seiler MJ, Aramant RB, Jones MK, Ferguson DL, Bryda EC, Keirstead HS. A new immunodeficient pigmented retinal degenerate rat strain to study transplantation of human cells without immunosuppression. *Graefes Arch Clin Exp Ophthalmol*. 2014;252(7):1079-1092. doi:10.1007/s00417-014-2638-y
362. Assawachananont J, Mandai M, Okamoto S, et al. Transplantation of Embryonic and Induced Pluripotent Stem Cell-Derived 3D Retinal Sheets into Retinal Degenerative Mice. *Stem Cell Reports*. 2014;2(5):662-674. doi:10.1016/j.stemcr.2014.03.011
363. Shirai H, Mandai M, Matsushita K, et al. Transplantation of human embryonic stem cell-derived retinal tissue in two primate models of retinal degeneration. *Proc Natl Acad Sci*. 2016;113(1):E81-E90. doi:10.1073/pnas.1512590113
364. Schwartz SD, Regillo CD, Lam BL, et al. Human embryonic stem cell-derived retinal pigment epithelium in patients with age-related macular degeneration and Stargardt's macular dystrophy: follow-up of two open-label phase 1/2 studies. *Lancet*. 2015;385(9967):509-516. doi:10.1016/S0140-6736(14)61376-3
365. Yaji N, Yamato M, Yang J, Okano T, Hori S. Transplantation of tissue-engineered retinal pigment epithelial cell sheets in a rabbit model. *Biomaterials*. 2009;30(5):797-803. doi:10.1016/j.biomaterials.2008.10.045
366. Aird AL, Nevitt CD, Christian K, Williams SK, Hoying JB, LeBlanc AJ. Adipose-derived stromal vascular fraction cells isolated from old animals exhibit reduced capacity to support the formation of microvascular networks. *Exp Gerontol*. 2015;63:18-26. doi:10.1016/j.exger.2015.01.044
367. Leblanc AJ, Touroo JS, Hoying JB, Williams SK. Adipose stromal vascular fraction cell construct sustains coronary microvascular function after acute myocardial infarction. *Am J Physiol Heart Circ Physiol*. 2012;302(4):H973-82. doi:10.1152/ajpheart.00735.2011
368. Traktuev DO, Prater DN, Merfeld-Clauss S, et al. Robust functional vascular network formation in vivo by cooperation of adipose progenitor and endothelial cells. *Circ Res*. 2009;104(12):1410-1420. doi:10.1161/CIRCRESAHA.108.190926
369. Volarevic V, Markovic BS, Gazdic M, et al. Ethical and Safety Issues of Stem Cell-Based Therapy. *Int J Med Sci*. 2018;15(1):36-45. doi:10.7150/ijms.21666
370. McKelvey KJ, Powell KL, Ashton AW, Morris JM, McCracken SA. Exosomes: Mechanisms of Uptake. *J Circ biomarkers*. 4:7. doi:10.5772/61186
371. Teng X, Chen L, Chen W, Yang J, Yang Z, Shen Z. Mesenchymal Stem Cell-Derived Exosomes Improve the Microenvironment of Infarcted Myocardium Contributing to Angiogenesis and Anti-Inflammation. *Cell Physiol Biochem*. 2015;37(6):2415-2424. doi:10.1159/000438594
372. Bian S, Zhang L, Duan L, Wang X, Min Y, Yu H. Extracellular vesicles derived from human bone marrow mesenchymal stem cells promote angiogenesis in a rat myocardial infarction model. *J Mol Med (Berl)*. 2014;92(4):387-397. doi:10.1007/s00109-013-1110-5
373. Lee J-K, Park S-R, Jung B-K, et al. Exosomes Derived from Mesenchymal Stem Cells Suppress Angiogenesis by Down-Regulating VEGF Expression in Breast Cancer Cells. *PLoS One*. 2013;8(12):e84256. doi:10.1371/journal.pone.0084256
374. Fu Y, Karbaat L, Wu L, Leijten JCH, Both S, Karperien M. Trophic effects of mesenchymal stem cells in tissue regeneration. *Tissue Eng Part B Rev*. 2017;23(6):ten.TEB.2016.0365. doi:10.1089/ten.TEB.2016.0365
375. Ti D, Hao H, Fu X, Han W. Mesenchymal stem cells-derived exosomal microRNAs

contribute to wound inflammation. *Sci China Life Sci*. 2016;59(12):1305-1312. doi:10.1007/s11427-016-0240-4
376. Yu B, Shao H, Su C, et al. Exosomes derived from MSCs ameliorate retinal laser injury partially by inhibition of MCP-1. *Sci Rep*. 2016;6(March):1-12. doi:10.1038/srep34562
377. Mead B, Tomarev S. Bone marrow-derived mesenchymal stem cells-derived exosomes promote survival of retinal ganglion cells through mirna-dependent mechanisms. *Stem Cells Transl Med*. 2017;6(4):1273-1285. doi:10.1002/sctm.16-0428
378. Du Y-M, Zhuansun Y-X, Chen R, Lin L, Lin Y, Li J-G. Mesenchymal stem cell exosomes promote immunosuppression of regulatory T cells in asthma. *Exp Cell Res*. 2018;363(1):114-120. doi:10.1016/j.yexcr.2017.12.021
379. Zhang B, Yin Y, Lai RC, Tan SS, Choo ABH, Lim SK. Mesenchymal Stem Cells Secrete Immunologically Active Exosomes. *Stem Cells Dev*. 2014;23(11):1233-1244. doi:10.1089/scd.2013.0479
380. Cosenza S, Toupet K, Maumus M, et al. Mesenchymal stem cells-derived exosomes are more immunosuppressive than microparticles in inflammatory arthritis. *Theranostics*. 2018;8(5):1399-1410. doi:10.7150/thno.21072
381. Tamura R, Uemoto S, Tabata Y. Immunosuppressive effect of mesenchymal stem cell-derived exosomes on a concanavalin A-induced liver injury model. *Inflamm Regen*. 2016;36(1):26. doi:10.1186/s41232-016-0030-5
382. Matthyssen S, Van den Bogerd B, Dhubhghaill SN, Koppen C, Zakaria N. Corneal regeneration: A review of stromal replacements. *Acta Biomater*. 2018;69:31-41. doi:10.1016/j.actbio.2018.01.023
383. Patel JI, Hykin PG, Gregor ZJ, Boulton M, Cree IA. Angiopoietin concentrations in diabetic retinopathy. *Br J Ophthalmol*. 2005;89(4):480-483. doi:10.1136/bjo.2004.049940
384. Funatsu H, Yamashita H, Nakanishi Y, Hori S. Angiotensin II and vascular endothelial growth factor in the vitreous fluid of patients with proliferative diabetic retinopathy. *Br J Ophthalmol*. 2002;86(3):311-315. http://www.ncbi.nlm.nih.gov/pubmed/11864890.
385. Gray H. *Anatomy of the Human Body*. Vol. 8. (Lea, Febiger, eds.).; 1878.
386. Moore DH. THE FINE STRUCTURE OF CAPILLARIES AND SMALL ARTERIES. *J Cell Biol*. 1957;3(3):457-462. doi:10.1083/jcb.3.3.457
387. Eberth C. Handbuch der Lehre von der Gewegen des Menschen und der Tiere (Vol. 1). *Leipzig: Engelmann*. 1871.
388. Rouget C. Memoire sur le developpement, la structures et les proprietes des capillaires sanguins et lymphatiques. *Archs Physiol Norm Pathol*. 1873;5:603–633.
389. Zimmerman K. Der feinere bau der blutcapillares. *Z Anat Entwicklungsgesch*. 1923;68:3-109.
390. Ross R, Everett NB, Tyler R. Wound healing and collagen formation. VI. The origin of the wound fibroblast studied in parabiosis. *J Cell Biol*. 1970;44(3):645-654. doi:10.3791/50556
391. Gabbiani G, Hirschel BJ, Ryan GB, Statkov PR, Majno G. Granulation tissue as a contractile organ. A study of structure and function. *J Exp Med*. 1972;135(4):719-734. http://www.ncbi.nlm.nih.gov/pubmed/4336123.
392. Nie T, Hui X, Gao X, et al. Conversion of non-adipogenic fibroblasts into adipocytes by a defined hormone mixture. *Biochem J*. 2015;467(3):487-494. doi:10.1042/BJ20140727
393. Dastagir K, Reimers K, Lazaridis A, et al. Murine embryonic fibroblast cell lines differentiate into three mesenchymal lineages to different extents: new models to

investigate differentiation processes. *Cell Reprogram*. 2014;16(4):241-252. doi:10.1089/cell.2014.0005
394. Liu H, Chen B, Lilly B. Fibroblasts potentiate blood vessel formation partially through secreted factor TIMP-1. *Angiogenesis*. 2008;11(3):223-234. doi:10.1007/s10456-008-9102-8
395. Holt DJ, Chamberlain LM, Grainger DW. Cell–cell signaling in co-cultures of macrophages and fibroblasts. *Biomaterials*. 2010;31(36):9382-9394. doi:10.1016/j.biomaterials.2010.07.101
396. Östman A, Augsten M. Cancer-associated fibroblasts and tumor growth – bystanders turning into key players. *Curr Opin Genet Dev*. 2009;19(1):67-73. doi:10.1016/j.gde.2009.01.003
397. Pardali E, Sanchez-Duffhues G, Gomez-Puerto MC, Ten Dijke P. TGF-β-Induced Endothelial-Mesenchymal Transition in Fibrotic Diseases. *Int J Mol Sci*. 2017;18(10). doi:10.3390/ijms18102157
398. Tang Y, Urs S, Boucher J, et al. Notch and transforming growth factor-beta (TGFbeta) signaling pathways cooperatively regulate vascular smooth muscle cell differentiation. *J Biol Chem*. 2010;285(23):17556-17563. doi:10.1074/jbc.M109.076414
399. Papetti M, Shujath J, Riley KN, Herman IM. FGF-2 Antagonizes the TGF-β1-Mediated Induction of Pericyte α-Smooth Muscle Actin Expression: A Role for Myf-5 and Smad-Mediated Signaling Pathways. *Investig Opthalmology Vis Sci*. 2003;44(11):4994. doi:10.1167/iovs.03-0291
400. Gomez IG, Roach AM, Nakagawa N, et al. TWEAK-Fn14 Signaling Activates Myofibroblasts to Drive Progression of Fibrotic Kidney Disease. *J Am Soc Nephrol*. 2016;27(12):3639-3652. doi:10.1681/ASN.2015111227
401. Kita T, Hata Y, Arita R, et al. Role of TGF-β in proliferative vitreoretinal diseases and ROCK as a therapeutic target. *Proc Natl Acad Sci*. 2008;105(45):17504-17509. doi:10.1073/pnas.0804054105
402. Behl T, Kotwani A. Potential of angiotensin II receptor blockers in the treatment of diabetic retinopathy. *Life Sci*. 2017;176:1-9. doi:10.1016/j.lfs.2017.03.020
403. Kumar A, Souza SSD, Moskvin O V, et al. Specification and Diversification of Pericytes and Smooth Muscle Cells from Mesenchymoangioblasts Article Specification and Diversification of Pericytes and Smooth Muscle Cells from Mesenchymoangioblasts. *CellReports*. 2017;19(9):1902-1916. doi:10.1016/j.celrep.2017.05.019
404. Leiter EH, Prochazka M, Coleman DL. The non-obese diabetic (NOD) mouse. *Am J Pathol*. 1987;128(2):380-383. http://www.pubmedcentral.nih.gov/articlerender.fcgi?artid=PMC1899627.
405. Kobayashi K, Forte TM, Taniguchi S, Ishida BY, Oka K, Chan L. The db/db mouse, a model for diabetic dyslipidemia: molecular characterization and effects of Western diet feeding. *Metabolism*. 2000;49(1):22-31. http://www.ncbi.nlm.nih.gov/pubmed/10647060.
406. Li L, Xia Y, Wang Z, et al. Suppression of the PI3K-Akt pathway is involved in the decreased adhesion and migration of bone marrow-derived mesenchymal stem cells from non-obese diabetic mice. *Cell Biol Int*. 2011;35(9):961-966. doi:10.1042/CBI20100544
407. Yang K, Wang X, He Y, et al. Advanced glycation end products induce chemokine/cytokine production via activation of p38 pathway and inhibit proliferation and migration of bone marrow mesenchymal stem cells. *Cardiovasc Diabetol*. 2010;9(1):66. doi:10.1186/1475-2840-9-66

408. Wang Z, Li H, Guo R, Wang Q, Zhang D. Antioxidants inhibit advanced glycosylation end-product-induced apoptosis by downregulation of miR-223 in human adipose tissue-derived stem cells. *Sci Rep*. 2016;6(February):23021. doi:10.1038/srep23021
409. Chen HY, Zhang X, Chen SF, et al. The protective effect of 17β-estradiol against hydrogen peroxide-induced apoptosis on mesenchymal stem cell. *Biomed Pharmacother*. 2012;66(1):57-63. doi:10.1016/j.biopha.2011.11.014
410. Yagi H, Tan J, Tuan RS. Polyphenols suppress hydrogen peroxide-induced oxidative stress in human bone-marrow derived mesenchymal stem cells. *J Cell Biochem*. 2013;114(5):1163-1173. doi:10.1002/jcb.24459
411. Wang F-W, Wang Z, Zhang Y-M, et al. Protective effect of melatonin on bone marrow mesenchymal stem cells against hydrogen peroxide-induced apoptosis in vitro. *J Cell Biochem*. 2013;114(10):2346-2355. doi:10.1002/jcb.24582
412. Progatzky F, Dallman MJ, Lo Celso C. From seeing to believing: labelling strategies for in vivo cell-tracking experiments. *Interface Focus*. 2013;3(3):20130001. doi:10.1098/rsfs.2013.0001
413. Nguyen PK, Riegler J, Wu JC. Stem cell imaging: from bench to bedside. *Cell Stem Cell*. 2014;14(4):431-444. doi:10.1016/j.stem.2014.03.009
414. McClellan S, Slamecka J, Howze P, et al. mRNA detection in living cells: A next generation cancer stem cell identification technique. *Methods*. 2015;82:47-54. doi:10.1016/j.ymeth.2015.04.022
415. Prigodich AE, Randeria PS, Briley WE, et al. Multiplexed nanoflares: mRNA detection in live cells. *Anal Chem*. 2012;84(4):2062-2066. doi:10.1021/ac202648w
416. Seferos DS, Giljohann DA, Hill HD, Prigodich AE, Mirkin CA. Nano-flares: probes for transfection and mRNA detection in living cells. *J Am Chem Soc*. 2007;129(50):15477-15479. doi:10.1021/ja0776529
417. Halo TL, McMahon KM, Angeloni NL, et al. NanoFlares for the detection, isolation, and culture of live tumor cells from human blood. *Proc Natl Acad Sci U S A*. 2014;111(48):17104-17109. doi:10.1073/pnas.1418637111
418. The Spherical Nucleic Acids mRNA Detection Paradox. *Sci Res*. April 2016. doi:10.14293/S2199-1006.1.SOR-CHEM.AZ1MJU.v2
419. West-Mays JA, Dwivedi DJ. The keratocyte: corneal stromal cell with variable repair phenotypes. *Int J Biochem Cell Biol*. 2006;38(10):1625-1631. doi:10.1016/j.biocel.2006.03.010
420. Qi H, Priyadarsini S, Nicholas SE, et al. Analysis of sphingolipids in human corneal fibroblasts from normal and keratoconus patients. *J Lipid Res*. 2017;58(4):636-648. doi:10.1194/jlr.M067264
421. Kaldawy RM, Wagner J, Ching S, Seigel GM. Evidence of apoptotic cell death in keratoconus. *Cornea*. 2002;21(2):206-209. http://www.ncbi.nlm.nih.gov/pubmed/11862097.
422. Kim WJ, Rabinowitz YS, Meisler DM, Wilson SE. Keratocyte apoptosis associated with keratoconus. *Exp Eye Res*. 1999;69(5):475-481. doi:10.1006/exer.1999.0719
423. Wilson SE, Chaurasia SS, Medeiros FW. Apoptosis in the initiation, modulation and termination of the corneal wound healing response. *Exp Eye Res*. 2007;85(3):305-311. doi:10.1016/j.exer.2007.06.009
424. Jester J V, Moller-Pedersen T, Huang J, et al. The cellular basis of corneal transparency: evidence for “corneal crystallins”. *J Cell Sci*. 1999;112 (Pt 5:613-622.

http://www.ncbi.nlm.nih.gov/pubmed/9973596.
425. Caplan AI. Mesenchymal Stem Cells: Time to Change the Name! *Stem Cells Transl Med*. 2017;6(6):1445-1451. doi:10.1002/sctm.17-0051

APPENDIX

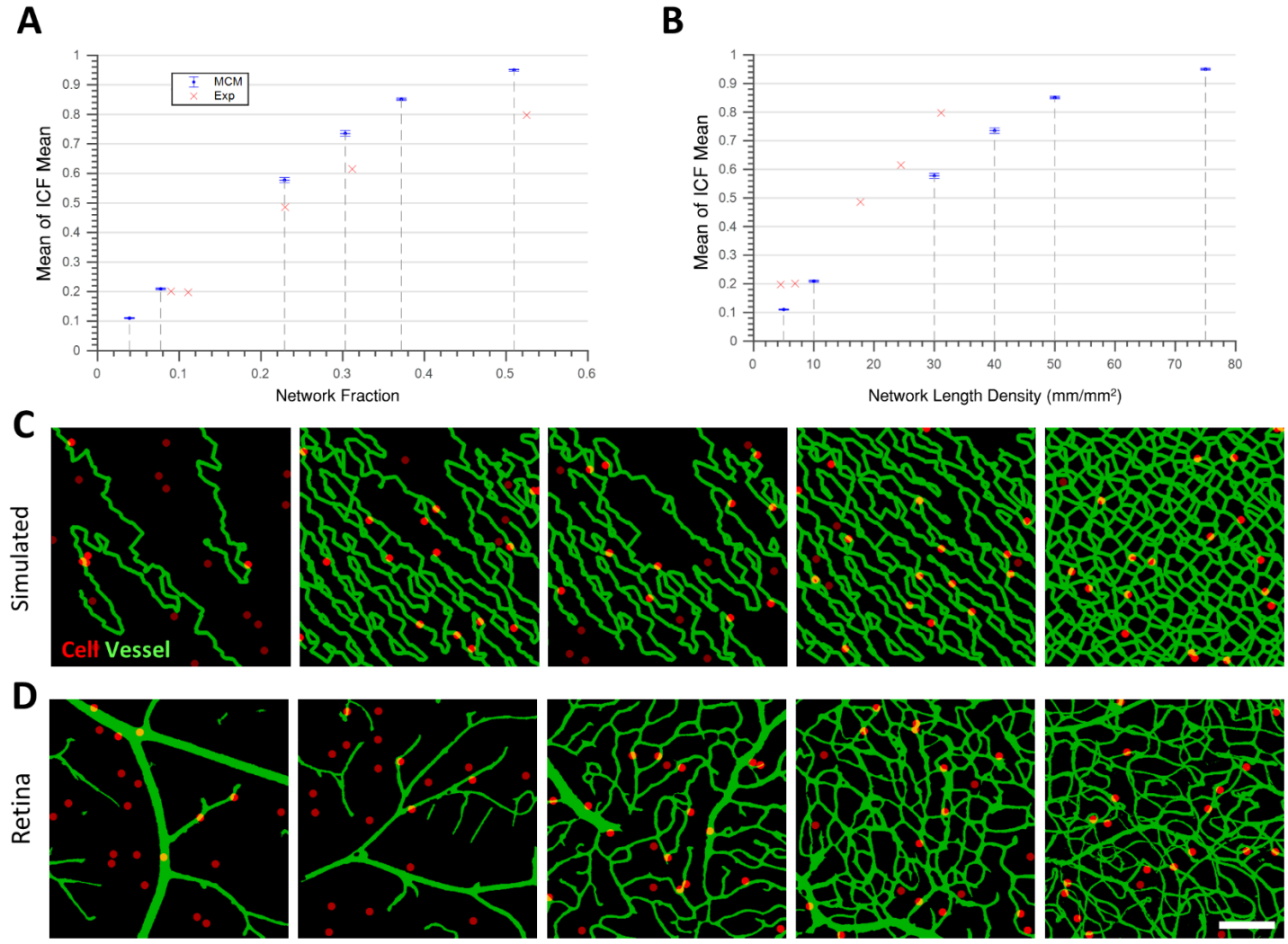

Supplemental Figure 1: The intercellular colocalization fraction (ICF) with vessel networks due to random chance can be used on a wide range of vessel densities. (A, B) Mean of cell colocation fraction mean versus network length density and network fraction from agent-based Monte Carlo model of random placement (MCMRP) from simulated blood vessel networks (blue) and retinal blood vessels (red, error bars standard deviation). Example images of **(C)** simulated networks (green: vessel) and ones acquired **(D)** in adult murine retina (green: lectin IB4) with simulated cells (red, scale bar 100 µm).

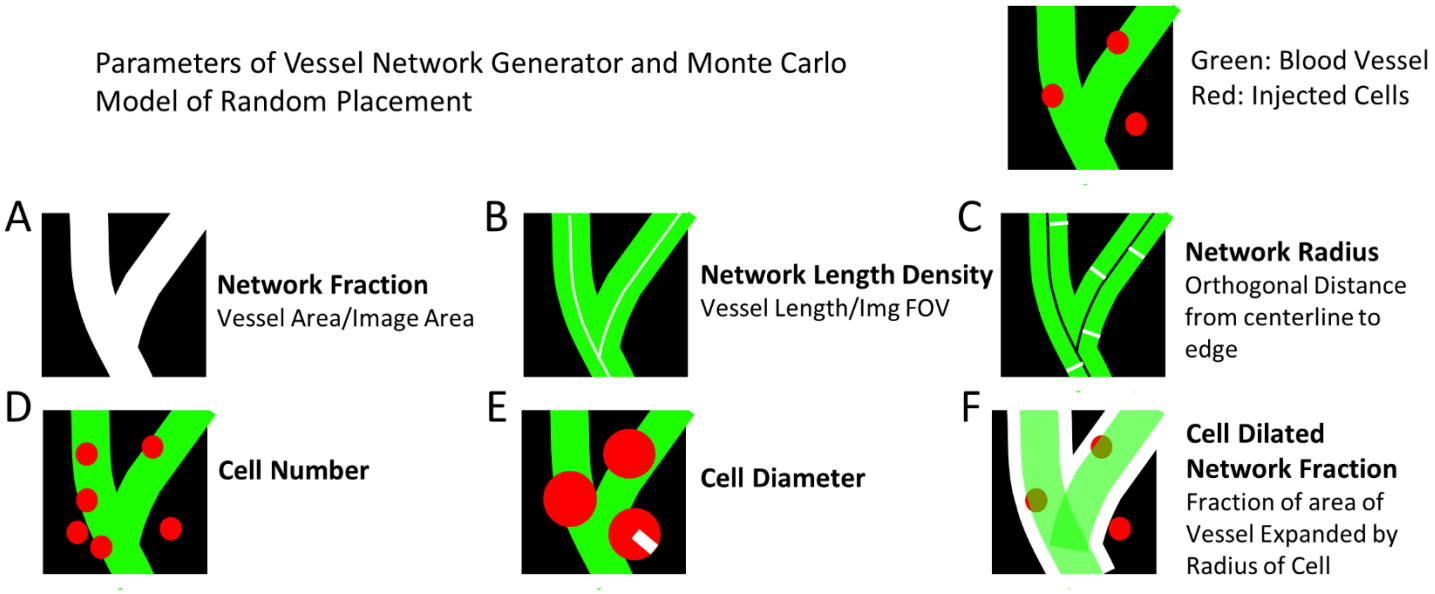

Supplemental Figure 2. Key Parameters of vessel networks and injected cells. (A) Network fraction, the fraction of pixels of segmented vessel out of image pixel area. **(B)** Network length density: the length of the centerline of all vessels. **(C)** Network radius: average orthogonal distance from centerline to edge of vessel. **(D)** Cell number. **(E)** Cell diameter. **(F)** Cell dilated network fraction (CDNF): area in which the center of a cell could land and still be colocalized with network (at least 1 pixel overlapping between cell and vessel).

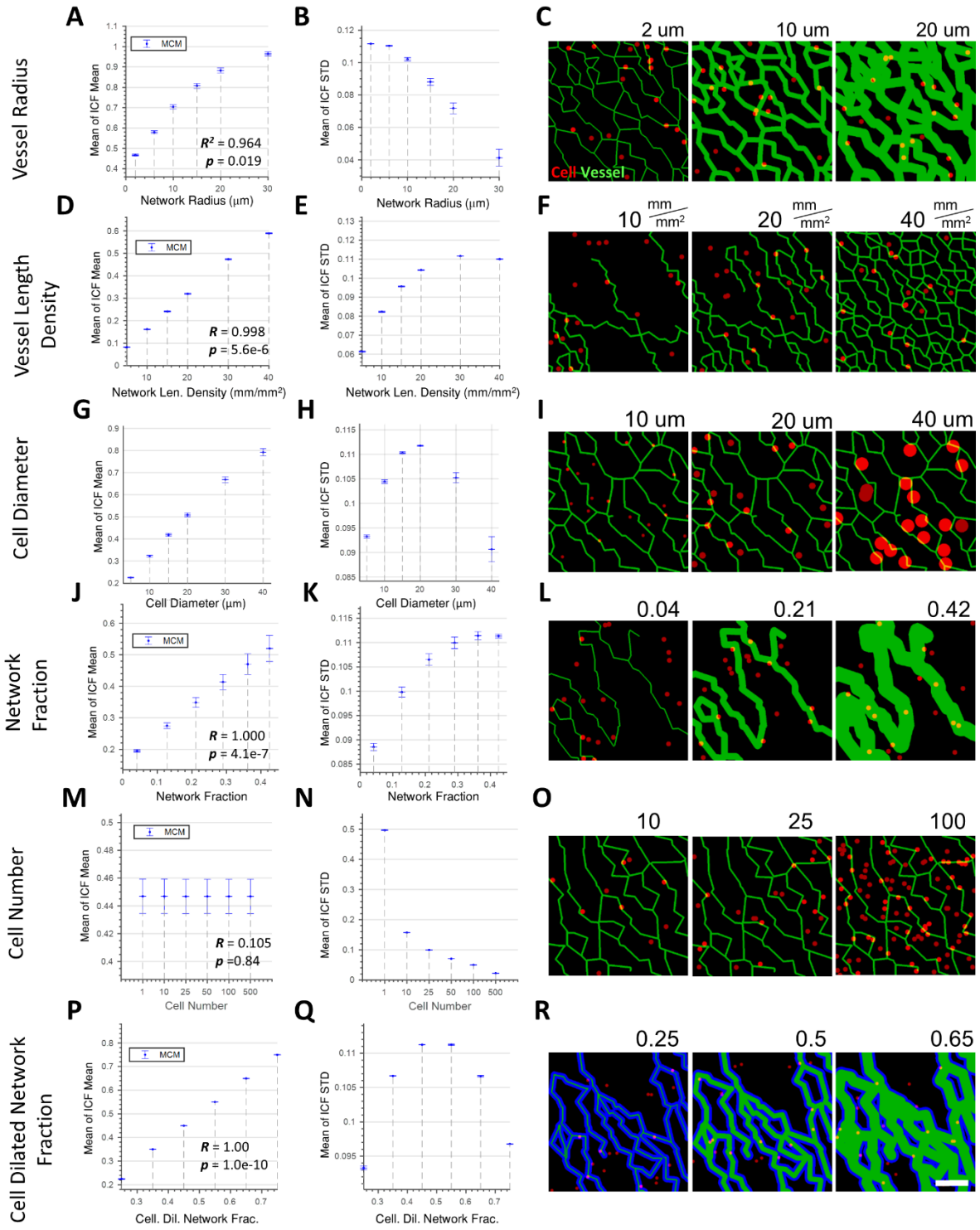

Supplemental Figure 3: Monte Carlo Model of random placement (MCMRP) reveals all parameters correlate with intercellular colocalization fraction except for cell number. Mean and standard deviation of mean ICF over sets of images with a single parameter varied, with Pearson correlation of mean ICF (N=8 generated image sets, 10,000 trials/image; red: cells, green: blood vessels). **(A, B)** Mean and standard deviation of mean ICF with varied network radius

(network length density 25 mm/mm^2, cell diameter 15 μm, 20 cells per image), **(C)** with example images labeled by network radius. (**D, E)** Mean and standard deviation of mean ICF with varied network length density (network radius 2.5, cell diameter 15 μm, 20 cells per image), **(F)** with example images labeled by network length density. **(G, H)** Mean and standard deviation of mean ICF with varied cell diameter (network length density 20 mm/mm^2, network radius 2.5 μm, 20 cells per image), **(I)** with example images labeled by cell diameter. **(J, K)** Mean and standard deviation of mean ICF with varied network fraction (network radius 2.5 μm, cell diameter 15 μm, 20 cells per image), **(L)** with example images labeled by network fraction. **(M, N)** Mean and standard deviation of mean ICF with varied cell number (network length density 20 mm/mm^2, network radius 2.5 μm, cell diameter 15 μm), with example images labeled by cell number (scale bar 100 μm, error bars are standard deviation).

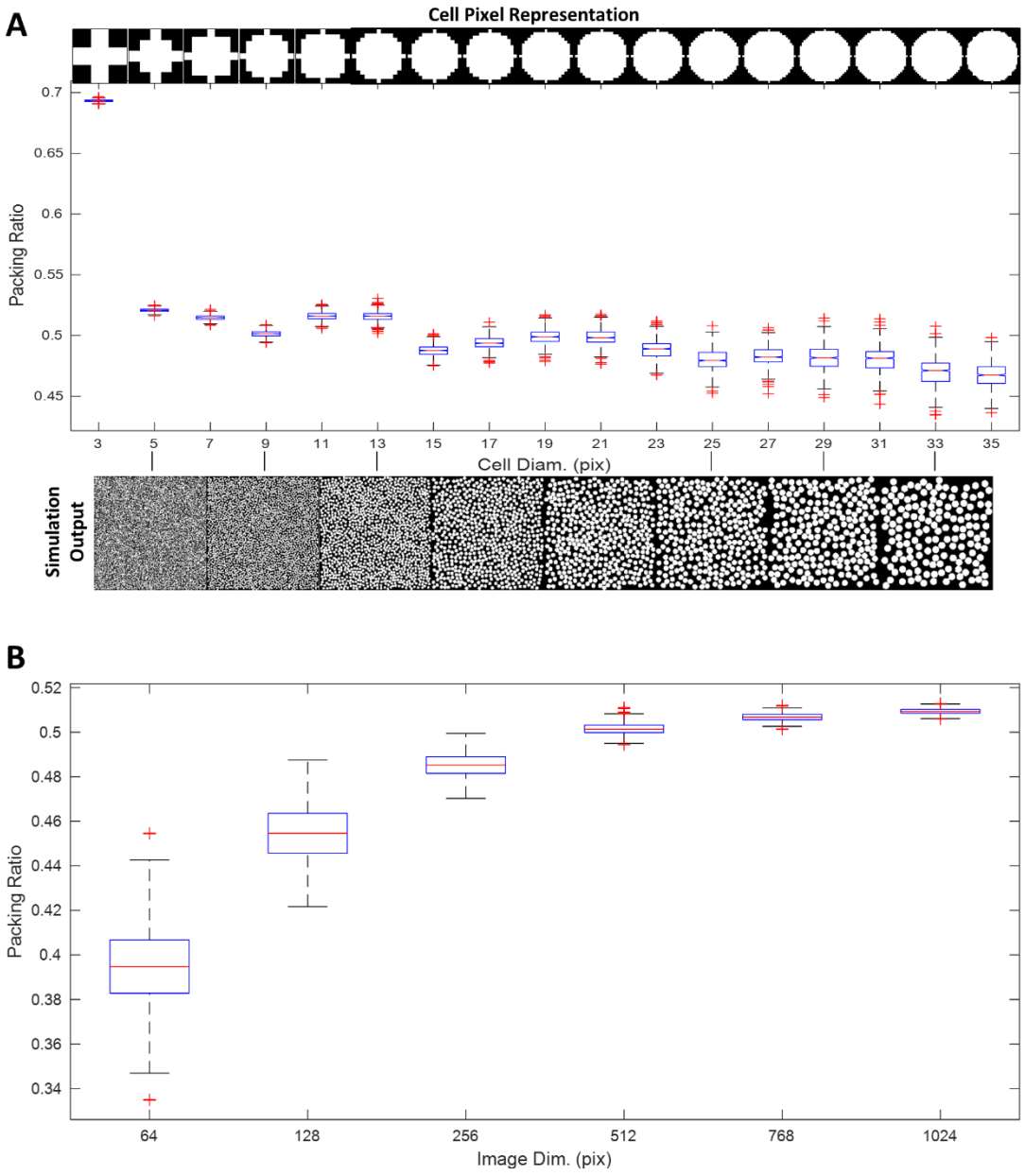

Supplemental Figure 4: Packing ratio of randomly placed cells changes with cell size and image dimension. (A) Packing ratio for non-overlapping fully contained randomly placed cells as a function of cell diameter, with example output images and kernel used to represent cells (p=0, Kruskal Wallis, N=100 trials, 512x512 simulated image). Kruskal Wallis used for unequal variances (p=0, Barlett's Test). For table of packing ratio by cell pixel diameter, see Supplementary Table 1. **(B)** Packing ratio as a function of image pixel dimension (p=0, Kruskal Wallis, N=100 trials, cell diameter 9 pixels). Kruskal Wallis used for unequal variances (p=0, Barlett's Test).

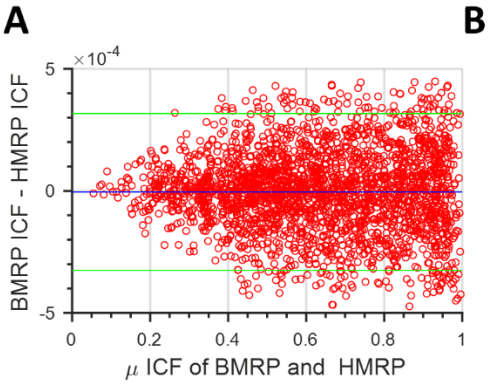

B

Multivariable linear regression of z-scored input parameters versus the z-score of the difference in mean ICF predicted by BMRP and HMRP (R^2 <0.00).

Predictor	Coefficient	SE	F-statistic	P-value
Intercept	-0.005	0.014		
Cell Diameter	-0.097	0.033	0	0.026
Cell Number	0.017	0.014	0.0084	0.418
Network Rad.	-0.040	0.048	0.397	0.585
Network Frac.	-0.078	0.067	97.18	0.425
Network Len. Dens.	-0.072	0.063	23.66	0.366
CDVF	0.160	0.070	9.504	0.060
Model			1.78	0.099

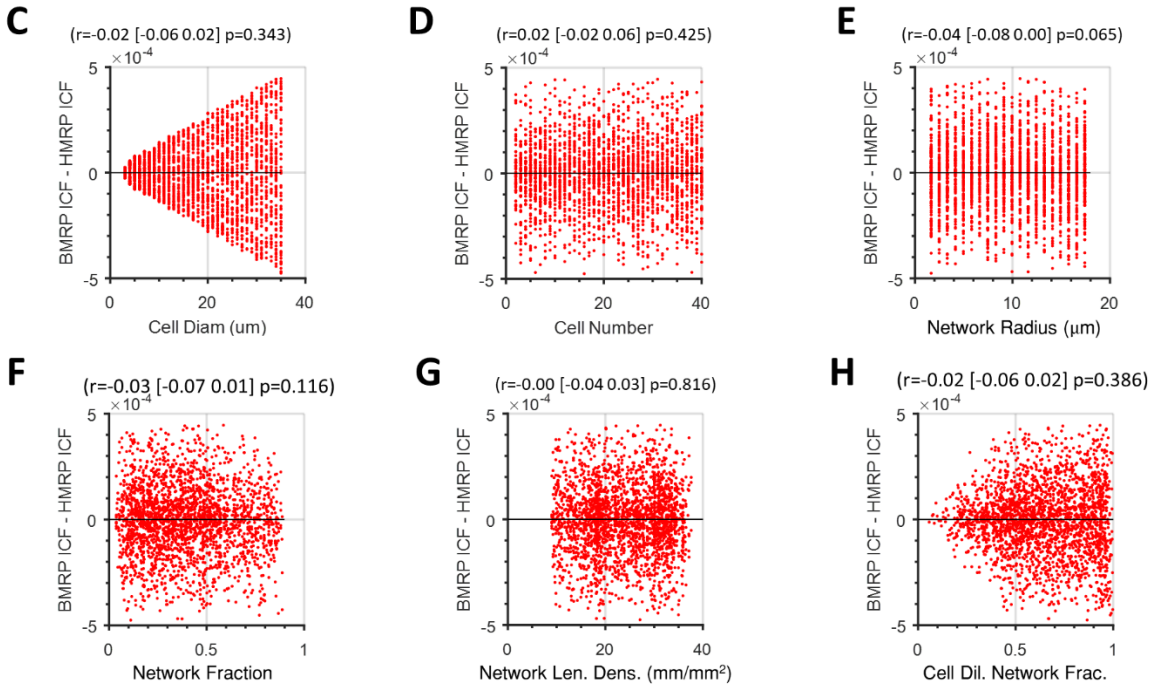

Supplemental Figure 5: Discrepancy between BMRP mean ICF and HMRP mean ICF versus the cell and vessel network input parameter values. (A) Bland Altman plot showing disagreement between models. **(B)** Multi-variate linear regression of z-scored predictors versus z-scored difference between models **(C-H)** Pearson correlation of each predictor versus difference between BMRP and MCMRP (Pearson r with [95 % CI] and p value).

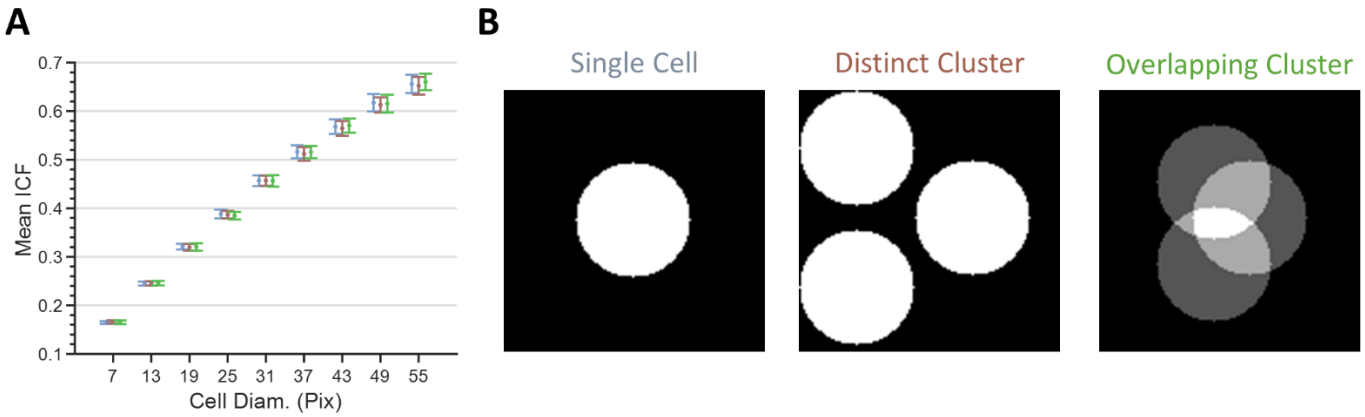

Supplemental Figure 6: Cells randomly placed in clusters yields no difference in ICF as randomly placed individual cells. (A) Plot of mean ICF from random cell placement (BMRP) over a range of cell diameters with either random placement of a single cell (Single Cell), random placement of a non-overlapping cluster of three cells (Distinct Cluster), or random placement of a cluster of three overlapping cells (Overlapping Cluster) ($p=0.996$ for cell placement method, 2-way ANOVA, error bars are 95% confidence interval of the mean, N=10 simulated vessel images with network length density of 15 mm/mm^2, 1000 simulations per data point). Each study group had the same total number of cells per trial in simulations ran, whether placed individually or in clusters. **(B)** Example images of cell kernels for each of the cell placement methods (21 cells placed in an image with pixel dimensions of 512 by 512, single vessel image used across all data points).

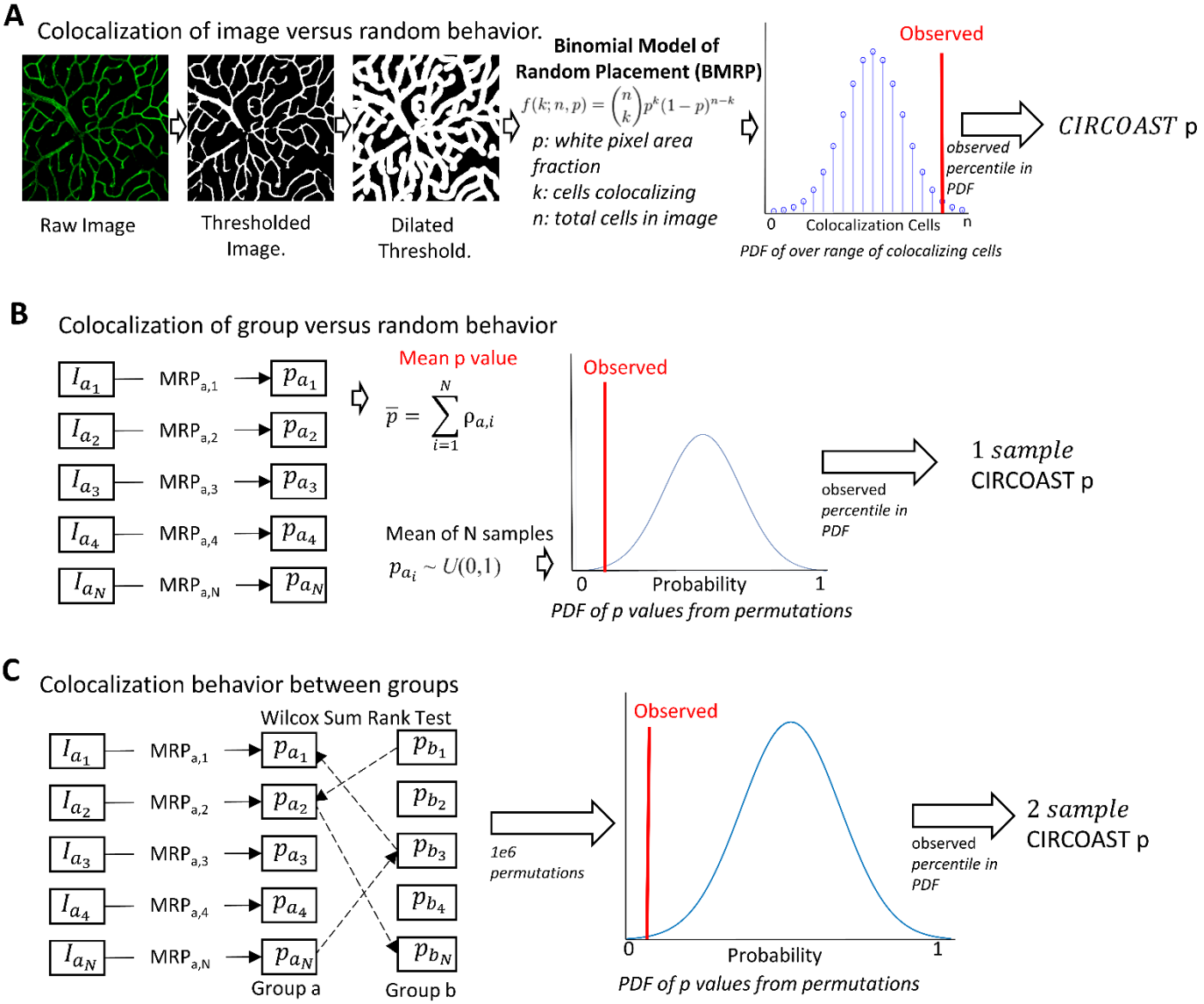

Supplemental Figure 7: CIRCOAST process pipeline for testing for non-random and unique colocalization between study groups. (A) The process to determine if a single image exhibits enriched colocalization, where the observed number of colocalizing cells is compared against a PDF generated by a model of random placement (MRP) to obtain a p value (either MCMRP, BMRP, or HMRP). **(B)** Process to determine if images from a study group exhibits enriched colocation over random behavior, where the mean of all the CIRCOAST p values from the images is compared to a PDF generated by p values assuming random behavior (sampled from a uniform PDF) to generate a 1-sample CIRCOAST p value. **(C)** Process to determine if colocation behavior using two study groups differs by comparing Wilcox Sum Rank Test of CIRCOAST p values compared to a PDF of WSRT of permuted samples to generate a 2-sample CIRCOAST p value.

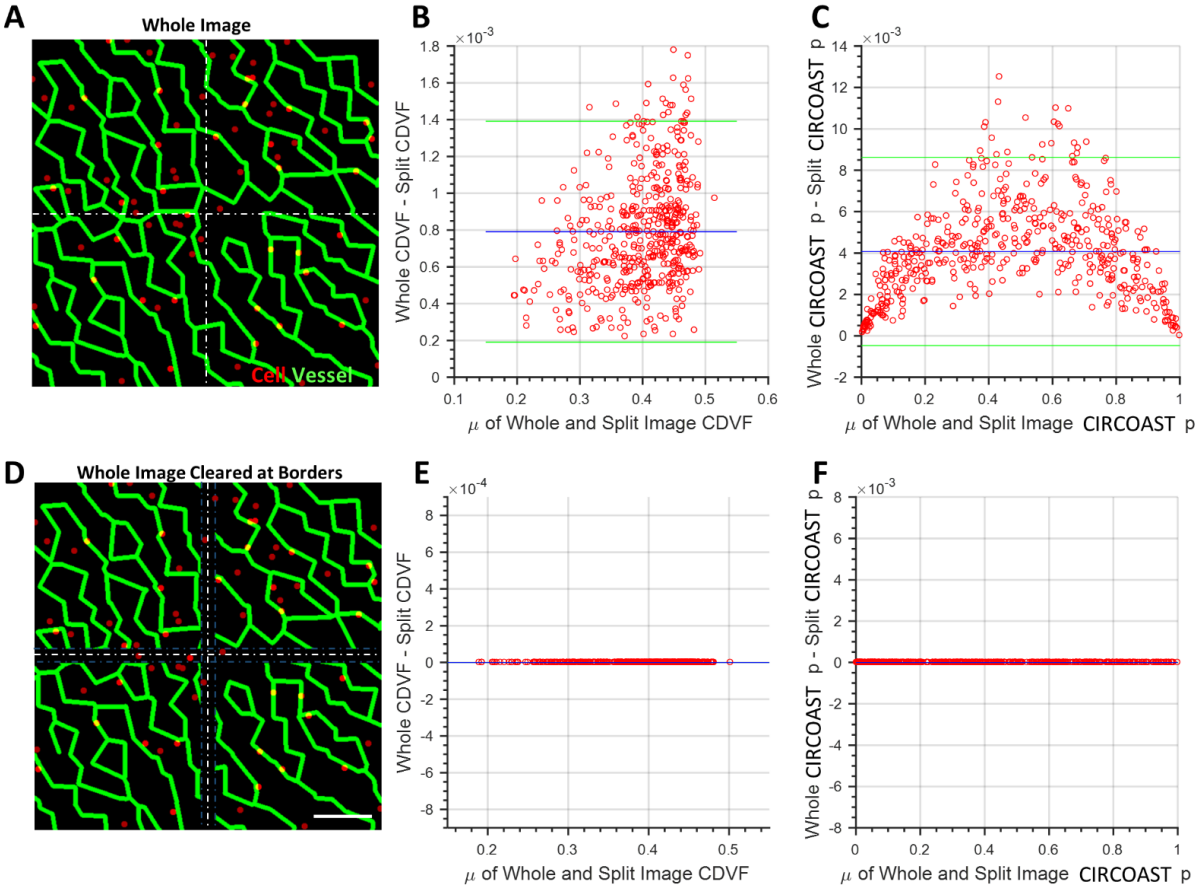

Supplemental Figure 8: Calculating the combined CDVF and summing injected cells across images yields the same CDVF and CIRCOAST p from an image before and after splitting. **(A)** A dataset of simulated vasculature and injected cells were generated, and the CDVF and CIRCOAST p value calculated for each image split into fourths (white line) compared to the original image, **(B)** revealing a small discrepancy in CDVF (p=6.60e-155, paired t-test) and **(C)** CIRCOAST p (p=4.75e-223, paired t-test) in split images versus whole. This disagreement was hypothesized to be from border effects of the split images, meaning the cell dilated vessel area from one split image could land across the image border to the adjacent image (an artifact of this validation test). **(D)** When the vasculature was removed one cell distance from the image border (white line) between sub images, the discrepancy no longer existed with **(E)** CDVF (p=NaN, paired t-test, values exactly the same) and **(F)** CIRCOAST p (p=NaN, paired t-test, values exactly the same) in the split images versus whole, indicating that this method is valid for combining information between images from a single biological replicate. N=500 images generated with vessel length density 29.4 ± 5.1 mm/mm^2 and 80 injected cells per field of view, with 8 µm cell size, scale bar 100 µm.

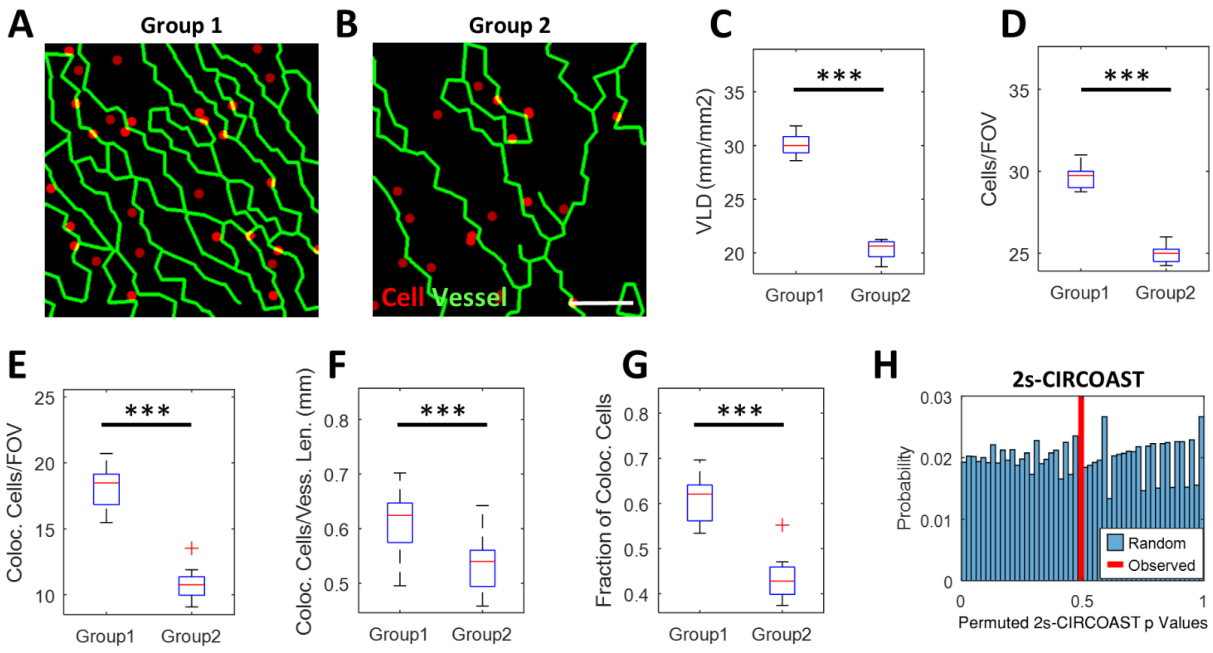

Supplemental Figure 9: Generic statistics leads to incorrect conclusions with ICF when confounded with cell and vascular density changes. A dataset of two study groups were generated, **(A)** one with high vascular and circular cell density (Group 1), **(B)** and one with lower vascular and circular cell density (Group 2) to represent the dropout seen in diabetes. Using the vessel network generator and Monte Carlo model (N=10 samples per group, n = 4 images per sample), cells were randomly placed in vascular images with a uniform distribution. A valid statistical method should reveal no changes in cellular colocalization behavior between groups. **(C)** Vessel length density decreased 33% (p=2.05e-14, 2 sample t-test) from group 1 (30.13±1.04 mm/mm2) to group 2 (20.24±0.98 mm/mm2). **(D)** Total cell density per field of view decreased 16% (p=2.07e-12) from group 1 (29.80±0.77cells) to group 2 (24.95±0.50 cells). **(E)** Examining the data by measuring colocalizing cells per FOV led to an erroneous conclusion that there was a 41% decrease in colocalization behavior (p=2.46e-09, 2 sample t-test) from group 1 (18.27±1.71cells) to group 2 (10.83±1.33 cells). **(F)** Examining the data by measuring colocalizing cells per vessel length (mm) led to an erroneous conclusion that there was a 12% decrease in colocalization behavior (p=1.12e-02, 2 sample t-test) from group 1 (0.61±0.06 cells per 1 mm vessel) to group 2 (0.54±0.05 cells per 1 mm vessel). **(G)** Examining the data by measuring the fraction of colocalizing cells led to the erroneous conclusion that there was a 30% decrease in colocalization behavior (p=6.68e-07, 2 sample t-test) from group 1 (0.61±0.05 cell fraction) to group 2 (0.43±0.05 cell fraction). **(H)** However, using the permuted binomial model of random placement for the cellular colocalization affinity with vasculature test, no change in colocalization behavior was correctly observed between groups (p=0.494 2-sample CIRCOAST, permuted WSRT, 1e7 permutations).

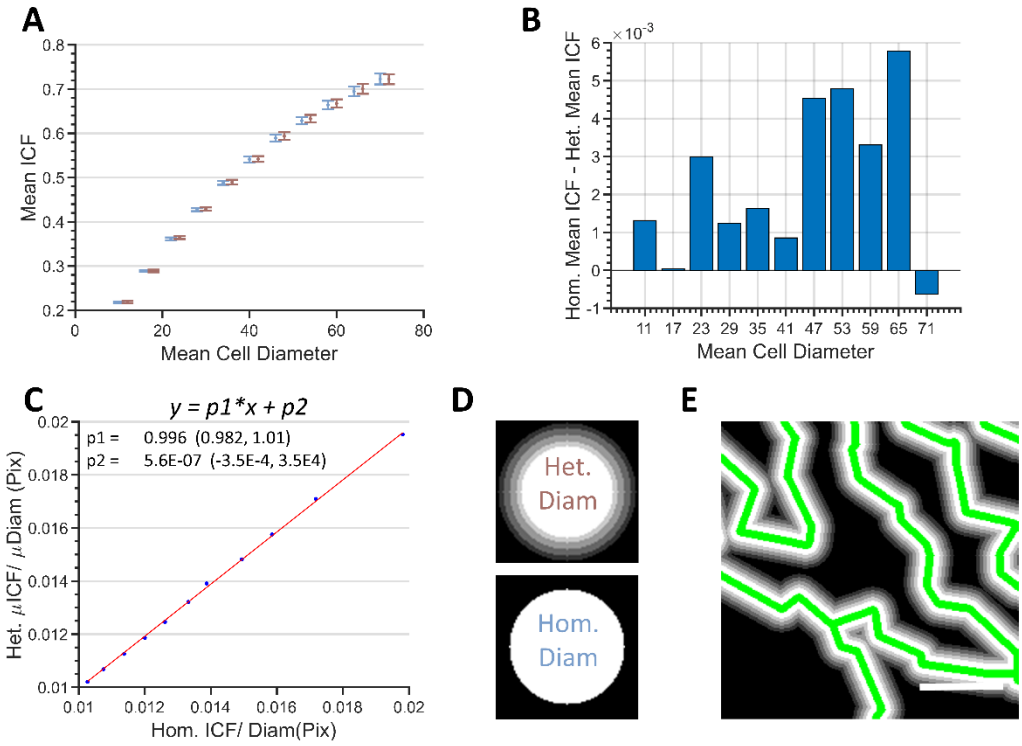

Supplemental Figure 10: Randomly placed cell populations of heterogeneous diameter yields similar ICF as cells with uniform mean diameter. **(A)** Comparison of mean ICF between random placement with the BMRP of homogenous cell size (blue) versus a heterogeneous mix of cell diameters (brown) around the homogenous value, showing a difference in mean ICF (p=0.038, paired t-test), but **(B)** very small effect size between groups (cell diameter sampled with uniform distribution from 90%, 95%, 100%, 105%, and 110% from mean, N=10 simulated vascular images with vessel length density of 15 mm/mm^2, 1000 simulations run per data point, error bars are 95% confidence error of the mean). **(C)** Since the mean of the sampled heterogeneous diameters do not exactly correspond to the homogenous cell diameter, ICF of heterogeneous group is normalized by mean of the sampled diameters (from the simulations run for each data point) compared to ICF of homogenous group normalized by diameter, with a fitted line whose 95% confidence interval (brackets) includes a value of one, suggesting a one to one correspondence between axes. **(D)** Example cell kernels used, with shades of gray in the heterogeneous diameter group denoting different size kernels. **(E)** Example vascular network image (green) with CDNF from a single set of cell kernels from the heterogeneous group (shades of grey, scale bar 25 um).

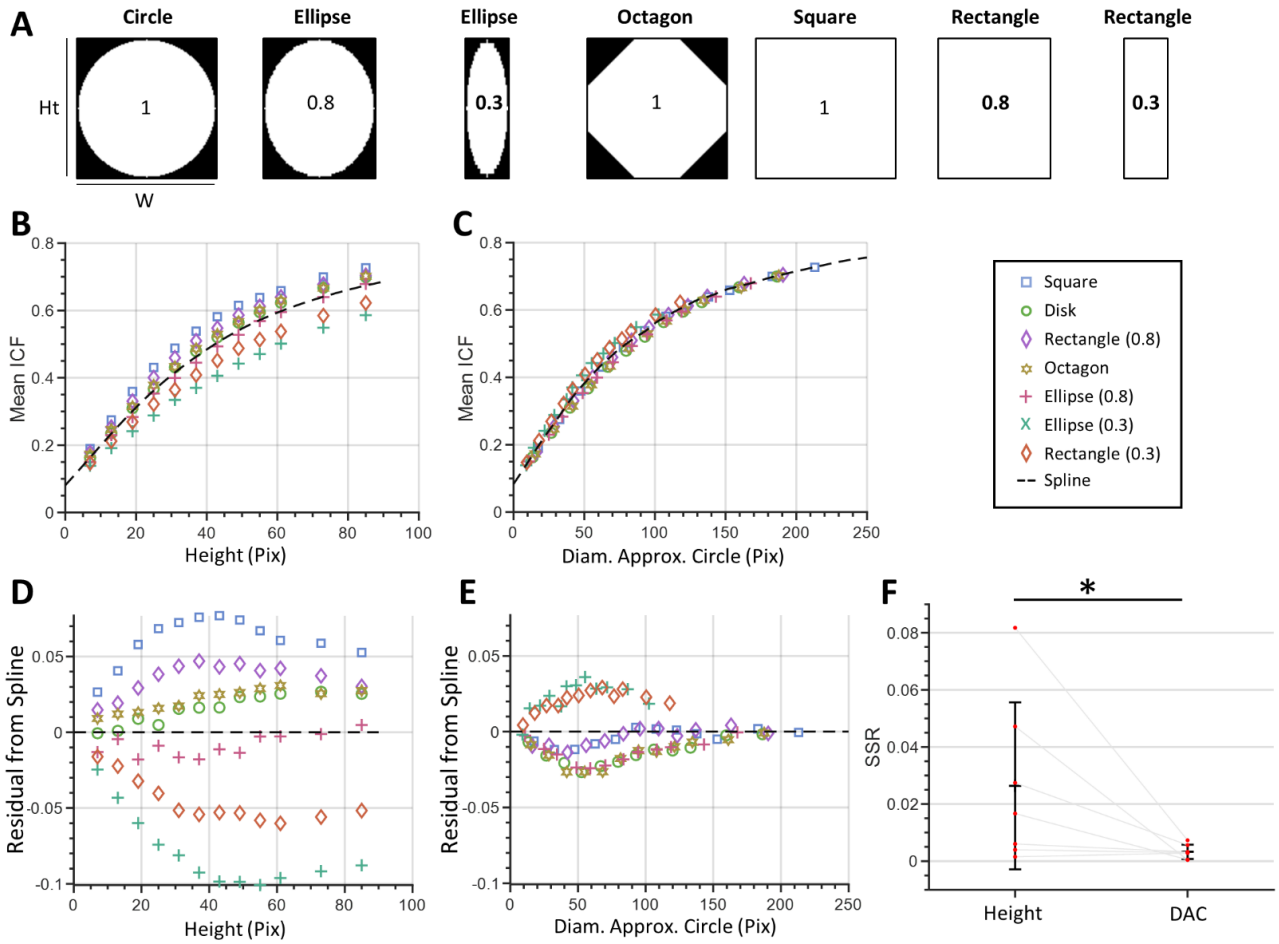

Supplemental Figure 11: Randomly placed geometric shapes have closer agreement with ICF when characterized by diameter-approximated circles (DAC) compared to cell height. **(A)** Library of kernels used to characterize how cell shape influences ICF from random kernel placement, with numeric values denoting the ratio between width and height. Kernels were characterized by either their height or the mean of their diameter-approximated circle (DAC), defined as the diameter of a circle whose area is equal to the area of the evaluated shape. The mean ICF from random placement was calculated using the BMRP for all shapes across a range of kernel sizes and plotted by both **(B)** Height and **(C)** DAC, with a smoothing spline fitted across all points (smoothing parameter 0.005 in MATLAB fit() function, N=10 simulated vascular images with vessel length density of 15 mm/mm^2, 1000 simulation runs per datapoint). The residuals of all shapes relative to the fitted smoothing spline by **(D)** Height and **(E)** DCA. **(F)** Sum of squared residuals (SSR) for the ICF from each of the shape groups compared to fitted smoothing spline, with an 82% reduction in mean SSR of DAC compared to Height (p= 0.0469, paired Wilcoxon signed rank test, N=7 shape types), and a 99.3% reduction in the variance of SSR of the DAC compared to Height (p=0.0157, paired permuted F-test, 1e6 permutations). (Data in (F) determined non-normal by One-sample Kolmogorov-Smirnov test: Height p=5.9E-13, DCA p=1.16E-8).

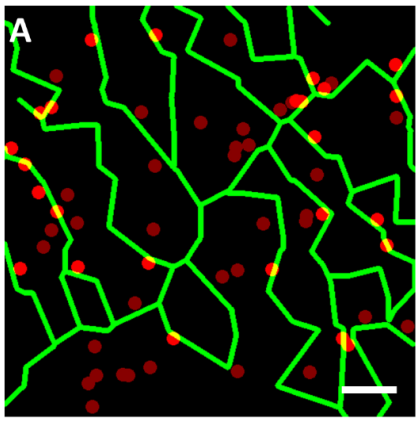

B

Model Description				Input Data			Output	
M#	Type	Cell Count	Cell Diam	Cell Count	% Clust	Cell Diam	Mean ICF	1s P Value
1	MCMRP	Actual	Actual	61	0	17	0.398	0.477
2	BMRP	Actual	Actual	61	0	17	0.399	0.484
3	BMRP	Obs., CC	Actual	61	0	17	4.000	0.328
4	BMRP	Obs., CC	Obs., DAC	50	31	20	0.435	0.524

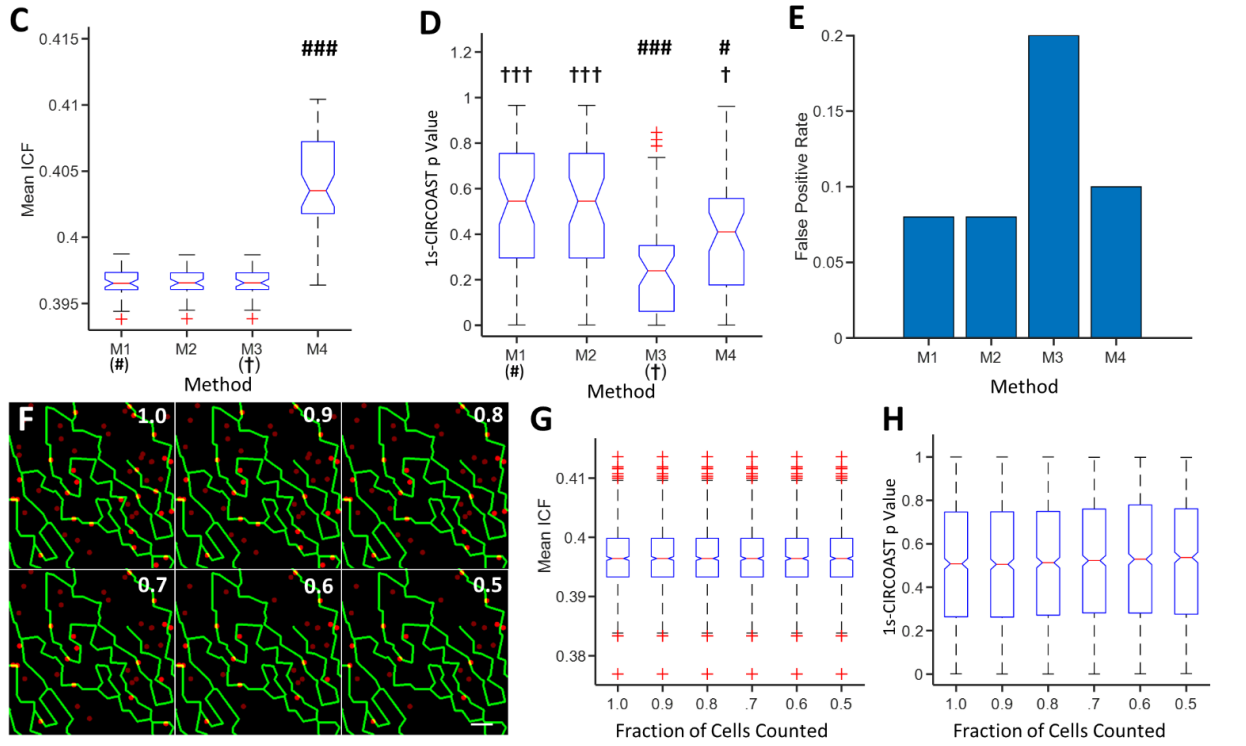

Supplement Figure 12: Variability in image analysis can change p values of CIRCOAST test. In order to investigate the effect of flawed input data on falsely altering the outcome of the CIRCOAST test, (**A**) a dataset of 2000 images were created with homogenous vessel length density (19.6 ± 0.12 mm/mm^2) and randomly seeded elevated total cell counts (60.4 ± 2.0 cells) to cause very significant overlap events to mimic a worst-case scenario of heavily flawed input data quantification (21.2% ± 1.1 cells part of multicellular clusters and misrepresented) (scale bar 100 um). Images were split randomly into 50 study groups with 20 images/ study group. (**B**) Four methods of analyzing the input data were used, with example output from a single image shown with the table: (Method 1: idealized) counting cells based on their coordinate (so all cells are counted correctly regardless of degree of overlap) and actual cell diameter using the MCMRP, (Method 2: idealized) counting cells based on their coordinate and actual cell diameter using the BMRP, (Method 3: flawed) cell counting based purely on connected components (worse case for cell counting, if cells touch they are considered one cell) and actual cell diameter using the BMRP,

(Method 4: flawed with mitigation) cell counting based purely on connected components and cell diameter calculated using the diameter approximated circle method (DAC) from mean connected components area using BMRP. (**C**) The mean ICF across all images in a study group was compared between methods (p=5.95e-54, 1 way ANOVA), along with (**D**) 1-sampe CIRCOAST p value for each study group (p=1.31e-07, 1 way ANOVA), and (**E**) false positive rate across study groups (# denotes significance from Method 1, † significance from Method 3). To model the effect of cell counting with missing cells in input images, (**F**) a portion of the cells in the input images were counted (100, 90%, 80%, 70%, 60%, 50%), and (**G**) mean ICF predicted by BMRP (p=1.0, 1 way ANOVA, N=2000 images/ study group) and (**H**) 1S CIRCOAST p values compared between groups (p=0.540, 1 way ANOVA, N=2000 images/ study group, tukey-kramer multiple comparisons) (scale bar 100 um).

Supplementary Table 1: Packing ratios of randomly placed non overlapping cells as a function of cell pixel diameter.

Cell Diam. (Pix)	Mean Pack. Ratio	STD Pack. Ratio
3	0.69325592	0.000914904
5	0.520709251	0.001339616
7	0.514762058	0.0019614
9	0.50140456	0.002446035
11	0.515966206	0.003274793
13	0.515891399	0.003867109
15	0.487618847	0.00450094
17	0.493858704	0.005078989
19	0.498641937	0.005734494
21	0.499130131	0.006595696
23	0.48872485	0.007417942
25	0.480217346	0.007926075
27	0.483155647	0.008468317
29	0.481239983	0.009415811
31	0.48027837	0.010227747
33	0.47099324	0.011287194
35	0.46812859	0.010955898
37	0.465189861	0.012521895
39	0.463105167	0.013354375
41	0.460029854	0.013564348
43	0.452998238	0.014227795
45	0.451910263	0.015901951
47	0.448864563	0.015581893
49	0.442819237	0.016561947
51	0.441543674	0.017762362
53	0.437041992	0.01872689
55	0.434697292	0.019495479

Note: Image dimension: [512 512], N=100 trials per cell diameter.

Supplementary Note 1: Monte Carlo Algorithm

The Monte Carlo simulation requires a binary image with vasculature in the image foreground (white pixels). For images that have high signal-to-noise ratio (SNR) for the vasculature, simple thresholding controls are provided within the GUI so the user can produce a binary vasculature image with minimal effort. Alternatively, for images that are more difficult to analyze due to low SNR, uneven background signal, or low contrast, the user can process these images with specialized image processing routines using an external program such as ImageJ, Photoshop, MATLAB, or Python, export the binary, and import it into CIRCOAST.

When the user first imports an image, the program displays the image data and determines whether it is a binary. If the image is not binary, it is converted into an 8-bit RGB and the user has the option to activate thresholding on one or multiple of the three channels with the controls on the right side of the program window. The vertical slide bars are used by the user to select a relative threshold for that channel that is scaled to the image's maximum pixel value. The threshold is computed and displayed in real time as the settings are adjusted. With the default behavior, any pixel greater than the threshold will become a white foreground pixel, but this can be inverted for each channel independently. If thresholding is completed on multiple channels, the resulting binary image is the union of the results from each channel.

Once a proper binary image of the vasculature is produced, the user sets the resolution of the image, the average diameter of the injected cell, the total number of injected cells found in that particular field of view, and the total number of trials run for the simulation. To initialize the Monte Carlo simulation, the user runs a single trial and examines the simulated cell size in the output image to verify that it qualitatively resembles those observed experimentally. This first trial also allows the program to provide a rough conservative estimation of the execution time for the entire simulation, and also calculate how many trials can be calculated concurrently based on the amount

of memory that is available to MATLAB for that system. When the full simulation is run, the program runs trials in batches, trading system RAM for accelerated execution speed, and provides updates with progress and time to completion.

The segmented vasculature undergoes a Euclidean distance transform to yield an image where each black pixel contains the distance to the closest white foreground pixel (vasculature). Sets of pixel coordinates that represent the locations of cells from a single trial are used to calculate the distance of each cell to the vasculature by sampling pixel values of the Euclidean distance transformed image of the vasculature. The distance values obtained from each cell are thresholded by the radius of the injected cell: cell distances less than or equal to the injected cell radius are considered colocalizing with the vasculature. The fraction of cells colocalizing is calculated for each trial, and the process is repeated until all of requested trials for the simulation is complete. The mean and standard deviation of the intercellular colocalization fraction is calculated across all trials and displayed as output.

Supplementary Note 2: Algorithm for Vessel Network Generator

The vessel network generator can create vessel networks with finely tuned parameters in a stochastic fashion. A point cloud is generated that marks the location of avascular areas in the network, and vessel segments are generated by applying a watershed, bisecting all points and creating a fully connected network with a honeycomb appearance. Points are iteratively added until a fully connected target vessel length density (VLD) or vessel area fraction (VAF) is reached, and then vessel segments are stochastically removed until a target final VLD or VAF is reached. Segments are removed according to a set of rules to reduce the density and interconnectedness of the network while maintaining the appearance of a vascular bed found *in vivo*.

To generate the point cloud used to seed the watershed segmentation, locations in a binary

image are marked iteratively with a uniform probability distribution. To avoid populating points too closely, the image indices around each point added are removed from the list of possible spawn locations for future points. After each point is added, a watershed is computed on the image and the VLD and VAF is calculated. If these values exceed the target values for the initial fully connected network, then the process of adding spawn point ceases, otherwise it continues until this condition is satisfied or no available spawn points are left in the image.

Once the vascular network has been populated, line segments are then iteratively removed and VLD and VAF is calculated until the final target value is reached. Line segments are prioritized with a scoring system that factors in segment orientation, line segment length, hole area that segments border, and whether the segment connects to an endpoint in the network. Additionally, the score is influenced with random probability to provide a stochastic element to the regression of vessel networks. The segments with the highest score is removed, and then all segments are rescored for each iterative round.

Supplementary Note 3: Cell Sources

Cell Sources: Human umbilical vein endothelial cells (HUVECS) were generously donated by Dr. Brian P. Helmke (University of Virginia). Mouse adipose-derived stem cells (mASCs) were obtained by adapting the previously described protocol (Mendel et al. 2013; Cronk et al. 2015 Mar 13). Briefly, epididymal fat pads of male mice were digested in type I collagenase digestion buffer for 1 h at 37°C. Digested tissue was filtered through a 200-μm mesh to discard undigested tissue, and excess collagenase was removed through centrifugation. Collected cells from centrifugation were incubated in red blood cell lysis buffer (eBioscience) for 5 min to remove red blood cells. The remaining cells were filtered through a 70-μm filter, and plated on tissue cultured treated

plastic.

Isolated HUVECs were cultured on tissue culture treated plastic (Corning) in Endothelial Basal Medium-2 (Cat. no. CC-3156, Lonza supplemented with Endothelial Cell Growth Medium-2 SingleQuot Kit Supplements and Growth Factors (Cat. no. CC-4176, Lonza, Walkersville, MD). mASCs were cultured on tissue culture treated plastic (Corning) in Gibco DMEM/F12 supplemented with 10% FBS and 1% Antibiotic-Antimycotic. Cells were passaged once they were 80% confluent using Stempro® Accutase® (Thermo). HUVECS were used from passage 7 to 10 in all studies, and mASCs were used from passage 4 to passage 6 in all studies. All cells were incubated at 37°C, 5% CO2, and 95% humidity.

Supplementary Note 4: In Vitro and In Vivo Validation

In Vitro validation: 200 μL of Cultrex® Basement Membrane Extract (BME) Reduced Growth Factor (Cat. no. 3433-005-01, Trevigen, Gaithersburg, MD) was added to the single wells of 8-well Nunc™ Lab-Tek® II Chamber slides (Cat. no.154534, Thermo Scientific, Waltham, MA), and the chamber slides were incubated at 37°C to solidify the BME. Prior to seeding in BME, HUVECs were labeled with Vybrant® DiO Cell-Labeling Solution (Cat. no. V22886, Thermo Scientific), and mASCs were labeled with Vybrant® DiI Cell-Labeling Solution (Cat. no. V22885, Thermo). A total of 40,000 HUVECs were added to each individual well in the chamber slides that contained BME. Immediately after seeding the HUVECs, 400 DiI-labeled mASCs, and/or FluoSpheres® Polystyrene Microspheres (Cat. no. F21012/F8843, Thermo) were immediately added to each individual well. 24 h after seeding the appropriate cells and microspheres in the BME, the network assays were imaged using a Leica TCS SP2 confocal with a DMIRE2 inverted micro-scope to determine the colocalization of microspheres and mASCs to the HUVEC network.

In Vivo Validation: All procedures performed with mice conformed to the guidelines within the ARVO Statement for the Use of Animals in Ophthalmology and Vision Research and were approved by the University of Virginia's Animal Care and Use Committee. Using previous techniques (Mendel et al. 2013), C57Bl/6J mice were immersed in 75% O2 from postnatal day 7 (P7) to postnatal day 12 (P12). At postnatal day 12, mice were returned to normoxia and 10,000 viable mASCs in 1.5 μL of PBS were injected into the vitreous gel of the eye. In the contralateral eye, 10,000 dead mASCs were injected in 1.5 μL of PBS. Dead cells were exposed to 4% PFA for 10 minutes and then washed with PBS. All cells were labeled with Vybrant® DiI Cell-Labeling Solution (Thermo) prior to intravitreal injections. Mice were euthanized 4 weeks post-intravitreal injections, and the eyes were harvested and fixed in 4% PFA for 10 min. Retinas were then dissected from each eye, flat-mounted on coverslip glass, and permeabilized with 1 mg/mL digitonin. Retinas were stained with isolectin GS-IB4 Alexa Fluor 647 Conjugate (Cat. no. I32450, Thermo) and SYTOX® Green Nucleic Acid Stain (Cat. No. S7020, Thermo). Retinas were imaged using a Leica TCS SP2 confocal with a DMIRE2 inverted microscope to determine the colocalization of micro-spheres and mASCs to the HUVEC network.

Supplementary Note 5: Image Acquisition, Thresholding, and Quantification

Image Acquisition: All biological samples were imaged on a Leica TCS SP2 confocal with Nyquist sampling. Retina samples were imaged with a 20X (0.7 NA, air, HC PL APO) objective lens and a confocal pin size of 2.38 AU, where a 20 μm z-directional volume was obtained at a sampling rate of 2 μm per optical z-slice. Frame-averaging was set at 2 and images were collected at a scan speed of 400 Hz. Pixel Resolution was set at 1024x1024 resulting in an image resolution of 0.791 μm/pix. Sytox Green and isolectin IB4 was imaged sequentially by laser excitation of 458 nm and 633 nm, respectively. For this laser excitation, emission bandpass filters were set at 470-

55 nm and 650-750 nm to collect the fluorescent signal. DiI was imaged at a laser excitation at 561 nm and the fluorescent signal was collected at an emission bandwidth of 575-625 nm.

Similarly, cell and bead cultures were imaged using a 10X (0.3 NA, air, HC PL FLUOTAR) objective lens with a confocal pin size of 2.38 AU, where a 300 µm z-directional volume was obtained at a sampling rate of 16 µm per optical z-slice. Frame-averaging was set at 2 and images were collected at a scan speed of 400 Hz. Pixel resolution was set at 1024x1024 resulting in an image resolution of 1.56 µm/pix. DiO and FluoSpheres™ Polystyrene Microspheres 645/680 (Thermo) were imaged concurrently by laser excitation of 488 nm and 633 nm, respectively. Emission bandpass filters were set at 500-550 nm and 650-750 nm to collect the fluorescent signals. DiI was imaged at a laser excitation at 561 nm and the fluorescent signal was collected at an emission bandwidth of 575-625 nm.

Image Acquisition Rationale: It is recommended that z stack sampling be as close to Nyquist sampling as is practical to capture all cell structures that could define colocalization events. Image acquisition parameters and z-stack volume should be kept constant between study groups to minimize any bias that the imaging could introduce. In terms of how much volume should be covered in a z-stack, it should large enough to capture the vessel network and enough COIs, but the larger the volume the greater chance for false positives from overlap between objects that are not actually colcoalized in the z axis.

Image Thresholding: The DiO channel that labeled endothelial cells in the in co-culture experiment was processed by thresholding with an adaptive median-filtered background subtraction. In short, the DII channel was blurred with a median filter kernel 200 pixels in size,

which was subtracted from the original image to create the foreground image. The foreground image was thresholded for values greater than 40 to be considered to be pixels marking endothelial cells. The segmented image was saved to disk and used for the CIRCOAST test.

For the in vivo images, IB4 lection was used to label the vessels, but lectin can also label activated microglia, macrophages, and the injected ASCs. However, vessel structures were differentiated from other lectin-positive cell types based on thickness, continuity of the network, and uniform edge. The images were preprocessed in an unbiased manner by loading the lectin channel in isolation into Photoshop and removing non-vessel lectin+ structures manually with the eraser tool. The images were then thresholded with a global value that was manually set for each image to capture the vascular network based on visual inspection. The binary images saved for input for the CIRCOAST test.

Image Quantification: colocalization was manually quantified in a blinded manner with the thresholded network channel overlaid with the channel for the cell of interest using ImageJ CellCounter Plugin (Rueden et al. 2017). Cells of interest were approximated with a circular shape based on mean area of twenty cells sampled per study group. For the in vitro experiment, live ASC cell diameter was 28.8 ± 6.0 μm and microspheres were 35.4 ± 1.2 μm. For the in vivo experiment, live ASC cell diameter was 14.7 ± 3.3 μm and dead ASC diameter was 12.1 ± 1.1 μm.